XMM

XMM Users' Handbook

Issue 1.1

Edited by: M. Dahlem
Simulations by: N. Schartel

Based on input from the entire **XMM** SOC Team

18.01.1999

Extensive contributions from the members of the **XMM** Science Working Team, the SSC, the Instrument Teams and NASA's **XMM** Guest Observer Facility are gratefully acknowledged.

Revision history

Revision number	Date	Revision author	Comments
Draft 3.0	August 1998	M. Dahlem	Complete draft
Issue 1.0	23.09.1998	M. Dahlem	Official release
Issue 1.1	18.01.1999	M. Dahlem	Release of Cal/PV/GT target tables

Contents

List of Figures

List of Tables

1 Glossary

For more information on frequently used technical terms, see also the **XMM** Glossary.

Acronym	Explanation
ADU	Analogue to Digital Unit
ACIS	*AXAF* CCD Imaging Spectrograph
ADU	Analogue to Digital Unit
AHF	Attitude History File
AMA	Absolute Measurement Accuracy
AO	Announcement of Opportunity (AO-1)
AOCS	Attitude and Orbit Control and Measurement Subsystem
AMS	Archive Management Subsystem
AXAF	Advanced X-ray Astrophysics Facility
CAL	Calibration Access Layer
CCD	Charge Coupled Device
CCF	Current Calibration File
CTE	Charge Transfer Efficiency
CVZ	Continuous Viewing Zone
DEC	Declination, δ(J2000)
DPU	Digital Processing Unit
EPIC	European Photon Imaging Camera
ERMS	EPIC Radiation Monitor Subsystem
ESTEC	European Space Research and Technology Centre
EW	Equivalent Width
FAQ	Frequently Asked Question
FITS	Flexible Image Transport System
FM	Flight Module
FOV	Field Of View
FWHM	Full Width at Half Maximum
GO	Guest Observer
GT(O)	Guaranteed Time (Observer)
GTI	Good Time Interval
GUI	Graphical User Interface
HEASARC	(NASA) High Energy Astrophysics Science Archive Research Center
HED	High Energy Detector (of the ERMS)
HEW	Half Energy Width
HER	RGS high event rate (selectable mode)
HETG	(*AXAF*) High Energy Transmission Grating
HRC	(*AXAF*) High Resolution Camera
HTR	High Time Resolution (mode of the RGS)
LED	Low Energy Detector (of the ERMS)
LETG	(*AXAF*) Low Energy Transmission Grating
LSF	Line-spread Function
METG	(*AXAF*) Medium Energy Transmission Grating

MOC	**XMM** Mission Operation Centre
MOS	Metal Oxide Semi-conductor
OBDH	Onboard Data Handler
OCB	On-Chip Binning
ODF	Observation Data File
ODS	Observation Data Subsystem
OGIP	(NASA's) Office of the Guest Investigator Program
OM	Optical Monitor
OTAC	Observatory Time Allocation Committee
PHA	Pulse Height Analyser
PHS	Proposal Handling Subsystem
PI	Principal Investigator
PPS	Pipeline Processing Subsystem
PSF	Point-Spread Function
PV	Performance Verification
QE	Quantum Efficiency
RA	Right Ascension, α(J2000)
RFC	RGS Focal Camera
RFS	Refreshed Frame Store mode of EPIC MOS
RGA	Reflection Grating Assembly (of the RGS)
RGS	Reflection Grating Spectrometer
RPE	Relative Pointing Error
XRPS	Remote Proposal Submission
SAS	Science Analysis Subsystem
SDF	Slew Data File
SER	RGS split event reconstruction (selectable mode)
SES	RGS single event selection (selectable mode)
SGS	Sequence Generator Subsystem
SMP	Science Management Plan
SOC	**XMM** Science Operations Centre
SSC	Survey Science Centre
SSD	Software Specification Document
TBC	To Be Confirmed
TBD	To Be Determined
TOC	Table of contents
ToO	Target of Opportunity
UHB	**XMM** Users' Handbook
URD	User Requirements Document
URL	Unique Resource Location
$W90$	90% energy width
WWW	World Wide Web
XDA	**XMM** Data Archive
XID	X-ray source identification (by the SSC)
XMM	X-ray Multi-Mirror Mission

2 Introduction

2.1 Scope of this document

This document is designed to be the starting point for **XMM** users in the search for information on the satellite. Users working with a printed (postscript or PDF) version of this document, please note that the online **XMM** Users' Handbook (UHB) is full of links to other components of our web-based information system (and other, external servers). Also, most of the figures are colour based and some do not reproduce well in black and white. Various appendices also provide introductions and links to other online services of the **XMM** Science Operations Centre (SOC) and the Survey Science Centre (SSC).
The **XMM** UHB is primarily intended to serve as a proposal preparation document, based on which potential **XMM** users will be able to assess the technical feasibility of their planned observations and the expected data quality. Details on how to fill out the proposal submission forms of the **XMM** Remote Proposal Submission (XRPS) software will be described in a separate document, the XRPS Users' Manual, which will become available at the time of the software release.
In addition, this document provides an overview of all aspects of **XMM** data calibration and analysis.

2.2 Structure and contents of the Users' Handbook

This document contains, in the order listed here:

1. A concise summary of **XMM**'s properties and the instruments onboard, intended for use as a guideline for observers writing **XMM** proposals, and a short description of how to conduct observations with **XMM**. Most of the information needed for this purpose is contained in § 3 and § 4 and some of the appendices (the necessary links are provided in §§ 3 and 4).

2. The next chapter (§ 5) describes the **XMM** Guest Observer (GO) program.

3. A brief description of the **XMM** Data Archive (**XMM** Data Archive; § 7) and of the data calibration and analysis, (§ 6), which also introduces the **XMM** Science Analysis Subsystem (SAS) software. Only users whose observations have been conducted successfully will need to read these chapters.

4. Appendices on related issues, like e.g., the **XMM** Science Simulator (SciSim; Appendix A) and the **XMM** Survey Science Centre (SSC; Appendix B), and lists of **XMM** Calibration & Performance Verification (Cal/PV) targets (Appendix C) and the **XMM** Guaranteed Time (GT) programme (Appendix D).

CAVEAT: The information contained in this document represents the best *current* understanding of **XMM** at the time of release. Since no in-flight data (and no in-flight calibration) are available yet, no guarantee can be given for the correctness of the information provided below. Updates, if necessary, will be made as soon as possible after evaluation of incoming new information.

The information contained in §§ 3, 4 and 5 and appendices A, C and D should supply sufficient detail to enable the reader to prepare the submission of an XMM observing proposal via the XMM Remote Proposal Submission software (XRPS). Note: The XRPS Users' Manual will be available on 1999 January 4.

2.3 Location

This document forms part of the online **XMM** SOC documentation server on the WWW, at the URL `http://astro.estec.esa.nl/XMM/`. The URL of the interface document leading to the **XMM** Users' Handbook is

`http://astro.estec.esa.nl/XMM/user/uhb_top.html`.

2.4 Sources of information

If not indicated otherwise (either in the text or in the captions accompanying the figures), information presented in this document comes from model simulations using the **XMM** Science Simulator (SciSim).

Only some figures display actual (ground-based) measurements.

Information on flux to count rate conversions comes from the HEASARC PIMMS software provided by the **XMM** Guest Observer Facility at NASA's Goddard Space Flight Center, based on datafiles provided by the **XMM** SOC, which were generated using SciSim 2.0.1.

2.5 Updates on this document

While the **XMM** SOC is being developed, this document will undergo updates and expansions. Updates will always be posted in the **XMM** Latest News section of our web server and the version number of the latest release of the UHB is always visible in the **XMM** Users' Handbook introduction page leading to this document.

No changes will be made to this document during a call for proposals, except possibly for the addition of previously unavailable information.

2.6 How to obtain further help and information

The Users' Handbook is an integral part of the SOC's web-based online information system and it contains lots of links to other components of the web server. All links can also always be reached via the SOC home page.
Additionally, in order to facilitate the search for more information, § 8 of this document contains a compilation of relevant links and references.
The contact address for users who need help or additional information, or who want to send suggestions to improve our system, is **xmmhelp@astro.estec.esa.nl**. All questions relating to AO and observing matters should be directed to this account. The SOC plans to collect users' questions and list them in a file with Frequently Asked Questions (FAQs). A link to this file will then be added here.

3 XMM – a concise overview

XMM is the second of ESA's four "cornerstone" missions defined in the Horizon 2000 Programme. Its scheduled launch date is 2000 January 21. It will carry two distinct types of telescopes: three Wolter type-1 X-ray telescopes, with different X-ray detectors in their foci (which are described in this chapter), and a 30-cm optical/UV telescope with a microchannel-plate pre-amplified CCD detector in its focal plane (see also below). Thus, **XMM** offers simultaneous access to two windows of the electromagnetic spectrum: X-ray and optical/UV.

XMM provides the following three types of science instruments:

1. European Photon Imaging Camera (EPIC)

   3 CCD cameras for X-ray imaging, moderate resolution spectroscopy, and X-ray photometry; the two different types of EPIC cameras, MOS and pn, are described in § 3.3. **XMM** will carry 2 MOS cameras and one pn.

2. Reflection Grating Spectrometer (RGS)

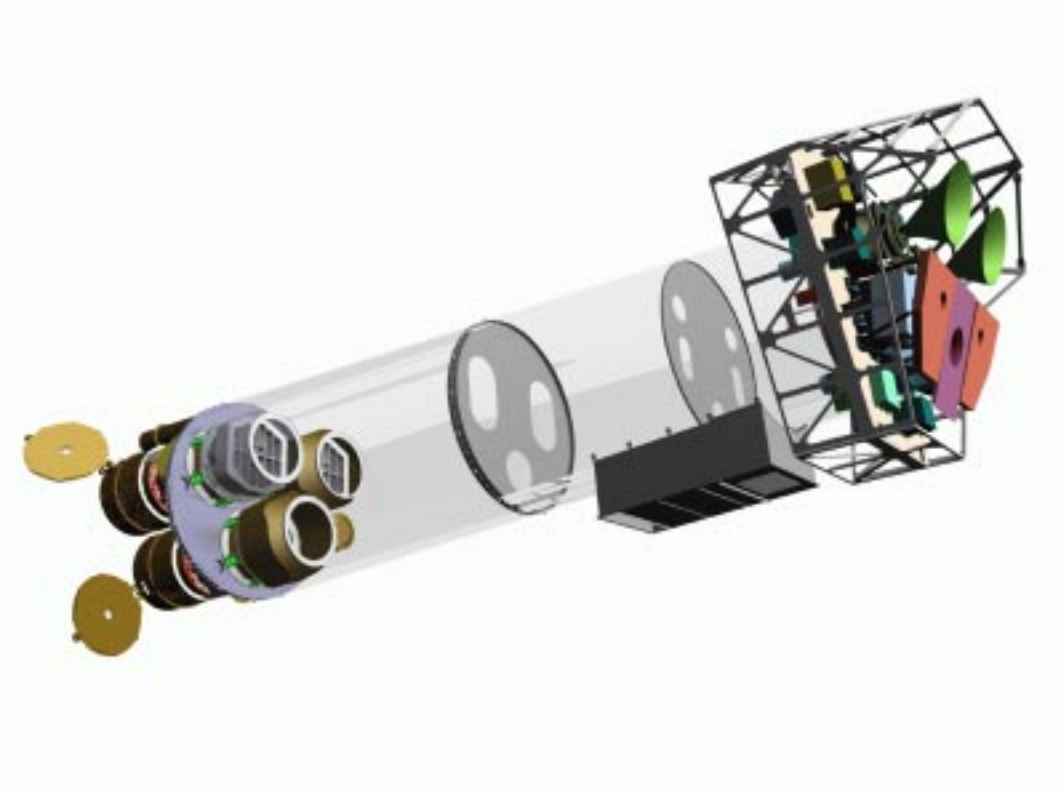

Figure 1: *Sketch of the* **XMM** *payload. The mirror modules, two of which are equipped with Reflection Grating Arrays, are visible at the lower left. At the right end of the assembly, the focal X-ray instruments are shown: The EPIC MOS cameras with their radiators (black/green "horns"), the radiator of the EPIC pn camera (violet) and those of the (light blue) RGS detectors (in pink). The OM telescope (orange) is obscured by the lower mirror module. Figure courtesy of Dornier Satellitensysteme GmbH.*

2 essentially identical spectrometers for high-resolution X-ray spectroscopy and spectro-photometry (§ 3.4).

3. Optical Monitor (OM)

   for optical/UV imaging and grism spectroscopy; § 3.5 provides an overview.

The three EPIC cameras and the two detectors of the RGS spectrometers reside in the focal planes of the X-ray telescopes, while the OM has its own telescope. A sketch of the **XMM** payload is displayed in Fig. 1. **There are in total six science instruments onboard XMM, which are operated simultaneously** (unless prohibited by constraints, like e.g., excessive target brightness). The instruments can be operated independently and each in different modes of data acquisition. Observers will receive data from all science instruments.

3.1 Basic characteristics

The most important characteristics of **XMM** are compiled in Table 1. More detailed numbers will follow in the chapters on the individual instruments (below) and a comparison with other X-ray satellites is provided in § 3.7. The basic characteristics of **XMM** are:

- Simultaneous operation of all science instruments

  If not prohibited by target brightness constraints, all six **XMM** science instruments operate simultaneously. They work independently (i.e., exposures of the individual instruments do not necessarily start and end at the same time).

- High sensitivity

  XMM carries the X-ray telescopes with the largest effective area of a focussing telescope ever: the total mirror geometric effective area at 1 keV energy is ca. 1550 cm^2 for each telescope, i.e., 4650 cm^2 in total.

- Good angular resolution

  XMM's high sensitivity is achieved by using 58 thin nested mirror shells in each X-ray telescope. The achieved point-spread function (PSF) has a full width at half maximum (*FWHM*) on the order of $6''$ and a *HEW*, at which 50% of the total energy are encircled, of ca. $15''$.

- Moderate and high spectral resolution

  The EPIC CCD cameras have moderate spectral resolution (with a resolving power, $E/\Delta E$, of ca. 20–50). The RGS spectrometers offer much higher spectral resolution, with a resolving power in the range of 200–800.

- Simultaneous optical/UV observations

  Observations with the co-aligned OM optical/UV telescope render possible the monitoring and identification of X-ray sources seen by the X-ray telescopes as well as imaging of the surrounding field.

Table 1: **XMM** *characteristics – an overview*

Instrument	**EPIC MOS**	**EPIC pn**	**RGS**	**OM**
Bandpass	0.1–15 keV	0.1–15 keV	0.35–2.5 keV[1]	160–600 nm
Orbital target vis.[2]	5–145 ks	5–145 ks	5–145 ks	5–145 ks
Sensitivity[3]	$\sim 10^{-14}$ (4)	$\sim 10^{-14}$ (4)	$\sim 8 \times 10^{-5}$ (15)	24 mag[13]
Field of view (FOV)	$30'$ [5]	$30'$ [5]	$\sim 5'$	$17'$ [6]
PSF (*FWHM/HEW*)[7]	$6''/15''$	$6''/15''$	N/A	$\sim 1''$
Pixel size	40 μm ($1.1''$)	150 μm ($4.1''$)	81 μm (9×10^{-3} Å)[14]	$0.5''$ [8]
Timing resolution[9]	1 ms	0.03 ms	16 ms	50 ms
Spectral resolution[10]	57 eV	67 eV	0.04/0.025 Å[11]	0.5/1.0 nm[12]

Notes to Table 1:
1) In the –1. grating order (wavelength range: 5–35 Å; λ [Å] $\times$ E [keV] = 12.3984).
2) Total visibility per orbit; minimum of 5 ks in order to ensure observatory efficiency. Maximum **continuous** visibility is ca. 70 ks.
3) After 10 ks; cf. overview tables on the individual instruments.
4) In the range 0.1–15.0 keV, in units of erg s^{-1} cm^{-2}, see § 3.3.9 for details.
5) See Fig. 15 for the detailed shape of the FOV.
6) Maximum window size that can be read out at a time: $8' \times 8'$.
7) See Fig. 4 for a ground-calibraton point source measurement.
8) $1''$ with default 2×2 binning. A higher resolution is achieved with the OM magnifier.
9) In the fastest data acquisition mode (i.e., fast mode for OM and EPIC, high time resolution mode for RGS, reading out only one of nine CCDs).
10) At 1 keV energy. At the energy of Fe Kα (6.4 keV), the energy resolution of both EPIC cameras is ca. 130 eV.
11) In –1. and –2. order, resp.; at 1 keV, this corresponds to 3.2/2.0 eV (*HEW*).
12) With grism 1 (UV) and grism 2 (optical), respectively.
13) For a 1000 s white light filter observation of a B0 star; dependent on pointing direction (celestial background).
14) In spectroscopy mode (standard 3×3 pixel on-chip binning applied).
15) O VII 0.57 keV line flux in photons cm^{-2} s^{-1}, for an integration time of 10 ks and a background of 10^{-4} photons cm^{-2} s^{-1} keV^{-1}. More details are provided in § 3.4.5.

- Long continuous target visibility

  A highly elliptical orbit offers continuous target visibility of up to more than 40 hours, with a minimum height for science observations of 40,000 km. This is very favourable for studies of source variability and also in order to achieve a high overall observatory efficiency. Due to the required off time near perigee and the telemetry gap near apogee, combined with the absence of onboard data storage devices, these 40 hours will be split into two visibility periods of ca. 70 ks each, with a short gap (of order one hour) in between.

For a comparison of these basic characteristics with those of other past or contemporaneous X-ray satellite missions, see § 3.7.

More detailed information on the mirrors and on the instruments listed in Table 1 and their observing modes is provided in the following sections (§§ 3.2–3.5).

3.2 X-ray telescopes and mirrors

XMM's three X-ray telescopes are co-aligned with an accuracy of better than about $1'$. One telescope has a light path as shown in Fig. 2; the two others have grating assemblies in their light paths, diffracting part of the incoming radiation onto their secondary focus. Fig. 3 shows the light path in the latter two X-ray telescopes onboard **XMM**. Ca. 42% of the incoming light focused by the multi-shell grazing incidence mirrors is directed onto the camera at the prime focus, while 40% of the radiation is dispersed by a grating array onto a linear strip of CCDs. The remaining light is absorbed by the support structures of the RGAs.
The focal instruments are described in §§ 3.3, 3.4 and 3.5. First we explain the most important properties of the mirror assemblies.

The performance of each mirror module is characterised by:

1. the image quality,
2. the effective area and
3. the straylight rejection efficiency,

which will be described in the following.

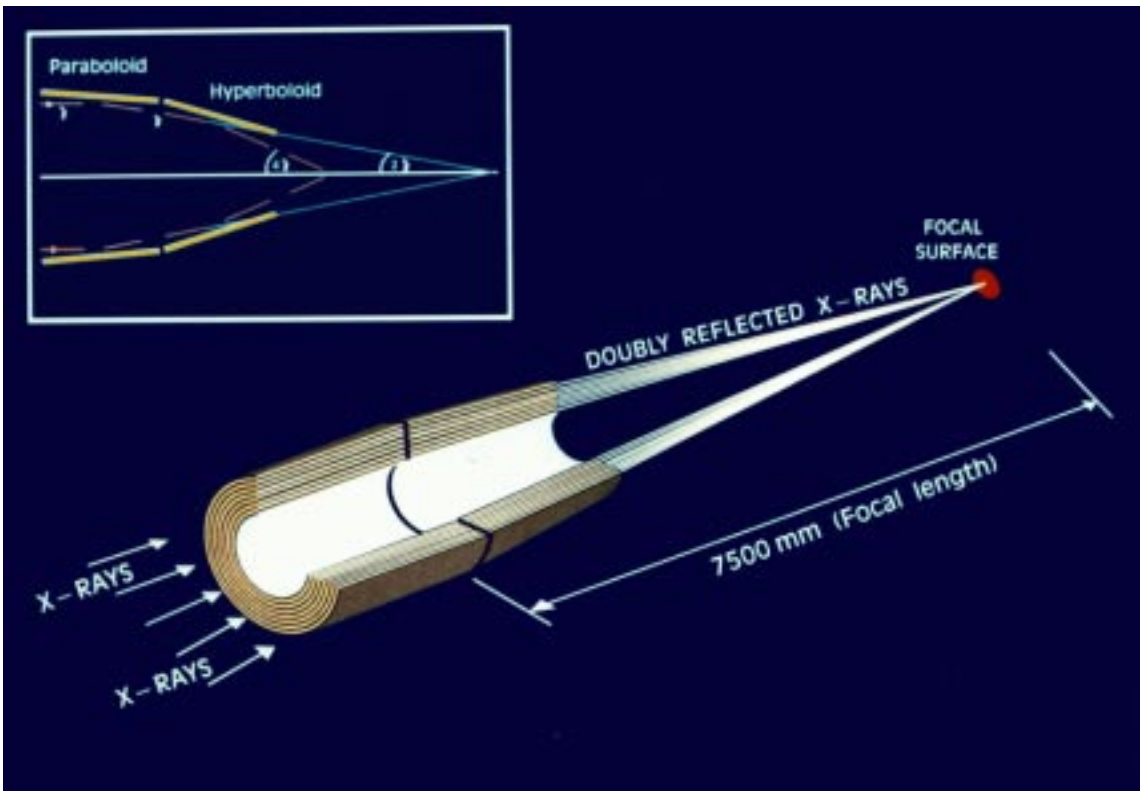

Figure 2: *The light path in* **XMM***'s open X-ray telescope (not to scale).*

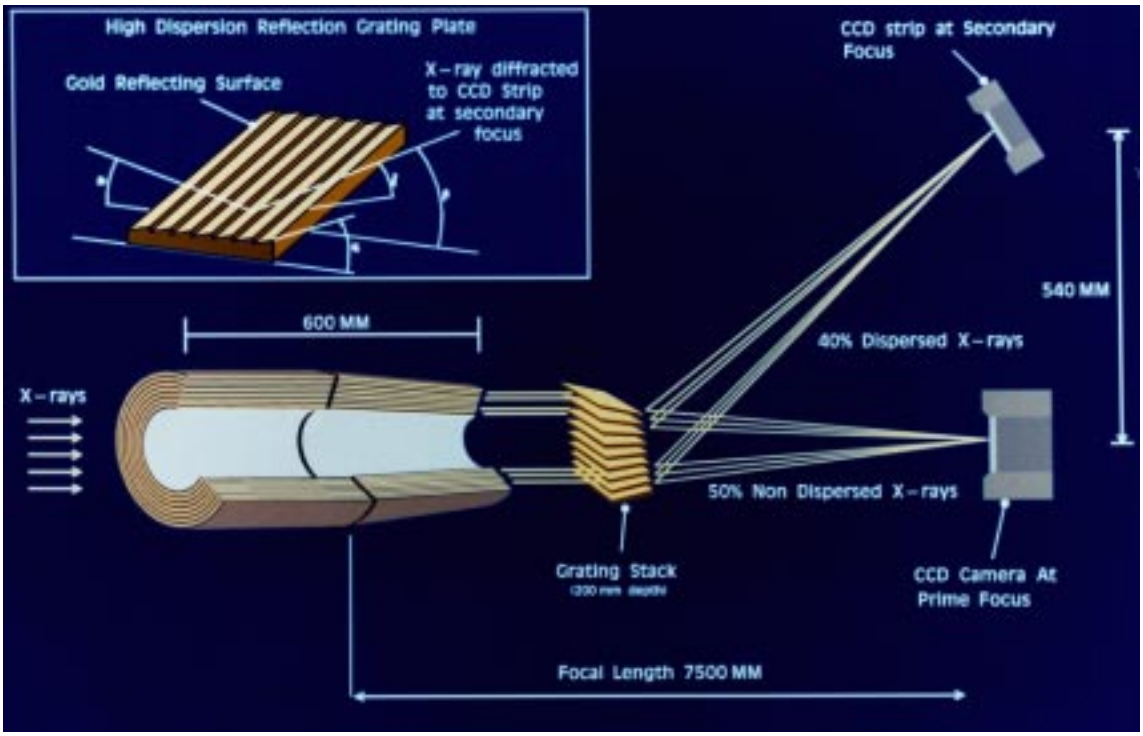

Figure 3: *The light path in the two* **XMM** *telescopes with grating assemblies (not to scale). Note that the actual fraction of the non-intercepted light that passes to the primary (EPIC) focus is 42%, while 40% of the incident light is intercepted by grating plates of the RGA.*

3.2.1 X-ray point-spread function

The first critical parameter determining the quality of an X-ray mirror module is its ability to focus photons. Here lies one of **XMM**'s major strong points: the core of its on-axis point-spread function (PSF) is narrow and varies little over a very wide energy range (0.1–10 keV).

3.2.1.1 On-axis PSF

Each of the three Wolter-type X-ray telescopes onboard **XMM** has its own point-spread function (PSF). As an example, Fig. 4 shows the on-axis PSF of one of the X-ray telescopes, as measured on-ground at the Panter test beam facility, at an energy of 1.49 keV. The PSFs of the two other telescopes are similar and therefore not displayed here.
Note that the on-ground PSF measurements will probably differ slightly, but measurably from the in-flight performance, because they are not fully illuminated by the source due to its finite distance. Fig. 4 is primarily provided to show the shape of the PSF, with for example the radial substructures caused by the spiders holding the mirror shells. Values for the PSF's *FWHM* and *HEW*, which come from SciSim modeling and fits of the modeled profiles to data, are listed in Tab. 2.
Fig. 5 displays the radially averaged profile of the PSF of one mirror module, from a SciSim model run.
Figs. 6 and 7 show the fractional encircled energy as a function of radius from the centre

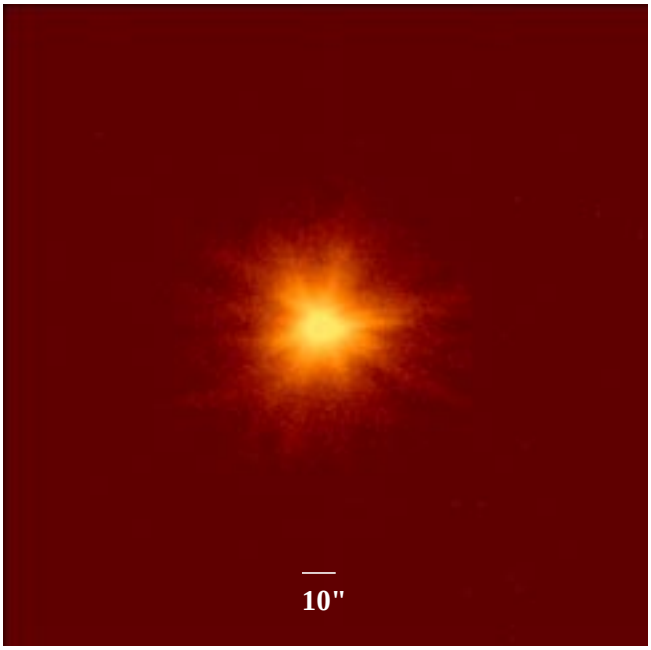

Figure 4: *The on-axis PSF of one* **XMM** *mirror module at an energy of 1.49 keV as measured at the Panter facility. The radial pattern created by the mirror support spiders is clearly visible. To enhance the visibility of the wings, intensities are scaled logarithmically.*

of the PSF for several different energies. One can see that the PSF wings become more prominent with increasing photon energy. At 14–15 keV the effective area, A_e, is very small, which makes simulations and the calibration of the PSF at such high energies unreliable.

3.2.1.2 Off-axis PSF

The PSF of the X-ray telescopes depends on the source off-axis angle, i.e., its distance from the centre of the field of view (FOV). It also depends slightly on the source azimuth within the FOV. In Fig. 8 the dependence of the shape of the **XMM** X-ray PSF on the position within the FOV is presented, based on actual measurements during ground calibration. One can see that the PSF at large off-axis angles is asymmetric, having a kind of "bean"

Table 2: *The on-axis 1.5 keV X-ray PSFs of the different mirror modules*

Mirror module	**1**	**2**	**3**
Instr. chain[1]	**pn**	**MOS-1+RGS-1**	**MOS-2+RGS-2**
FWHM [$''$]	6.6	6.0	4.5
HEW [$''$]	15.1	13.6	12.8
$W90^2$ [$''$]	53.3	50.7	58.4

Notes to Table 2:
1) The instruments located behind the mirror module.
2) Diameter of area encircling 90% of the total energy.

shape. The exact shape of the PSFs needs to be determined in orbit, because full mirror illumination by the X-ray source is required for an accurate measurement (which is not the case on-ground due to finite source distance). The calibration files will be updated in due time to include the azimuthal shape of the mirror module's PSF.
For the two EPIC MOS cameras, the PSF is also affected at a level of a few times 10^{-4} (integral relative intensity) by scattering off the RGA rib structures.

It is important to know the shape of the PSF at different positions in the FOV, e.g., to use the correct extraction areas for source photons. In Fig. 9 we show the dependence of the radius at which 90% of the total energy is encircled, $W90$, on the off-axis angle. Note that beyond an off-axis angle of about $10'$ part of the source flux is lost off the edges of the CCD chips, especially at high energies, where the wings of the **XMM** PSF are most prominent. This loss of part of the photons in the PSF wings leads to the apparent decrease of $W90$ above 3 keV in Fig. 9.
The off-axis vignetting in the two telescopes with an RGA has a dependence on angle with respect to the RGAs' dispersion direction. A source at an off-axis position perpendicular to the dispersion direction will be vignetted by a different amount to one at a position parallel to the dispersion direction. Detailed in-orbit measurements will be performed to quantify this effect.

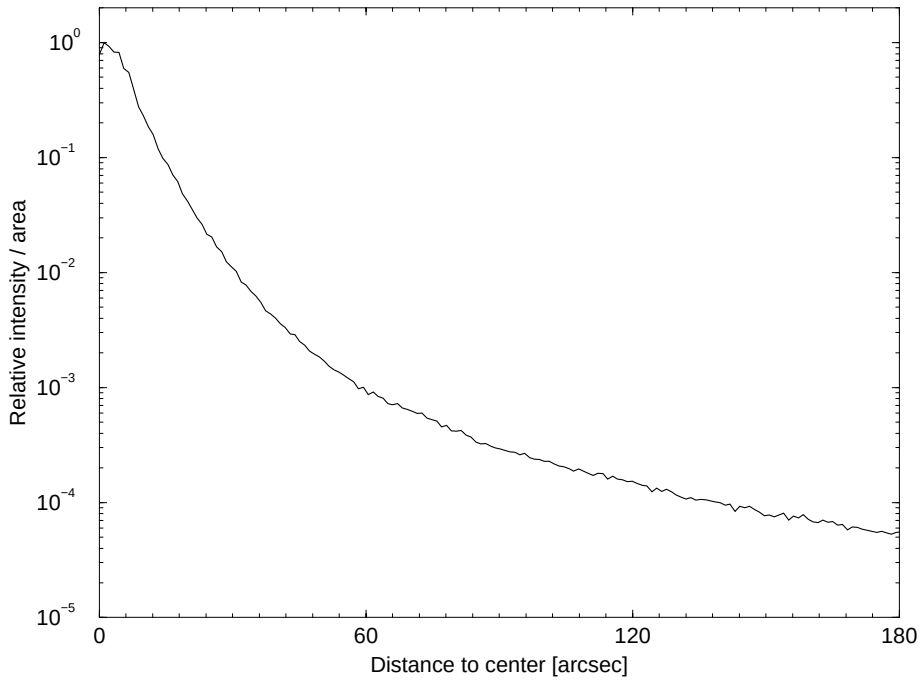

Figure 5: *Radial average of one* **XMM** *mirror module's on-axis PSF, from a SciSim model simulation.*

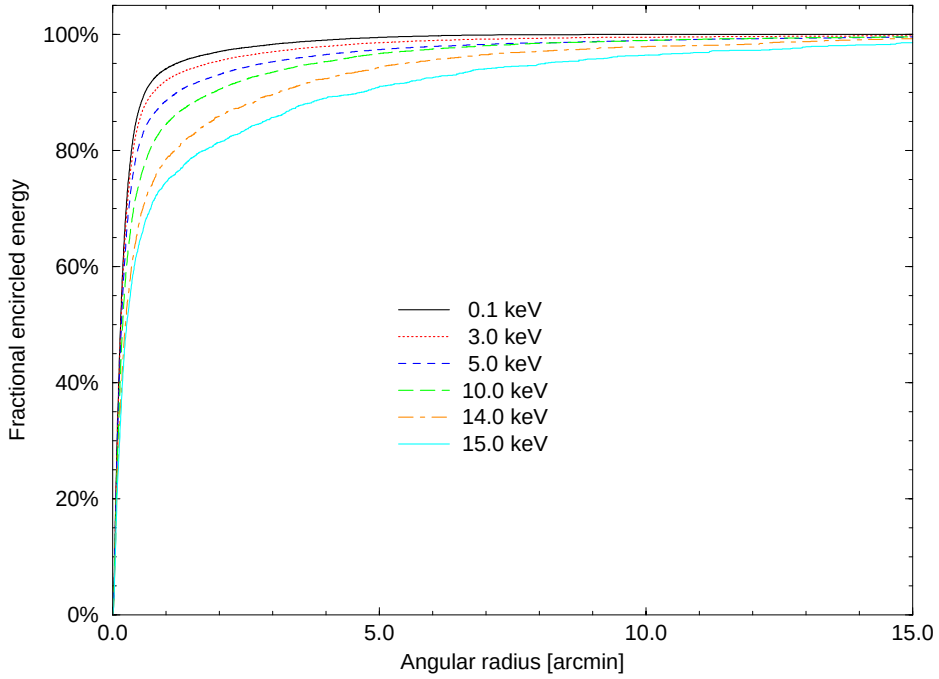

Figure 6: *Curves of fractional encircled energy as a function of angular radius (on-axis), at several different energies (linear scale).*

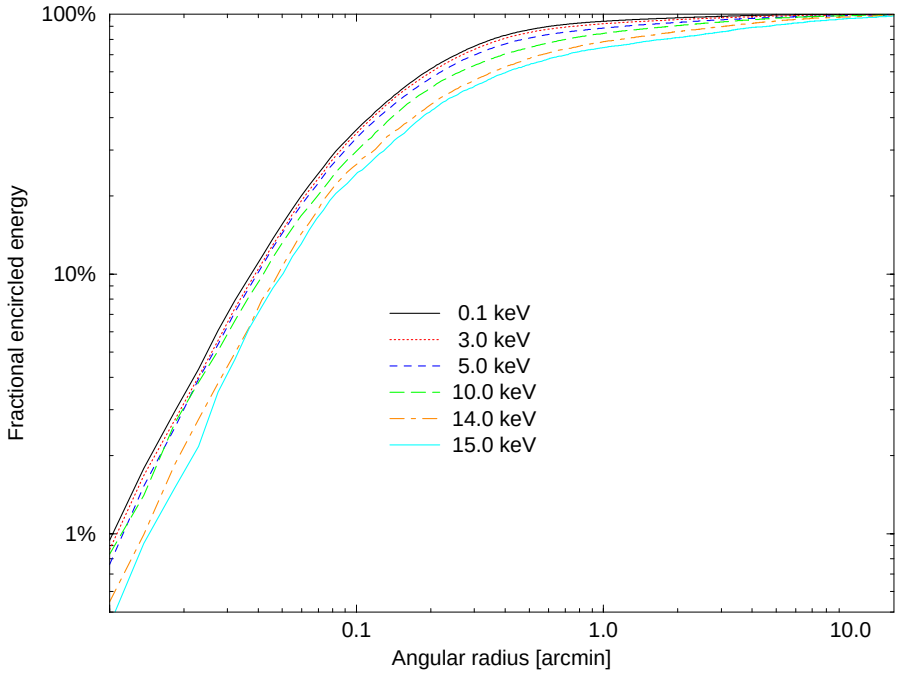

Figure 7: *Curves of fractional encircled energy as a function of angular radius (on-axis), at several different energies (logarithmic scale).*

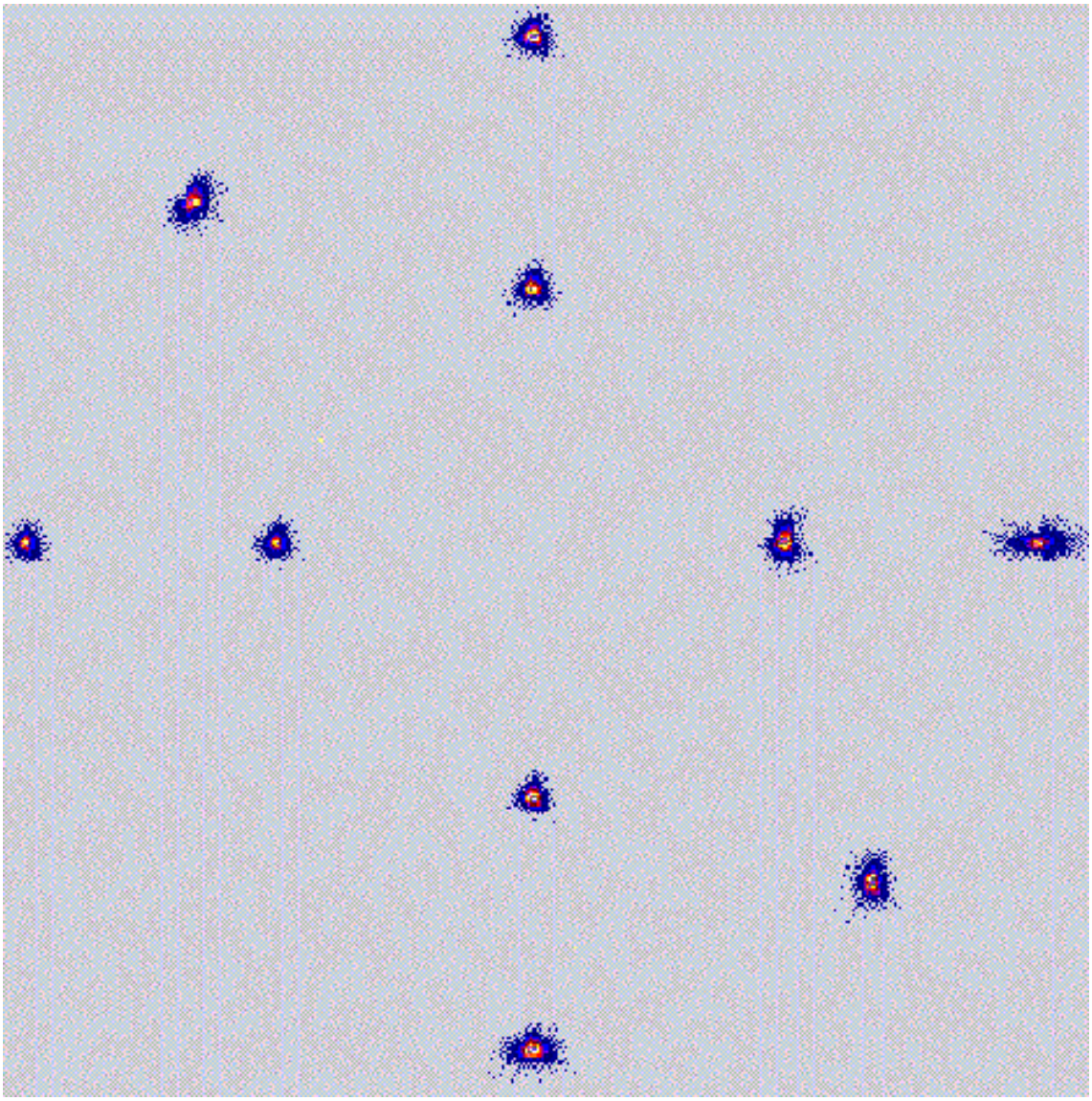

Figure 8: *The dependence of the X-ray PSF's shape on the position in the field of view. This image was made from Panter measurements, thus not under flight conditions, but the PSFs are still representative. Measurements were taken at off-axis angles of* $7'$ *and* $14'$*, at 4(6) different azimuthal positions. The intensity scale is logarithmic.*

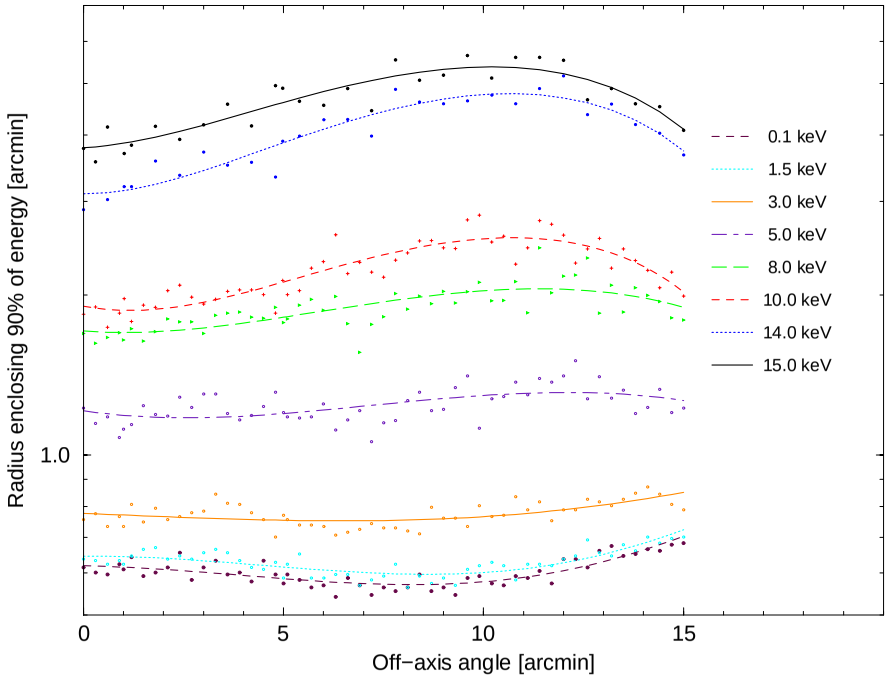

Figure 9: *Curves of radii encircling 90% of the total energy of a point source at various off-axis angles. Beyond an off-axis angle of about* $10'$ *part of the source flux is lost off the edges of the CCD chips, especially at high energies, where the wings of the* **XMM** *PSF are most prominent. This loss of part of the photons in the PSF wings leads to the apparent decrease of* $W90$ *above 3 keV.*

3.2.2 Effective area of the XMM mirrors

The second critical measure of the mirror performance is their effective area, A_e, which reflects the ability of the mirrors to collect radiation at different photon energies.

3.2.2.1 On-axis effective area

XMM's on-axis effective area of all three mirror modules combined, in comparison with the total effective mirror area of a few other X-ray missions, is shown in Figs. 10 and 11. One can see that the **XMM** mirrors are most efficient in the energy range from 0.1 to 10 keV, with a maximum at about 1 keV and a pronounced edge near 2 keV (the Au M edge). A tabular comparison of the **XMM** mirrors' properties with those of other X-ray satellites is provided in Tab. 20 (§ 3.7).
The most important information for **XMM** users is the mirror effective area, folded through the response of the different focal instruments. These are shown in Figs. 12 and 13. Note that **throughout the UHB we show EPIC effective area calculations with the thin filter in place**, which will probably be the most commonly used filter (except for stellar observations). The effective areas of the two MOS cameras are lower than that of the pn, because only part of the incoming radiation falls onto these detectors, which are partially obscured by the RGAs (Fig. 3).

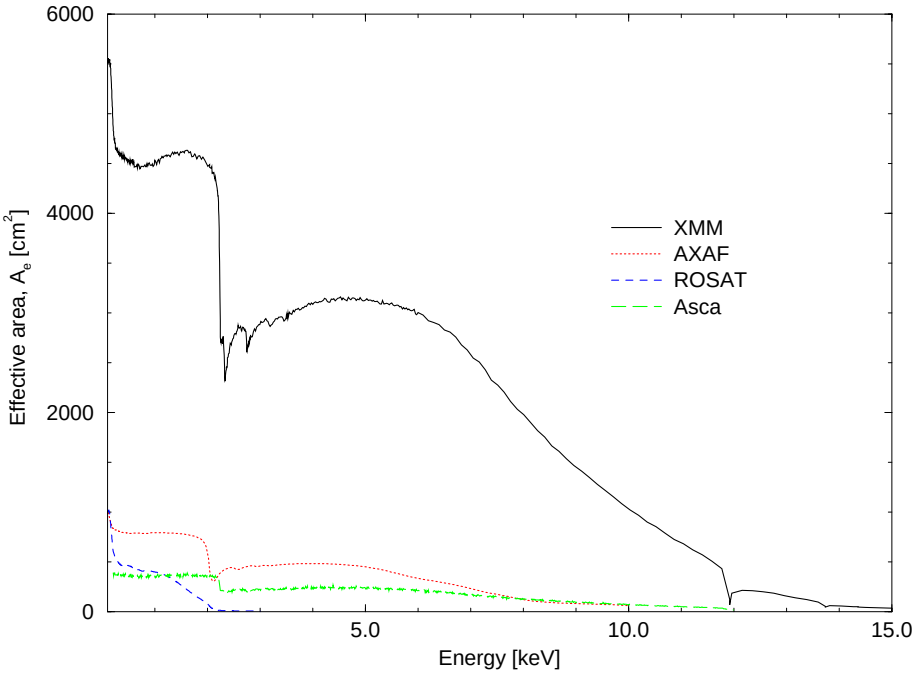

Figure 10: *The effective area of all* **XMM** *mirror modules, in comparison with those of other X-ray satellites (linear scale).*

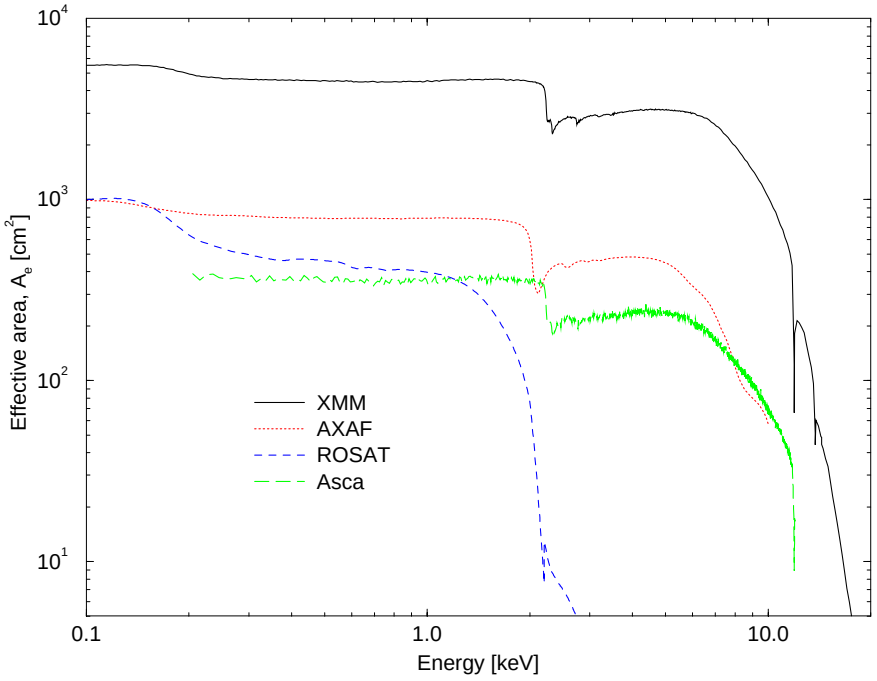

Figure 11: *The effective area of all* **XMM** *mirror modules, in comparison with those of other X-ray satellites (logarithmic scale).*

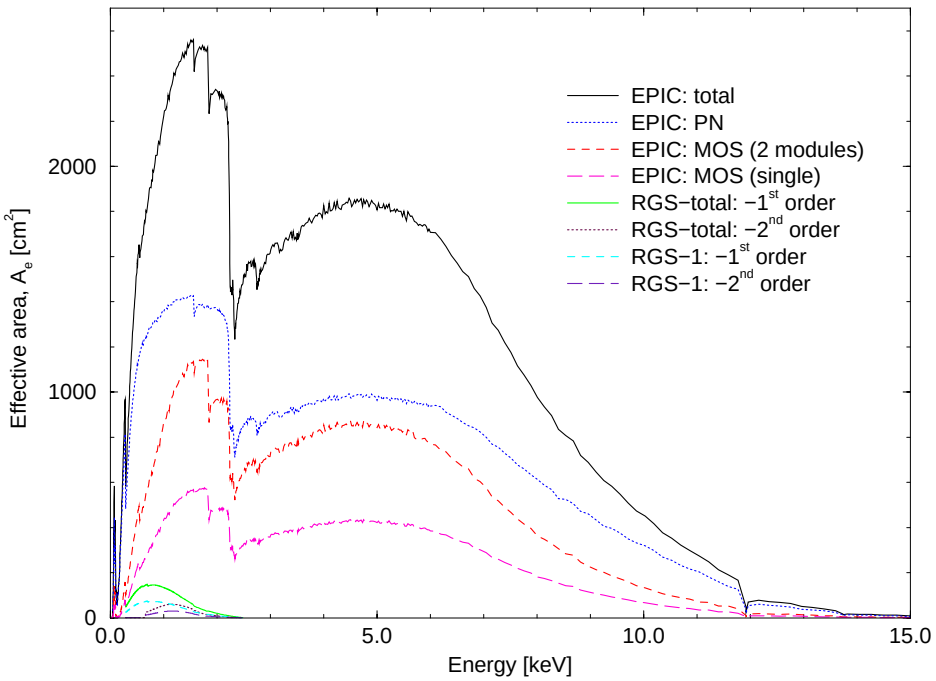

Figure 12: *The net effective area of all* **XMM** *mirror modules, combined with the response characteristics of the focal X-ray instruments, EPIC and RGS (linear scale).*

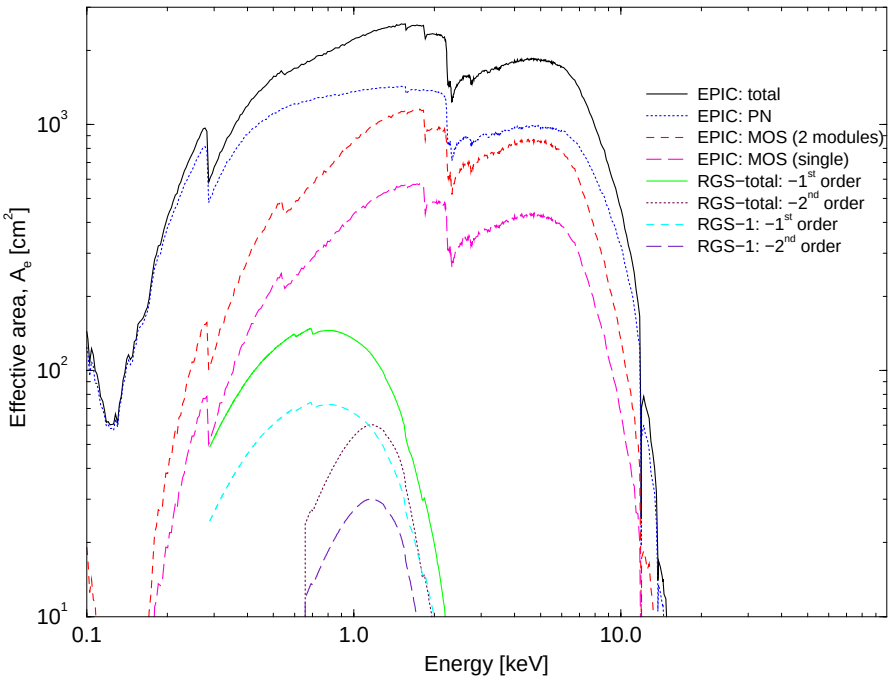

Figure 13: *The net effective area of all* **XMM** *mirror modules, combined with the response characteristics of the focal X-ray instruments, EPIC and RGS (logarithmic scale).*

3.2.2.2 Off-axis effective area

Not only the shape of the X-ray PSF, but also the effective area of the mirrors is a function of off-axis angle within the mirrors' 30′ FOV. With increasing off-axis angle, less of the photons entering the telescopes actually reach the focal plane. This effect is called "vignetting". The vignetting of the **XMM** telescopes, which is reflected by the decline of the mirror module's effective area as a function of off-axis angle, is displayed for a few energies in Fig. 14.

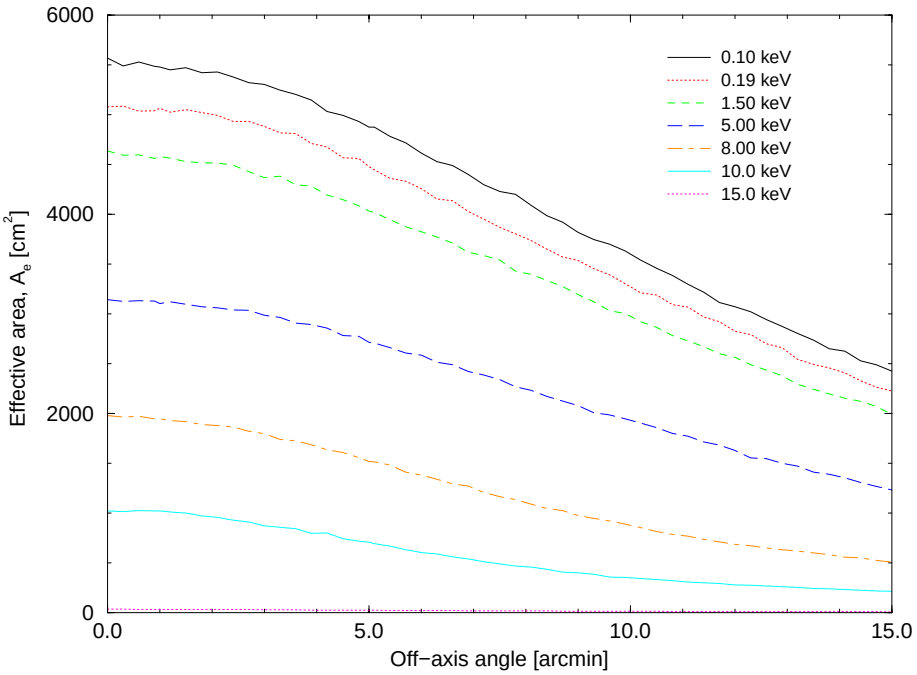

Figure 14: *The total effective area, A_e, of all* **XMM** *mirror modules, at a few selected energies, as a function of off-axis angle (0′–15′). The numbers shown here do not include any reductions due to detector responses.*

3.2.3 Straylight rejection

The third critical parameter of the mirror performance, as listed above, is the efficiency of the straylight rejection.

Without X-ray baffles, the **XMM** mirror modules would suffer from X-ray straylight entering the tubes. The effect is that the image of a 30′ area of the sky (the EPIC FOV) would be contaminated by a diffuse light background produced by X-ray sources located outside this field. X-ray straylight in EPIC is produced by rays which are singly reflected by the mirror hyperbola and which reach the sensitive area of the camera unfocused. An X-ray baffle was implemented to shadow those single reflected rays. It consists of two sieve plates made of concentric annular aperture stops located in front of the mirrors at 85 mm and 145 mm, respectively. The design is such that the entrance annular aperture of each mirror remains unobstructed for on-axis rays. Most of the rays with large off-axis angle are vignetted and cannot reach the detectors anymore via a single hyperbola reflection.

The straylight collecting area in the EPIC detector as a function of off-axis angle of a point source is anticipated to be lower than 3 cm^2 for stray sources located between $20'$ and 1.4° from the optical axis. At higher off-axis angles it is completely negligible. The ratio of the X-ray straylight collecting area to the on-axis effective area is smaller than 0.2% at 1.5 keV for a point source located at off-axis angles of 0.4–1.4° and negligible at higher off-axis angles. This ratio, expressed in surface brightness values, is even smaller since the stray-image is unfocused at detector position.
Assuming a 10 counts/s source, for EPIC MOS on-axis observations half of the incoming photon flux is distributed over ca. 150 pixels (adopting a $15''$ *HEW*), with a central peak. The light of the same source, observed at a large off-axis angle, is distributed over about 1/4 or 1/5 of the total EPIC FOV (of order 10^6 pixels), leading to a *mean* count rate of 10^{-5} counts s^{-1} $pixel^{-1}$ of diffuse straylight. However, this is only a rough approximation, because the stray radiation due to an off-axis point source is not uniformly distributed in the EPIC FOV, but produces near-annular structures in the image.
This illustrates the high straylight rejection efficiency of the **XMM** mirror modules. EPIC observations of isolated sources and RGS spectra are hardly affected. For bright extended sources (which are larger than the EPIC FOV, such as some supernova remnants, clusters of galaxies, stellar clusters and star forming regions), on the contrary, there might be a degradation in the ability to perform spatially resolved spectroscopy.

Simulations using SciSim (Appendix A) are strongly recommended prior to proposing observations in case the target is within 1.5° of a bright X-ray source, or in case imaging is foreseen of an extended object that is larger than the EPIC $30'$ FOV. Which level of straylight is problematic for a given proposal depends largely on the scientific objectives and on the ratio of the flux of the off-axis source and the required minimum detectable source flux within the FOV.

3.3 EUROPEAN PHOTON IMAGING CAMERA (EPIC)

Principal Investigator: Dr. M. J. L. Turner, Leicester University

Two of **XMM**'s X-ray telescopes are equipped with EPIC MOS (Metal Oxide Semiconductor) CCD arrays, the third carries a different CCD camera called EPIC pn. In a nutshell, the **XMM** EPIC cameras offer the possibility to perform extremely sensitive imaging observations over a field of view of $30'$ and the energy range from 0.1 to 15 keV, with moderate spectral ($E/\Delta E \sim 20-50$) and angular resolution ($6''$ *FWHM*; $15''$ *HEW*). The pn type camera can be operated with very high time resolution (down to 0.03 ms in the timing mode, albeit with a very low duty cycle).

The detector layout and the baffled X-ray telescope FOV of both types of EPIC cameras are shown in Fig. 15. In both cases the sensitive area of the detector is about $30'$ across. Note that Fig. 15 is just a rough sketch. It does **not** show details, such as:

- The pn chip array is slightly offset with respect to the optical axis of its X-ray telescope so that the nominal, on-axis observing position does not fall on the central chip boundary. The offset of the chip array amounts to about $1.5'$ both parallel and perpendicular to the readout direction. This ensures that $\geq 90\%$ of the energy of an on-axis point source are collected on one pn CCD chip.

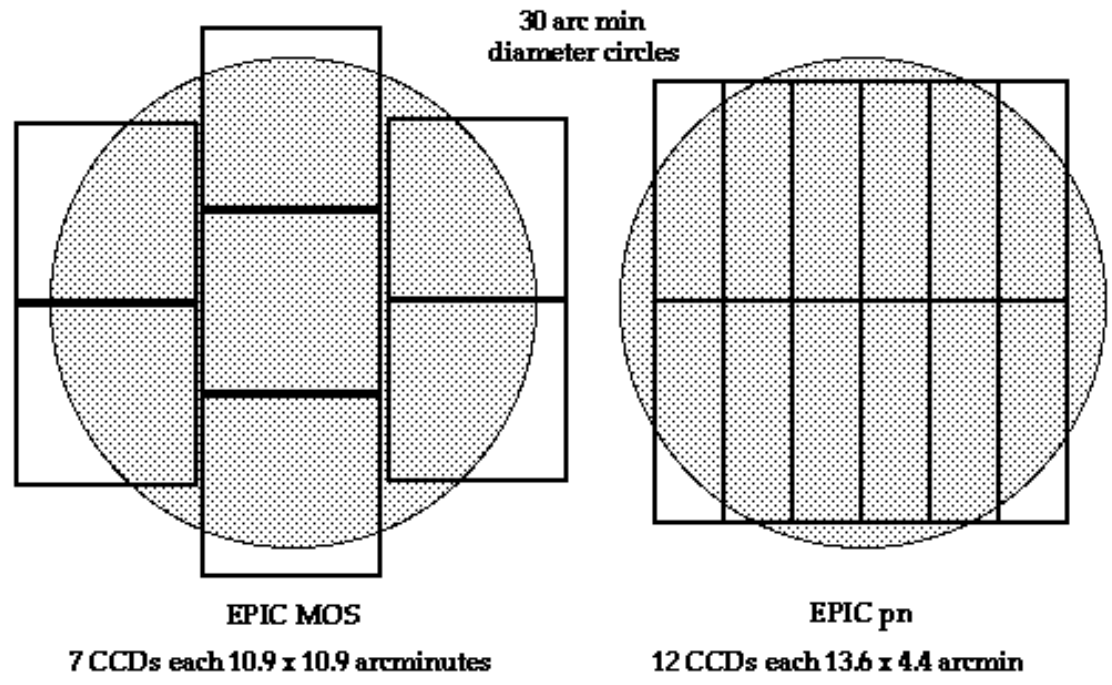

Figure 15: *The field of view of the two types of EPIC cameras; EPIC MOS (left) and EPIC pn (right). The shaded circle depicts a* $30'$ *diameter area. For the alignment of the different cameras with respect to each other in the* **XMM** *focal plane refer to the text.*

- Onboard **XMM** there will be two EPIC MOS cameras, which will be rotated by 90° with respect to each other.
- The size of the gaps between the individual chips is exaggerated.
- The dead spaces between the MOS chips are not gaps, but unuseable areas due to detector edges (the MOS chips physically overlap each other, the central one being located slightly behind the ones in the outer ring).

All EPIC CCDs operate in photon counting mode, producing event lists.[1] This allows for simultaneous imaging and non-dispersive spectroscopy due to the intrinsic energy resolution of the pixels.

Note: If for any reason a user should decide to observe a target with EPIC **not on-axis, but instead off-axis**, for off-axis angles in excess of $2.5'$ the RGS spectrum might slip off the detector array (because the RGS FOV is about $5'$ across in the cross-dispersion direction).

3.3.1 Two types of EPIC cameras: MOS and pn

The two types of EPIC cameras are fundamentally different. This does not only hold for the geometry of the pn chip array and the MOS chip array (Fig. 15), but other properties as well, like e.g., their readout times. The readout of the pn chips is much faster than that of the MOS cameras, because each pixel column has its own readout node. Another important difference is that the MOS chips are front-illuminated, while the pn CCDs are back-illuminated, which affects the detector quantum efficiencies decisively (§ 3.3.5).

3.3.1.1 EPIC MOS chip geometry

The MOS chip arrays consist of 7 individual identical, front-illuminated chips. The individual CCDs are not co-planar, but offset with respect to each other, following closely the slight curvature of the focal surface of the Wolter telescopes. Technically, this leaves space for the connections to the central CCD. The numbering scheme for the EPIC MOS chip array, the individual chip coordinate frames and the directions of the detector coordinates are displayed in Fig. 16. The figure also shows that the MOS chips have a frame store region which serves as a data buffer for storage before they are read out through the readout nodes, while the rest of the chip is obtaining the next exposure.
As indicated above, the MOS cameras are mounted on those X-ray telescopes that also carry RGS instruments. Therefore, they receive only 42% of the incident light.

3.3.1.2 EPIC pn chip geometry

The pn chip array is a camera based on a single wafer with 12 CCD chips on it. The pn chip array numbering scheme, the individual chip coordinate frames and the directions of the detector coordinates are displayed in Fig. 17.

[1] An event list is a table with one line per received photon, listing (among others) attributes of the photons such as the x and y position at which they were registered, their arrival time and their energy.

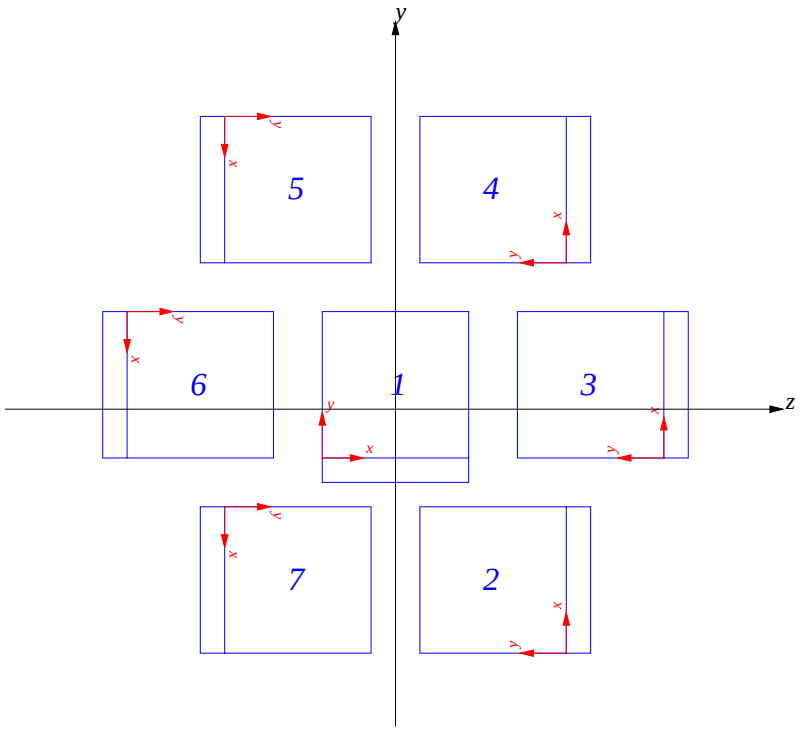

Figure 16: *Sketch of the numbering and coordinate system definitions within the EPIC MOS camera.*

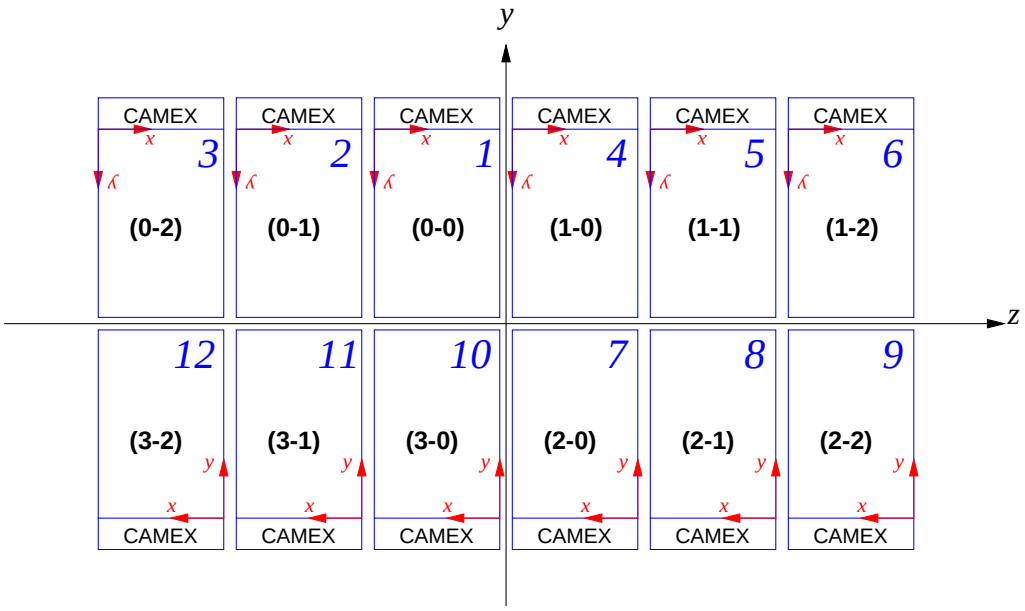

Figure 17: *Sketch of the numbering and coordinate system definitions within the EPIC pn camera.*

3.3.2 Science modes of the EPIC cameras

The EPIC cameras allow several modes of data acquisition. Note that in the case of MOS the outer ring of 6 CCDs remain in standard imaging mode while the central MOS CCD can be operated separately. The pn camera CCDs can be operated in common modes in all quadrants, or a single CCD in one quadrant can be operated independently. Thus all CCDs are gathering data at all times, independent of the choice of operating mode.

1. "full window",

   In this mode, all pixels of all CCDs are read out and thus the full FOV is covered.

2. "partial window"

   In a partial window mode one of the CCDs of both types of EPIC cameras can be operated in a different mode of science data acquisition, reading out only part of the CCD chip.

3. "timing"

   In the timing mode no two-dimensional imaging is performed, but data from a predefined area on one CCD chip are collapsed into a one-dimensional row to be read out at high speed.

4. "burst" (pn only)

   A special flavour of the timing mode of the EPIC pn camera, with very high time resolution, but very low duty cycle.

The most important characteristics of the EPIC science modes and the allowed choice of parameters for astronomical observations are tabulated in Table 3. Table 4, especially

Table 3: *The science data acquisition modes of EPIC*

EPIC MOS Mode	**Description**
Full window	Full field of view on all seven chips; low time resolution (ca. 3 s).
Partial window	Only part of the central chip is read out as a 2-D image; several partial window sizes are possible.
Timing	The central chip is not read out in a 2-D mode, but data are collapsed into a single 1-D row over a user-defined pixel area for fast photometry (down to 1.5 ms).
EPIC pn Mode	**Description**
Full window	Full field of view on all chips; relatively low time resolution (70 to 250 ms).
Partial window	2-D imaging readout over part of the array with increased time resolution. Several sizes of partial windows are allowed.
Timing	The information from one chip is collapsed into a 1-D row before readout. Max. time resolution of 30 μs.
Burst	A special flavour of the timing mode, with extremely high time resolution (down to 7 μs), but also a very low duty cycle with only ca. 3% live time.

Table 4: *Basic numbers for the science modes of EPIC*

MOS (central CCD; pixels)	**Time resolution**	**Max. count rate[1] diffuse (total) [s^{-1}]**	**Max. count rate[1] (flux) point source [s^{-1}] ([mCrab])**
Full window (600×600)	2.5 s	700	0.70 (0.24)
Full window 2 nodes(600×600)	1.4 s	1250	1.30 (0.45)
Partial window (100×100)[2]	0.4 s	125	5 (1.7)
Partial window (300×300)	0.9 s	500	1.8 (0.6)
Partial window (600×600)	0.2 s	9000	10 (3.5)
Refreshed frame store[4]	1 ms – 2.8 s		
Partial Window (100×100)[3]	0.2 s	250	10 (3.5)
Partial Window (300×300)[3]	0.7 s	600	2.5 (0.9)
Timing	1.5 ms	N/A	100 (35)
pn (array or 1 CCD; pixels)	**Time resolution**	**Max. count rate diffuse (total) [s^{-1}]**	**Max. count rate (flux) point source [s^{-1}] ([mCrab])**
Full window (400×384)	73.4 ms	1000(total)	8 (0.9)
Full window extended[5]	0.28 s	300	2 (0.26)
Large partial window (200×384)	48 ms	1500	20 (2.1)
Small partial window (64×64)	6 ms	1500	130 (14)
Timing	0.03 ms	N/A	1500 (200)
Burst	7 μs	N/A	60000 (6300)

Notes to Table 4:
1) "Maximum" to avoid deteriorated response due to photon pile-up, see § 3.3.10. Note that telemetry limitations are in some cases more stringent than the pile-up constraints. For the MOS cameras the maximum count rates are about 150 counts/s for full window imaging and 300 counts/s for partial window imaging and timing mode. The pn telemetry limit is approximately 1150 counts/s in all modes.
2) 1 node readout.
3) Free running readout.
4) Variable live time for full field imaging of bright extended sources. Usage of this mode in AO-1 is discouraged.
5) "Extended" means that the image collection time is extended by a programmable parameter (not user-selectable).

for the MOS camera, provides specimen performance data concerning time resolution and count rate capability for selected modes. The actual time resolution performance may change in *detail* by launch, but as count rate guidelines will scale inversely with time resolution and are not expected to change greatly, the GO is advised to be aware that *minor* modifications may be announced in the future. The count rate limitations are defined for a 1% pile-up case (see § 3.3.10 for details on pile-up), which occurs at about 2 photons per MOS CCD frame, and 0.5 photons per pn CCD frame. Early estimates of spectral fitting errors without any response matrix corrections show that a doubling of these count rates could lead to systematic errors greater than the nominal calibration accuracies. The SOC Team intends to develop tools to alleviate this pile-up effect, but

GOs are advised that this will be a long-term effort.
One of the major differences between the two types of cameras is the high time resolution of the pn chip array. With this camera high-speed photometry of rapidly variable targets can be conducted, down to a minimum integration time of 30 (7) μs in the timing (burst) mode.

The XRPS forms currently have non-descriptive "Partial Window n" choices for the EPIC MOS. This is because at the time of preparation of the XRPS the window modes were not yet well-defined. At the time of writing it is suggested to use the following mapping (but again there might be minor changes in the future).

XRPS Name	**Descriptive Name**	**Window Size (active pixels)**	**Time Resolution (s)**
PRI FULL MOS	FULL WINDOW (1 node)	600×600	2.5
PRI PART RFS	REFRESHED FRAME STORE	600×600	selectable; 1 ms – 2.8 s
PRI PART W2	PARTIAL WINDOW (1 node)	100×100	0.4
PRI PART W3	PARTIAL WINDOW (1 node)	300×300	0.9
PRI PART W4	PARTIAL WINDOW (free running)	100×100	0.2
PRI PART W5	PARTIAL WINDOW (free running)	300×300	0.7
PRI PART W6	FULL WINDOW (2 nodes)	600×600	1.4
FAST UNCOMP	TIMING	100 wide	1.5 ms

Explanations:
Refreshed frame store (RFS):
This mode is designed for the case where the user requires to collect data from the whole of the inner CCD (600×600), but knows that the photon flux rate is so high as to lead to significant pile-up. Then the refreshed frame store mode can be invoked, in which the frame integration time is defined, but the data which collects during the remainder of the normal readout of 2.8 seconds must be discarded. Thus, a frame collection of as rapid as 1 ms could be utilised, but in this case the live time is only 0.04%. Only one RFS value will be available, which must be determined in-orbit and is therefore not known yet. There are very few extended objects that can be considered to require this facility, rather than a normal windowed selection, and therefore it is **not recommended for normal GO usage**.
Window mode with "free run":
The SOC instrument team has identified windowing modes with either timed and synchronised readouts, or a free-running readout. The advantage of faster readout with free-running mode should be traded-off against a possible problem of clock interference between readouts of different CCDs.

3.3.3 EPIC imaging – angular resolution

EPIC's angular resolution is basically determined by the PSF of the mirror modules. This is due to the fact that the EPIC MOS and pn cameras have pixels with sizes of 40 and 150 μm, respectively. For the focal length of the X-ray telescopes (7.5 m), this corresponds to 1.1″ (4.1″) on the sky. Given the *FWHM* of the PSF of ca. 6″ (Table 2), the Nyquist theorem is thus fulfilled for the MOS cameras and images are fully sampled. The pixel size of the pn camera slightly undersamples the core of the PSF.

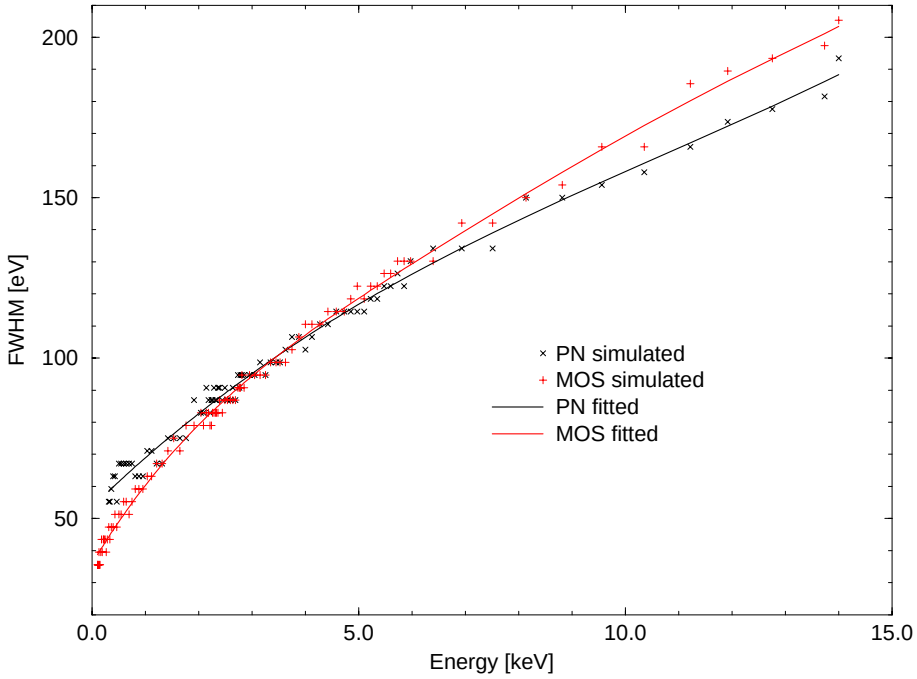

Figure 18: *The EPIC pn and MOS energy resolution (FWHM) as a function of energy. The data points come from SciSim simulations.*

There is one notable exception to the above, namely when the count rate of an X-ray source is so high that photon pile-up on the EPIC chips plays an important role. This is described in § 3.3.10.

3.3.4 Intrinsic energy resolution of EPIC

The CCD pixels of the EPIC cameras are energy sensitive, enabling non-dispersive spectroscopy. The resolving power of these cameras is determined by the intrinsic energy resolution of the individual pixels and not by the PSF of the X-ray telescopes. The spectral resolution of both the EPIC MOS and pn CCDs, as a function of energy, is displayed in Fig. 18.

3.3.5 EPIC quantum efficiencies

One of the factors to be taken into account when determining the effective area of the EPIC cameras is their quantum efficiency (QE). The QE of both types of EPIC CCD chips as a function of photon energy is displayed in Fig. 19. It is the QE of the EPIC MOS chips that in practice limits the energy passband at its high end, while the pn camera can detect photons with high efficiency up to 15 keV.

3.3.6 EPIC filters

The next factor influencing the EPIC effective area, specifically in the low energy part of the passband, are its optical blocking filters. These are used, because the EPIC CCDs are not only sensitive to X-ray photons, but also to IR, visible and UV light. Therefore,

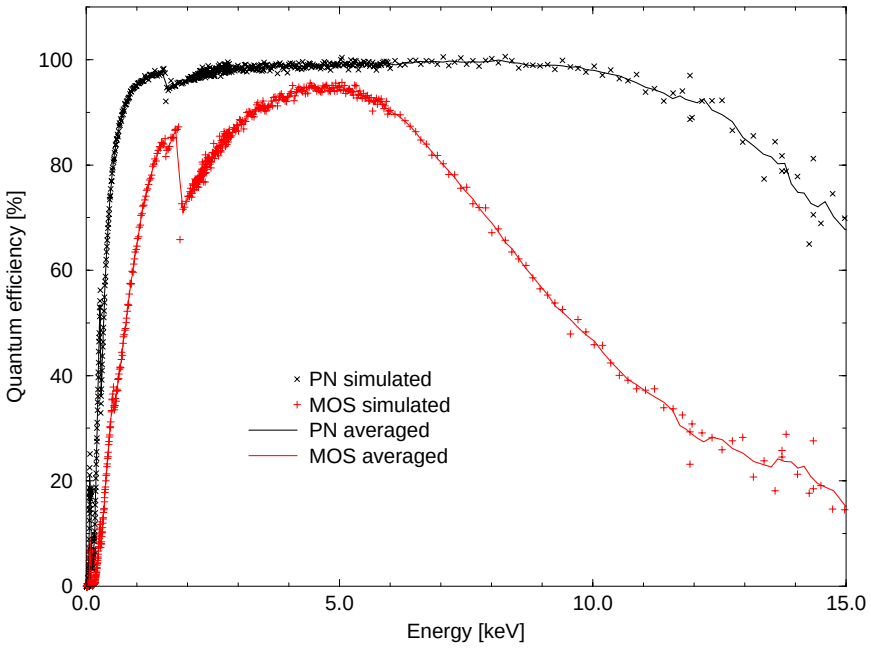

Figure 19: *Quantum efficiency of the two types of EPIC CCD chips (pn and MOS) as a function of photon energy.*

if an astronomical target has a high optical to X-ray flux ratio, there is a possibility that the X-ray signal becomes contaminated by those photons. The resulting analysis of data would be impeded in three ways:

1. Shot noise on the optically-generated photo electrons will increase the overall system noise, and hence lower the energy resolution. Spectral fitting will be inaccurate, because the calibration files will assume narrower spectral lines than observed.

2. The energy scale will be incorrectly registered, because a nominally zero signal pixel will have a finite offset. For each optically generated photo electron which is registered, the energy scale shifts by about 3.6 eV. This is comparable with the accuracy with which we expect brightest emission line features can be centroided. Consequently, contamination by visible light plays a crucial role in defining the proper energy scale.

3. Excess signal and noise fluctuations can affect the detection efficiency as well, by disguising single pixel X-ray events as events split between pixels.

To prevent this, the EPIC cameras include aluminised optical blocking filters, and also an internal "offset table" which is calculated before each exposure to subtract the constant level of (optical) light or other systematic shifts of the zero level of charge measurements. This is the reason why there is always a calibration exposure before the start of a science observation.
If these measures work perfectly, the above problems are minimised. However, the use of a thick blocking filter capable of minimising the optical light contamination for *all* scenarios

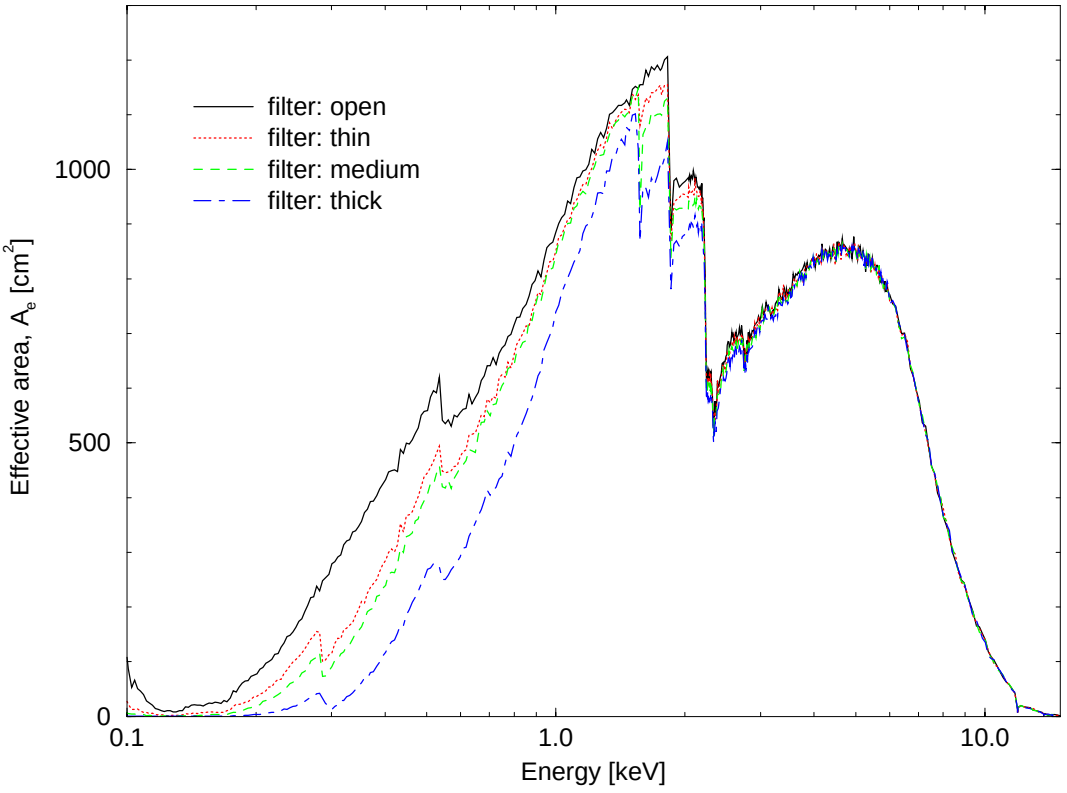

Figure 20: *The EPIC MOS effective area for each of the optical blocking filters and the "open" (no filter) position.*

would necessarily limit the softest X-ray energy response. Each EPIC camera is therefore equipped with a set of 4 separate filters, named **thick, medium, thin** and **open**. It is necessary for the observer to select the filter which maximises the scientific return, by choosing the optimum optical blocking required for the target of interest.
The following guidelines apply to point sources of optical light. Extended objects are not expected to be a significant problem. The calculations have been performed for a worst case, i.e., for the brightest pixel within the core of the PSF. Therefore, averaging the brightness of an extended object over a scale of one PSF (say, 20″) should provide a corresponding estimate with a significant margin of safety.

- Thick filter

  This filter should be used if the expected visible brightness of the target would degrade the energy scale and resolution of EPIC. It should be able to suppress efficiently the optical contamination for all point source targets up to m_V of 1–4 (MOS) or m_V of 0–3 (pn). The range depends on the spectral type, with only extremely red or blue colours (M stars for example) causing the change to 3 magnitudes fainter level.

  Note that these data apply to full window modes only, and that a change to a partial window mode with an order of magnitude faster readout rate can allow suppression of optical contamination at 2–3 visible magnitudes brighter for *ALL* filters. The GO can make an estimate on optical contamination

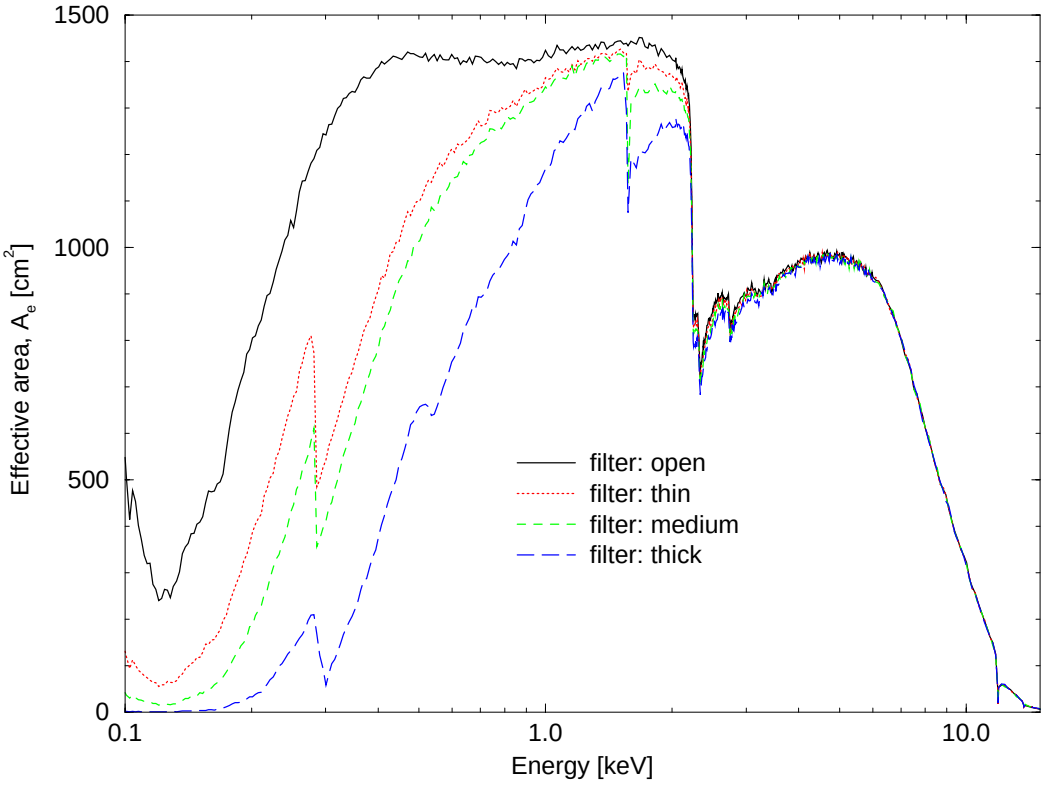

Figure 21: *The EPIC pn effective area for each of the optical blocking filters and the "open" (no filter) position.*

improvement based on the mode time resolution compared with full window mode (Table 4).

- Medium filter

  The optical blocking is expected to be about 10^3 less efficient than the thick filter, so it is expected that this filter will be useful for preventing optical contamination from point sources as bright as $m_V = 8$–10.

- Thin filter

  The optical blocking is expected to be about 10^5 less efficient than the thick filter, so the use of this filter will be limited to point sources with optical magnitudes about 14 magnitudes fainter than the corresponding thick filter limitations.

- Open filter

  This should only be used when trying to detect the very softest photons in the bandpass. Even the diffuse zodiacal light will produce measureable optical light contamination, so the energy response will be compromised *every* time the "open" position is employed. Furthermore, present calculations show that the CCDs could become contaminated with ice and hydrocarbons on a timescale of about one day, leading to loss of calibration and a necessity to initiate a

bakeout and re-calibration sequence. Therefore **observations in the open position are not recommended by the SOC** as a routine operation. To request open filter position observations, the GO must supply strong scientific arguments that the response to the softest photons around 0.1 keV is crucial for the proposed investigation and, moreover, that the expected visible light contamination is expected to be minimal.

The default filter, which is the most sensible choice for most observations, is the thin filter. Figs. 20 and 21 display the impact of the different filters on the soft X-ray response of both types of EPIC cameras.

3.3.7 EPIC background

The EPIC background comprises both external (diffuse X-ray) and internal (particle generated) components. The intensity and spectrum of these background components impact on the sensitivity, however we are limited at present in our knowledge of the expected contributions.

3.3.7.1 EPIC internal background

The internal background is dominated mainly by γ-rays generated within the spacecraft in response to the cosmic ray flux. An industry study indicates that for a nominal particle flux, and a best estimate of the spacecraft mass distribution, the event rate in EPIC MOS would be of order 1.5×10^{-4} counts cm^{-2} s^{-1} keV^{-1}. The spectrum is expected to be virtually flat. No detailed model was performed for the EPIC pn camera, but it was estimated that with an active layer some 4–5 times thicker than the MOS CCDs, the rate might be typically a factor of 2 higher. The uncertainty due to variation of the cosmic ray rates around the orbit and with time is probably also a factor 2 at best.
For some basic assumptions on the pulse height invariant channel widths and other factors, the following estimates for the PHA file characteristics of the particle background component in the **XMM** cameras were estimated by us:

- EPIC MOS (channel width = 3.4 eV): $4.4 \times 10^{-9} + (\mathrm{B} \times 3.32 \times 10^{-13})$
- EPIC pn (channel width = 4.25 eV): $8.7 \times 10^{-9} + (\mathrm{B} \times 8.3 \times 10^{-13})$
- RGS MOS (channel width = 1 eV) $8.82 \times 10^{-10} + (\mathrm{B} \times 6.6 \times 10^{-14})$

where the units are counts mm^{-2} s^{-1} channel^{-1} and B is the channel number, giving the weak energy dependence.
If it proves possible to correlate a particle-induced background component with the event rates measured in the EPIC Radiation Monitor (ERMS, § 3.6.2), then it should also be possible to include this as part of a background correction calibration file.
The dark currents of both types of EPIC CCDs are negligible sources of background noise under nominal operating conditions.

3.3.7.2 EPIC external background

Except for energies $\geq$6 keV, calculations show that EPIC observations will be dominated by the diffuse X-ray background from the sky. This can be modeled as two thermal plasma components within the Galaxy (at kT = 0.05 and 0.12 keV; the former being unabsorbed, the latter with an average absorbing column density of 1.66×10^{20} cm^{-2}), and an extragalactic power law component (with a photon spectral index of 1.46 and the same absorbing column density as above), see Chen, Fabian and Gendreau (1997; MNRAS). The former is known from ROSAT sky maps to vary in intensity by a factor of two with location. It is difficult to assess what fraction of the truly diffuse background will remain unresolved at the angular resolution level of **XMM**, and hence what the eventual point source detection sensitivity of EPIC will be.
An additional caveat to consider is the detection cell size, because the signal-to-noise ratio will depend dramatically on the extraction radius assumed. For the associated plots herein, we have adopted a region confined to the order of a PSF core.

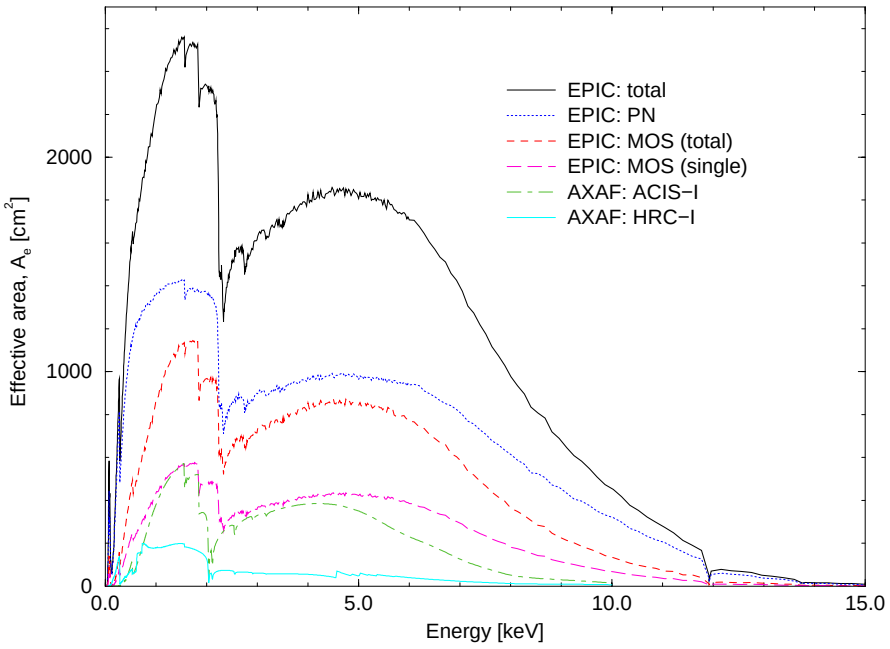

Figure 22: *The effective area of* **XMM**, *with various combinations of EPIC detectors (total, pn only, 2 MOS cameras, 1 MOS only), compared with* AXAF *ACIS-I and* AXAF *HRC-I (linear scale).*

3.3.8 Imaging effective area

Both types of EPIC cameras, MOS and pn, have high maximum quantum efficiencies (see Fig. 19). Figs. 22 and 23 display the total effective area of the **XMM** mirror modules with various combinations of EPIC detectors (total, pn only, 2 MOS cameras, 1 MOS only). As mentioned earlier on, **all EPIC effective area calculations were performed with the thin filter** in place. For comparison, the *AXAF* effective areas with both the ACIS-I and HRC-I instruments are shown too.

Note that the above refers to on-axis sources. The mirror vignetting described in § 3.2.2.2 folds into the graphs shown in Figs. 22–23 for off-axis sources. This reduces the EPIC off-axis effective area (not displayed) as displayed in Fig. 14.

Ontop of this, the EPIC MOS effective areas are affected by the presence of the RGAs. The effective area along the RGS dispersion direction differs slightly from that in the cross-dispersion direction.

Note that the EPIC cameras have an effective area of up to 500 cm^2 below 0.1 keV (0.05–0.1 keV). However, photons from EPIC observations in this energy range will probably not be scientifically useable, because the EPIC event detection threshold will be somewhere in the range from 70–90 eV. All events below this energy will be filtered out in order to reject spurious events (including electronics noise). Details, in particular the exact level of this threshold, will be determined and set as part of the in-orbit calibration program.

3.3.9 EPIC's sensitivity limits

The EPIC sensitivity limits depend on the angular structure and the spectral characteristics of the source that is observed. The numbers for an unresolved point source with a

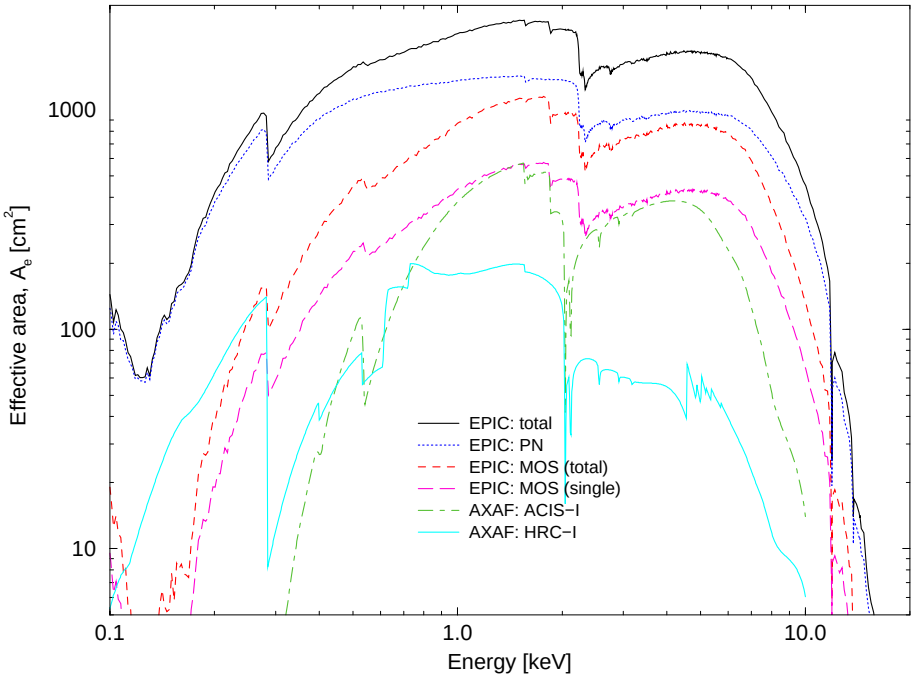

Figure 23: *The effective area of* **XMM**, *with various combinations of EPIC detectors (total, pn only, 2 MOS cameras, 1 MOS only), compared with* AXAF *ACIS-I and* AXAF *HRC-I (logarithmic scale).*

power law emission spectrum are listed in Table 5.

Table 5: *5-σ point source sensitivity of the EPIC pn camera*[1]

Int. time [ks]	**0.1–2.4 keV**	**0.4–4.5 keV**	**2–10 keV**	**0.1–15 keV**
10	17	20	64	33
20	9	11	33	18
30	7	8	20	13
60	4	5	13	8
100	2.7	3.5	8.7	5.7

Notes to Table 5:
1) All fluxes are in units of [10^{-15} erg cm^{-2} s^{-1}], for an $\alpha_E = 0.7$ power law spectrum, assuming only extragalactic X-ray background radiation (as described in § 3.3.7).

Both internal (particle-induced) and external (celestial X-ray) background was included in the calculations, as described in § 3.3.7. A detect cell the size of the *FWHM* of the **XMM** PSF were used.
The sensitivity limits for two selected emission lines are tabulated in Tables 6 and 7. Here the background was treated as if it were part of the underlying continuum flux. In Tables 5–7 and Figs. 24–26 **the sensitivity limits of only the EPIC pn camera are provided**. Using the effective area curves from above, one can estimate that the numbers should be multiplied by a factor of 0.75 to obtain the approximate sensitivity of **all** EPIC cameras combined.

Table 6: *EPIC pn O VII 0.57 keV line sensitivity*[1]

Cont. flux[2]	**10 ks**	**100 ks**
10^{-3}	103	32.2
10^{-4}	33.6	10.3
10^{-5}	11.8	3.36
10^{-6}	5.07	1.18
10^{-7}	3.35	0.51
10^{-8}	3.08	0.34
10^{-9}	3.05	0.31

Notes to Table 6:
1) All line fluxes are in units of [photons cm^{-2} s^{-1}].
2) In [10^{-6} photons cm^{-2} s^{-1} keV^{-1}].

Table 7: *EPIC pn Fe XXV 6.63 keV line sensitivity*[1]

Cont. flux[2]	**10 ks**	**100 ks**
10^{-3}	82.3	25.7
10^{-4}	27.1	8.23
10^{-5}	9.79	2.71
10^{-6}	4.56	0.98
10^{-7}	3.32	0.46
10^{-8}	3.15	0.33
10^{-9}	3.13	0.31

Notes to Table 7:
1) All line fluxes are in units of [photons cm^{-2} s^{-1}].
2) In [10^{-6} photons cm^{-2} s^{-1} keV^{-1}].

Fig. 24 displays the minimum detectable source flux for a point source with an α_E = 0.7 power law spectrum, Fig. 25 that of an α_E = 3.0 ("soft excess") source. Fig. 26 shows the minimum detectable source flux for 30″ extended sources with a kT = 0.3 keV Mewe-Kaastra-Liedahl (in the following "Mekal") thermal plasma.

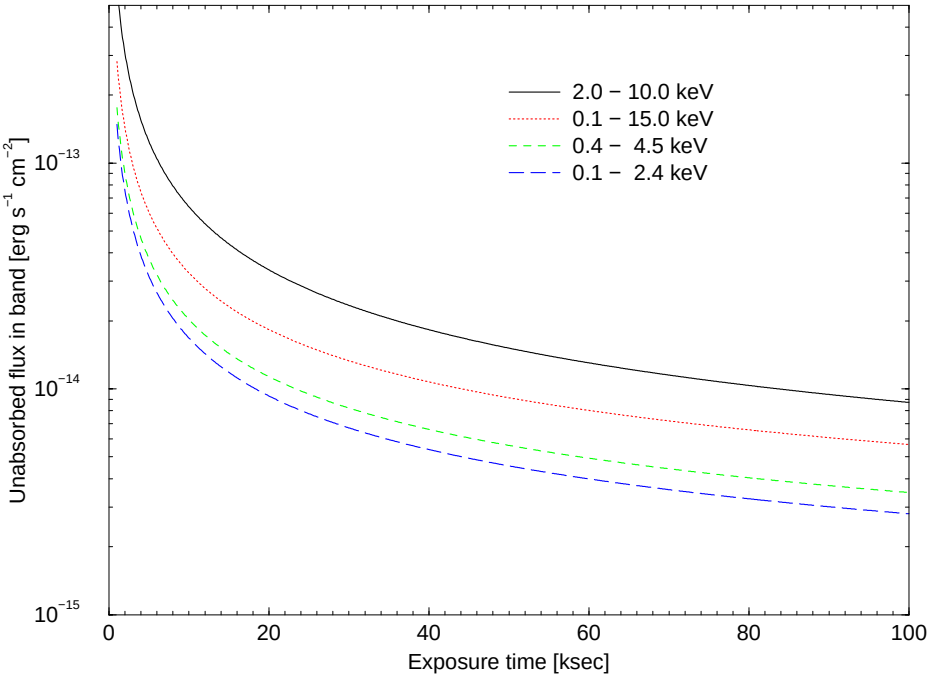

Figure 24: *EPIC pn sensitivity limits for a point source with an α_E = 0.7 power law spectrum, for different energy bands, see Table 5.*

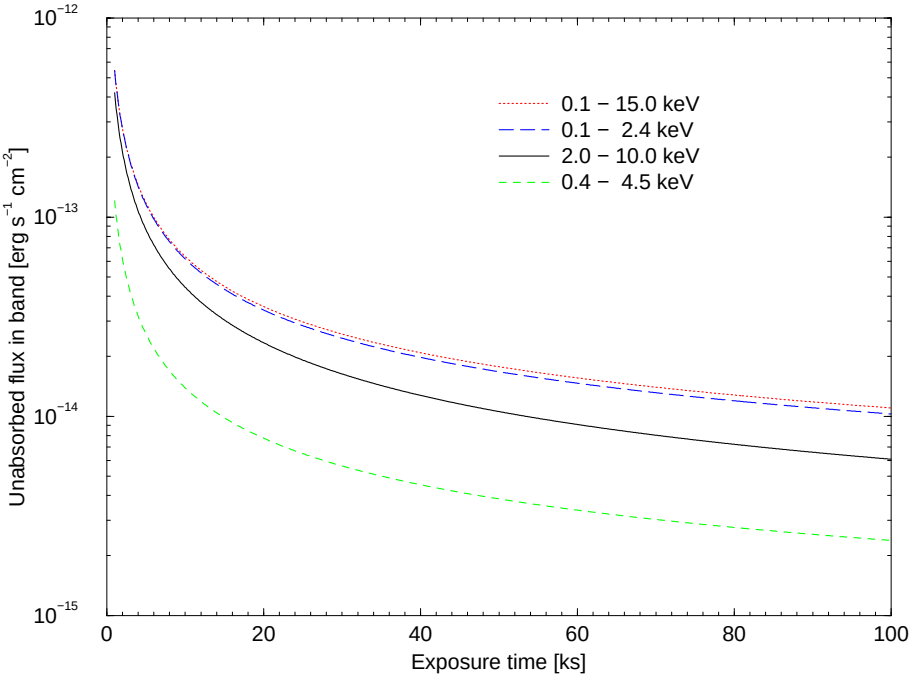

Figure 25: *EPIC pn sensitivity limits for a point source with an α_E = 3.0 power law spectrum, for different energy bands, see Table 5.*

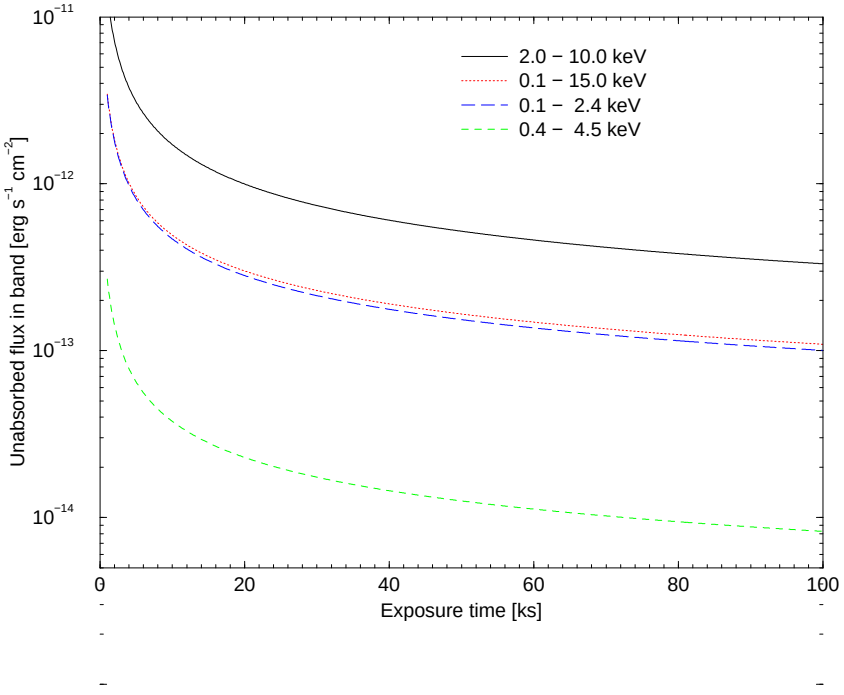

Figure 26: *EPIC pn sensitivity limits for a* $30''$ *extended source with a* $kT = 0.3$ *keV Mekal thermal plasma spectrum.*

3.3.10 EPIC photon pile-up

Photon pile-up, i.e., the arrival of more than one X-ray photon in one camera pixel before it is read out, can affect both the spectral response of EPIC and its PSF:
The spectral response is compromised, because the charge deposited by more than one photon is added up before being read out, thus creating artifical "hard" photons where there have actually been two or more soft photons.
The PSF is influenced by pile-up, because in the core of the PSF many photons arrive at almost the same time (within one readout frame), creating multi-pixel photon patterns which, for the MOS camera, are then rejected by the onboard event reconstruction software (which is supposed to suppress spurious events, such as cosmic rays). This leads, in the most extreme case, to a PSF with an artificial "hole" at its centre, as displayed in Fig. 27. For the pn camera, event reconstruction is performed offline in the SAS.
As an example for the influence of pile-up on spectral analyses, a kT = 1 keV Raymond-Smith model spectrum with N_H = 3×10^{20} cm^{-2} has been fed into SciSim and the fit to the resulting "observed" spectrum compared with the input for EPIC MOS observations in the full window mode (Tab. 8). One can see how the best-fitting N_H, kT and normalisation vary as a function of input source flux (and thus count rate per frame). Note that, because of the photon pile-up, one apparently loses soft photons (whose charge combines and is then seen at higher energies), thus requiring a higher N_H and also a higher kT to reach the minimum χ^2 for the fit. Therefore, the change in the relative normalisation (right column) is not the only, and also not the most severe problem in an attempt to provide the best possible spectro-photometric calibration. The peculiarity that for low fluxes the fitted kT is a bit lower than the input value is explained by the fact that the SciSim simulation was performed without event reconstruction. What is important to note is the relative change in kT. A similar change is also caused in the best-fitting slope of a power law, as displayed in Fig. 28. The effect of pile-up on the PSF has been taken into account in these simulations by choosing an appropriately large photon extraction region for the spectral analysis.
Note: No error bars are provided in Tab. 8, because the input spectrum is a numerical model spectrum without noise. Differences in the output "fit" spectrum with respect to the noise-free input occur only because of re-grouping of photons due to pile-up. The relevance of the effect depends on the scientific goal of the observing programme. For up to 2 counts per MOS frame, the error in N_H stays below 10%, that of kT and the normalisation at a level of 2%, which in many cases will be below the uncertainty of the spectral fit anyway.
Table 4 provides estimates of count rates for the different EPIC instrument modes for which pile-up should not be a problem. For the MOS full imaging mode, e.g., ca. 0.7 counts/s should not be exceeded.

A quantitative comparison of both types of EPIC cameras with the *AXAF* ACIS-I instrument in this respect is provided in § 3.7.1.3.

3.3.11 EPIC event grade selection

Users should be aware of the different methods of processing events that are detected in the EPIC MOS and pn cameras. Event selection is performed on-board in order to allow transmission of useful data only (i.e., removal of empty pixels from the data stream). Also a significant number of X-ray events are expected to be split between pixels, and these must be recognised as such.

The MOS camera uses an event pattern recognition scheme. All detected events are transmitted to ground with a pattern identification (similar to the *ASCA* "grades") and a number of energy data. The Science Analysis Subsystem (SAS) software will automatically allow these data to be reconstructed to a single energy value in an event list. However, the user will be able to select sub-sets of pattern types because optimal energy resolution may be obtained from a sub-set of events (one and two pixels in size). If maximum source detection efficiency is required all patterns might be selected. Therefore, users must choose carefully the dataset for the science of interest, and further beware that not all pattern combinations may be calibrated as well as some default sets.
The pn camera conversely telemeters all pixels above a certain threshold, and the X-ray event selection and processing is performed wholly on-ground, e.g., through the use of the SAS. However, we emphasise that default processing should be followed, because the

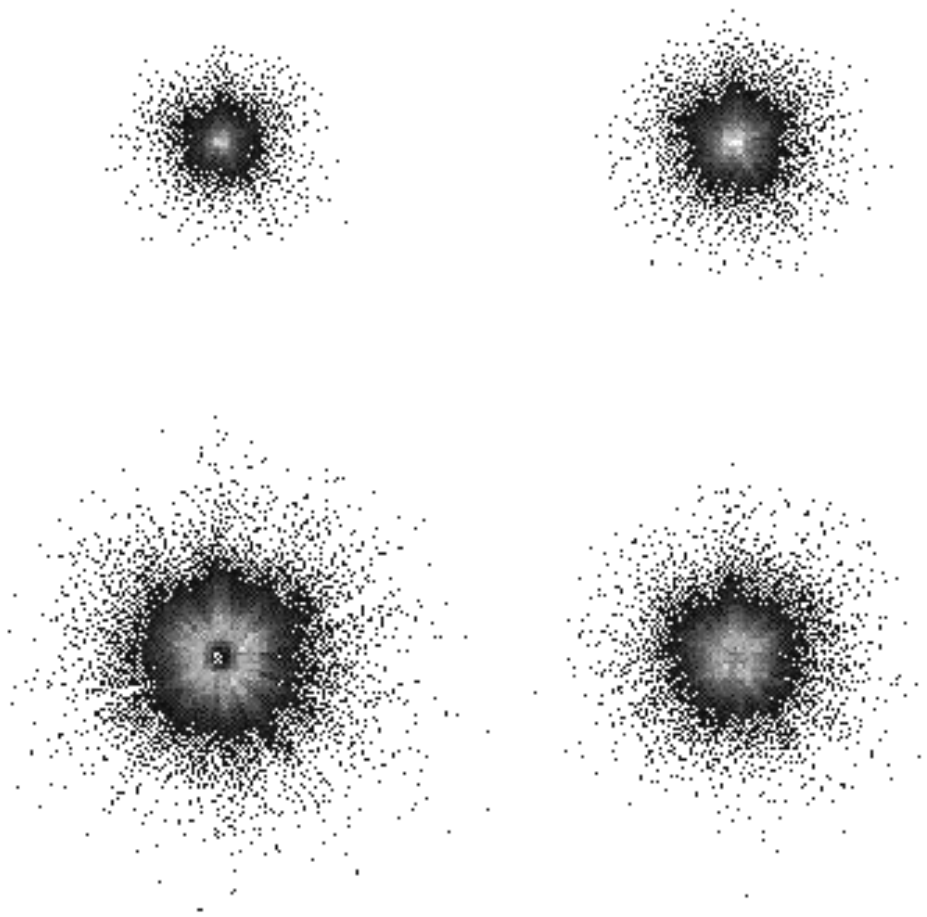

Figure 27: *SciSim simulation of the EPIC MOS PSF with increasing photon count rate per frame. The panels are arranged clockwise, with the lowest count rate (and thus pile-up rate) in the upper left and the highest in the lower left. The simulated count rates are 0.37, 5.92, 12.6 and 23.7 counts/s, respectively.*

Table 8: *The effect of pile-up on spectral fits*

Input flux[1]	**Output count rate** [s^{-1}]	**Counts per MOS frame**	**N_H** [10^{20} cm^{-2}]	**kT [keV]**	**Norm./ expect**
4.05	1.08	0.22	3.0	0.967	1
13.4	3.56	0.71	3.05	0.972	1
40.5	10.5	2.1	3.2	0.979	0.98
134	33.3	6.65	3.5	1.010	0.95
405	85.4	17.1	4.1	1.022	0.80

Notes to Table 8:
1) 0.1–10 keV flux in units of [10^{-12} erg s^{-1} cm^{-2}].

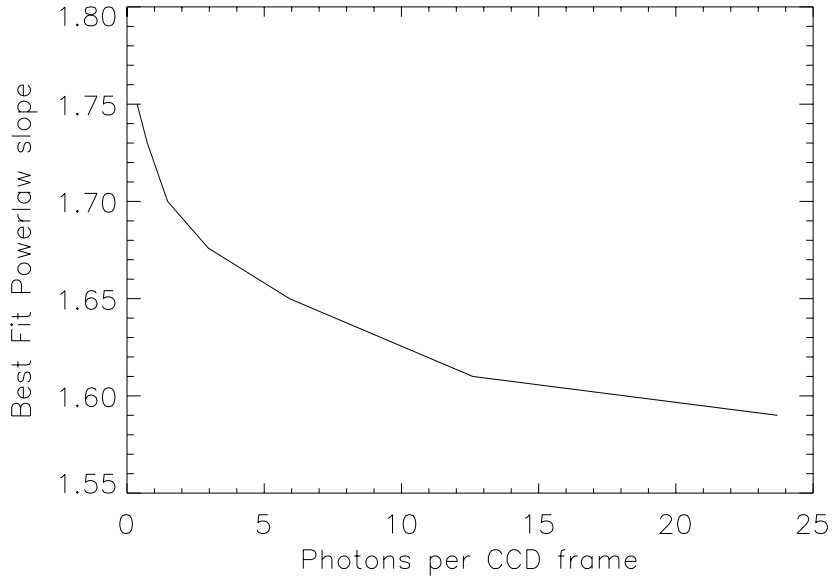

Figure 28: *The best-fitting power law slope, α, for an $\alpha = 1.7$ input spectrum into SciSim, with different input count rates, leading to different levels of pile-up.*

details of events carried in the event list are crucial to performing proper gain calibration for example.
A host of secondary effects of event processing is foreseen (for example the amount of pile-up in the PSF may depend on event pattern selection, particle background rejection is heavily dependent on event selection criteria), but the scope may not fully be appreciated until further reduction of ground calibrations is performed by the instrument PI teams, or after in-orbit experience accumulates.

3.3.12 EPIC-specific proposal submission information

In the preparation of EPIC observing proposals, the following information should be taken into account in order to assess the technical feasibility of intended **XMM** observations; see § 4 for additional, more general information.

3.3.12.1 EPIC spectral quality

In Figs. 29–33 we display a series of Mekal model spectra at different energies, ranging from 0.1 to 10.0 keV, with successively increasing total photon numbers (from 500 to 20000 counts). These show which data quality can be reached for a given total number of counts. All model spectra have been produced with SciSim, feeding in a Mekal model spectrum produced with *xspec*, using the thin filter and the full window mode. For the 0.1 keV model, the MOS and pn cameras are compared directly (Figs. 29 and 30), while for all other energies only the MOS model spectra are displayed. No processing of the spectra (like e.g., background subtraction or rebinning) has been performed.

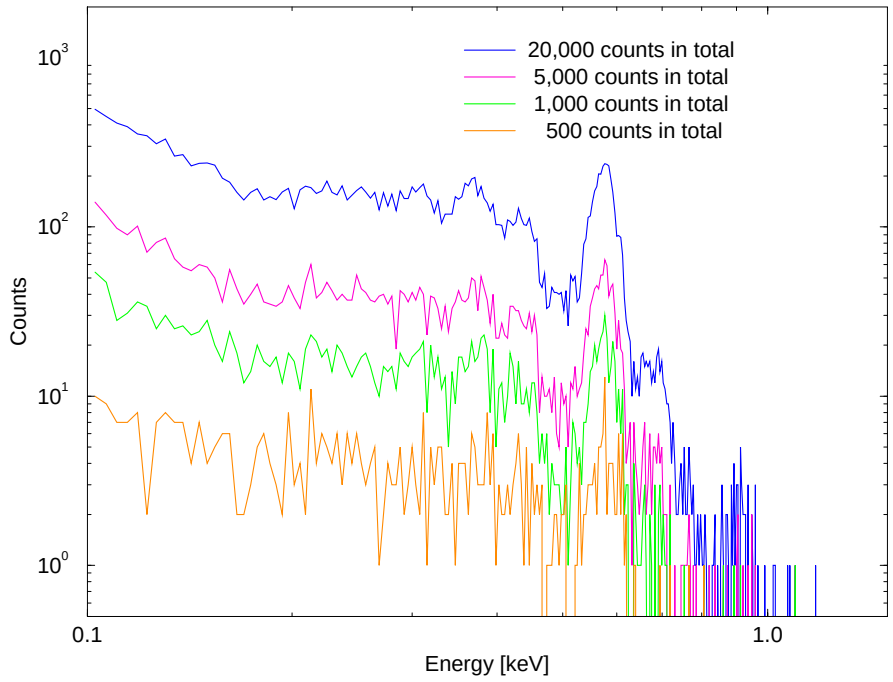

Figure 29: *Series of EPIC MOS model spectra of a Mekal thermal plasma with a temperature of 0.1 keV. From the bottom to the top, the total number of counts in the* **XMM** *passband (0.1–15 keV) increases from 500 to 20000.*

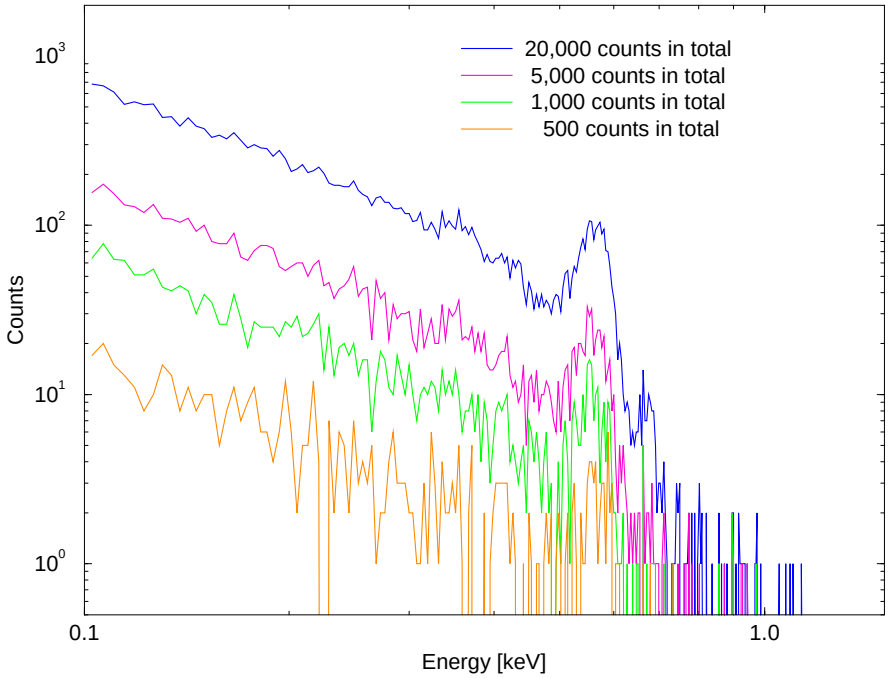

Figure 30: *Series of EPIC pn model spectra of a Mekal thermal plasma with a temperature of 0.2 keV. From the bottom to the top, the total number of counts in the* **XMM** *passband (0.1–15 keV) increases from 500 to 20000.*

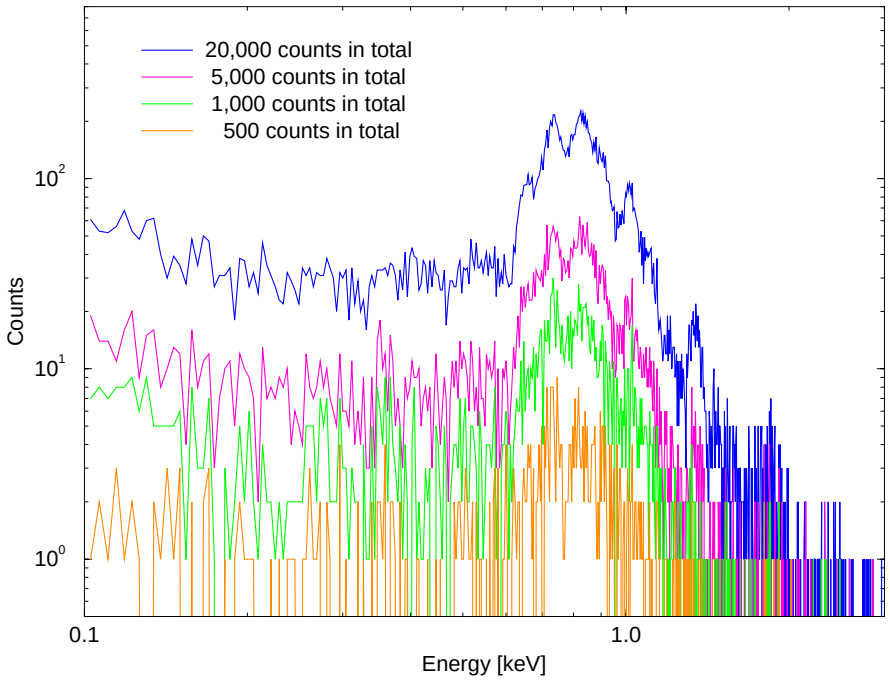

Figure 31: *Series of EPIC MOS model spectra of a Mekal thermal plasma with a temperature of 0.5 keV. From the bottom to the top, the total number of counts in the* **XMM** *passband (0.1–15 keV) increases from 500 to 20000.*

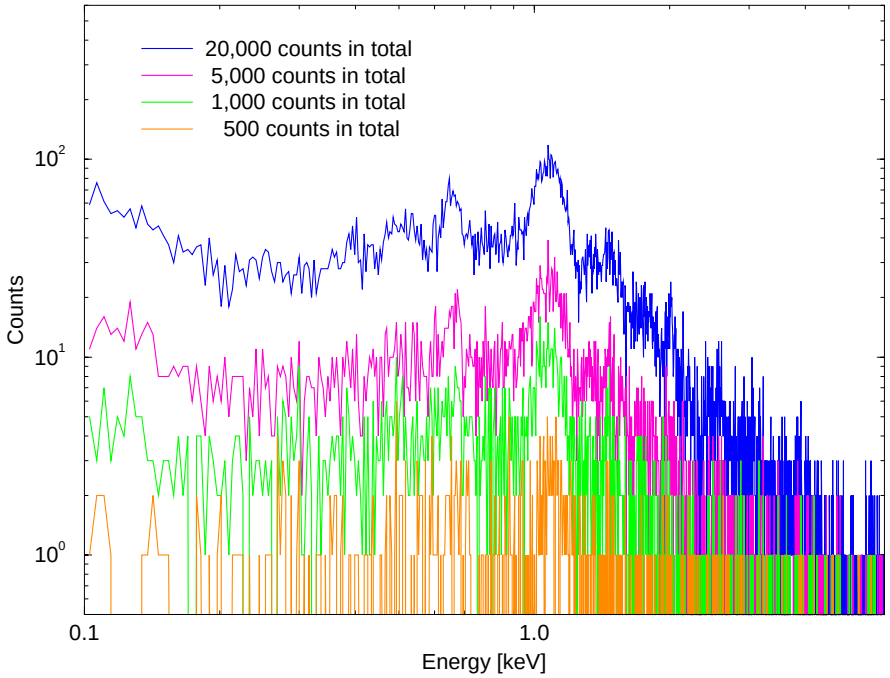

Figure 32: *Series of EPIC MOS model spectra of a Mekal thermal plasma with a temperature of 2.0 keV. From the bottom to the top, the total number of counts in the* **XMM** *passband (0.1–15 keV) increases from 500 to 20000.*

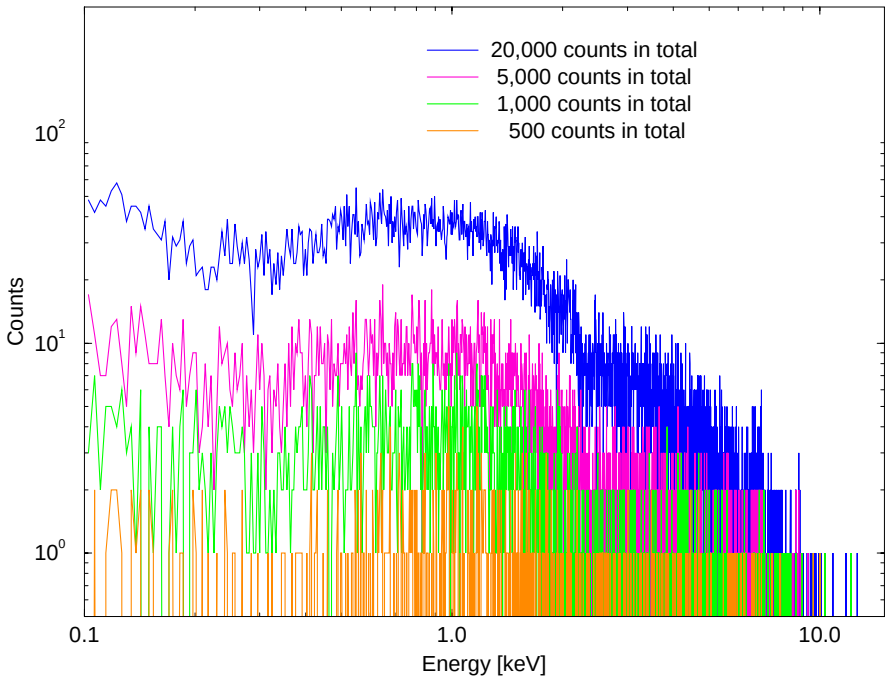

Figure 33: *Series of EPIC MOS model spectra of a Mekal thermal plasma with a temperature of 10.0 keV. From the bottom to the top, the total number of counts in the* **XMM** *passband (0.1–15 keV) increases from 500 to 20000.*

3.3.12.2 EPIC flux to count rate conversion

The following set of figures (Figs. 34–41) provides EPIC flux to count rate conversion factors for a variety of standard spectral models, for each camera type (pn and MOS), with the thin and medium optical blocking filters. Families of curves for various values of the foreground absorbing column density, N_H, are plotted. Both the (unabsorbed) fluxes (i.e., after taking into account the attenuation by the foreground gas) and the count rates are calculated for the 0.1–12 keV band.
Note that the conversion factors for the MOS cameras refer to **one MOS camera only**.
The order of the plots is:

1. Power law models
2. Thermal plasma (Raymond-Smith) models with solar metallicities
3. Black body models

For each model type, two pn camera plots are shown first (thin and medium filter, in that order), then two MOS plots.

3.3.12.3 Count rate conversion from other X-ray satellite missions

For the conversion of count rates from other X-ray satellites to count rates expected for the different **XMM** detectors, we recommend the use of the PIMMS software from NASA's HEASARC (at the URL `http://heasarc.gsfc.nasa.gov/Tools/w3pimms.html`).

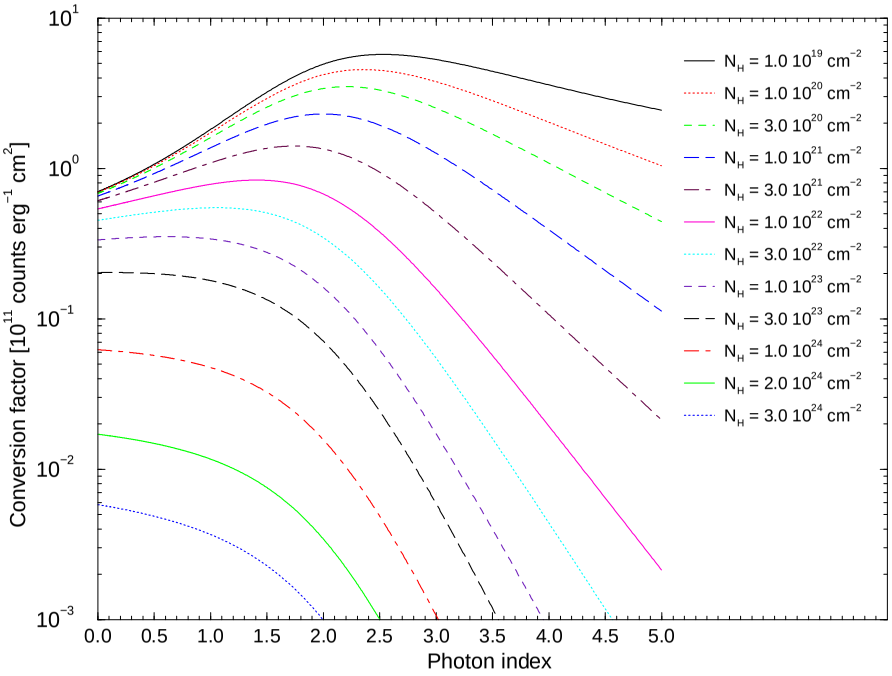

Figure 34: *EPIC pn flux to count rate conversion factors for various power law spectra and different values for the absorbing column density, N_H (thin filter).*

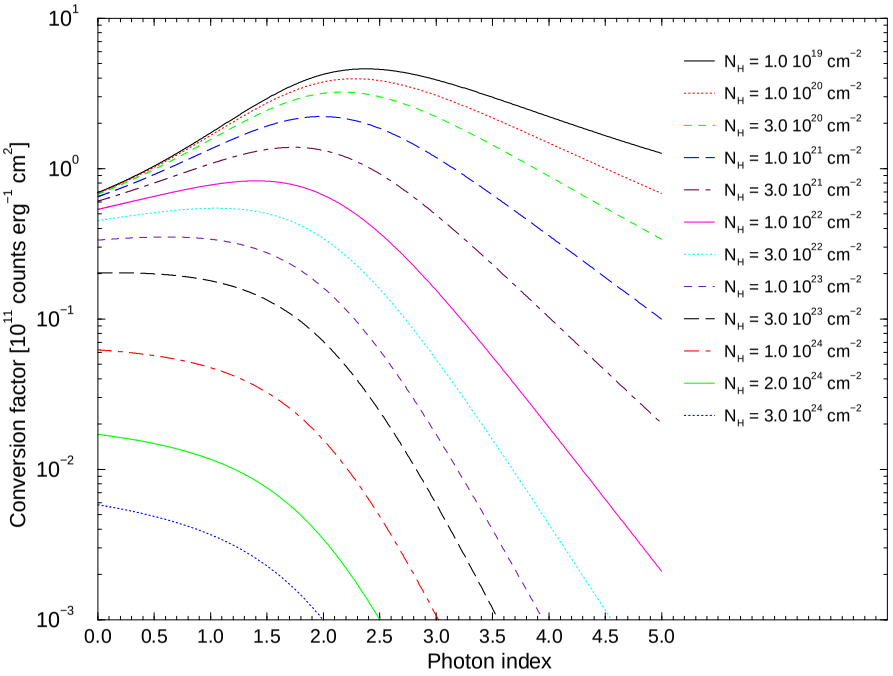

Figure 35: *EPIC pn flux to count rate conversion factors for various power law spectra and different values for the absorbing column density, N_H (medium filter).*

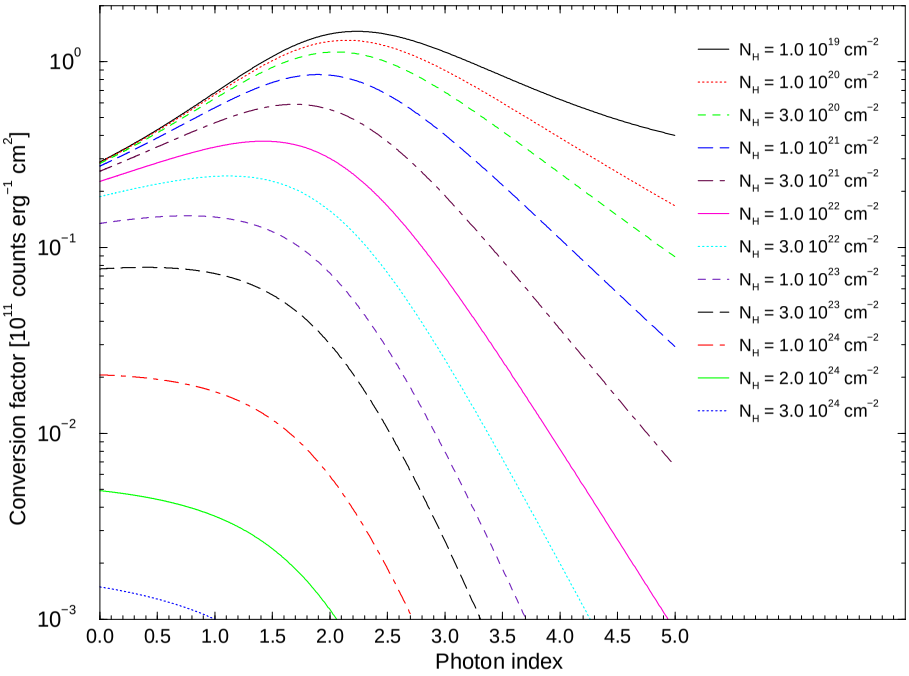

Figure 36: *EPIC flux to count rate conversion factors for one MOS camera for various power law spectra and different values for the absorbing column density, N_H (thin filter).*

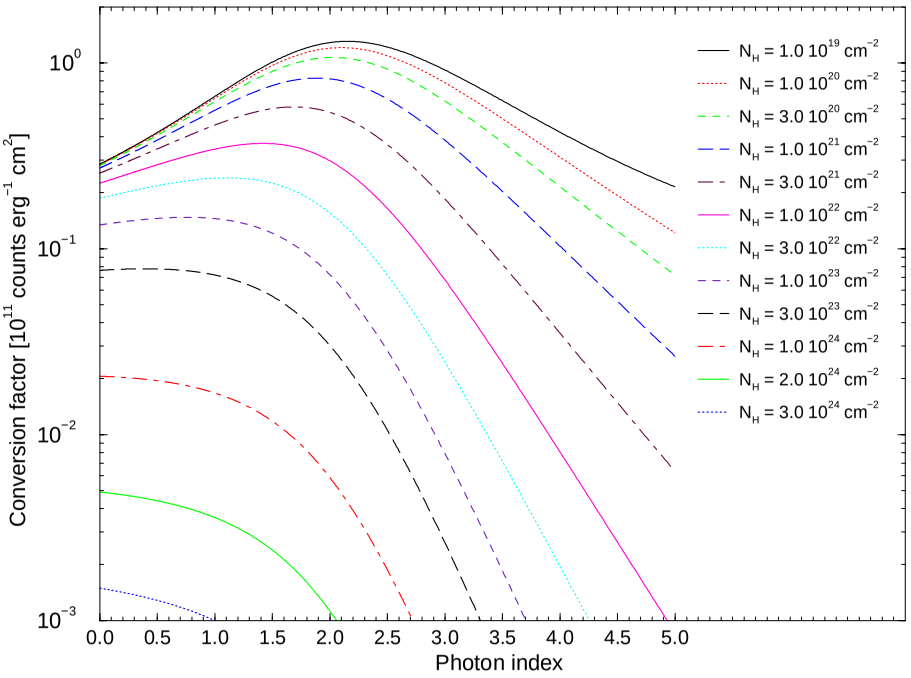

Figure 37: *EPIC flux to count rate conversion factors for one MOS camera for various power law spectra and different values for the absorbing column density, N_H (medium filter).*

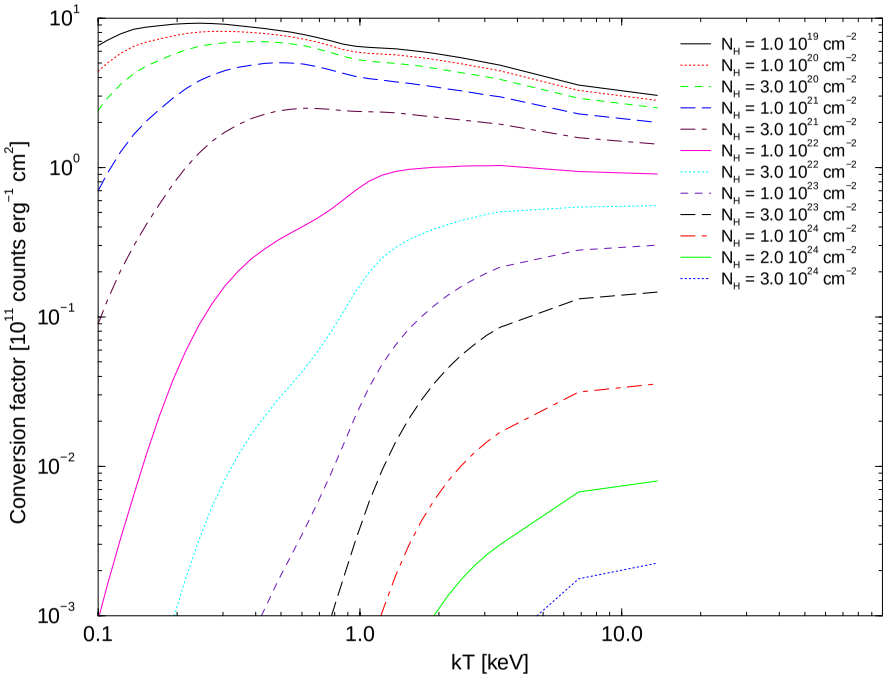

Figure 38: *EPIC pn flux to count rate conversion factors for various Raymond-Smith spectra and different values for the absorbing column density, N_H (thin filter).*

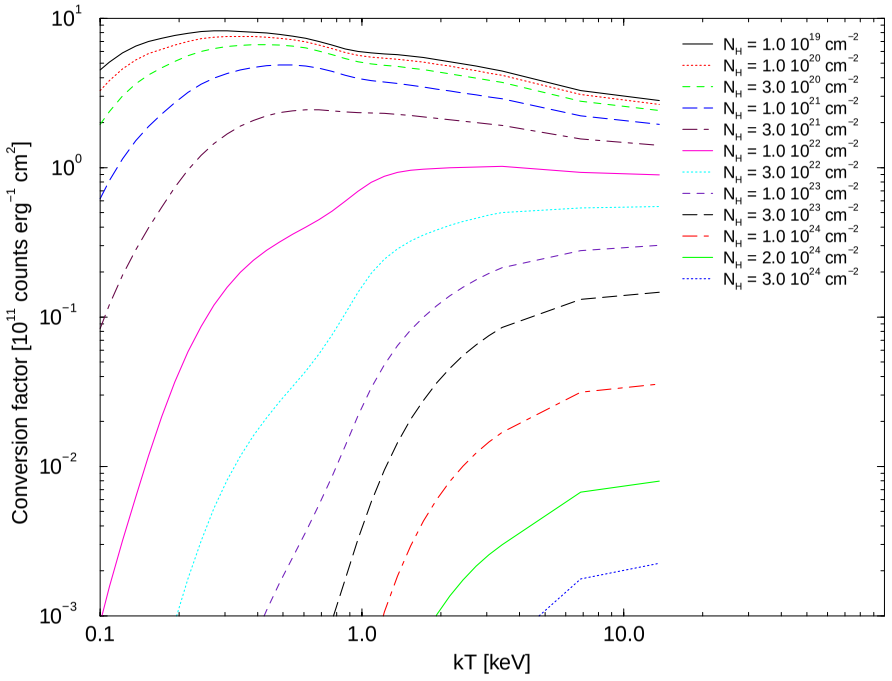

Figure 39: *EPIC pn flux to count rate conversion factors for various Raymond-Smith spectra and different values for the absorbing column density, N_H (medium filter).*

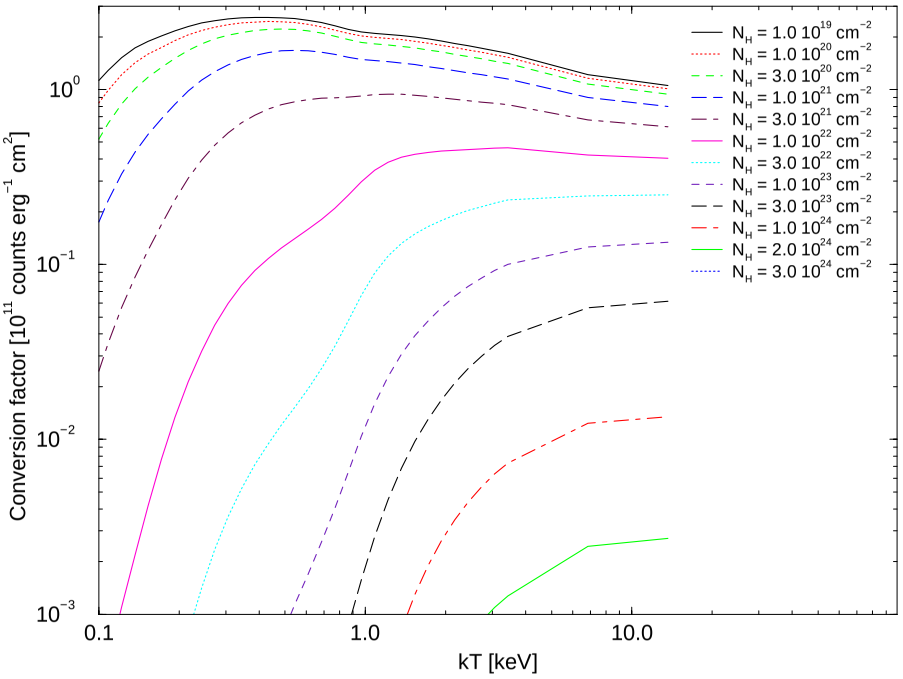

Figure 40: *EPIC flux to count rate conversion factors for one MOS camera for various Raymond-Smith spectra and different values for the absorbing column density, N_H (thin filter).*

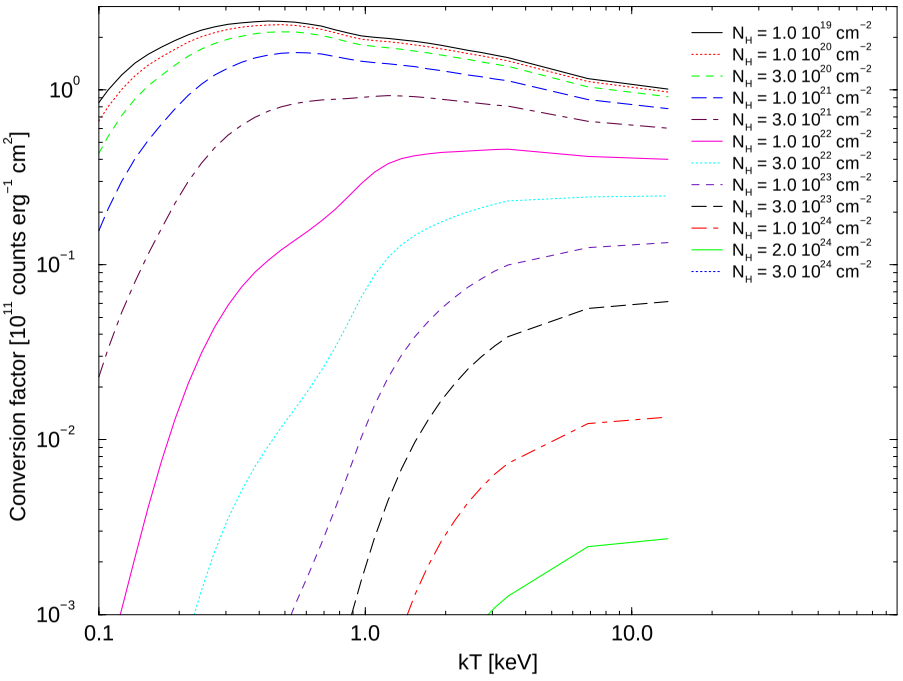

Figure 41: *EPIC flux to count rate conversion factors for one MOS camera for various Raymond-Smith spectra and different values for the absorbing column density, N_H (medium filter).*

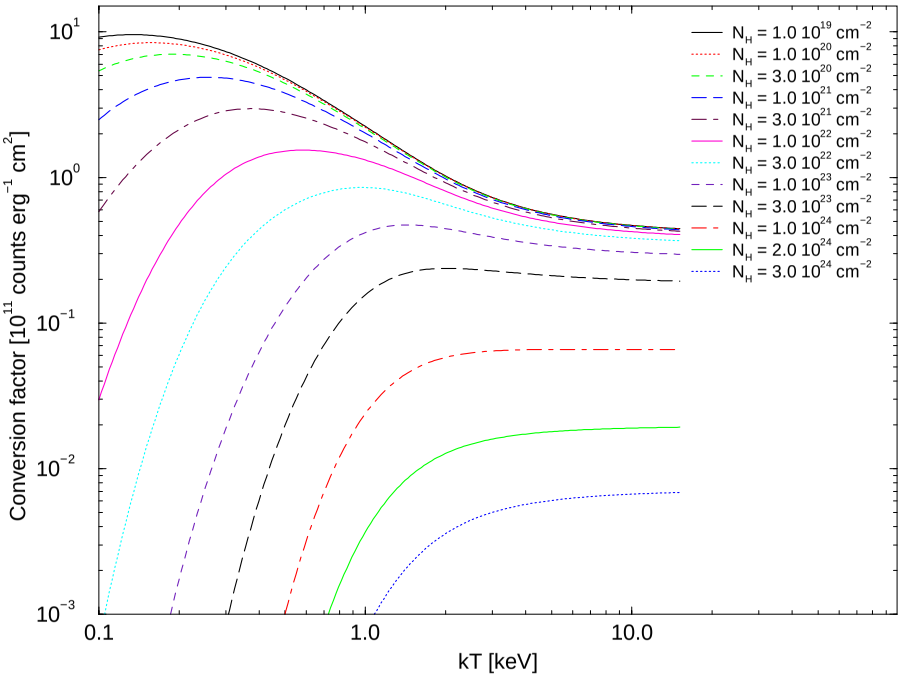

Figure 42: *EPIC pn flux to count rate conversion factors for various black body spectra and different values for the absorbing column density, N_H (thin filter).*

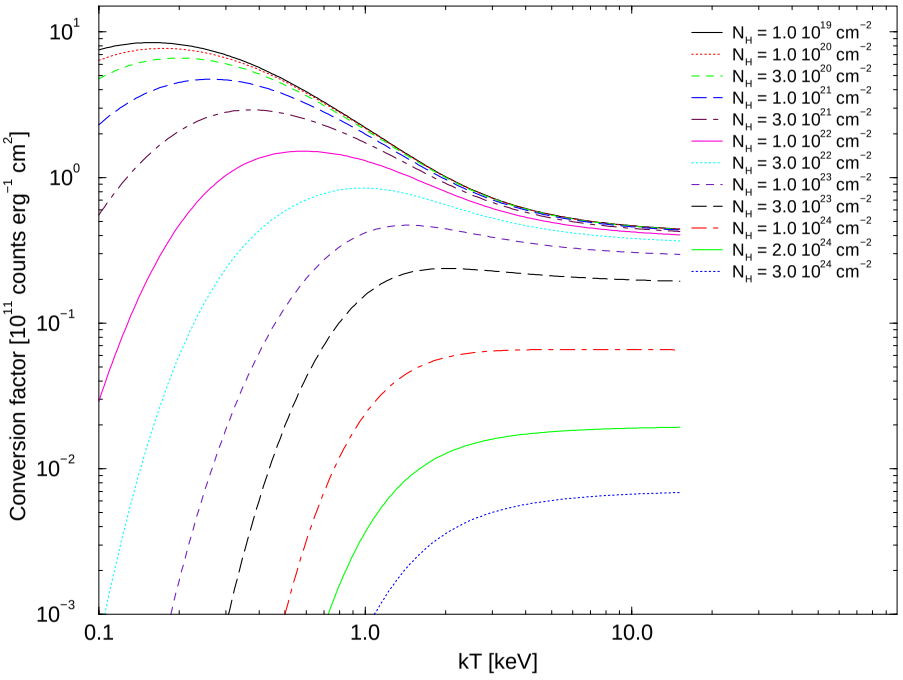

Figure 43: *EPIC pn flux to count rate conversion factors for various black body spectra and different values for the absorbing column density, N_H (medium filter).*

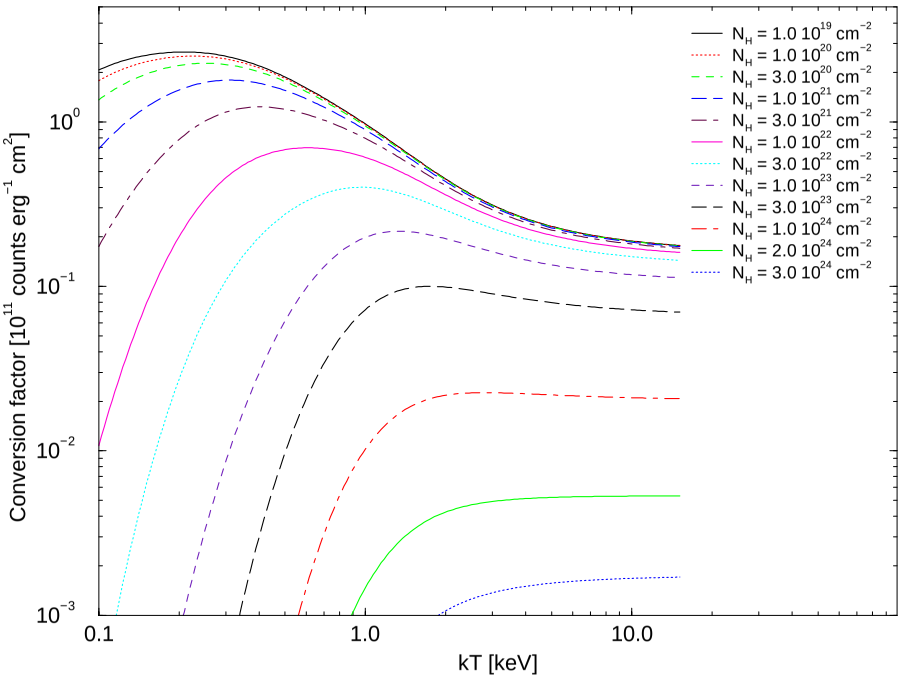

Figure 44: *EPIC flux to count rate conversion factors for one MOS camera for various black body spectra and different values for the absorbing column density, N_H (thin filter).*

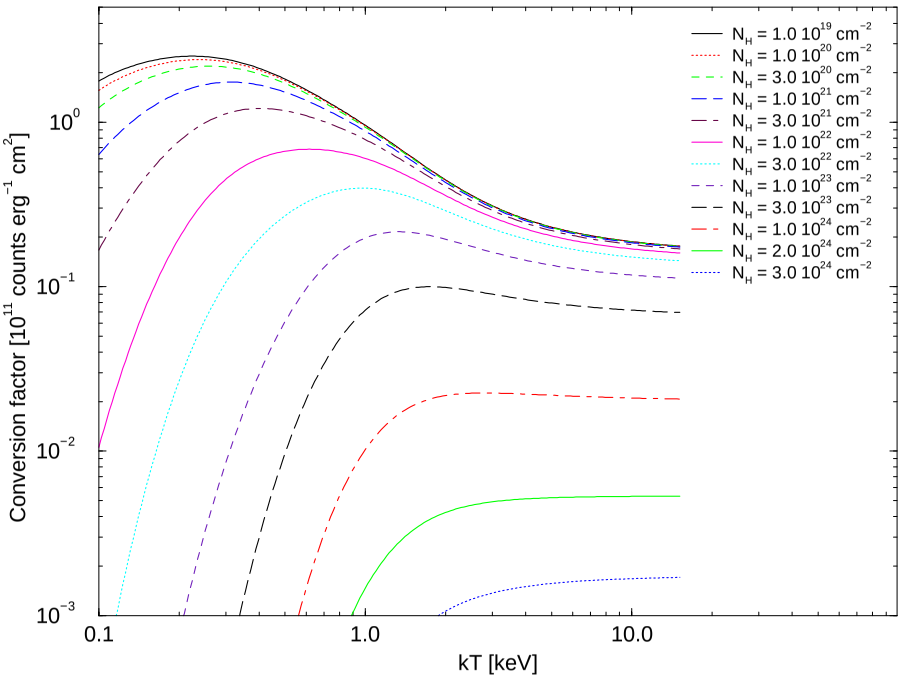

Figure 45: *EPIC flux to count rate conversion factors for one MOS camera for various black body spectra and different values for the absorbing column density, N_H (medium filter).*

3.4 REFLECTION GRATING SPECTROMETER (RGS)

Principal Investigator: Dr. A. C. Brinkman, Space Research Organization of the Netherlands

Two of the three **XMM** X-ray telescopes are equipped with RGS units. These consist of Reflection Grating Assemblies (RGAs) and RGS Focal Cameras (RFCs), see Fig. 3. Among the science instruments of **XMM**, RGS is best suited for high spectral resolution ($E/\Delta E$ from 200 to 800) X-ray spectroscopy in the energy range 0.35–2.5 keV (5–35 Å).[2] The energy range covered by the RGS has a particularly high density of X-ray emission lines, thus offering a large number of diagnostic tools to investigate the composition of the emitting material, e.g., the L shell transitions of heavy elements like Fe and Ni, and K shell transitions of lighter elements, such as N, O, Ne, Mg, and Si. In its high time resolution mode, the RGS offers the possibility to conduct fast soft X-ray spectro-photometry of individual lines.

The grating plates in the RGAs have mean groove densities of ca. 645.6 lines mm^{-1}. The dispersion of the instrument is 7.39 and 11.144 mm/Å for orders –1 and –2, respectively. The RGAs are mounted in the light path of the two X-ray telescopes with EPIC MOS cameras in their primary focus. Each RGA intercepts about 58% of the total light focused by the mirror module.

The RFCs consist of linear arrays of 9 MOS CCD chips (similar to those in the EPIC MOS cameras), which are located along the dispersion direction of the RGAs. The RGS MOS chips are back-illuminated in order to maximise their soft energy response and aluminium-coated on the exposed side in order to suppress optical/UV light. They have 1024×768 $(27\mu m)^2$ pixels, half of which (1024×384) are exposed to the sky, while the other half is used as a storage area. During readout, 3×3 pixel on-chip binning (OCB) is performed in the default spectroscopy mode, leading to a pixel size for RGS observations of $(81\ \mu m)^2$, which is sufficient to fully sample the RGS line-spread function (LSF). For an on-axis source the zeroth order image of the gratings is not visible on the detector array.

There are small, but measurable differences between the two RGS units. While these do not lead to a noticeable effect on the effective areas, it is expected that the energy resolution of RGS-2 will be lower than than that of RGS-1 (as shown in Figs. 48–49).

[2] The formula for rough conversion of wavelengths into energies is λ [Å] $\times$ E [keV] = 12.3984.

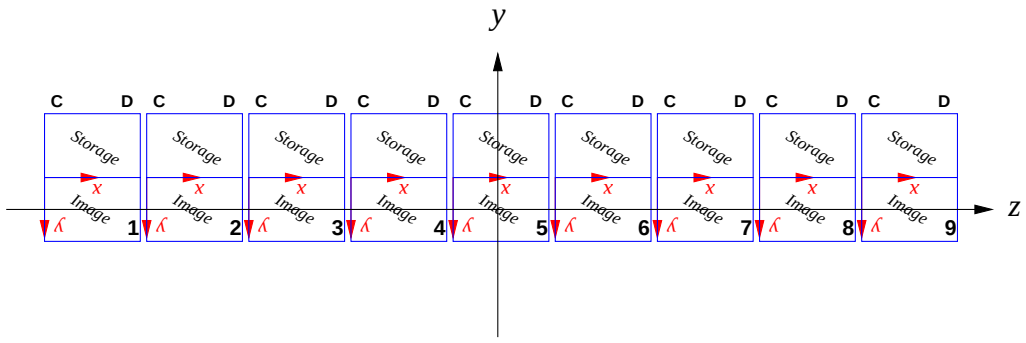

Figure 46: *Sketch of an RFC chip array, with 9 MOS CCDs. The half of each CCD at large camera-y coordinates is exposed to the sky, the other half is used as a storage area. The –1. order spectrum of a source observed on-axis starts on the left chip. The dispersion direction is along the "Z" axis, so that higher energies are dispersed to higher values in Z.*

3.4.1 RFC chip arrays

MM
Fig. 46 displays a sketch of the chip geometry in an RFC. The two RFCs will be offset with respect to each other along their dispersion direction so as to fill the gaps in between each other's chips (i.e., providing continuous coverage along the dispersion direction).
The chip on the left side of Fig. 46 has number 1 (the low Z end of the coordinate scale), the one on the right is number 9 (high Z value). For an on-axis source, the individual chips cover approximately the energy ranges listed in Table 9. The numbers tabulated there relate to a nominal case (the design geometry). Detailed simulations should be performed in case the user is interested in lines that are close to the chip boundaries. To move important lines away from chip boundaries, users may want to consider changing the pointing (boresight coordinates) accordingly and observing with a fixed position angle.

Table 9: *The wavelength and energy ranges covered by the chips of RGS for an on-axis source, for the design instrument geometry*

Chip no.	**Energy Range [eV]**		**Wavelength Range [Å]**	
	–1. order	**–2. order**	**–1. order**	**–2. order**
1	328.2–374.3	656.4–748.7	37.78–33.12	18.89–16.56
2	374.9–432.4	749.9–864.8	33.07–28.67	16.53–14.34
3	433.1–506.1	866.3–1012.3	28.62–24.50	14.31–12.25
4	507.1–602.2	1014.2–1204.5	24.45–20.59	12.22–10.29
5	603.5–731.6	1207.0–1463.1	20.54–16.95	10.27–8.47
6	733.3–913.2	1466.6–1826.4	16.91–13.58	8.45–6.79
7	915.7–1183.5	1831.4–2367.0	13.54–10.48	6.77–5.24
8	1187.4–1622.0	—	10.44–7.64	—
9	1628.6–2440.2	—	7.613–5.08	—

Table 10: *The energy ranges covered by the RGS in different grating orders*

Order	Energy range [keV]
–1	0.35 – 2.5[1]
–2	0.62 – 2.5[1]
–3	1.20 – 2.5[1]

Note to Table 10:
1) Practical limitation due to very low effective area above 2.5 keV. The theoretical upper limit is 2.5 keV × m, where m is the order number.

3.4.2 RGS grating orders

X-rays are reflected into spectral orders –1 and –2 with the highest efficiency, so these are the orders expected to produce useful data in the majority of observations. Count rates in the –3. order are about 8 times lower than in the –2. Depending on grating order, the RGS covers the energy ranges listed in Table 10.
The exact location of a source spectrum on the RGS CCD chips depends on the source's location within the field of view of the X-ray telescopes. For a target on-axis the observed spectrum is well centred on the RFC chips in the cross-dispersion direction and the wavelength scale is known with the best calibration accuracy. The wavelength scale for sources off-axis in the cross-dispersion direction is the same as for those on-axis, but will be different for sources off-axis in the dispersion direction.
Due to the grating relation ($m \times \lambda$), the orders overlap spatially on the CCD detectors of the RFC. Separation of the spectral orders is achieved by using the CCDs' intrinsic energy resolution. The dispersion of a spectrum onto an RFC array is shown in Fig. 47. The –1. (lower) and –2. order (next) are most prominent and are clearly separated in the vertical direction (i.e., in CCD PHA space). Photons of higher orders are also visible.

3.4.3 RGS spectral resolution

The two RGS units operate independently of one another. Their LSFs depend on the shapes of the telescopes' PSF behind which they are located and on the characteristics of the RGS units.
The PSF of the **XMM** telescopes presented above (§ 3.2.1.1) thus determines the width of that RGS's LSF core and thus its capability to resolve X-ray lines. The spectral resolution for a point source is displayed in Figs. 48–50 for both RGS units separately. Fig. 48 displays the *HEW* as a function of energy, E, Fig. 49 shows the *FWHM*.
In order to assess whether two closely spaced spectral lines can be resolved, the resolving power based on *FWHM* is the appropriate measure. To evaluate the detectability of a weak feature against a strong continuum, the resolving power based on *HEW* is the appropriate figure.

Fig. 50 shows the spectral resolving power ($\lambda/\Delta\lambda = \mathrm{E}/\Delta\mathrm{E}$) as a function of wavelength. In the –1. order, RGS-1 has an almost constant resolution in wavelength space, of ca. 0.04 Å.
An example for an individual line, the Al-K line at 1.49 keV, along the dispersion direction, is displayed in Fig. 51. One can see the narrow core of the LSF and the underlying broad wings. The same line, perpendicular to the dispersion direction, is presented in Fig. 52.

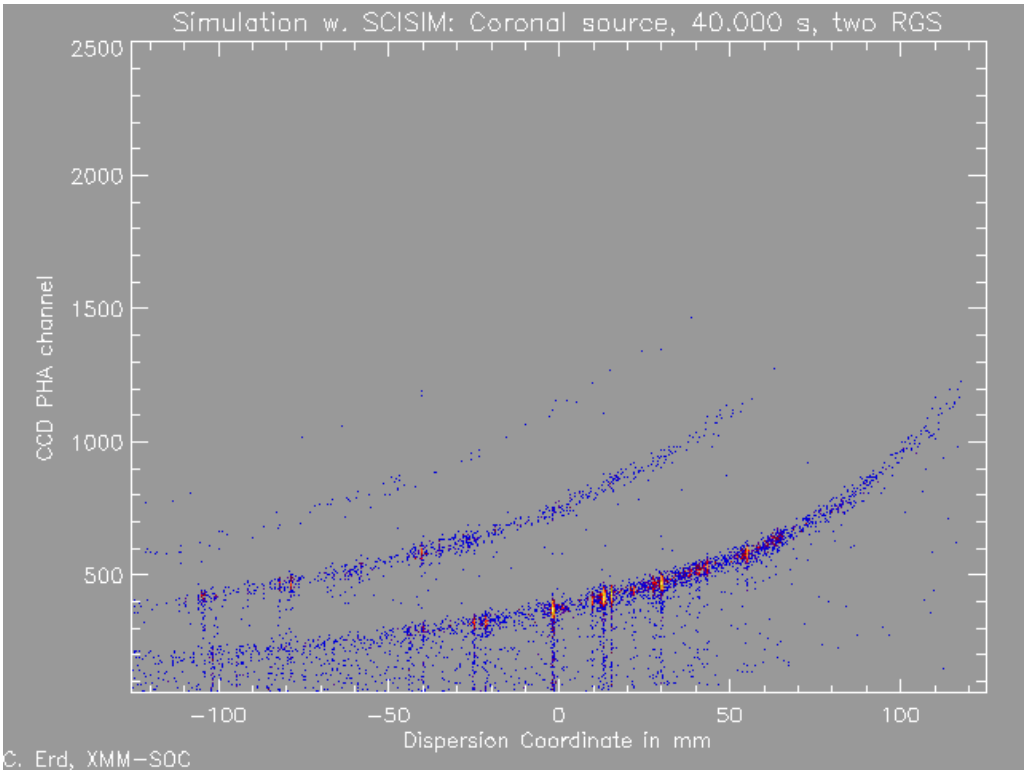

Figure 47: *The dispersion along the dispersion coordinate, Z (in mm), vs. CCD PHA-channel output of an RGS spectrum in –1. and –2. grating orders onto the RGS focal cameras, assuming equal gains of all CCD output nodes. This also illustrates the mechanism used for separating spectral orders.*

3.4.3.1 Components of the RGS LSF

The RGS angular (or wavelength-) response to monochromatic radiation – and thus its LSF – consists of two distinct physical components. The core of the profile is determined by geometrical optics: the telescope angular response, the grating figures, the grating-to-grating alignment, and the focusing of the telescope. This core can be calculated reliably with a raytrace code, based on an explicit model for the various components of the RGS. The parameters of this model have been calibrated in separate tests at sub-assembly level (telescope, RGA, individual gratings), and the resulting model has been validated in end-to-end tests of both spectrometers at the Panter X-ray testing facility of the Max Planck Institut für extraterrestrische Physik.
Microroughness on the gratings causes scattering of light, the amplitude and angular distribution of which scale completely differently with wavelength and dispersion angle (or spectral order) from the core shape. A theoretical model for the redistribution of light due to scattering was developed, based on first order perturbation theory for scalar diffraction. The free parameters of this model, the rms amplitude and correlation length of the surface fluctuations, were calibrated on a large subset of the gratings and the resulting scattering redistribution kernel was verified in the end-to-end tests at Panter.
The characteristic two-component shape of the resulting LSF (response integrated over the cross-dispersion direction) can be seen in Fig. 53, which shows the response of RGS-1

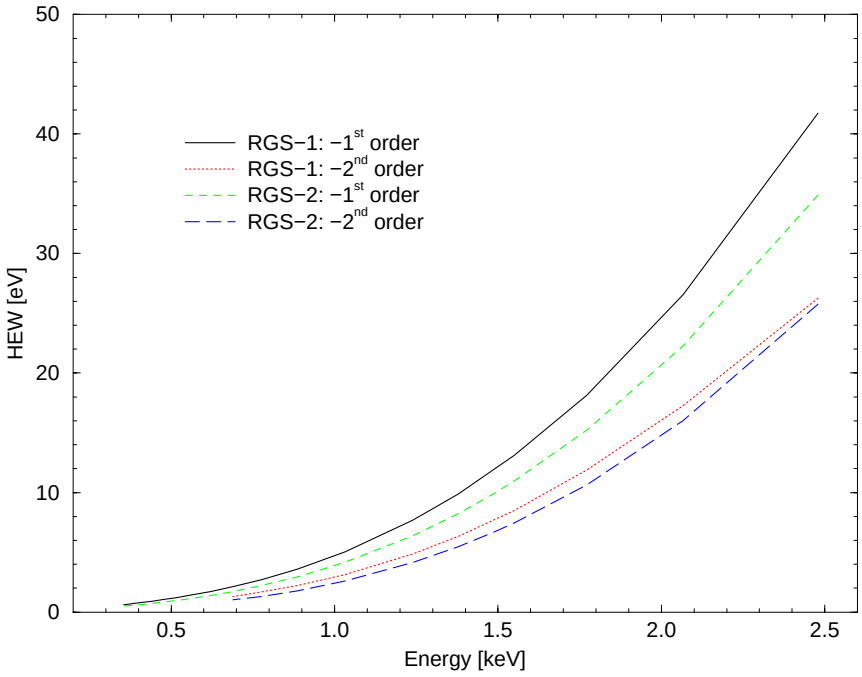

Figure 48: *The resolving power (*HEW*) of both RGS in the –1. and –2. grating orders.*

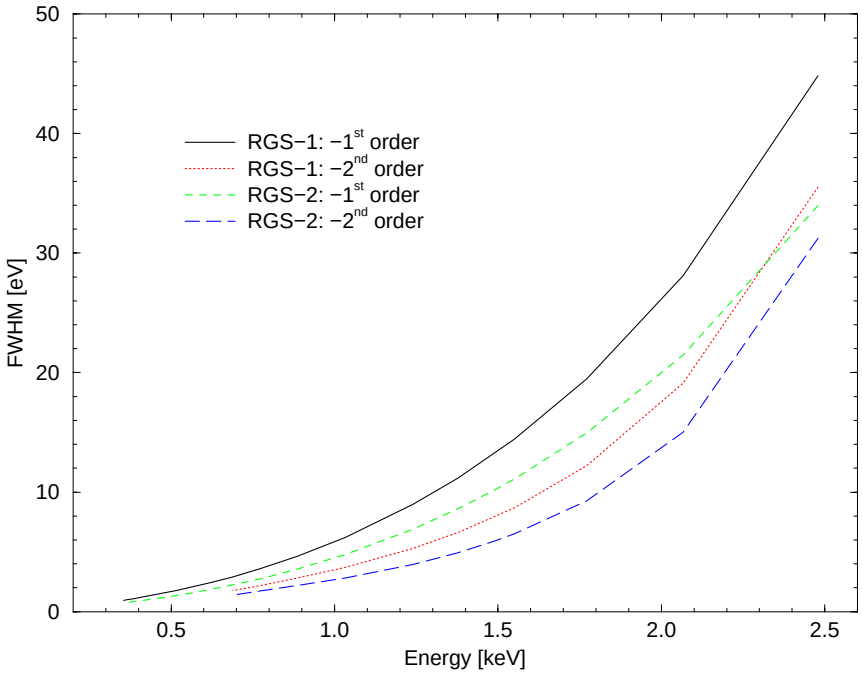

Figure 49: *The resolving power (*FWHM*) of both RGS in the –1. and –2. grating orders.*

to Mg Kα radiation at 1.25 keV energy in the –1. and –2. spectral order, as measured at Panter, on a logarithmic scale so as to enhance the visibility of the line wings. Overlaid on the data are simulations calculated with the current best model for the instrument. As

is clear from these figures, the LSF can not adequately be represented by a single simple profile function (e.g., Gauss or Lorentzian) at all wavelengths. Therefore, to characterize the resolving power of the RGS, two separate measures are shown above, one based on the *HEW* of the LSF, one based on the *FWHM* (Figs. 48 and 49).
At low energies (long wavelengths), scattering is unimportant, and the LSF is dominated by the nearly-Gaussian core of the profile. The resolving power therefore asymptotically approaches approximately

$$\mathcal{R} \equiv \lambda/\Delta\lambda \sim \text{constant} \times \lambda \quad (1)$$

since $\Delta\lambda$ for the core is only a weak function of λ. At short wavelengths, scattering is relatively more important, and the resolving power curves decline faster than proportional to λ. Final modeling of the scattering behaviour in this regime is still in the process of refinement, and the precise shape of the resolving power curves for energies above ca. 1.5 keV ($\lambda \leq$ 8 Å) may therefore change somewhat with improved modeling.

3.4.3.2 RGS spectral resolution for extended sources

The RGS spectral resolution depends on the angular extent of the observed source. For an extended source ($\geq 30''$), emission lines are broadened according to the relation

$$\Delta\lambda(ext) = 0.124/m \times \theta(ext), \quad (2)$$

where $\Delta\lambda$(ext) is the resolution (in Å) in case of an extended source, for the spectral order m and a source extent of θ(ext), in arcmin. This illustrates that, for a source extent of order $1'$, RGS still clearly outperforms EPIC in terms of spectral resolution.

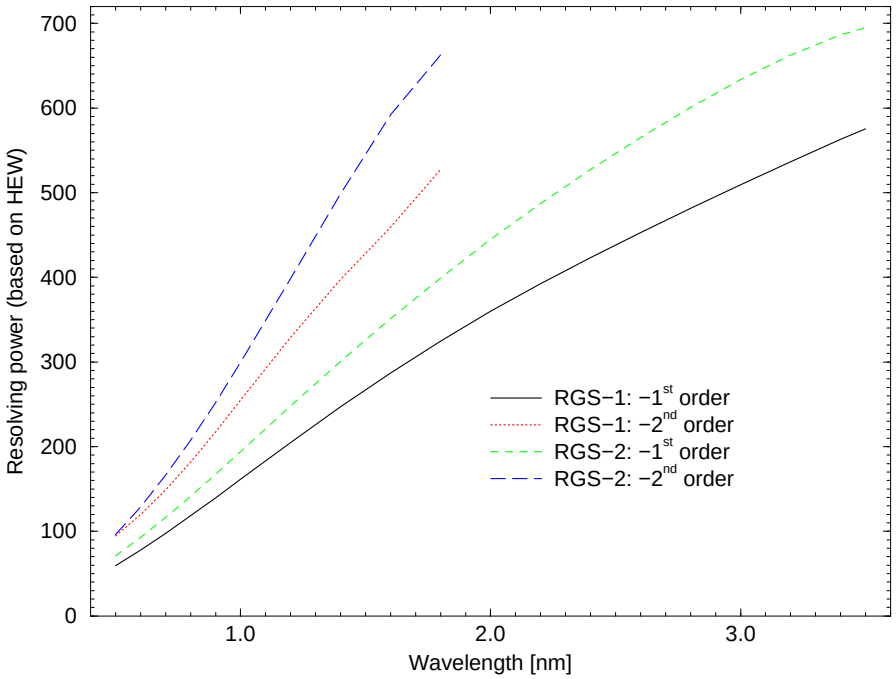

Figure 50: *The resolving power ($\lambda/\Delta\lambda = E/\Delta E$) of both RGS in –1. and –2. grating order.*

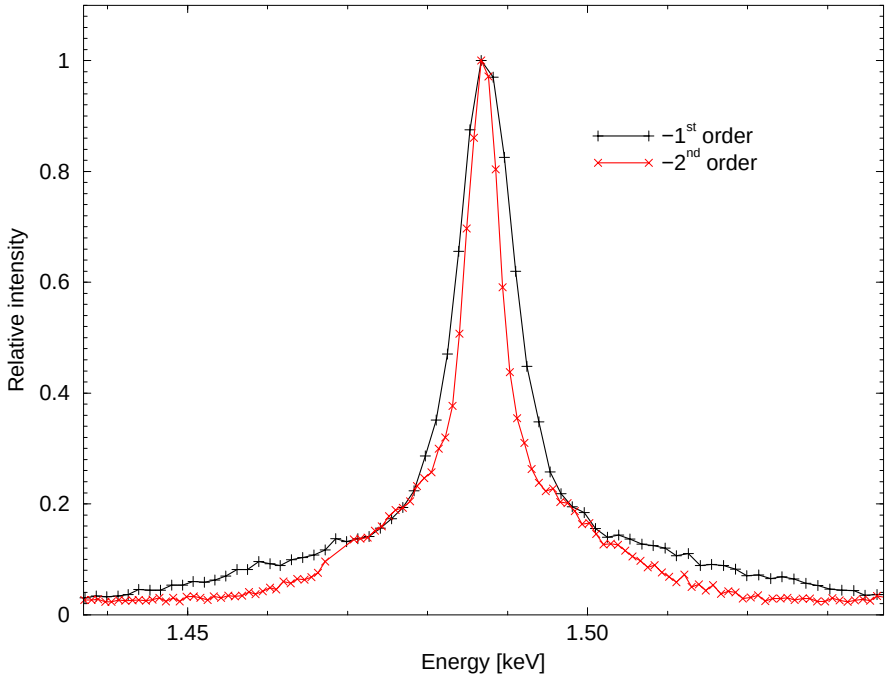

Figure 51: *A close-up view of the Al K line at 1.49 keV, from an RGS model spectrum produced with SciSim, along the dispersion direction.*

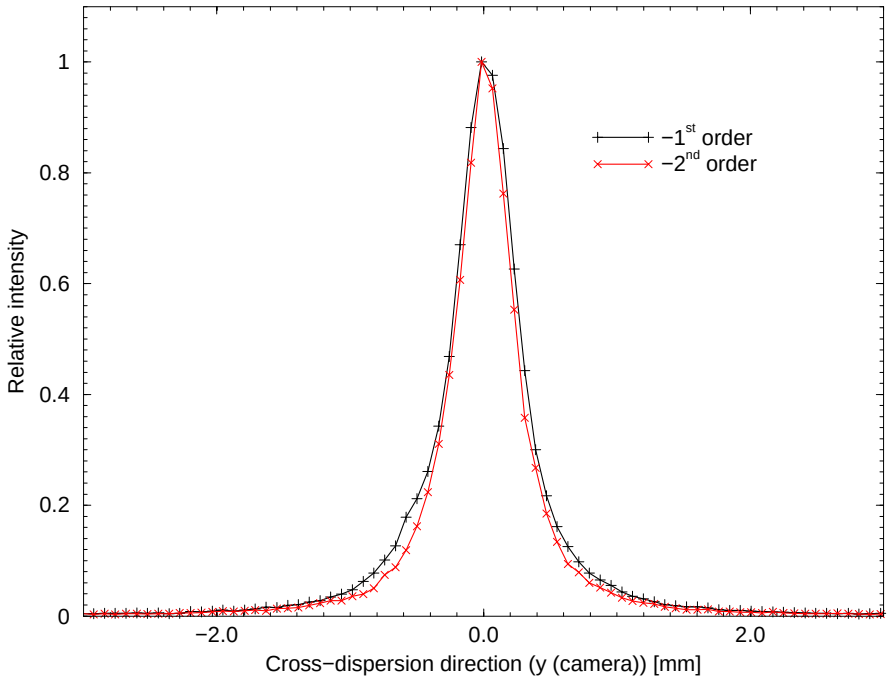

Figure 52: *A close-up view of the Al K line at 1.49 keV, from an RGS model spectrum produced with SciSim, along the cross-dispersion direction.*

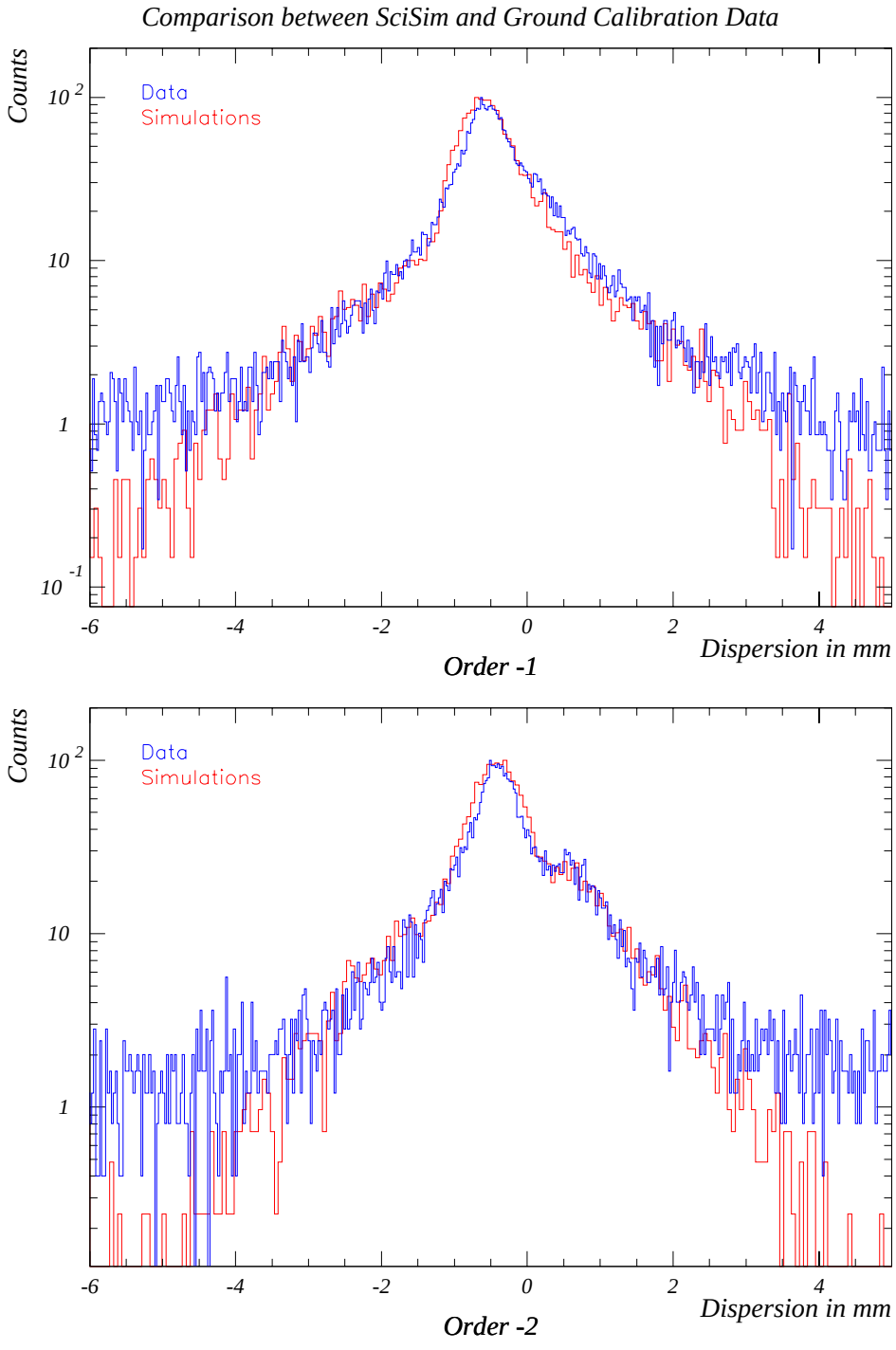

Figure 53: *Response of RGS-1 to Mg Kα radiation ($E = 1.25$ keV; $\lambda = 9.89$ Å), in orders $m = -1, -2$, respectively, as measured at Panter. The excess seen on the right side of the profile is due to the presence of fainter, slightly higher energy lines in the emission spectrum of the calibration source (which was also included in the input to the simulations). The second order profile shows that the outer wings of the scattering distribution are currently underpredicted. For reference, 1 mm in the focal plane equals 0.104 Å at Mg Kα, $m = -1$, and 0.0665 Å at Mg Kα, $m = -2$.*

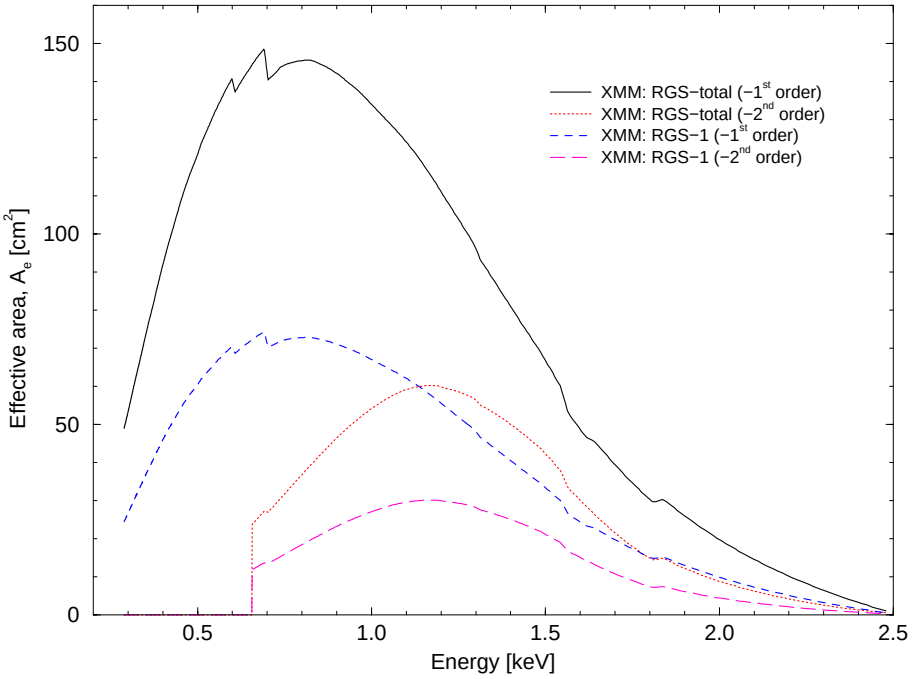

Figure 54: *The effective area of both RGS units combined and RGS-1 (linear scale). Seam losses between the CCDs are not taken into account.*

3.4.4 RGS effective area for dispersive spectroscopy

Several parameters determine the RGS effective area. The first is the effective area of the mirror modules (see § 3.2.2). Next, the amount of light from the mirrors intercepted by the grating arrays is a key quantity and how much of this light is diffracted to the different spectral orders and then absorbed on the RFCs.

The next factor influencing the RGS photon efficiency is the RFC CCDs' quantum efficiency (QE). This varies from 70% to 95% over the RGS passband from 0.35 to 2.5 keV. The value of 70% for the lowest energies will drop (by up to about 10%) when event selection with a lowest photon energy threshold is performed. The QE, without energy threshold selection, has been taken into account in the calculations of the effective area of the RGS, as displayed in Fig. 54.

To assess the total efficiency of the RGS instrument per spectral order, the efficiency with which the different spectral orders can be selected must also be taken into account. One can see in Fig. 47 that the RGAs' spectral orders spatially overlap in the dispersion direction. However, the intrinsic energy resolution of the CCDs allows the separation of X-ray photons in different orders, i.e., photons which are of different energies, but have the same position along the dispersion direction. Default masks for the spatial extraction of photons from the different orders (using PHA vs. dispersion coordinate plots, as in Fig. 47), are provided as part of the Current Calibration File (CCF) for each **XMM** RGS instrument. The expected efficiency in the post-observation RGS order selection with the SAS is ca. 90%. Since the order selection is part of the offline processing, it is **not** included in the effective area calculations presented here.

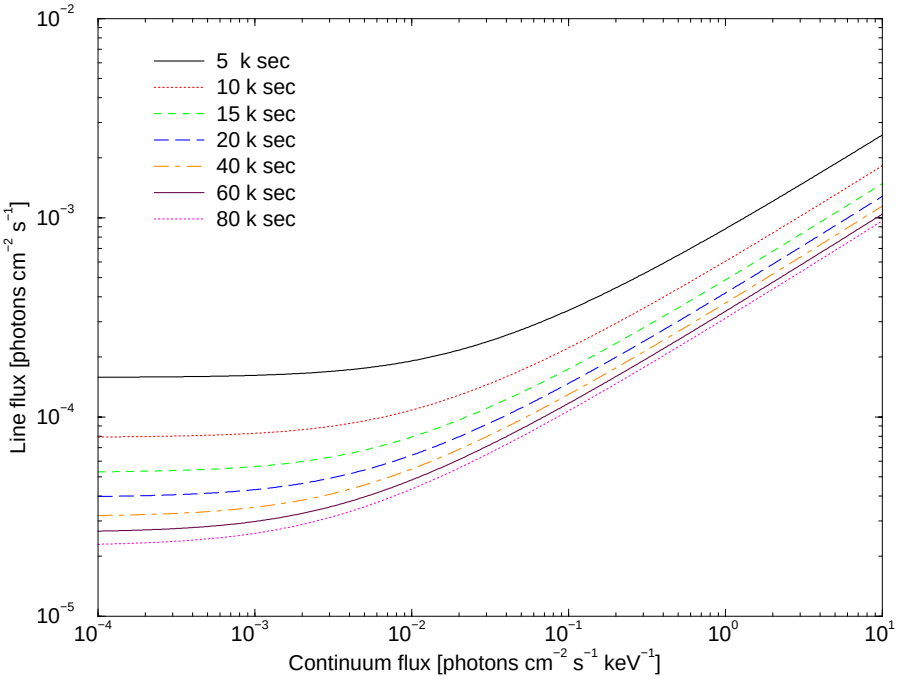

Figure 55: *The RGS sensitivity limits of one RGS for a 5-σ detection on the* O VII *emission line complex at 0.57 keV of a point source.*

Fig. 54 displays the effective area of both RGS units together, taking into account the factors listed above. This is ca. 150 cm^2 at 1 keV. Seam losses between the CCDs were excluded from this calculation.

3.4.5 RGS sensitivity limits

As a measure of the RGS sensitivity the detection threshold for a few prominent lines in the 0.35–2.5 keV range has been modeled using SciSim. As examples, the following lines were chosen: the O VII line complex (at 0.57 keV), the Ne X line (at 1.022 keV) and the Si XIII line (at 1.86 keV). The RGS line sensitivity plots displayed in Figs. 55–57 provide an estimate of the exposure time necessary to detect a line above a certain underlying continuum at a significance level of 5-σ. The calculations were performed **for one RGS**. It is in all cases assumed that the line emission emanates from a point source.
The calculations are based on the line flux integrated over the *HEW* of the line profile, assuming Gaussian error propagation. For such an estimate, four contributing components must be considered:

1. The flux of the line,
2. the flux of the underlying continuum of the source,
3. the X-ray background and
4. the particle background.

The X-ray background varies over the sky. In order to provide a graphical representation of RGS's sensitivity which is independent of the source coordinates on the sky, the X-ray

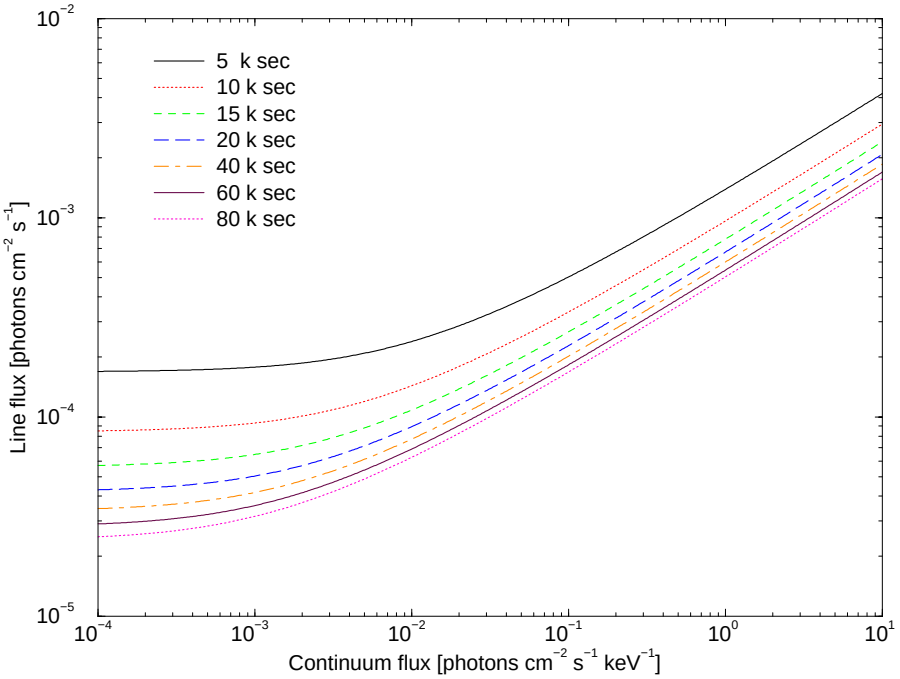

Figure 56: *The RGS sensitivity limits of one RGS for a 5-σ detection on the Ne* X *emission line at 1.022 keV of a point source.*

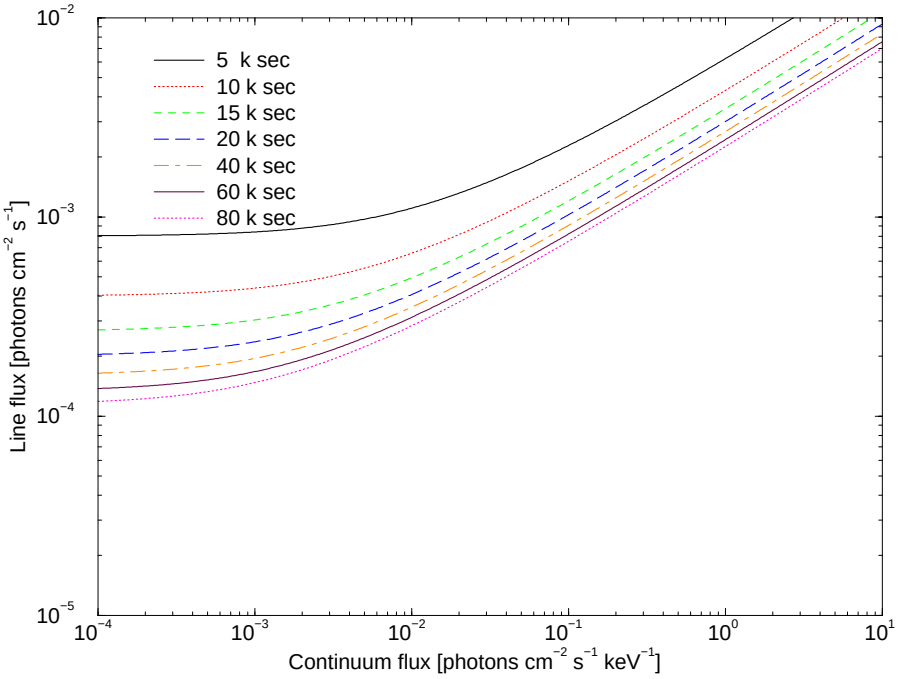

Figure 57: *The RGS sensitivity limits of one RGS for a 5-σ detection on the Si* XIII *1.86 keV emission line of a point source.*

background was not considered directly. However, at the discussed energies the extragalactic X-ray background can well be reproduced by a power-law spectrum. This allows us to consider the X-ray background simply by adding an additional component to the continuum flux of the source. In general, the "continuum flux" in the plots can therefore be assumed to contain in practice a contribution from both the source continuum and the X-ray background at the position of the source.
The particle-induced background, which depends on the design of the instruments, is considered in the calculation of the curves. We assume a particle-induced background of 3.0×10^{-9} counts mm^{-2} s^{-1} keV^{-1}. This is a mean number, which accounts for the normal fluctuation in solar activity. For the given lines we assumed a geometrical area for particle hits of 7.2, 10.8 and 12.5 mm^2.
The plots allow a first estimate of the exposure time in the sense that unreasonable sources can be rejected during a pre-selection of possible targets. They give a basic idea of whether or not it is possible to detect lines. They are not intended to (and cannot) substitute detailed simulations with realistic spectra with SciSim for sources where a detection and/or separation of one or more emission lines is the main scientific goal.

3.4.6 RGS response

Various components may feature in the data from RGS observations, such as:

- In-flight X-ray calibration source background

  Four calibration sources permanently illuminate the CCD of the RFC. The emission is primarily in F-K and Al-K and care has been taken such that the energies of these lines do not coincide spatially with the equivalent energies in the diffracted spectrum. The source intensity is 0.1 counts cm^{-2} s^{-1}. Using both spatial and energy information, their contribution to the celestial spectra can be estimated.

- Optical load on the CCDs

  This is caused by various optical straylight components. Detected optical photons will modify the gain calibration of the CCDs through an introduction of an additional energy offset. Using diagnostic mode data, these offsets can be measured.

- Particle-induced background

  This is expected to cause a uniform distribution of low surface brightness background across the surface of the RFC (see § 3.4.5 for assumptions on the intensity).

- Diffuse cosmic X-ray background

  At any location on the RFC, the grating equation is satisfied for a wide range of energies and celestial locations, but most photons from the diffuse background will be discriminated by the spatial/spectral filtering meachanism. Any remnant signals will manifest as a uniform low surface brightness feature (seen as in the particle background above). Given an appropriate model of the celestial background spectral distribution and assuming an isotropic spatial distribution, the response of the instrument can be satisfactorily modeled. Independently, EPIC data can be used to directly measure the background.

- Apparent cross-talk between orders

  The CCD response includes a low energy tail due to a finite number of photons producing anomalously low energy signatures. In the case of bright emission feature being measured in the second order spectrum, the intensity of this tail may become significant, as it may produce counts in the co-located first order spectrum. These effects can be modeled and can be easily identified in the PHA dispersion plane (cf. Fig. 47, e.g., at Z = 0-110 mm).

- Effects of scattering by the gratings

  Due to X-ray scattering off the gratings (about 20% at mid band), there is an additional tail of the LSF. While true source continuum emission follows the dispersion equation, scattered light appears as an horizontal distribution in the PHA versus dispersion plot (cf. Fig. 47). This effect can be modeled and is included in SciSim (cf. e.g. Fig. 63).

3.4.7 Operating modes of the RGS

All RGS CCDs are operated in the so-called "frame store" mode, in which half of each CCD is exposed to celestial radiation. The contents of this half is transfered to the second (shielded) half, which works as a storage area before readout, while the first half is acquiring the next frame. Thereby, the two-dimensional dispersed photon distribution is stored.

The RGS has two science modes, "spectroscopy" and "high time resolution" (see Table 11 for a summary of their basic characteristics). Most data will be obtained in the former. Only if high time resolution (down to $\sim$ 16 ms) is required, will the latter be used.

1. Spectroscopy mode

   The baseline on-chip binning (OCB) factor in this mode is 3×3 pixels. A variety of options to reduce the data rates to within the RGS telemetry bandwidth limits are available. Each CCD readout takes 0.6 s. Each individual chip (and any combination of chips) can be read out. This leads to a duty cycle for the normal sequential readout of the full array of 9 CCDs of 5.4 s. The energy range covered depends on which CCDs are read out and on the position of the source within the FOV. Reading out all 9 CCDs, the full energy range and all spectral orders are sampled, as listed in Table 10. A rough estimate of which

Table 11: *The RGS science data acquisition modes*

Mode	**Description**
Spectroscopy	2-D readout of up to all 9 CCDs over the full energy range with a long duty cycle (5.4 s readout time); each CCD readout takes 0.6 s. 3×3 pixel OCB is applied. See text for details.
High time resolution (HTR)	Continuous readout of strips of 74 pixels collapsed along the cross-dispersion direction. Either all 9 or selected sequences of CCDs can be read out; if only 1 CCD is read out, higher time resolution (down to 16 ms) is achieved.

energies are sampled if a given CCD (or combination of CCDs) is read out is provided in § 3.4.1.

A fraction of the X-rays produces events in more than one readout pixel. With the basic readout configuration (spectroscopy mode) all detected events are transmitted, stored in the ODF, and (re-)combination of the charges of these pixels (by adding them up) must be performed as part of the offline data analysis. This is the preferred configuration, as full flexibility is retained in the data analysis.

In the case of bright celestial sources, however, these additional data may cause the available telemetry bandwidth to be exceeded. The following configurations of the RGS spectroscopy mode are available for reduction of the instrument telemetry:

- High Event Rate (HER): minor filtering of pixels takes place, which practically is only a noise reduction; split pixels remain to be transmitted;
- HER with Split Event Reconstruction (SER): in this configuration the addition of pixels is performed by the on-board processor before transmission;
- HER with Single Event Selection (SES): Only isolated pixels (without energy contained in neighbouring pixels) are selected on-board for transmission.

2. High Time Resolution (HTR) mode

   In the HTR mode those halves of the RGS chips exposed to celestial light are divided into 74-pixel strips parallel to the dispersion direction. Each of these strips is collapsed into one row in the storage section (the half of the CCD chips shielded from celestial light) for readout. In order to obtain good absolute timing, a short observation of the target in spectroscopy mode must be obtained first, before starting the HTR exposure, to determine the exact location of the source's spectrum in the RGS FOV, which is needed for the determination of the absolute timing. Either all nine CCDs or selected sequences of them can be read out in HTR mode. The time resolution is roughly inversely proportional to the number of CCDs that is read out. As in the spectroscopy mode, the energy range covered depends on which CCDs are read out and on the position of the source within the FOV.

Some basic characteristics of the RGS science modes are listed in Table 11. Each RGS CCD is read out via two nodes.

3.4.8 RGS specific proposal submission information

In the preparation of RGS observing proposals, the following information should be taken into account. A few more instrumental effects, which partly also affect instruments other than the RGS, are listed in § 4.8.

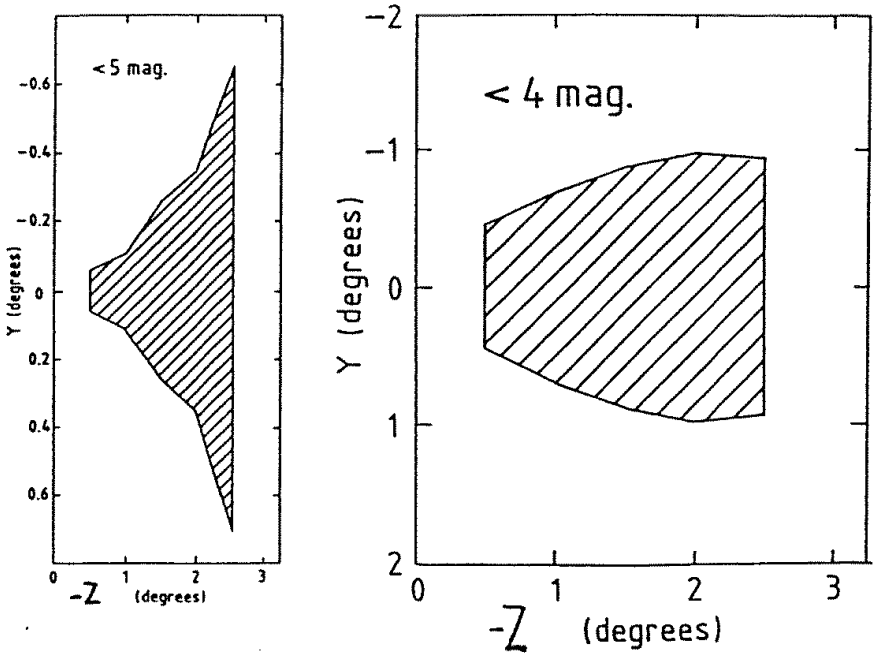

Figure 58: *RGS avoidance angles for sources brighter than 4 (5) optical magnitudes (right/left panel). -Z is the dispersion direction of RGS, Y is the cross-dispersion direction.*

3.4.8.1 RGS avoidance angles

Optical light from bright sources close to a science target can enter the RGS under certain angles. To avoid contamination of RGS observations, such sources must be avoided, with approximate avoidance angles as displayed in Fig. 58. Nearby bright X-ray sources should also not be located along the dispersion direction of the RGS during an observation in order to avoid spectral overlaps. Information on how to choose a position angle in order to avoid bright sources is provided in § 4.4.
The choice of avoidance angles is entirely at the responsibility of the GO. Should an observation become too constrained due to these avoidance angles, GOs may consider violating these regions, depending on the scientific impact on the proposal.

3.4.8.2 RGS spectral quality

In Figs. 59–62 we display a series of RGS spectra of Mewe-Kaastra-Liedahl (in the following "Mekal") model plasmas with different energies, kT, ranging from 0.1 to 10.0 keV, with successively increasing total photon numbers (from 500 to 10000 counts). These show what RGS data quality can be expected for a given number of counts. All model spectra have been produced with SciSim, using a Mekal model spectrum from *xspec*.

3.4.8.3 RGS flux to count rate conversion

Figs. 63–65 provide RGS flux to count rate conversion factors for a variety of standard spectral models. Families of curves for various values of the foreground absorbing column

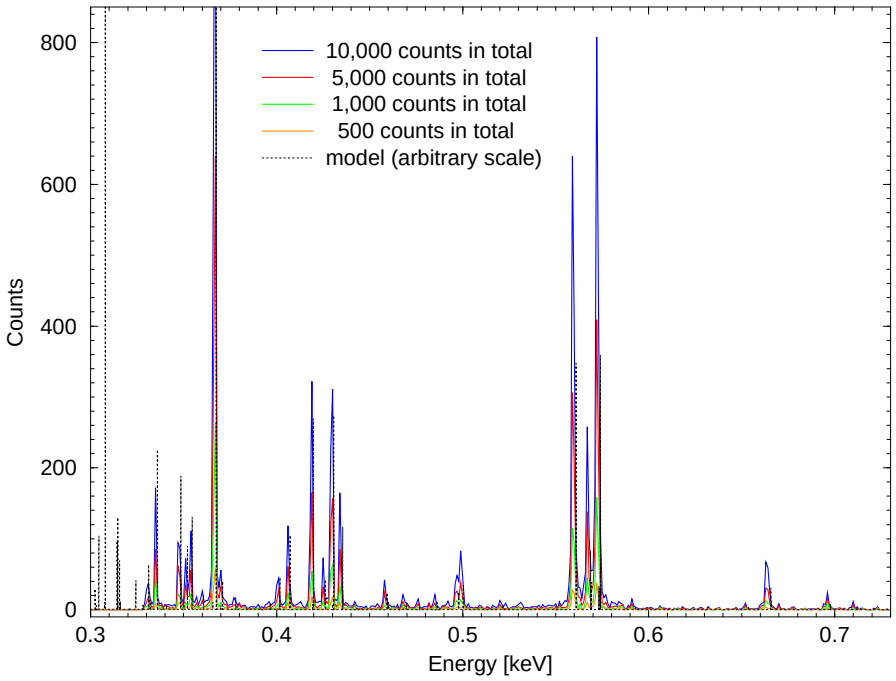

Figure 59: *Series of RGS model spectra of a Mekal thermal plasma with a temperature of 0.1 keV. From the bottom to the top, the total number of counts increases from 500 to 10000.*

density, N_H, are plotted. Fluxes and count rates are calculated for the 0.3–2.0 keV band; fluxes are unabsorbed values. All calculations are performed for the –1. grating order.

3.4.8.4 Count rate conversion from other X-ray satellite missions

For the conversion of count rates from other X-ray satellites to count rates expected for the different **XMM** detectors, we recommend the use of the PIMMS software at NASA's HEASARC (at the URL `http://heasarc.gsfc.nasa.gov/Tools/w3pimms.html`).

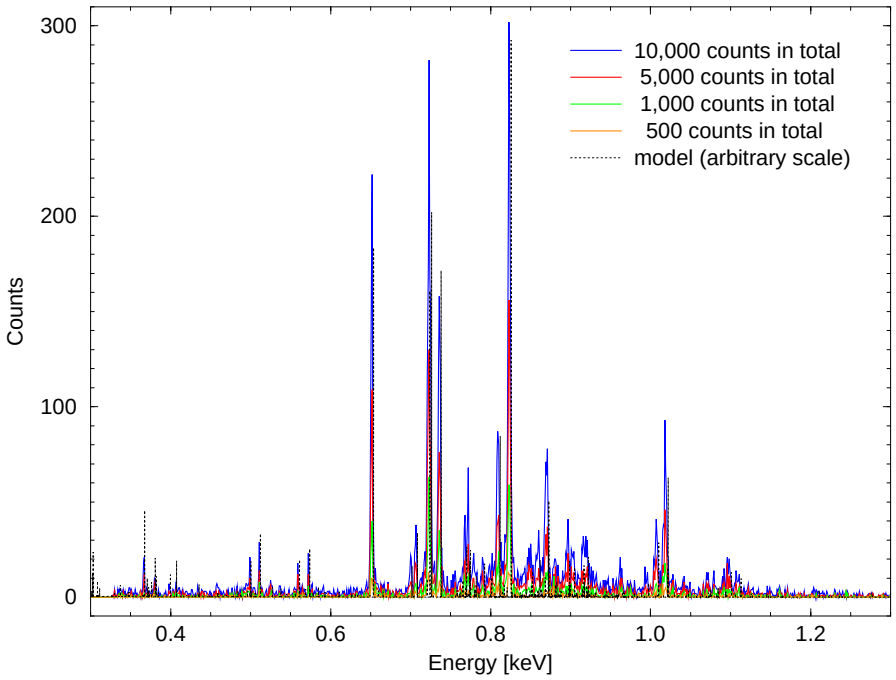

Figure 60: *Series of RGS model spectra of a Mekal thermal plasma with a temperature of 0.5 keV. From the bottom to the top, the total number of counts increases from 500 to 10000.*

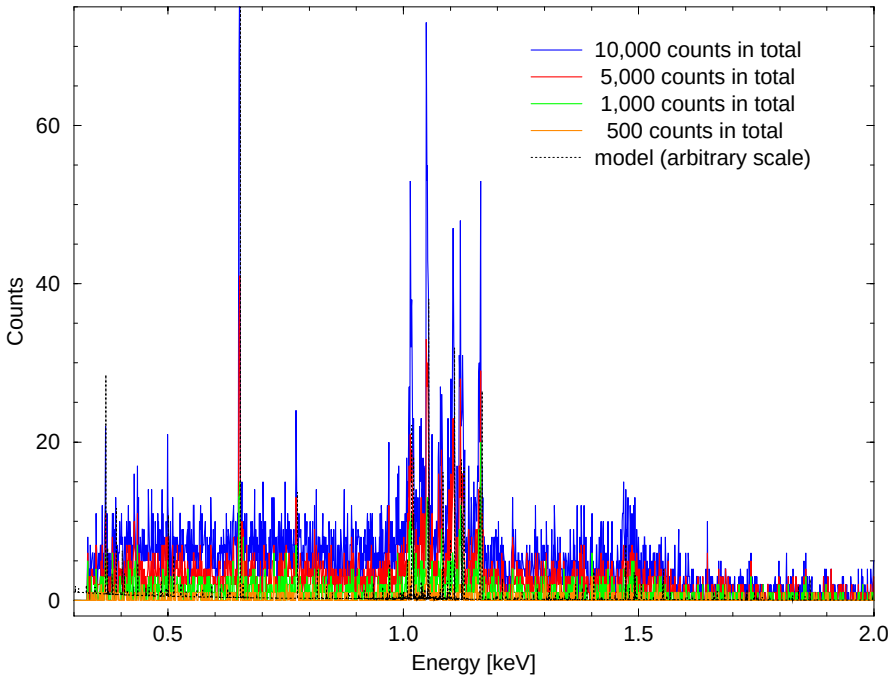

Figure 61: *Series of RGS model spectra of a Mekal thermal plasma with a temperature of 2.0 keV. From the bottom to the top, the total number of counts increases from 500 to 10000.*

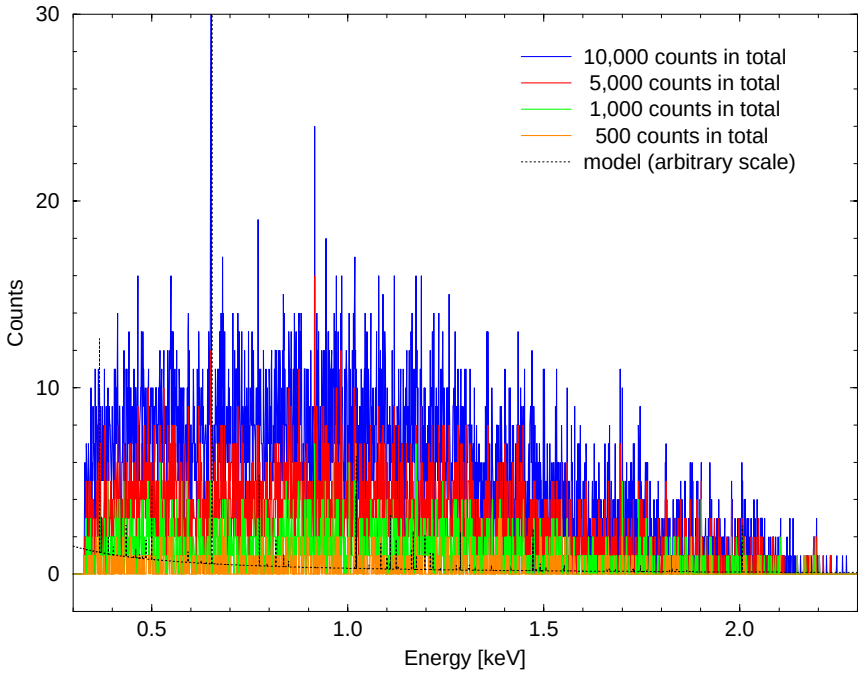

Figure 62: *Series of RGS model spectra of a Mekal thermal plasma with a temperature of 5 keV. From the bottom to the top, the total number of counts increases from 500 to 10000.*

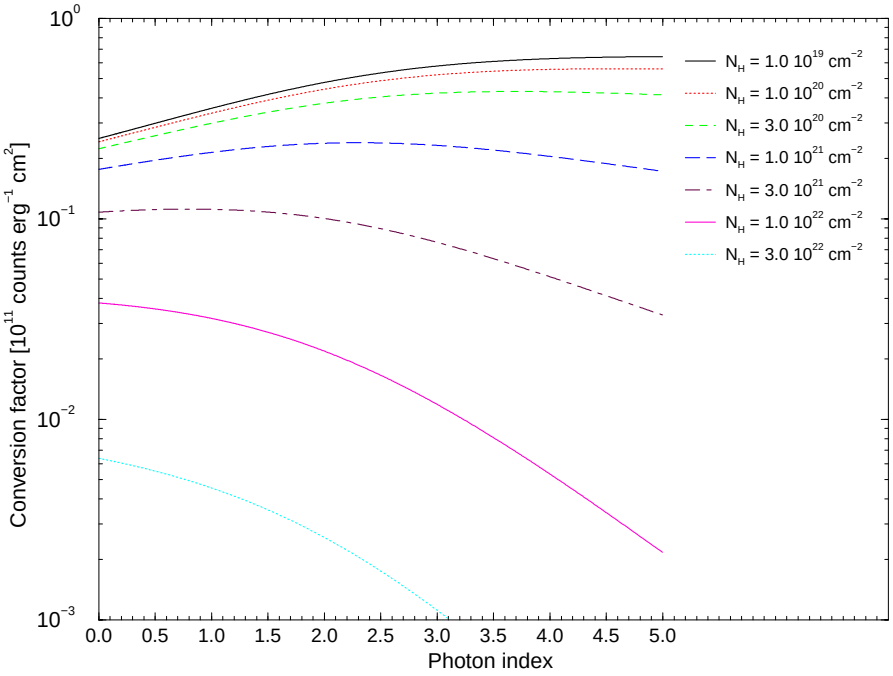

Figure 63: *RGS flux to count rate conversion factors for various power law spectra and different values for the absorbing column density, N_H. All numbers were obtained for the –1. grating order only.*

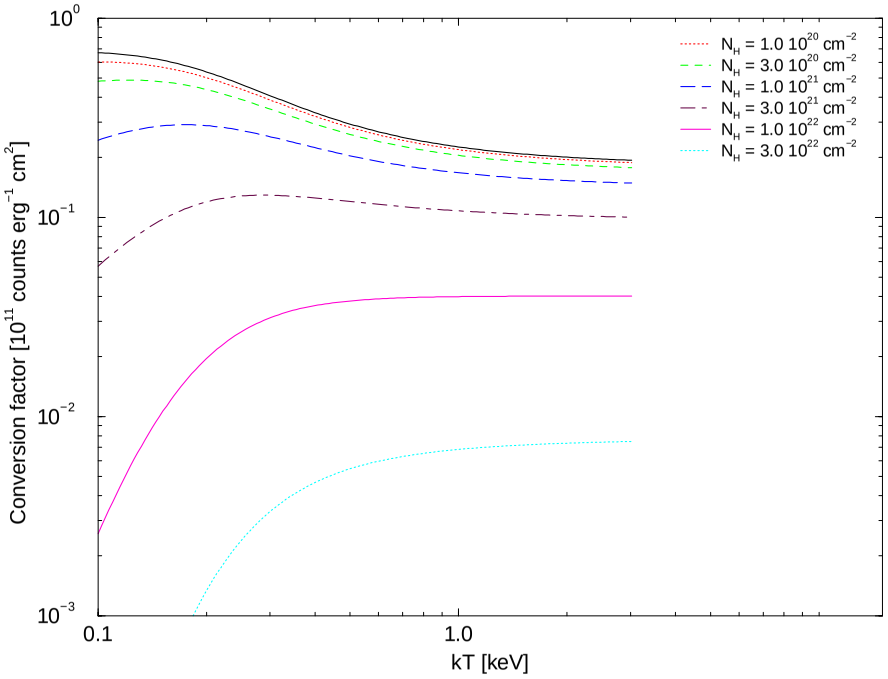

Figure 64: *RGS flux to count rate conversion factors for various black body spectra and different values for the absorbing column density, N_H. All numbers were obtained for the –1. grating order only.*

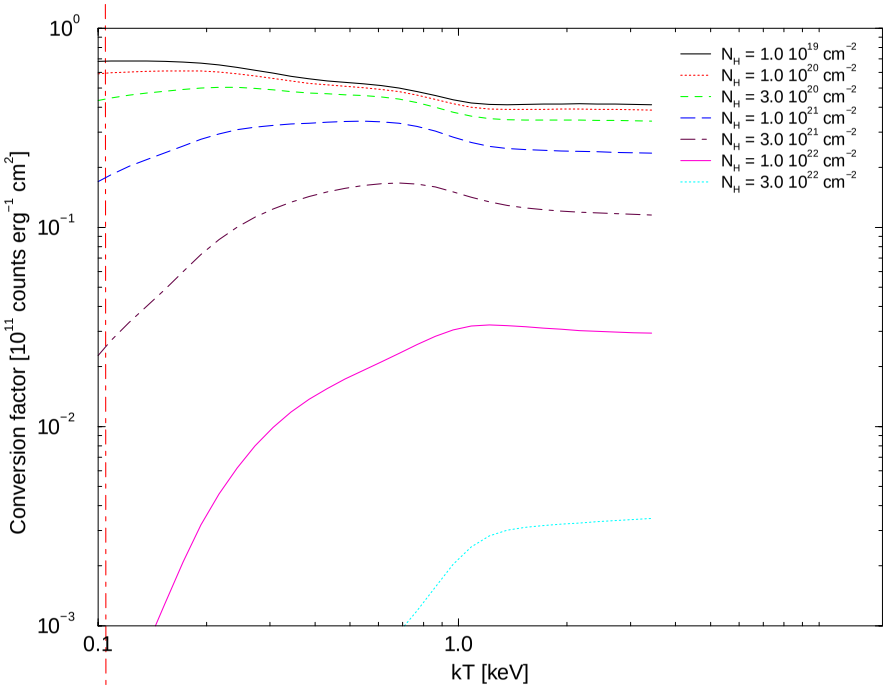

Figure 65: *RGS flux to count rate conversion factors for various Mekal thermal plasma spectra and different values for the absorbing column density, N_H. All numbers were obtained for the –1. grating order only.*

3.5 OPTICAL MONITOR (OM)

Principal Investigator: Prof. K. O. Mason, Mullard Space Science Laboratory

Besides its three X-ray telescopes, **XMM** also has a co-aligned 30-cm optical/UV telescope (OM), providing for the first time the possibility to observe simultaneously in the X-ray **and** optical/UV regime from a single platform. A summary of OM's salient properties is provided in Tab. 12. Although small in size, the OM is a powerful instrument because of the absence of atmospheric extinction, diffraction and background. It can obtain simultaneous optical/UV observations of sources in the field of view in the waveband from 160 to 600 nm. Imaging over the central part of the X-ray field of view with a resolution of ca. $1''$ (depending on instrument configuration), low-resolution grism spectra of X-ray sources or high time-resolution photometry can be obtained. Due to the extreme sensitivity of its detectors, the OM cannot be used for observations of optically bright sources ($m_V \leq$ ca. 10 mag).

3.5.1 OM telescope

The OM telescope consists of an $f/12.7$ modified Ritchey Chrétien optics (see schematic in Fig. 66). From the primary mirror incoming light is reflected onto a secondary, from where it is reflected onto a rotatable 45° flat mirror located behind the primary, which can direct the beam onto one of two detector assemblies operated in cold redundancy.

3.5.2 OM detector

The OM is operated as a photon-counting instrument. Each of the (redundant) OM detectors has a format of 2048×2048 pixels, each $0.5'' \times 0.5''$ on the sky. The field of view

Table 12: *OM characteristics – an overview*

Total bandwidth[1]	160 – 600 nm
Spectral bandwidth[2]	160 – 550 nm
Sensitivity limit[3]	24 mag
Field of view	ca. $17'$ [4]
PSF (*FWHM*)	ca. $1''$
Timing resolution[5]	50 ms
Spectral resolution[6]	0.5/1.0 nm
Brightness limit[7]	$m_V = 10$ mag

Notes to Table 12:
1) See Fig. 69 for filter bandpasses.
2) Covered by two grisms.
3) For a 1000 s white light observation of a B0 star; see Table 16 for expected integration times on three stellar types.
4) Maximum observable FOV per exposure due to onboard memory constraints: ca. $8' \times 8'$ (cf. § 3.5.9.2).
5) In the fast mode.
6) With the UV and optical grism, respectively.
7) For an A0 star with the V filter; see Tab. 19.

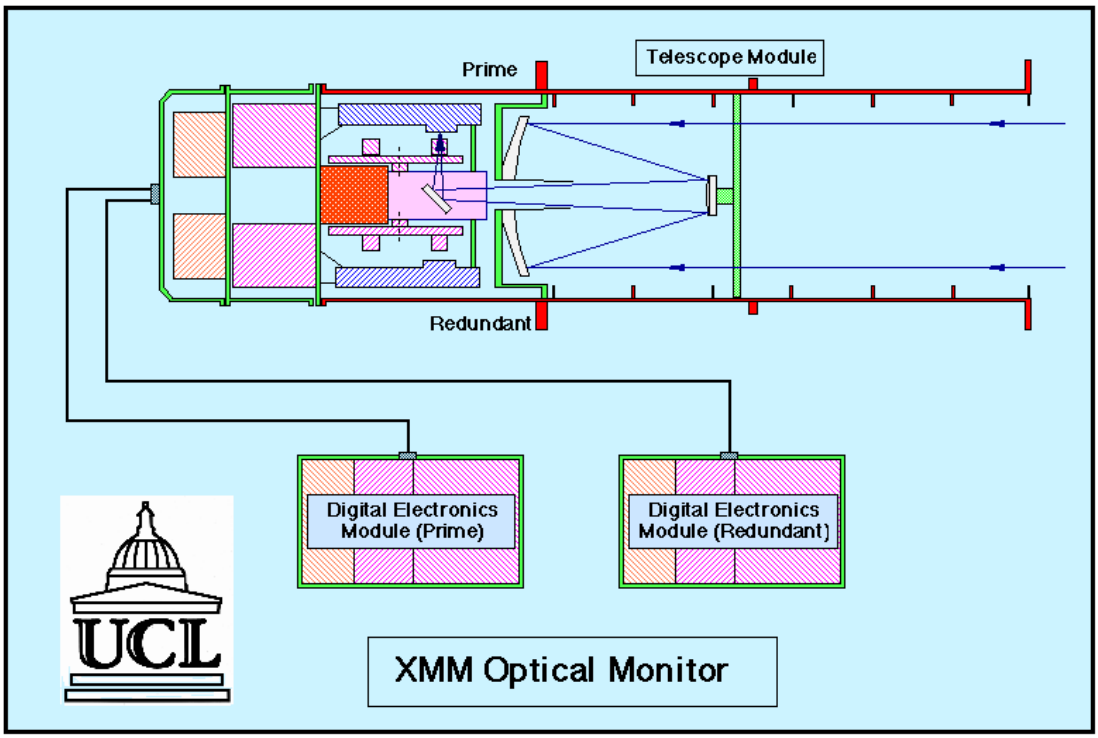

Figure 66: *The light path in* **XMM***'s optical/UV telescope, OM.*

is therefore $1024''$ on a side, or $17' \times 17'$. The light-sensitive surface is an S20 photocathode optimised for the UV and blue. This provides sensitivity from 160 nm (set by the detector window) to 600 nm.
The resolution of the detector is wavelength-dependent, from 15 μm in the red to ca. 32 μm at about 250 nm, before improving again. With the filters described below, this corresponds to $< 1''$ to ca. $1.8''$, and with the magnifier (§ 3.5.6.3), it corresponds to the range $0.25'' - 0.45''$.
The internal noise (dark noise) of the detectors is extremely low, and can generally be ignored by comparison with other, cosmic sources of background.
The OM detectors consist of a micro-channel plate (MCP) intensified CCD (MICs) with 384×288 pixels, 256^2 of which are useable for science observations. Each CCD pixel has a size of $4'' \times 4''$ on the sky. Photons coming from the 45°-mirror enter the detector and hit the photo-cathode, from where electrons are pre-amplified by three successive MCPs (Fig. 67). This leads to an amplification of the signal by a factor of ca. 10^5. The detector achieves a large format through a centroiding technique, subsampling the 256^2 CCD pixels into 8×8 pixels each, as described in the following.

3.5.2.1 Imaging with OM

As mentioned above and shown in Fig. 67, photons entering the OM detector hit a photo-cathode, which is located at the backside of the detector entrance window. Electrons emanating from the photo-cathode are amplified by the MCPs, creating photon splashes at the location of the OM CCD. The detection of a photon entering the detector is performed

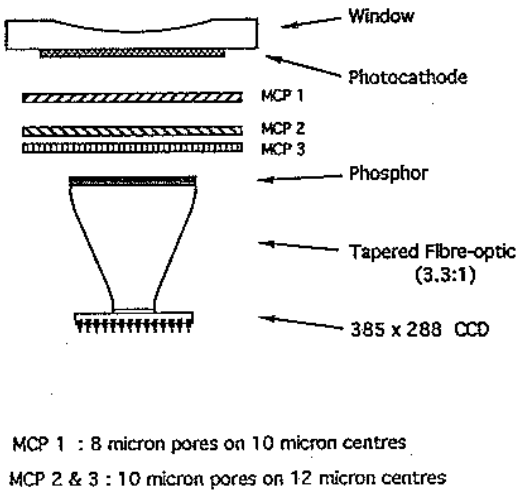

Figure 67: *Sketch of the OM micro-channel plate intensified CCD (MIC) detector.*

by reading out the CCD and determining the photon splash's centre position using a centroiding algorithm, which is part of the onboard software. In the process of centroiding a grid of 8×8 "in-memory" pixels is defined, leading to an array of 2048×2048 in-memory pixels with a size of $0.5''$ on the sky. In the resulting images at some level there is always a pattern repeating on an 8×8 grid. This can be removed by subsequent processing on ground.
As with all photon-counting detectors, there is a limit to the maximum count rate achievable before saturation sets in. The frame rate of the OM detectors is 10 ms at slowest, so a dead time correction must be applied in the offline data processing for count rates above ca. 10 counts/s for point sources. In addition, sources which are too bright can depress the local sensitivity of the photocathode: this is a cumulative effect, so that fainter sources observed for long times have the same effect as brighter sources observed for shorter periods. This places some operational constraints on the instrument.
Cosmetically, the OM detectors are good, with few hot or dead pixels, and little global variation in quantum efficiency. There is a small-scale granularity on the photocathode, which can be removed by flat-fielding in the ground processing. To some extent, the granularity (and the 8×8 pattern mentioned above) is smoothed by the spacecraft drift.

3.5.3 OM windows and field of view

While the OM can access a large part of the field viewed by EPIC, there are limitations on what can be observed in any one exposure. These limitations are set in the first place by the amount of on-board memory, and secondly by the telemetry rate allocated to the instrument. The observer can therefore choose up to 5 "windows", of which up to two may be operated in the "fast" mode (see § 3.5.5, below). These can be placed where required, with restrictions as identified in § 3.5.9.
In addition to these windows, the instrument assigns itself several small windows for tracking guide stars (§ 3.5.9). The tracking information is included with the other science data.
In general, an observation with the OM will consist of a sequence of exposures in different

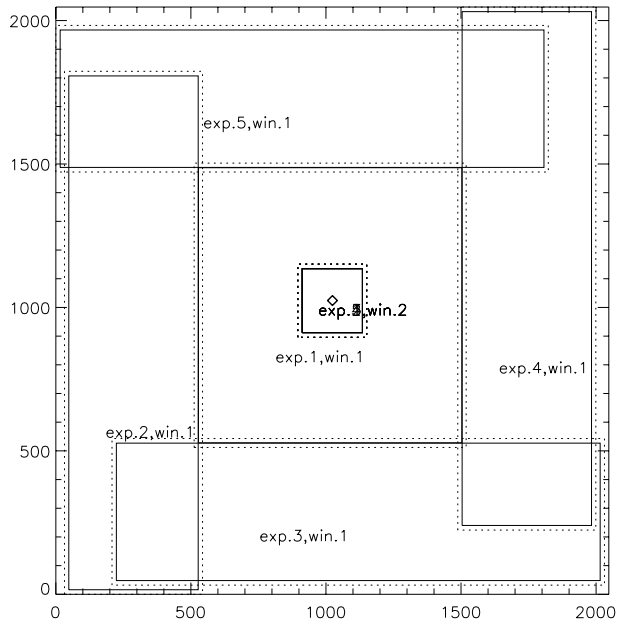

Figure 68: *Setup of OM imaging mode default mode observations consisting of a sequence of 5 exposures. The science windows are indicated by solid lines, the detector windows by dashed lines. A 16 in-memory pixel margin around the science window is allocated to accommodate spacecraft drifts.*

filters and/or with a sequence of different window setups to cover the full field of view. A set of default OM window configurations is available: these will generally be satisfactory for most proposals. **SOC support for non-default OM observations will be limited. For AO-1, a specific scientific justification will be required to use a non-default configuration. It is therefore strongly recommended to use the OM default configurations.** The default setups are as follows.

For details on the intricacies of non-default OM window choice and the applicable restrictions, please refer to § 3.5.9.2.

3.5.3.1 OM default configurations

To ease the use of the OM and to maximise the scientific yield of observations in cases when no particular instrument configuration is requested, OM default configurations have been defined. There is one type of default configuration per OM observing mode, thus one for the imaging mode and one for the fast mode (§ 3.5.5). For each default configuration slightly different setups are offered, depending on the prime X-ray instrument, in order to align the OM science windows properly with the boresight of the prime instrument. If possible within the total time allocated for X-ray observations – and not overriden by GO input in XRPS– the OM will conduct the following set of default observations.

1. Imaging mode default

- Imaging with (default) 2×2 in-memory pixel binning ($1.0''$ pixels).
- A setup of 5 consecutive exposures per filter, covering 92% of the total ($17' \times 17'$) OM FOV.
- In each of the 5 exposures per filter a large fraction of the FOV will be covered by one large window, while a second, smaller imaging mode window ensures continuous monitoring of the prime target (at the centre of the FOV; see Fig. 68).

2. Fast mode default

   - Window configuration as under 1.
   - An additional central window is operated in the OM fast mode. Its size is 22×23 in-memory pixels ($11'' \times 11.5''$).
   - Two imaging mode windows per exposure, covering the maximum possible FOV while not exceeding the hardware and software limits to operate at the same time a third window in the fast mode.

Within a default configuration observation, OM users can specify their choice of filter(s) and exposure times.

- Integration time for exposures

  To achieve the best possible efficiency in the use of the limited hardware capabilities, **an integration time of 1 ks is recommended for each exposure**. With a setup of 5 exposures per filter, this leads to 5 ks duration per default observation with one given filter. Note that longer integration times per exposure are allowed (§ 3.5.5). Shorter exposure times are limited by the OM telemetry allocation vs. required downlink time as described in § 3.5.9.2.

- Filter choice

  For maximum scientific yield (including the consideration of creating a useful archival database), **the use of the following filters (in that order) is recommended**:

  1. B
  2. UVW2
  3. U
  4. UVW1

  A different set of filters for observations in the OM default configuration may be chosen by the user based on scientific considerations (and a special scientific justification should be provided). However, **the sequence in which the filters are used must comply with the instructions provided in § 3.5.6.1**. The four filters listed above would be used in the order U, B, UVW1 and UVW2.

Example 1: With an exposure time of 1 ks, an observation using the imaging default mode (with 5 exposures) takes 5 ks (per filter). Within a total observing time of, e.g., 10 ks (which is determined by the feasibility of the planned X-ray observations), there would be time for only two filters. The recommended choice of filters would then be B and UVW2 (in that order).

Example 2: A 20 ks X-ray observation allows for four imaging default mode OM observations, preferably with the U, B, UVW1 and UVW2 filters.

Example 3: Users interested in U, B, V photometry would choose the filters in the order V, U and B. In order to reach similar limiting magnitudes within a total observing time of 20 ks, two default mode imaging observations with the V filter (requiring 10 ks) and one each with the U and B filter (in that order) can be chosen (cf. § 3.5.6.1). Alternatively, instead of choosing two 1 ks integrations in the V filter, 2 ks exposures may be defined.

3.5.4 Optical/UV point spread function of the OM and tracking

The OM telescope produces images on the detector which are nominally diffraction-limited over the field of view (ca. $0.35''$ at 400 nm, decreasing with increasing wavelength). However, this is convolved with the somewhat larger detector resolution noted above (about $1''$ generally, decreasing with increasing wavelength). The resulting $\simeq 1.2''$ resolution images are optimally sampled by the $0.5''$ pixels.
This image quality is much better than that obtained with the X-ray instrumentation, and is significantly degraded by the spacecraft drift. The OM therefore contains software which calculates the spacecraft drift from guide stars in the tracking windows and continually corrects the incoming photons from the detector to register them correctly in the accumulating image ("shift & add" in-memory). This can be done only in steps of an integral number of pixels, so some further broadening (on the scale of another $0.5''$) still occurs. The final image quality will have a *FWHM* of $\simeq 1.5''$. Under the nominal 2×2 pixel binning (see below), the image is marginally undersampled and the resolution thus determined by the pixel size. Inserting the magnifier (which transmits in the optical region of the spectrum) increases the image scale on the detector by a factor of 4, resulting in $0.125'' \times 0.125''$ pixels: in this case the detector resolution is effectively increased by a factor of 4 (at the expense of a similar factor reduction in field of view) and the overall resolution is dominated by the telescope diffraction limit.

3.5.5 OM operating modes

The OM can operate in the two modes listed in Table 13. These allow either imaging or fast photometry or both simultaneously.

- Imaging mode

  Imaging can be performed with different pixel sizes. The tradeoff is that the images with unbinned pixels take more memory and more telemetry, and therefore the windows must be small or the exposures long in order to allow the instrument memory to empty. A 2×2 pixel onboard binning is the default, resulting in pixels $(1'')^2$, but 1×1, 2×2 and 4×4 pixel binning is possible. Up to 5 imaging mode windows of up to 480×480 pixels can be assigned.

Table 13: *The science data acquisition modes of OM*

Mode[1]	**Special feature**
Imaging	2-D imaging with long exposure times (> 100 s)
Fast	High time resolution, providing 2-D time-sliced images over small areas.

Notes to Table 13:
1) Both modes can be used simultaneously, as long as total memory capacity and telemetry bandwidth are not exceeded.

One such image covers ca. the central quarter of the OM FOV, which again is about 1/4 of the EPIC FOV. To collect data over the entire OM FOV, more than one exposure must be obtained.

The maximum allowed integration time for an OM imaging mode exposure is 5 ks. Since the OM in its imaging mode produces accumulated images, there is no timing information attached to individual incoming photons.

- Fast mode

  In its fast mode, the OM does not produce accumulated two-dimensional images, but instead produces event lists like the X-ray instruments. This mode is useful for monitoring rapidly variable sources, for example AGN or accreting binaries. Two small windows can be assigned, each of a maximum of 512 pixels only. The data are obtained in 50 ms time slices, each preserving the pixel information. No drift correction is performed, but the drift information is telemetered, so that the correction can be applied in the post-processing on the ground.

  The maximum allowed integration time for one fast mode window is 4.4 ks, and 2.2 ks each if two are used simultaneously.

3.5.6 OM optical elements

The OM is equipped with a filter wheel holding several optical elements that can be moved into the light path. These elements, which are described here, comprise not only filters, but also two grisms and a magnifier. The complete set of optical elements is collected in Tab. 14. Their arrangement on the OM filter wheel is indicated by the position number on the filter wheel. **Sequences of exposures using different optical elements must always have increasing filter wheel position numbers.** Observations with the three optical broad-band filters U, B and V, for example, must always be conducted in the order V, U and B (positions 1, 3 and 4).

Table 14: *OM optical elements*

Filter wheel position number	**Filter name**
0	Blocked
1	V
2	Magnifier
3	U
4	B
5	White
6	Grism 2 (visible)
7	UVW1
8	UVM2
9	UVW2
10	Grism 1 (UV)

3.5.6.1 OM filter bandpasses

The OM is equipped with a set of filters with bandpasses covering part of the UV and optical range. The filter throughput curves are displayed in Fig. 69. The plotted quantity is the OM effective area with these filters, including the size of the telescope aperture and mirror geometric areas, the reflectivity of the three mirrors and the detector response. In the calculation of the detector response the following effects were taken into account: the open area of the MCP, the RQE of the photocathode and the entrance window transmission.
As part of the OM default configuration (§ 3.5.3.1), **the use of the B, UVW2, U and UVW1 filters is recommended. A specific scientific justification is necessary for the use of a different set of filters.** To minimise wear and tear on the OM's moveable parts, users wanting to define a different filter combination **must** adhere to the order defined above and listed in Tab. 14.

3.5.6.2 OM grisms

In addition to the filters, the OM filter wheel holds two grisms. The throughput of the OM grisms depends on wavelength. This, folded with the OM detector response, is displayed in Fig. 70. The grisms cover wide wavelength ranges, but it is evident that Grism 1 is the best choice for wavelengths from 160 to 290 nm, while for wavelengths from 290 to 600

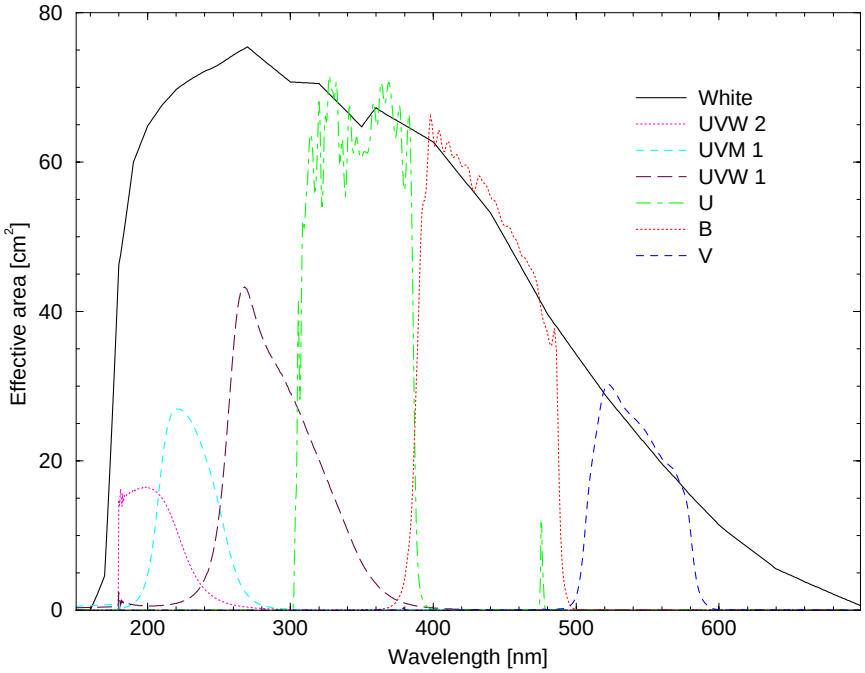

Figure 69: *Throughput curves for the OM filters, folded with the detector sensitivity (the cutoff in the throughput curve of the UVW2 filter is an artifact due to a lack of measured data below 180 nm).*

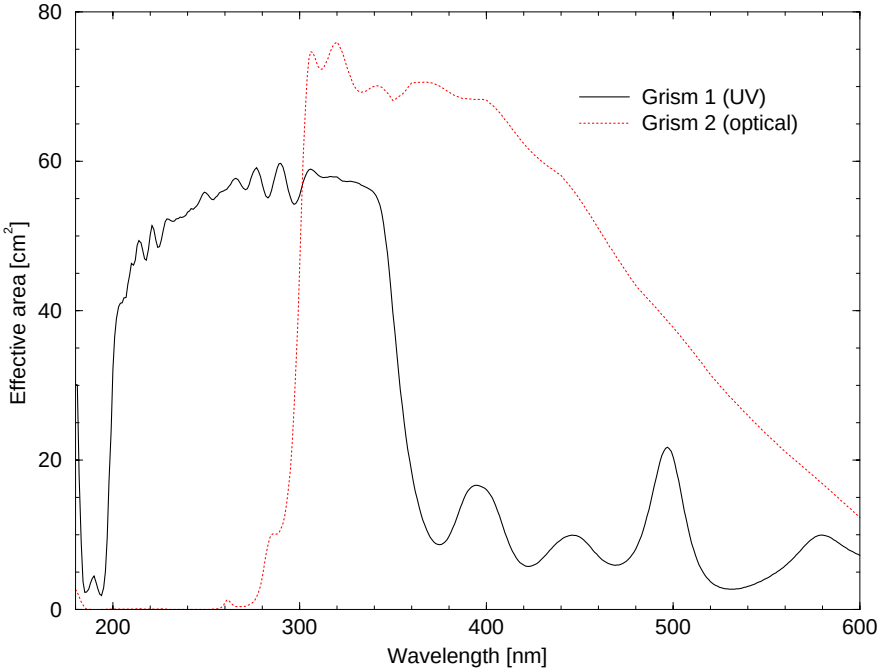

Figure 70: *The OM grism throughput, folded with the detector response.*

nm Grism 2 has a higher throughput. Only one grism can be used at any time, because they are mounted – together with the other optical elements (see Table 14) – on the OM filter wheel. For the same reason, the grisms can also not be used in combination with the magnifier (§ 3.5.6.3).
The spectral resolution of the grisms is almost constant over their wavelength ranges. The former (in the UV) has a spectral resolution of ca. 0.5 nm per $1''$ pixel, the latter (in the optical regime) 1 nm per pixel. The grisms can thus be used for moderate resolution optical and UV spectroscopy in conjunction with the X-ray observations. Only one grism can be used at any time. An image of the target area should be taken for identification of spectral sources prior to or after obtaining spectroscopic exposures with a grism. Note that grism observations currently cannot be modeled with SciSim.

The optical grism is blazed and the zeroth order image should accordingly be weak. The UV grism is not blazed, however, and ca. 1/3 of the light is expected to go into the zeroth order image, which is expected to be visible near the edge of the FOV when the first order spectrum is centred.

3.5.6.3 OM magnifier

The OM offers a possibility to change the instrument setup by inserting a lens system – which is mounted on the filter wheel – into the light path, extending the focal length of the telescope by a factor of 4. Thereby, the pixel size (in angular units) and the size of the FOV for a given pixel array can be reduced by a factor of 16. This leads to an in-memory pixel size of $(0.125'')^2$. Using 1×1 pixel binning, this translates into the same size for the resulting image pixels. The magnifier thus offers the user a chance to perform high-resolution, low-background imaging with a small FOV.

One particular application of the magnifier that might be of interest to users is the **avoidance of bright sources within the OM's FOV** (cf. § 3.5.8).
Normally, when trying to perform very sensitive observations, one will want to use a filter with a high throughput, such as, e.g., the white light filter of the OM. The problem with bright sources in the field of view then is the danger of damaging the OM photocathode with their incident high photon flux. This is the reason why it is not possible to avoid such bright sources by just choosing a science window that will not read out the source's photons. Instead, the source must be kept out of the FOV so that it does not damage the photocathode. For field sources more than $5'$ away from the pointing position exactly this can be achieved by choosing the magnifier as the optical element in the lightpath, which reduces the size of the FOV. Since the magnifier has good throughput in the optical, its sensitivity is comparable to that of the white light filter. When using the magnifier, only the imaging scale is changed compared to "normal" observations with a filter. Thus, the magnifier can be used, in the standard fashion, with the default configurations introduced above (§ 3.5.3.1). In this fashion, bright sources at distances of order $5'$ from the target can be avoided while performing sensitive imaging of sources with a small extent (the OM FOV with the magnifier is about $4.25'$).

3.5.7 OM sensitivity and detection limits

Both Fig. 71 and Tab. 15 provide the expected count rate of the OM, in counts per second, for $m_V = 20$ mag stars of various types, with the different filters introduced above. These

numbers were obtained from SciSim simulations, under the assumption of a perfect, i.e., deadtime-free, detector.

Table 15: *OM count rates [10^{-4} counts/s] as function of spectral type for stars with m_V = 20 mag under the assumption of a zero deadtime detector*

Filter	B0	A0	F0	G0	G2	K0	M0
UVW2	5534	722	59.2	9.66	5.54	0.963	0.306
UVM2	6599	931	114	21.4	17.0	1.41	0.150
UVW1	11368	1898	744	449	369	65.5	7.23
U	14945	3962	2596	1952	1676	845	115
B	10035	8384	6070	4806	4094	3675	2075
V	1893	1847	1790	1778	1806	1743	1667
White	75280	22335	13055	10376	9293	7636	5323

The numbers listed in Tab. 15 can be used to calculate the expected count rates of stars of given magnitude, C_{mag}, by the formula

$$C_{mag} = C_{20} \times 10^{0.4\times(20-b_{mag})} \quad , \tag{3}$$

where C_{20} is the count rate of an $m_V = 20$ mag star, b_{mag} is the magnitude of the target of interest and C_{mag} is the count rate of a star with $m_V = b_{mag}$.

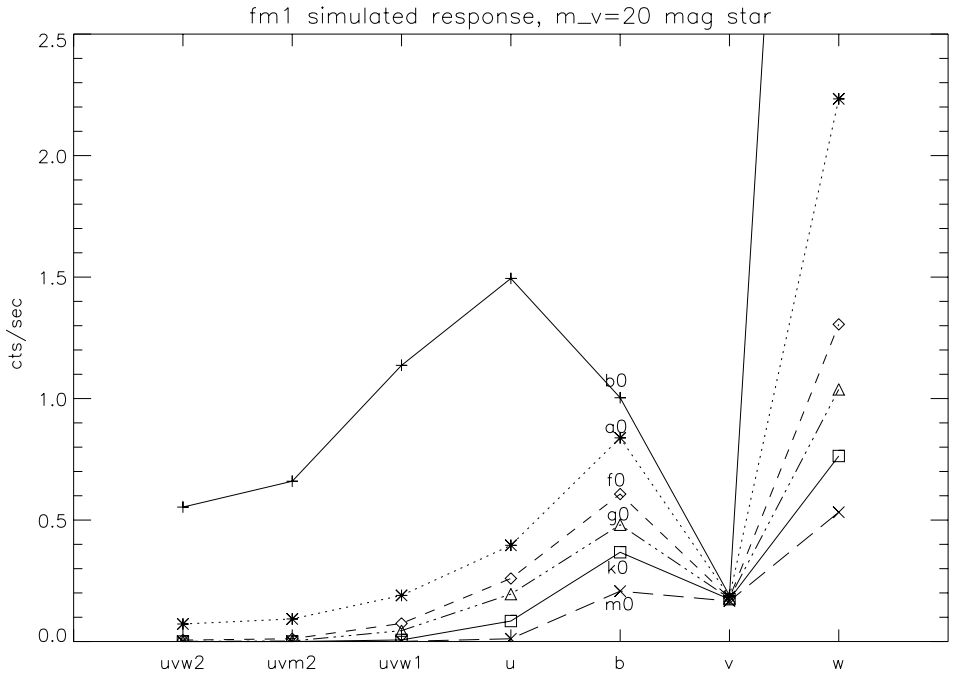

Figure 71: *OM count rates vs. filter selection for stars of different spectral type with $m_v = 20$ mag.*

Table 16: *Required exposure times for different types of stars with $m_V = 23$ mag*[1]

Filter	**Spectral type**		
	B0	**A0**	**G0**
U	340	2100	6400
B	750	980	2400
V	4300	4400	4700
White	70	370	1300

Notes to Table 16:
1) In seconds, for a 5-σ detection. Numbers obtained adopting a zodiacal light level of 87 S10 units, where S10 is the brightness of one $m_V = 10$ mag A0 star per square degree.

However, OM deadtime (coincidence losses) must be taken into accout. This can be done by scaling the above numbers of C_{mag} by applying the following equation:

$$C_{det} = C_{mag} \times (1 + p/2 + p^2/6 + p^3/24) \times e^{-p} \quad , \tag{4}$$

with $p = C_{mag} \times \tau$, where C_{mag} is the count rate of incident photons from eq. 3 and τ is the frame time of the OM fast-scan CCD. The frame time is a function of the OM science window configuration, as described in § 3.5.3. In this context a conservative value for the OM CCD frametime is 10 ms. For the 20th magnitude stars in Fig. 71 and Tab. 15, OM deadtime is negligible. For the worst case, which is an B0 star observed with the white light filter, the deadtime correction amounts to 3.7%.
In Table 16 estimates of required OM integration times for 23rd magnitude stars are provided. The values listed are the integration times, in seconds, for a 5-σ detection.
Table 17 tabulates the limiting magnitudes that can be detected by OM in an integration time of 1000 s at the 5-σ confidence level.

Table 17: *Limiting magnitudes for a 5-σ detection in 1000 s*[1]

Filter	**Spectral type**			
	B0	**A0**	**G0**	**K0**
U	23.9	22.5	21.7	20.8
B	23.2	23.0	22.4	22.1
V	21.9	21.8	21.8	21.8
White	25.0	23.7	22.9	22.5

Notes to Table 17:
1) Numbers obtained adopting a zodiacal light level of 87 S10 units.

The expected levels of different external background radiation processes in the optical/UV are tabulated in Table 18. A spectral representation of the diffuse galactic and zodiacal light is contained in SciSim. The intensity of these background sources, which depends on the target coordinates, is a user-selectable parameter in SciSim.
In addition to these external sources of background radiation, the instrumental background must be taken into account. However, with a count rate of $< 4 \times 10^{-5}$ counts s^{-1} arcsec^{-2} the dark count rate of the detector is generally negligible.

3.5.8 OM brightness limit

To avoid damage of the OM photocathode, the maximum allowed source brightness is set to a count rate of $\sim$ 1900 counts/s, corresponding to an $m_V = 10$ mag A0 star in the V filter. The equivalent brightness limits for the other filters and optical elements are tabulated in Table 19. For calculating the brightness limits an A0 type spectrum was assumed.
In case an optically bright source beyond these limits is in the OM FOV (not just within an active science window!), users must specify in their proposals that the OM will be in the "GO-off" position. It is the user's responsibility to check for the presence of such bright sources. The Guide Star Catalogue (GSC V1.1), which is released as part of SciSim, can be used to check for bright stars. However, it is incomplete at the bright end of the bright end of the magnitude range. Therefore, it is recommended to also check the catalogue USNO-A (V1.0) from the US Naval Observatory (at the URL `http://psyche.usno.navy.mil/pmm/`).

3.5.9 OM specific proposal submission information

In the preparation of OM observing proposals, the following information should be taken into account.

3.5.9.1 OM star tracking windows

Before each OM science exposure a reference tracking frame is obtained. On this frame suitable guide stars are identified by the onboard software and tracking windows defined around these.
The guide stars are used to calculate the OM attitude solution for the process of shift & add of the tracking frames of the science windows. The reference tracking frame taken first provides the coordinate reference point. OM guide star tracking windows are small windows (64×64 in-memory pixels), defined as such so as to read out a minimum of data as fast as possible and take away a minimum of OM's processing capacity from the science observations.
Images of star tracking windows are not down-linked to the ground, but processed onboard. Only the x and y position of the tracking stars in units of in-memory pixels, the number of

Table 18: *Levels of different OM background contributors*

Background source	**Occurrence**	**Count rate range**[1]
Diffuse Galactic	all directions	0.081–0.0007
Zodiacal[2]	longitude $90^\circ \pm 20^\circ$	$0.212–2.6\times10^{-5}$
Earth	Off-axis angle $< 30^\circ$ (3)	0.219–0
Moon	Off-axis angle $< 30^\circ$	$0.0016–10^{-5}$

Notes to Table 18:
1) In units of [counts s^{-1} $arcsec^{-2}$].
2) In differential ecliptic coordinates, i.e., the angle between the Sun and the pointing position of **XMM**. Maximum is for l,b = 70,0 in the white filter, minimum is for l,b = 110,70 in the UVW2 filter.
3) Forbidden by observatory constraints anyway.

Table 19: *The m_V brightness limits for all OM filters*

Filter	Max. m_V
U	10.8
B	11.6
V	10.0
UVW1	10.0
UVW2	8.9
UVM2	9.2
White	12.7
Magnifier	12.2
Grism 1 (UV)	8.7
Grism 2 (opt.)	9.6

counts from the stars per tracking frame and the pointing offset information is transmitted as part of the telemetry stream. The number and the properties of OM star tracker windows for a science observation are determined by an onboard algorithm and therefore **not** user-selectable.

3.5.9.2 Choice of non-default OM science windows

For OM observations more than one science window may be defined. However, it is not possible to select the entire OM FOV for science observations. There are several boundary conditions that limit the user's choice and which **must** be taken in account properly if a non-default instrument configuration is to be used. Note that the use of non-default OM instrument configurations is discouraged by the SOC for AO-1.

- Maximum number of windows

  Up to five science windows in total (of which up to two in the fast mode) are allowed (Fig. 72).

- Allowed detector window locations and sizes

  The size of an OM science window must be integer multiples of 16 in-memory ($0.5''$) centroiding pixels, i.e., 2×2 CCD pixels.

  The minimum width of a detector window is the equivalent of 4 CCD pixels, the maximum width in one direction is limited to 64 CCD pixels (equivalent to 512 in-memory pixels).

  CCD windows must start at an even pixel number in both the horizontal (x-) and the vertical (y-) direction. OM science windows can therefore start, e.g., at the in-memory pixel coordinates (16,16), (32,32) ... and end at (n×16,n×16), where n is an integer number. Starting at pixel coordinate (0,0) is not possible because of the necessity to allocate a 16 pixel wide margin to accommodate spacecraft drift.

  A science window may be larger than 512×512 in-memory pixels, but if so it requires more than one detector window (as defined, e.g., in the imaging mode default configurations).

- Science window overlaps

  Different scenarios for OM science window configurations are displayed in Figs. 72 and 73. **OM science windows must overlap either entirely or not at all**. This must be true for all satellite position angles allowed by the specifications made during proposal submission, in particular if the windows are specified in celestial coordinates (Fig. 73).

- Limited onboard memory capacities

  OM tracking frames are stored in the so-called "small word memory" (SWM). From one tracking frame to another, the pointing direction can change due to spacecraft drift. Using one tracking frame as reference, the attitude solution of the other is determined, a mean shift calculated and applied, before they are added in-memory. Because of the possible shifts, the allocated SWM area must include a $\pm 16''$ margin around the specified science window. Including this margin, the maximum SWM capacity is 1,007,616 in-memory pixels.

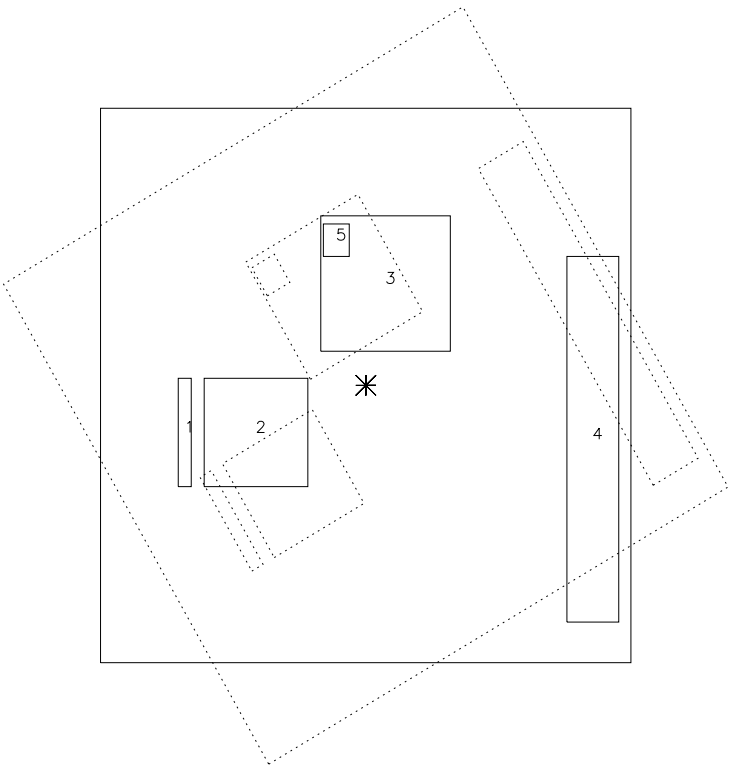

Figure 72: *When the boundaries of OM science windows are defined in detector pixel coordinates, the relative location of the windows with respect to each other does not change. However, different areas on the sky are imaged under different position angles.*

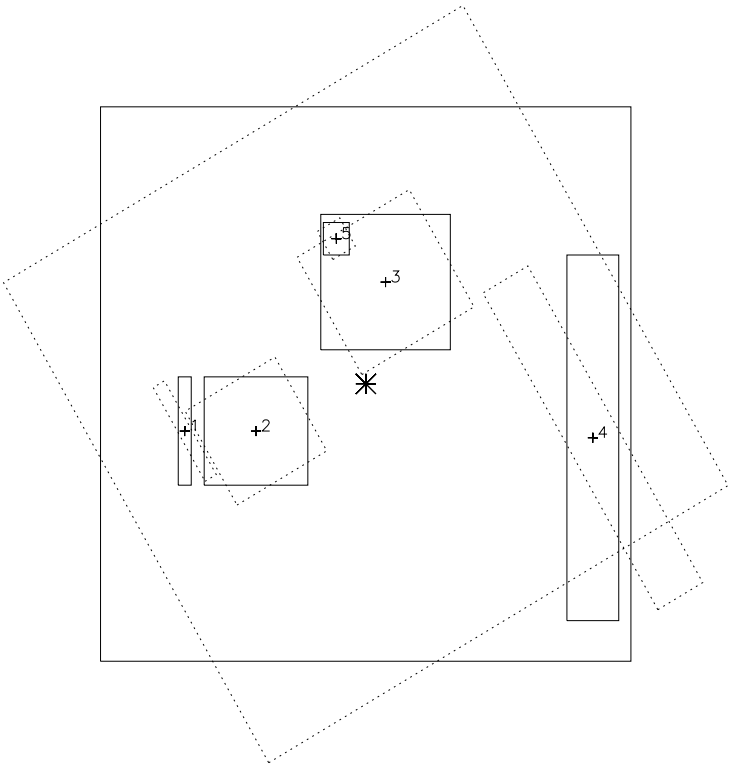

Figure 73: *Defining the locations of OM science windows in sky coordinates one makes sure that (approximately) the same area of the sky is imaged under different position angles. Now, however, the OM science windows can change their relative locations. Windows 3 and 5 (which used to be in the upper left corner of window 3, see Fig. 72) are now partially overlapping, which is not allowed and window 4 is now partly outside the OM FOV (which is also not allowed).*

The final image(s) is (are) then accumulated in the "big word memory" (BWM). The BWM will also contain tracking history information, reducing the size of the available memory space for science data. The sum of all image mode pixels for each exposure must not exceed 432,698 pixels.

Fast mode data are stored in a special memory partition. The maximum length of a fast mode exposure is 4.4 ks with one fast mode area in use and 2.2 ksec with two. These numbers assume that there is only one bright source in each fast mode window.

- Limited onboard processing capabilities

  The tracking frame time for image mode observations must be long enough to calculate the attitude solution and to complete the shift & add of the previous tracking frame. For 2×2 pixel binning of a 700×700 pixel size image mode

window, this takes ca. 4.2 s.

The minimum fast mode time slice duration (in ms) for a fast mode window must be longer than the total number of fast mode pixels in that area divided by 64. An additional 50% safety margin will be added to the time slice duration.

For a more detailed explanation see the technical note on Constraints on the OM Window Configuration and Definition of the OM Default Configurations (§ 8).

3.6 XMM support instruments

The so-called "non-science" instruments onboard **XMM** are the EPIC Radiation Monitor System (ERMS) and the Attitude and Orbital Control System (AOCS).

3.6.1 Attitude & Orbit Control Subsystem (AOCS)

The AOCS determines the attitude of the **XMM** spacecraft while in orbit, based on the information from one of **XMM**'s two star trackers (which are operated in cold redundancy) and its "Fine Sun Sensors". During slews and the post-slew phase (comprising attitude determination, trim, and settling of the spacecraft), entries are made into the Attitude History File (AHF) every 10 (TBC) seconds. Note that during slews the AHF will not contain attitudes reconstructed from actual AOCS telemetry, but the results of a slew time/path predictor, based on the actually observed slew start/end times and attitudes. The accuracy of the attitude reconstruction during slews is expected to be better than $1'$.
In the "stable pointing mode" (i.e., after the slews and the post-slew phase), the conditions under which entries into the AHF are made are programmable parameters. An entry is made into the AHF only in case of Relative Pointing Errors (RPEs) exceeding the programmed limit. The minimal programmable limit (i.e., the smallest programmable deviation from the nominal boresight) is $2''$. The minimal time resolution with which entries into the AHF can be made in case of such instantaneous excursions is 2 seconds. For a single nominal pointing entry, only a mean RPE will be provided.
The AOCS attitude information is independent of that from the OM's star tracking windows (§ 3.5.3).

3.6.2 EPIC Radiation Monitor Subsystem (ERMS)

The ERMS will register the total count rate and also basic spectral information on the background radiation impinging on **XMM** and its science instruments. This is done not only during science observations, but during the entire lifetime of the mission. In this way, the ERMS monitors the total radiation dose that **XMM** is exposed to. When the level of radiation intensity exceeds a certain threshold, the ERMS issues a warning to the OBDH (Onboard Data Handler). Depending on the mode in which the ERMS is operated, it updates background radiation information once in 512 seconds (slow mode) or 4 seconds (fast mode).
The ERMS can also be used to predict the background in the X-ray instruments. The data consist of three measurements per readout, two spectra from the High Energy Detectors (HEDs) and one from the Low Energy Detector (LED). 256 spectral bins each will be available in the LED and HED. The HEDs are sensitive to electrons above 200 keV and protons above 10 MeV, while the LED is sensitive to electrons with energies above 50 keV. The two high energy spectra are the "HE detector spectrum", with events from either one or both HE detectors, and the "coincidence HE spectrum", in which only events detected by both HEDs will be recorded.
The data from the ERMS comprise the following quantities:

- one header keyword (warning flag),
- seven broad-band count rates, three from the LED, four from the HEDs,
- LE detector spectrum (256 channels),

- HE detector spectrum (256 channels),
- HE coincidence spectrum.

3.6.3 Data from the XMM support instruments

Here we describe briefly the use that is made of data from the non-science instruments onboard **XMM**.

3.6.3.1 Data from the EPIC Radiation Monitor Subsystem (ERMS)

ERMS data will be delivered to the PI as part of the **XMM** science data. This will make it possible to use ERMS data in the offline data processing with the SAS for correct background subtraction. Note that these data will not be properly calibrated and therefore not suitable for scientific use.

3.6.3.2 Data from the Attitude & Orbit Control Subsystem (AOCS)

The AHF is a file containing processed AOCS telemetry. Clipped to the start/end times of an observation or slew, the relevant portion of the AHF becomes an ODF or SDF component which is delivered to the observer. For "stable pointing periods" the data records identify intervals of time during which the spacecraft's boresight did not deviate by more than a configurable limit from the mean boresight during that period. For open loop slews and post-slew attitude trims, the AHF provides the instantaneous boresight at equidistant points in time (typically 10 seconds). It should be noted that attitudes for open loop slews are derived from a "slew model" into which the boundary conditions (actual start/end times and attitudes) have been entered, i.e., the intermediate attitudes provided for slews are not based on sensor data telemetered during the slews.

3.7 Comparison with other X-ray satellites

A basic comparison of **XMM**'s mirror effective area with those of *AXAF*, *ROSAT* and *ASCA* is presented above (§ 3.2.2), in Figs. 10 and 11.
Other salient properties, like e.g., the PSFs, are tabulated in Tab. 20. It is visible immediately from Tab. 20 that *AXAF* and **XMM** have complementary characteristics and that both constitute a new generation of X-ray missions, with enormously improved capabilities compared to their predecessors.

Some special strengths of **XMM** are e.g.:

- The high time resolution of **XMM** with the EPIC pn camera.
- The high sensitivity of **XMM** + EPIC pn at high energies.
- Excellent low energy response down to 0.1 keV.
- Extreme sensitivity to extended emission.
- High-resolution spectroscopy (RGS) with **simultaneous** medium-resolution spectroscopy and imaging (EPIC) and optical/UV observations (OM).

3.7.1 A comparison of XMM vs. AXAF

The basic difference in instrument operation between **XMM** and *AXAF* is that on **XMM** all instruments, unless prohibited by constraints (§ 4.2), operate simultaneously, while science instruments on *AXAF* are alternated.

Several plots have already been shown above comparing the characteristics of **XMM**'s science instruments with those of *AXAF*, namely:

- Mirror effective area: Figs. 10 and 11.
- Imaging effective area: Fig. 22 and Fig. 23.

A few more examples are collected here.

Table 20: *Comparison of* **XMM** *with other X-ray satellites*

Satellite	**Mirror PSF *FWHM* [″]**	**Mirror PSF *HEW* [″]**	**E range [keV]**	**A_e at 1 keV [cm^2]**[1]	**Orbital target visibility [hr]**
XMM	6	15	0.1 – 15	4650	40[2]
AXAF	0.2	0.5	0.1 – 10	800	50
ROSAT	3.5	7	0.1 – 2.4	400	1.3[3]
ASCA	73	174	0.5 – 10	350	0.9[3]

Notes to Table 20:
1) Mirror effective area (Figs. 10 and 11).
2) Orbital visibility (above 40,000 km) split into two parts of ca. 70 ks each due to ground station telemetry gap at apogee (Fig. 79).
3) Low orbit with Earth occultation.

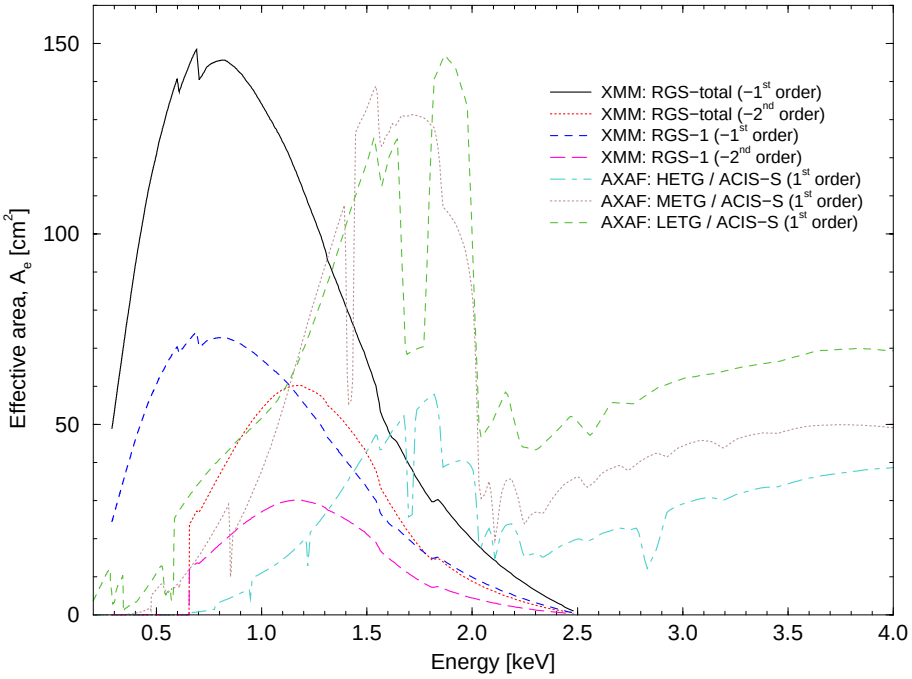

Figure 74: *The effective area of both RGS units combined and RGS-1 (linear scale), compared with* AXAF*'s ACIS-S instrument with various transmission gratings.*

3.7.1.1 Effective area for dispersive spectroscopy

Fig. 74 displays the effective area of both RGS units together (from Fig. 54), compared with different *AXAF* instrument combinations. In order to avoid overcrowding the figure, the combination of *AXAF* HRC+LETG is not shown.

3.7.1.2 Non-dispersive spectroscopy: an example

For illustrative purposes, we add here a direct comparison of an **XMM** EPIC and an *AXAF* ACIS-I observation of a cluster with a 6 keV thermal plasma spectrum, 0.3 solar metallicity, a redshift of 0.3 and an X-ray flux in the 0.1–10 keV band of 10^{-12} erg cm^{-2} s^{-1} (thus a fairly luminous system). Such a comparison gives a good feel for the capabilities of both instruments for performing studies of faint objects. We simulated the response of the *AXAF* ACIS front-illuminated CCD imaging instrument, using the response matrices supplied for the guest observer proposal submission. With a 30 ksec observation ACIS is able to measure the temperature of the cluster to about 10% accuracy (assuming only poissonian noise and neglecting systematic effects).
For comparison, we simulated (using SciSim) the combined response of the 3 EPIC focal plane cameras on **XMM**, using the same input spectrum and observing time. Using a preliminary response matrix for EPIC, we estimate a temperature measurement accuracy of order 2.5% (neglecting systematic effects).

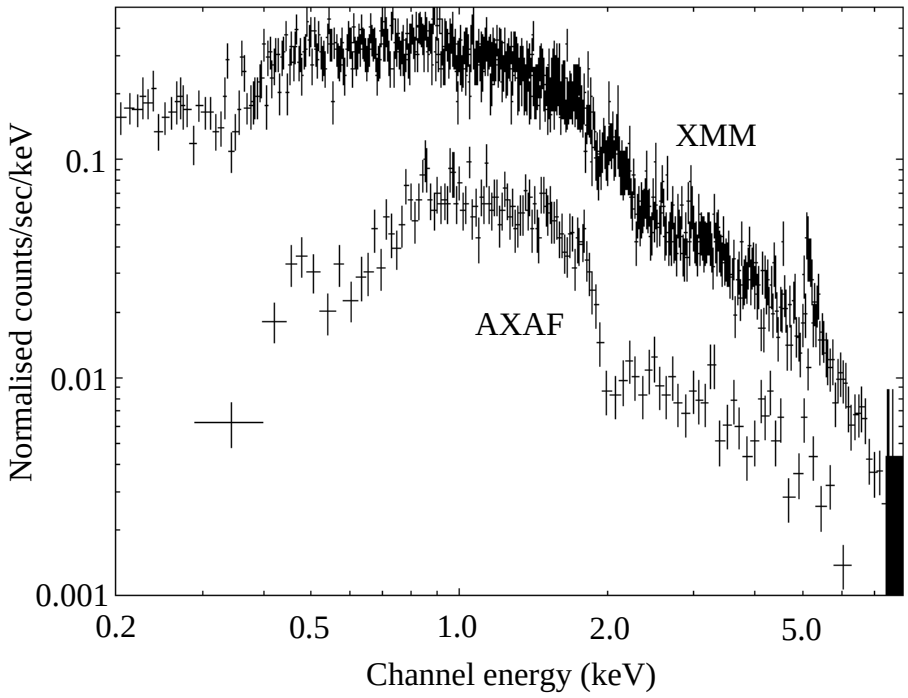

Figure 75: *Comparison of a 30 ks observation of a cluster with a 6 keV thermal plasma spectrum with* AXAF *ACIS-I (bottom) and* **XMM** *EPIC (top). Normalised counts are counts per spectral bin.*

3.7.1.3 XMM EPIC vs. AXAF ACIS-I pile-up comparison

It has been shown above (§ 3.3.10) how pile-up affects the accuracy of spectral fits and the shape of the X-ray PSF. Figs. 76 and 77 show the fraction of piled-up events for different numbers of counts per CCD frame (in full window imaging mode). One can see in Fig. 77 that pile-up effects for given source fluxes are more severe for ACIS-I by more than an order of magnitude compared to EPIC MOS and even by two orders of magnitude compared to EPIC pn.

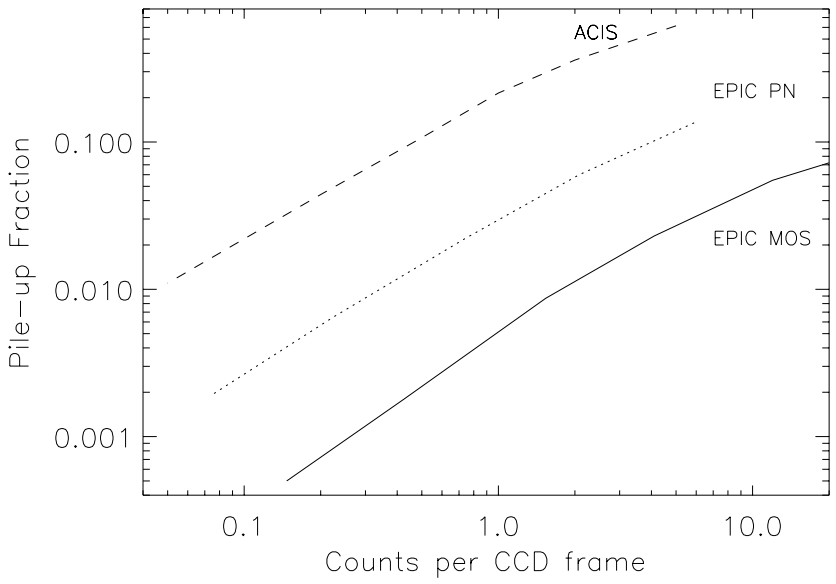

Figure 76: *Comparison of* AXAF *ACIS-I vs.* **XMM** *EPIC (pn and MOS) pile-up for different total frame count rates. The frame times are 3.3, 2.8 and 0.07 seconds for ACIS-I, MOS and pn, respectively.*

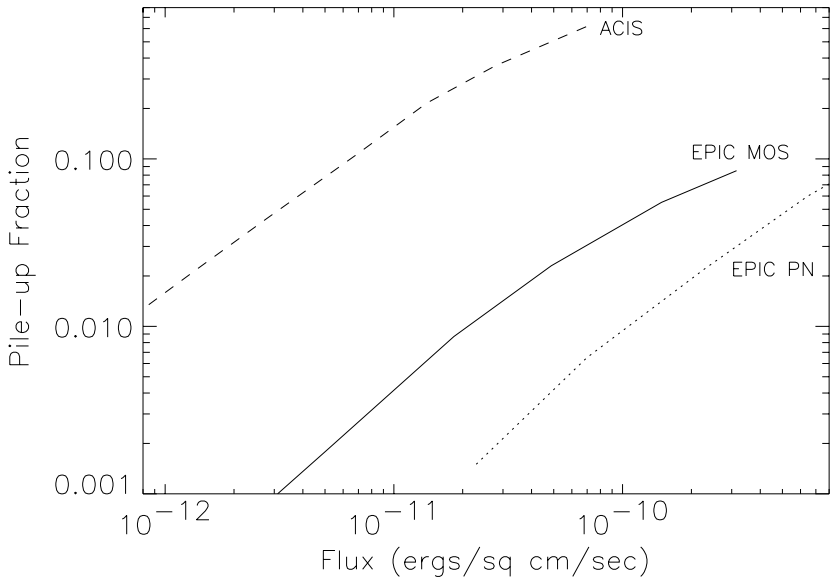

Figure 77: *Comparison of* AXAF *ACIS-I vs.* **XMM** *EPIC (pn and MOS) pile-up for different incident source fluxes, after conversion of counts per frame to flux units, adopting an* $\alpha = -1.7$ *power law spectrum with an absorbing hydrogen column density of* 3×10^{20} cm^{-2}.

4 Observing with XMM

XMM observes with all instruments simultaneously, brightness limits and other constraints permitting. All instruments can be operated independently (i.e., the exposure times of individual instruments are not coupled to each other) and observers will receive the science data of all science instruments operating during an observation.

When planning **XMM** observations several boundary conditions must be taken into account. The constraining parameters are listed in this section.

Note that part of the information provided in this chapter, in particular on target visibility during the mission, depends on the launch date.

4.1 XMM orbit

XMM will be launched by an Ariane 5 launcher into an highly elliptical orbit, with an apogee of about 114,000 km and a perigee of ca. 7000 km (the minimum elevation for science observations will be 40,000 km; see Fig. 78). The orbital inclination is 40°, the right ascension of ascending node is 260° and the argument of perigee 50°. Such an orbit provides the best visibility in the southern celestial hemisphere. The numbers provided here are based on a launch date of 2000 January 21.

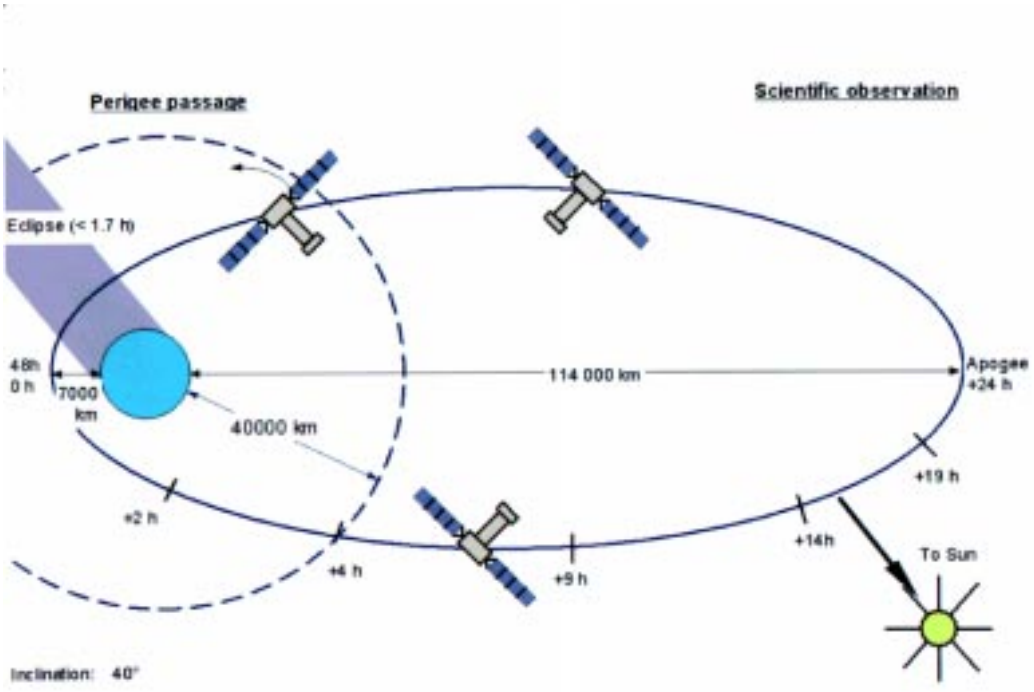

Figure 78: *Sketch of the highly elliptical* **XMM** *orbit. Figure provided by Dornier Satellitensysteme GmbH.*

Note that objects will **not** be continuously observable during the entire visibility period in an orbit due to an apogee telemetry gap, which splits each orbit into two visibility periods of up to ca. 70 ks. This gap is caused by a gap in ground station contact. **XMM**

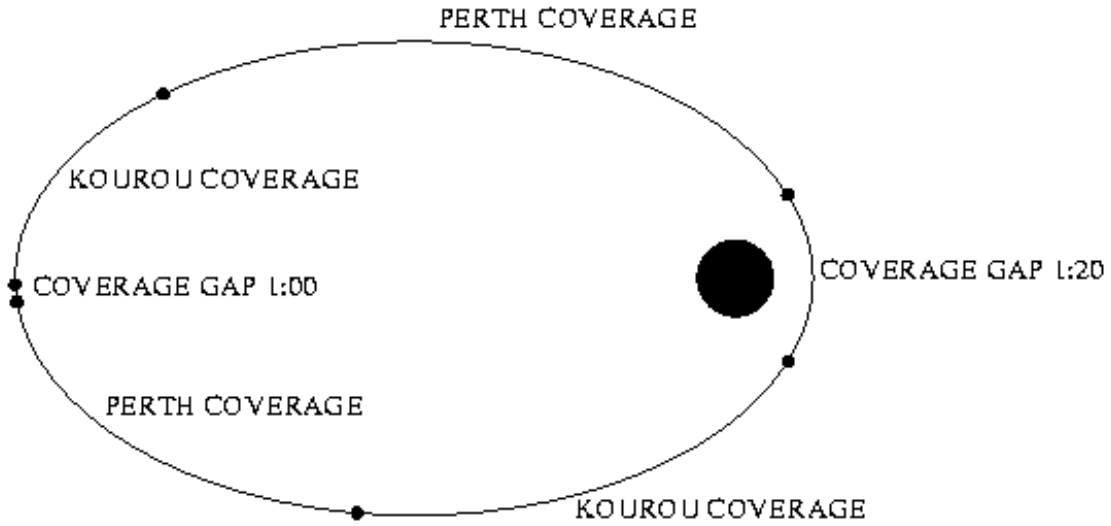

Figure 79: *Sketch showing the location of the* **XMM** *apogee telemetry gap.*

is operated with two ground stations, located at Perth and Kourou. The approximate location of the apogee telemetry gap is presented in Fig. 79. More details are provided in § 4.2.2 (see also § 4.2.5).

4.2 XMM observing constraints

For the individual instruments, and also the **XMM** observatory in general, different observing constraints apply, which may affect the schedulability of targets significantly. These are:

4.2.1 Radiation belts

The radiation background will be variable around the **XMM** operational orbits, depending on the satellite's location with respect to Earth's magnetosphere. For useful **XMM** science observations to be conducted, the minimum satellite elevation is 40,000 km. Closer to Earth, the background is prohibitively high. Because of this, about 40 hours of the 48-hour orbital period can be used for science observations, with a total target visibility period of approximately 145 ks per orbit. Thus, due to the highly elliptical orbit, **XMM** spends most of its time outside Earth's radiation belts. Particle background outside the belts is dominated by the solar particle emission. The incident flux is therefore coupled to the level of solar activity. During intense solar flares the **XMM** payload instruments may be switched off.

4.2.2 Telemetry gap

The **XMM** orbital target visibility period of 145 ks can in practice **not** be used for **continuous** observations, because of incomplete ground station coverage, as displayed in Fig. 79. There is a telemetry gap of ca. 1 hour (constant to within a few minutes during

the first 1000 orbits) close to apogee, during which no data can be transmitted. Since **XMM** data transmission is via telemetry during direct contact, it does not carry onboard data storage devices and no observations can be recorded during these gaps. Thus, each orbit is split into two visibility periods. Fig. 80 shows how this gap shifts over time. When it is located at "24 hours", it is exactly during apogee and thus splits the orbital visibility period exactly into halves (about days 550–750, i.e., orbits 275–375). In all other cases, one visibility period is longer than the other. In the beginning, e.g., the offset of the gap with respect to apogee is ca. 4 hours (about 14.4 ks), making one visibility period approximately 56 ks long, the other about 85 ks.

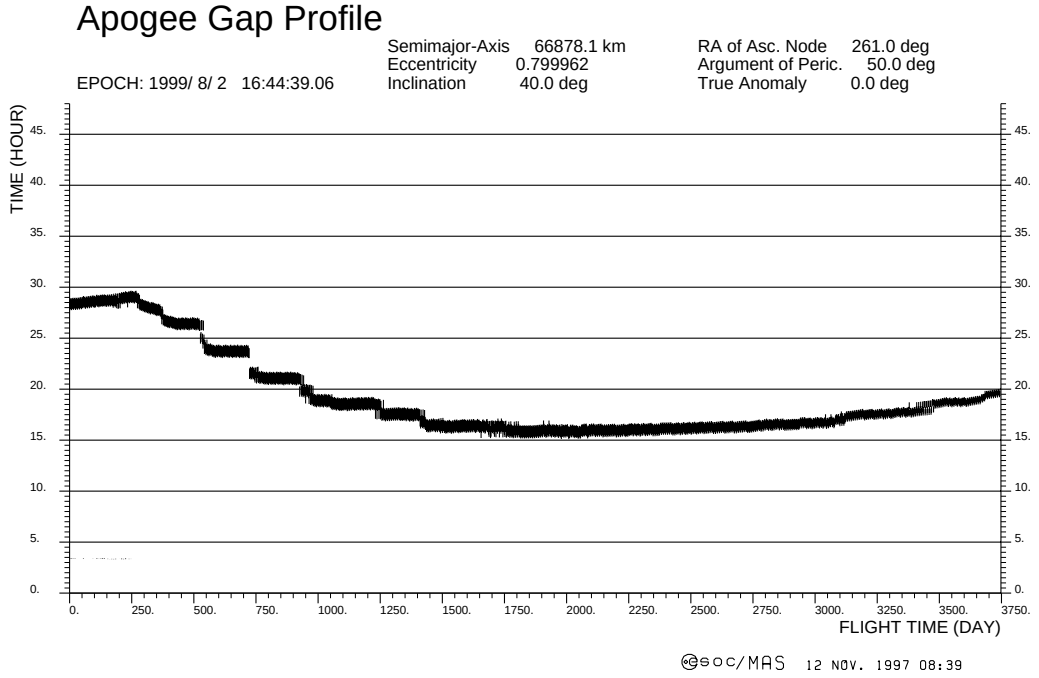

Figure 80: *Location of the* **XMM** *ground station telemetry gap with respect to orbital position, apogee being the position at 24 h.*

4.2.3 Bright source avoidance

In both the X-ray (EPIC/RGS) and the optical/UV regime (OM) there are restrictions with respect to the brightness of sources within the field of view, albeit of a different nature.

- OM bright optical/UV source avoidance

  With increasing count rate of a target, the science quality of OM data for that source is compromised by deadtime effects. The effect is of the order of 5% for a source with a count rate of 10 counts/s, increasing to approximately 30%

for sources with count rates of 50 counts/s (assuming in both cases a CCD framerate of 100 Hz).

A different kind of limitation is imposed on science observations by the OM detector photocathode. MCP-based intensifier tubes show localised gain depressions caused by bright point sources. The main cause of the sensitivity loss is related to the defects in the photocathode. From measurements made with OM test tubes, a non-linear relationship between the local sensitivity loss with accumulated count dosage was established. The brightness limits for all OM filters are tabulated in Table 19 in § 3.5.8.

OM observations of sources beyond these brightness limits are not allowed. **These limits hold for any source in the OM FOV, even if it resides outside an active OM window.** One way of avoiding bright sources within the FOV located near science targets is to use the magnifier (which reduces the size of the FOV, as described in § 3.5.6.3).

Since the above refers to point source limits, the quantity to be specified in **XMM** observing proposals for extended sources, like e.g. galaxies with active nuclei, is the maximum surface brightness (in most cases of the central object) in V magnitudes per square arcsec. The limits (at the position of the brightest emission) are the same as for point sources (see Tab. 19).

In addition, the following solar system sources must be avoided by the OM, with avoidance angles as listed:

- Mars – 3.5°
- Jupiter – 4.5°
- Saturn – 2°
- Uranus and Neptune are treated as normal bright sources which must be outside the OM FOV.

Avoidance of planets will be ensured by the SOC and is thus not a concern to the user.

- RGS bright optical/UV source avoidance

  Bright optical/UV light entering the RGS under certain angles can deteriorate the quality of the science observations. This is described in § 3.4.8.1.

- EPIC bright X-ray source avoidance

  The **X-ray** count rate must be kept below a threshold (0.8 cts per full frame for EPIC in order to keep pile-up below 1%) in order to obtain high-quality data. Otherwise the energy resolution and the quality of spectro-photometry would be compromised. The count rate limit depends on EPIC observing mode, as quantified in Tab. 4.

  Observations with an expected high level of photon pile-up are not *per se* disallowed, but a special scientific justification is required stating why and how the scientific goals of the proposal can be achieved despite the expected pile-up (and thus the deteriorated spectral response and PSF quality; §§ 3.3.10 and 3.7.1.3).

The EPIC telemetry limits are not hard-wired, making it difficult to provide universal guidelines. For EPIC MOS imaging modes the baseline count rate allowed is about 150 photons/s. For EPIC pn it is about 300 photons/s and therefore observations of single bright point sources at the pile-up limit are not constrained by telemetry. The brightest extended objects, such as the Cas A supernova remnant approach the telemetry limits, and can be accommodated by limited change of telemetry allocation depending on instrument usage, or by graceful loss of data frames. For timing modes the event rates are limited to about 1500 events per second by both the camera and telemetry constraints.

- No RGS bright X-ray source avoidance

  Due to the much smaller effective area of RGS compared to EPIC and the dispersion of the source spectra over many detector pixels, the source count rates per pixel will be much lower. Therefore, photon pile-up in RGS will be negligible. Only optically bright sources can impose constraints on RGS observations, as mentioned above. However, radiation nearby X-ray sources should not fall on the dispersed spectrum of the program source (§ 4.4).

4.2.4 Celestial constraints

The visibility of sources on the sky depends on several constraints, including avoidance of solar system sources. These are:

- Earth limb avoidance

  Minimum avoidance angle: 47°.

- Solar avoidance

  A solar aspect angle within the range $70° - 110°$ must be maintained at all times. Note that this is not a bright source avoidance cone, but driven by requirements on the spacecraft's alignment with respect to the Sun to ensure sufficient energy supply.

- Lunar avoidance

  Minimum avoidance angle: 22°.

The numbers listed here coincide with the avoidance angles used by the **XMM** Target Visibility Tool.

4.2.5 Duration of observations

- Minimum total observation length

  The total duration of an **XMM** observation should not be less than 5 ks.

- Maximum total observation length

  The maximum observation length is limited by the maximum possible continuous ground station coverage. Depending on the exact location of the apogee telemetry gap during the **XMM** mission (see Figs. 79 and 80), the maximum ranges from about 70 to 85 ks. Longer observations must be split up **by the**

proposer and will be scheduled individually. Requests to have long observations extending over more than one continuous visibility period back-to-back ("concatenated observations") are discouraged, because they require manual intervention; see § 4.9.1.

Note that the **XMM** scheduling software does not contain the functionality to automatically divide long observations (e.g., 200 ks) into schedulable bits (in the present example, of 70+70+60 ks). Therefore, **it is the observer's responsibility to propose only observations that can be scheduled within one target visibility period** (which has a maximum of about 70 ks; see § 4.1; Fig. 79).

- Maximum length of OM exposures

  OM imaging mode science exposures may not be longer than 5 ks each in order to limit the amount of memory allocation by tracking history information.

4.2.6 Position angle constraints

In particular the RGS, but also the OM with its grisms, can place position angle constraints on observations, if one wants to avoid spatial overlaps of the dispersed spectra of adjacent sources. Therefore, adjacent sources should not be aligned with the dispersion direction. In the case of RGS, avoidance of bright sources outside the field of view, as described in § 3.4.8.1, can also lead to position angle constraints. A description of how to avoid such sources is provided in § 4.4).
If nothing is specified during proposal submission, there is by default no orientation constraint on **XMM** observations. Note that any constraint imposed on an observation make it "time-critical" and thereby more difficult to schedule.

4.2.7 Raster observing mode

XMM does not have any capability to create a "raster" of nearby pointings via small aspect motions with minimal operational overhead. Each observation must be requested individually (via XRPS) and will be handled separately. This implies that each observation has the full operational overhead of a slew to the target and the acquisition of a tracking star attached to it and from the viewpoint of scheduling it implies that such observations will not automatically be scheduled consecutively within one or consecutive orbits.

4.2.8 Dithering mode

XMM also does not have a dithering mode. This means that users must, in order to overcome inhomogeneities in the coverage of a FOV (different net exposure times, e.g., because of chip boundaries), conduct observations of slightly offset positions on the sky. However, since **XMM** does not have a raster observing mode either (see above), this leads to a sequence of separate observations that are, from the standpoint of scheduling, treated as independent and might thus not be scheduled back-to-back.

As a secondary point, users should be aware that when proposing such partly overlapping observations to cover a field of view larger than $30'$, one should make sure that within a single observation the required OM filter coverage is achieved (because the position angle of the spacecraft might have changed by the time a neighbouring observation is scheduled, which would lead to different coverages on the sky).

4.3 Sky visibility during the XMM mission

All visibility information provided here and also by the **XMM** Target Visibility Tool is based on an expected launch date of 2000, January 21.

Target visibility should **always** be checked using the **XMM** Target Visibility Tool, which is located at the URL `http://astro.estec.esa.nl/XMM/user/vis/vis_top.html`. Currently, it contains information for orbits 3–430 after launch, i.e. the time period for AO-1 observations. Fig. 81 displays only a first-order approximation of the sky visibility during this time. It is shown for illustrative purposes and should be used only as a rough guideline to assess whether any visibility problems, in particular in the dark area around Cyg X-1, might exist, but not for quantitative statements. The map is not accurate, because it is based on $2^\circ \times 2^\circ$ bins. Since a whole bin is rejected even if only a tiny fraction of it is affected by an observing constraint (like e.g., bright source avoidance), the actual visibility is underestimated.
The **XMM** Target Visibility Tool determines the visibility, if any, for certain target coordinates under configurable conditions. Note that basic parameters, like e.g., avoidance

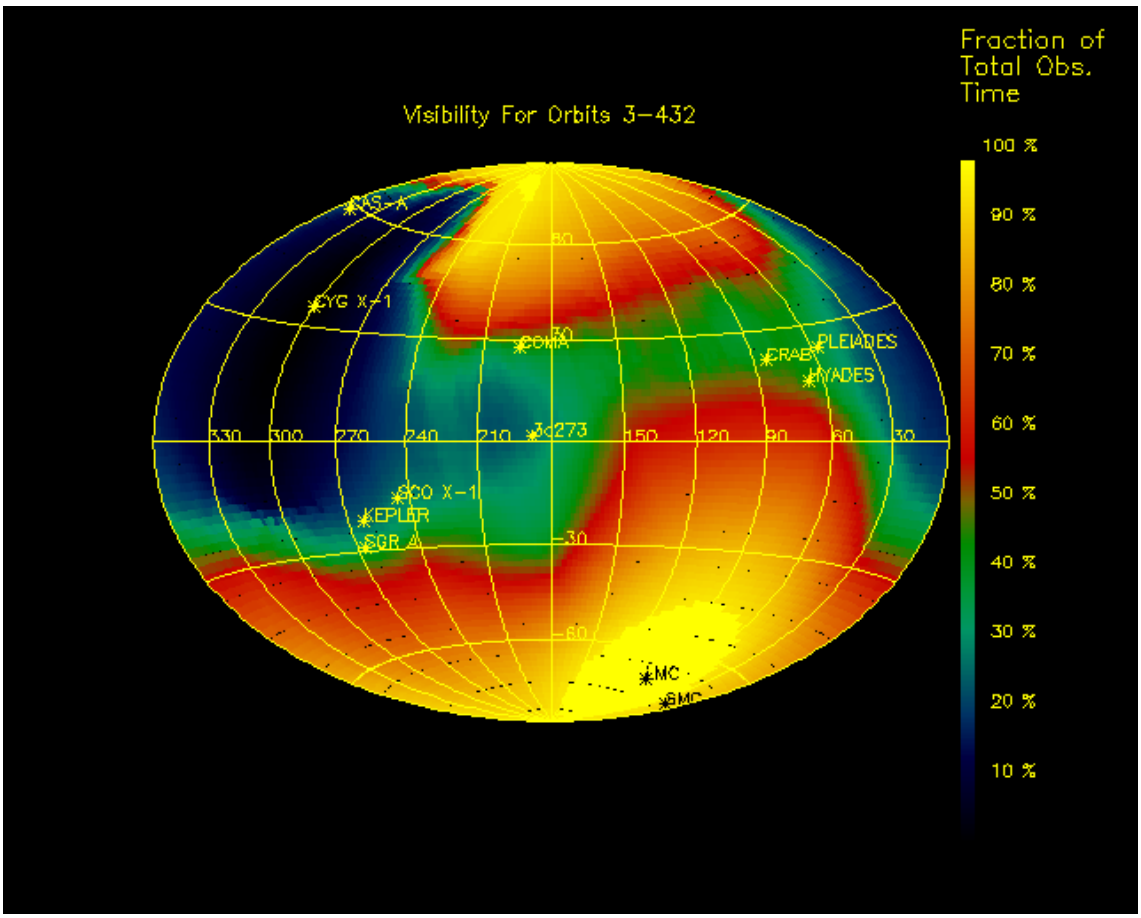

Figure 81: *Approximate sky visibility (in % of the total theoretically available time) during orbits 3–430 of* **XMM** *operation. Coordinates are equatorial, in units of degrees, centred on (180,0).*

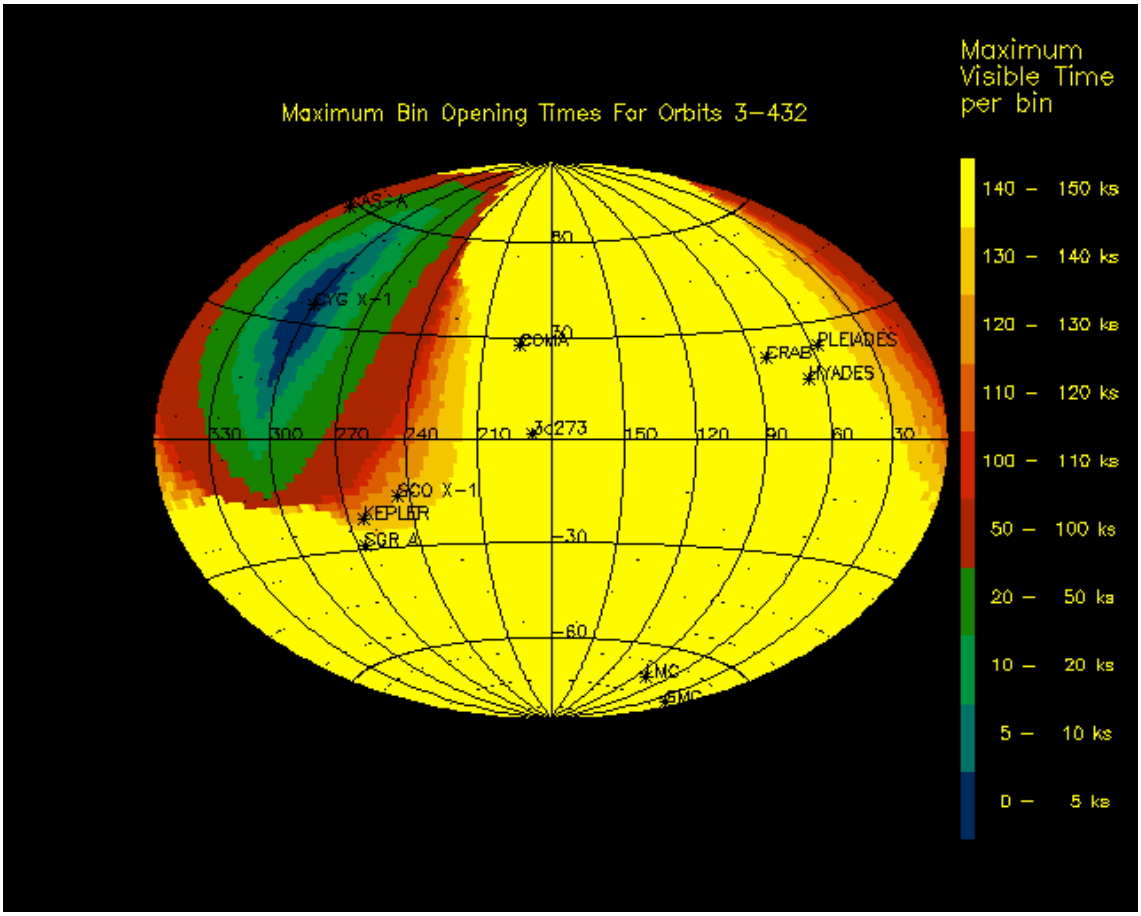

Figure 82: *Sky areas for which a given maximum target visibility is not reached during orbits 3–430 of* **XMM** *operation. Same coordinates as in Fig. 81.*

angles, should not be changed when running it. The defaults represent the values that are actually used for satellite operation. More details are provided by the **XMM** Target Visibility Tool online help.

Fig. 82 is a complementary representation of those areas on the sky for which there is **no** adequate visibility during the first 430 orbits of the **XMM** mission. Note that, despite its appearance, this is not just an inverted version of Fig. 81. It shows areas for which a certain maximum continuous target visibility is not reached in any orbit (up to orbit 430). Again, this image is only a first-order approximation, based on a 2° grid. For more accurate information for given target coordinates, the **XMM** Target Visibility Tool **must** be used. Targets for which no adequate visibility is available during the first two years in orbit should be proposed at a later AO.

4.4 Position angle determination for XMM observations

First a few words on **XMM** nomenclature: the **XMM** "roll angle" is defined as the rotation angle between the plane defined by the major rotation axis of the spacecraft (the spacecraft X-axis) and the spacecraft Z-axis, to that defined by the spacecraft X-axis and the spacecraft-Sun direction. The roll angle increases in a clockwise direction with respect

to the positive X-axis.
The "position angle", on the other hand, is defined as the rotation between the spacecraft X-Z plane and the plane defined by the spacecraft X-axis and celestial North. Again, the position angle increases in a clockwise direction with respect to the positive X-axis. Note that the satellite's –Z-axis, which is also the RGS dispersion axis, is North-aligned under a position angle of 0°, i.e. the declination axis.

Users can determine the best position angle at which to obtain their planned observations, while avoiding nearby bright sources, using SciSim (Appendix A) as follows.
The SciSim GUI (Appendix A.2, Fig. 84) shows the field of view (FOV) of the spacecraft when viewed along the -X axis of the spacecraft, i.e., from the focal plane towards the mirrors and outwards. The tool also displays the RGS dispersion axis, in the form of two blue horizontal lines, the separation of these lines representing the cross-dispersion direction extent of the illuminated part of the CCD chip array. This view can be rotated in terms of the position angle of the spacecraft.
It is therefore a simple matter of creating a model field in SciSim containing the sources which could potentially cause confusion, and finding a suitable position angle value for which these sources are **not** aligned along the RGS dispersion axis. Sources can be defined in SciSim by clicking on "Sources" and using the Source editor GUI, which, amongst other properties, allows the user to enter target coordinates.
Users can get a rough idea of when the observation might be scheduled, by using the **XMM** Target Visibility Tool (§ 4.3), which outputs the average of the position angles at the start and the end of each visible period for a nominal roll angle of 0 degrees. Be aware that the roll angle is required to be kept within operationally imposed limits at all times. As a consequence of the apparent motion of the Sun in the course of a revolution this roll angle requirement might necessitate minor position angle adjustments during each period of stable pointing.

4.5 XMM observation overheads

As for all telescopes, **XMM** observations are also affected by operational overheads. Proper instrument setup, e.g., requires some calibration exposures in order to provide optimal instrument performance and thereby high-quality science data. As the mission evolves and the knowledge about the instruments improves, additional items may be added or some of those mentioned below might be taken from the list.

We outline here which overheads apply to **XMM** observation for the users' information only. **None of these need to be taken into account in XMM observing proposals**, because they will be added ontop of the requested science duration as warranted.

There are two categories of overheads:

1. Operational overheads and
2. instrument and calibration overheads.

4.5.1 Operational overheads

XMM operational overheads are:

- Slew time to move to the target coordinates: variable, depending on the relative target position with respect to the starting spacecraft attitude; the **XMM** slew rate (except for the first slew after perigee passage and the last slew before perigee passage) is 20°/h.
- AOCS reference star acquisition time and fine trim to the actual target position after a slew – about half an hour per observation.

4.5.2 Instrument and calibration overheads

The following instrument and calibration overheads apply to **XMM** science observations. Note that some of them will occur simultaneously, at the start of an observation.

- EPIC setup time (of order 15 minutes per exposure) for offset calculations, during which the amount of optical loading of the CCD chips is determined (which leads to pixel charges that must be subtracted to set the correct zero level for X-ray observations).
- RGS diagnostic mode image (max. ca. 15 minutes) before the start of RGS science observations for background determination.
- Time estimates for calculations of OM field acquisition overheads are mainly driven by the guide star recognition and the acquisition of a reference tracking frame. Both are estimated to be of order 1 minute, and therefore negligible.
- Between different OM science exposures, e.g. when performing filter changes, an overhead of approximately 2–4 minutes is expected.
- No special calibration overheads are foreseen for OM for each individual exposure. The acquisition of OM flat fields does not cause an operational overhead on OM observations, because they will be taken during slews.

In general, instrument calibration overheads refer to exposures, not entire observations. Therefore, if there is no need to change the data acquisition mode during the observations, it is recommended to not interrupt the integration during an observing run. Otherwise, additional overheads will be created, which leads to a decrease in the overall observing efficiency of a program.

4.5.3 Special science exposures

Optimal scientific usage of the **XMM** instruments sometimes requires special (science) exposures. These are **not** overheads and therefore part of the requested science observing time:

- RGS spectroscopy mode data to be taken before or after high time resolution mode observations in order to identify the location of the incident spectrum on the CCD array (and thus the timing of the readouts) very accurately.
- An OM image should be acquired before every grism exposure.
- OM fast mode images should be embedded in an image mode science window. This will help with the fixed pattern noise correction, as it provides a template at the proper count rate level.

4.6 Instrument alignment

XMM has three independent X-ray telescopes and an optical/UV telescope, with a total of six science instruments. Neither the telescopes' optical axes nor the centre positions of the detector FOVs are aligned perfectly. Thus, radiation from sources in the spacecraft's boresight direction does not fall onto the nominal on-axis position of all detectors simultaneously. The specification for the **XMM** instrument alignment in the focal plane allows for offsets from perfect alignment with respect to each other of up to ca. $\pm 1'$. This means that two detectors can be misaligned with respect to each other by up to $2'$ on the sky. This is the reason why **it is important to specify in an XMM observing proposal which instrument should be the prime detector** so that the target is properly centred in the FOV of the detector that is most important for the science objectives of the observing programme. Measurements of the relative alignment and the creation of a correction matrix will ensure that the primary instrument will be pointed on source with an expected accuracy of the order of $15''$. The offsets of the X-ray source position from the centre position of the other detectors can be much larger, up to ca. $2'$, as mentioned above. The actual alignment of the instruments is not yet known, because the **XMM** flight hardware has not yet been finally integrated and tested.

4.6.1 Choice of primary instrument

The relative alignment, i.e., the offsets with respect to each other of the different **XMM** focal instruments, determines where a source that is "on axis" for one particular X-ray telescope will be imaged in the others. For most applications, off-axis angles of order $1'$ are not important, in particular for EPIC full window mode observations. However, RGS has a much smaller "field of view" or rather area for optimal placement of the dispersed spectra on the elongated CCD array. For best energy and flux calibration, source spectra should be optimally centred. Therefore, if high-resolution spectroscopy (i.e., observations with an emphasis on RGS science data) are required, RGS should be specified as the primary instrument. The same holds for EPIC and OM, if operated with small science windows. In case EPIC is prime, it is recommended to choose the pn camera as the prime instrument to avoid the inter-CCD gap at the centre of the pn array.

4.7 Absolute and relative pointing accuracy

The so-called "Absolute Measurement Accuracy" (AMA), i.e., the error on the **XMM** boresight, after application of all corrections on-ground, is anticipated to be ca. $3''-4''$ (on average). The absolute pointing error (APE), i.e., the offset between actual and required pointing direction, is expected to be about $15''$ (95% radius). The relative pointing error (RPE) during an exposure, after correction for spacecraft drift (leaving mostly spacecraft jitter), will be about $2''$ (rms; likely better).
Independent pointing information will come from the Attitude and Orbital Control System (AOCS) and the OM, when operating. The OM information is expected to provide about the same AMA as the AOCS data. Thus, if OM data are available, these can be used to cross-check the AOCS attitude solution. The necessary functionality to analyse OM data will be contained in the SAS (§ 6.1).

4.8 Points of concern

Some more parameters that might influence certain **XMM** observations, and should therefore be taken into account, are:

- Seam losses between abutted CCDs

  Although small, there **are** gaps between the chips of the different X-ray detectors onboard **XMM**. The two EPIC MOS cameras are mounted orthogonal with respect to each other, so that in final images, after adding up the data from two X-ray telescopes, the gaps should not be visible after correction for exposure. There will only be a reduced total integration time in areas imaged at the location of chip boundaries. The pn camera has a different chip pattern, leading to mimimal losses in other areas of the field of view. It is also offset with respect to the X-ray telescope's optical axis so that the central chip boundary does not coincide with the on-axis position. The inter-CCD gaps of the EPIC MOS chip array are 400 μm ($11''$) wide. Those between neighbouring CCDs within one quadrant of the pn chip array are 40 μm ($1.1''$) wide, the gaps between quadrants about 150 μm ($4.1''$).

  The nine CCDs in each RGS also have gaps of about 0.5 mm in between them. Table 9 lists the energies affected by the gaps in RGS-1. However, the two RGS units will be offset with respect to each other along the dispersion direction to ensure uninterrupted energy coverage over the passband.

  By choosing the instrument that is most important for the planned research as the primary instrument, **XMM** users can ensure that the programme source is placed properly, away from chip boundaries.

- Charge transfer efficiency (CTE)

  While being transported from their original location to the readout nodes, the charges of CCD pixels are transfered from pixel to pixel up to several hundred times. During each transfer, a small fraction of the charge (which depends mostly on impurities in the semi-conducting layer) can be lost. This effect can be quantified roughly and corrected for in the offline data calibration process.

- "Out of time" events

  The **XMM** X-ray detectors do not have shutters and are therefore at all times exposed to incoming radiation from the sky. Trying to prevent photon pile-up (see above), the CCDs are read out frequently. During readout, photons can still be received. However, they hit pixels while their charges are being transfered to the readout nodes, i.e., when they are not imaging the location on the sky they would normally observe during the exposure. Thus, events hitting them during readout are "out of time" (and also "out of place"). One cannot correct for this effect in individual cases, but only account for it statistically.

  The MOS CCDs have frame store areas, which helps suppress the effect of out-of-time events. The frame shift times of a few ms are much shorter than the maximum frame integration time of 2.8 s. Therefore, the surface brightness background of smeared photons is only a fraction of a percent divided by the ratio of the PSF size to the CCD column height.

For pn the full window mode has a readout/shift ratio of 1/11, so the surface brightness of the background is 9% divided by the ratio of the size of the PSF to the CCD column height. This is noticeable for any sources brighter than about 10^{-13} erg s^{-1} cm^{-2}. The large partial window mode counteracts this by using half the image height as a storage area, but the reduced smear is penalised by a loss in live time. Another strategy is to use a programmable "wait time" to extend the full frame imaging, but at the cost of count rate capability before pile-up.

- RGA rib scattering

  Light scattered off the stiffening ribs of the grating plates of the RGAs will produce diffuse ghost images in the EPIC FOV in the ±Y direction (i.e., the RGS cross-dispersion direction). The intensity of these images is of the order of 10^{-4} relative to the intensity of the focused image. For off-axis sources at azimuth angles corresponding to the ±Y direction, the intensity of the ghost images increases to a few times 10^{-4}.

  Rib reflection is currently implemented in SciSim (v. 2.0.1), but the reflection coefficient is too high, and the diffuse nature of the scattered light ghosts is not modeled. Simulations with SciSim will therefore overestimate the surface brightnesses of RGA scattered light due to this effect.

Except for event selection, which is performed onboard for EPIC MOS, the above effects are dealt with in the offline data analysis with the SAS.

4.9 Linked, pilot/follow-up and concatenated observations

XMM offers the possibility to conduct three special kinds of observations, namely "linked", "pilot/follow-up" and "concatenated".

1. Concatenated observations

   Concatenated observations are two or more observations that are executed "back-to-back".

2. Pilot/follow-up observations

   Based on a first short ("pilot") observation it is decided, with rapid turn-around, based on a success criterion, whether this will be followed as fast as possible by a longer ("follow-up") observation of the target, still within the same orbit.

3. Linked observations

   Linked observations are observations consisting of "test" observations in one orbit and "main" observations in a later orbit which depend on the results obtained from the test observations.

4.9.1 Concatenated observations

Observations are normally concatenated in an attempt to observe an object with different instruments or instrument configurations in a direct series of exposures. Since on **XMM** all

instruments operate simultaneously and because it implies the necessity for special **XMM** SOC support and a restriction in the schedulability of the observing run, **proposing concatenated observations with XMM needs a specific scientific justification and is in general discouraged by the SOC**.

4.9.2 Pilot/follow-up observations

XMM scheduling supports pilot/follow-up observations, which work as follows:
A success criterion is defined for a (normally short) first pilot observation of a target. If the pilot observation fails, no long follow-up observation will follow and **XMM** will continue observing according to the original schedule (which is developed based on the assumption that the pilot observation will fail). If, on the other hand, the success criterion of the pilot observation is met, then the **XMM** observing schedule will be manually interrupted and new commands, with the follow-up observation following the pilot as fast as possible, will be linked up to the satellite.
One example for such a pilot/follow-up observation could be an attempt to observe a strongly variable source only when it is in its "on" state.

4.9.3 Linked observations

Linked observations require special arrangements to be made to ensure a fast turnaround for the test data analysis. Because the **XMM** SOC will operate with only very few staff astronomers, user support will under normal circumstances be restricted to normal working hours. Therefore, it will be the observer's responsibility to analyse the test data before the main observing run, which may require his/her presence during/after the test observations. Moreover, linked observations cannot be entered during proposal submission via XRPS as "fixed-time" in order to give the SOC maximum flexibility in selecting the optimal interval between the test and the main observation.
Proposals requesting linked **XMM** observations will therefore need a very strong specific scientific justification. In general, **proposals for linked XMM observations are discouraged**.

4.10 XMM slew observations

XMM will conduct EPIC science observations during slews from one target to another. The expected accuracy for the attitude reconstruction during **XMM** slews is better than $1'$. **Slew observations cannot be proposed.** The data obtained during slews are stored in so-called "Slew Data Files" (SDFs). Slew data will be processed by the PPS pipeline and the resulting science data files put into the **XMM** data archive (**XMM** Data Archive; § 7).

5 XMM Guest Observer Program

5.1 XMM calendar of events

In the following we list the most important dates relating to the upcoming **XMM** mission.

Date	Event
23.09.1998	Release of **XMM** Users' Handbook (Issue 1.0)
30.09.1998	First **XMM** Workshop at ESTEC
19.01.1999	Release of AO-1
19.01.1999	Release of XRPS software for proposal submission
19.01.1998	Release of **XMM** Users' Handbook (Issue 1.1)
17.04.1999	00:00 UT - Deadline for AO-1
02.08.1999	SAS release
21.01.2000	**XMM** launch date
02.07.2000	Approximate start of **XMM** open time observations (TBC)

5.2 Mission overview

The total available **XMM** time will be subdivided into several categories, as shown in Fig. 83.

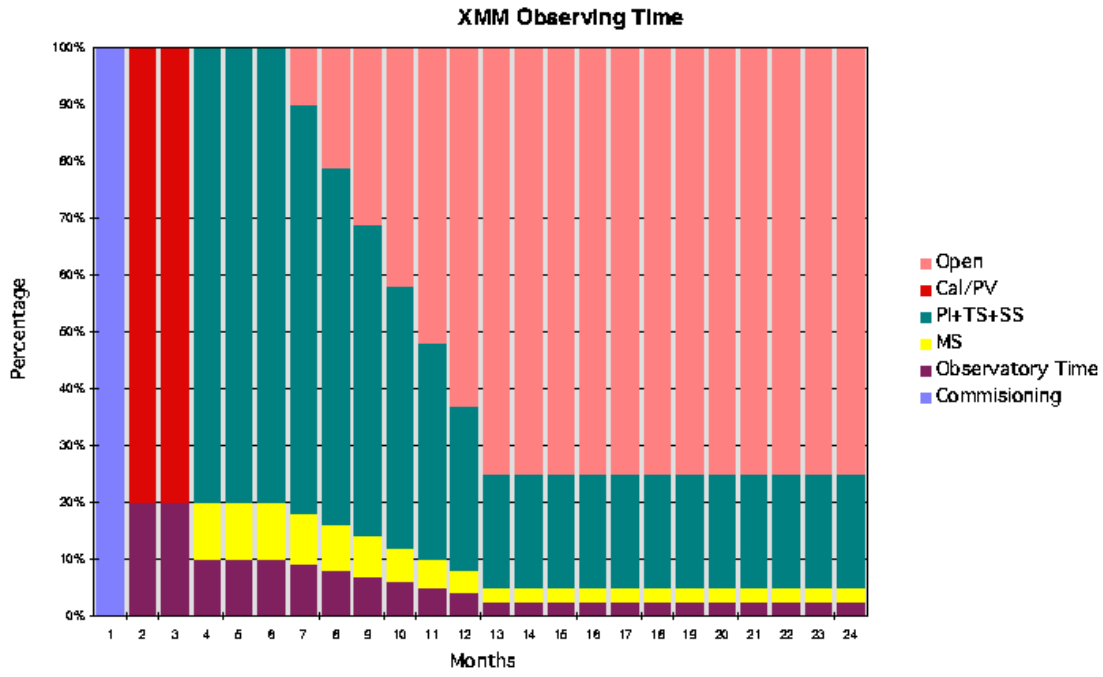

Figure 83: *The division of* **XMM** *observing time during the first two years.*

Observations as part of the **XMM** Guest Observer (GO) programme will commence approximately six months after launch. Starting at that time, the GO share of the total observatory time will increase to 75%, at which it will stay for the remainder of the first 27 months in orbit.

The **XMM** Science Management Plan (SMP; ESA/SPC(88)20) identifies four phases of activity during the first two years of **XMM** operations. These are:

- Commissioning

  The commissioning phase, including outgassing of payload and spacecraft, in-orbit switch-on and check-out, is expected to last for ca. four weeks. During this period basic engineering checks on the system will also be performed.

- Calibration and Performance Verification (Cal/PV)

  This time is allocated to a first characterisation of the telescope and instruments, to determine sensitivities etc. It is expected to last about 11–12 weeks.

- Full guaranteed observing time

  During this phase 80% of the observatory time is set aside for the Principal Investigators (PIs), Telescope Scientist (TS), Project Scientist (PS) and Survey Scientist (SS) and the Observatory Team. The remaining 20% of the time are Mission Scientist (MS) and Observatory time (10% each).[3] This phase will last for three months and terminate approximately six months after launch.

- Mixed observing time

  During the second six month period of the first year in orbit, open time proposals will be interleaved with the guaranteed time observations such that, on the average, the time is split 50/50, with a linear run of the guaranteed time from 80% at the beginning to 20% at the end of the period.

  After the completion of the second six-month period, until the end of AO-1, 75% of the time will be open for GO proposals, 20% for guaranteed time observations. 5% are allocated as Observatory Time.

Although the approved implementation of the **XMM** mission is only for a duration of 27 months, the expected lifetime is ca. 10 years.

The expected spacecraft observing efficiency (time available for science observation out of the total observatory time) is about 70%. Therefore, the total amount of GO time available, starting with the second year in orbit, is ca. 12.35 Ms per year. In AO-1, a total of about 13.9 Ms will be available for GO observations.

5.3 XMM proposal preparation and submission

The **XMM** Project Scientist will issue calls for proposals in "Announcements of Opportunity" (AOs) in regular intervals. The first AO, AO-1, is for open time during the first 27 months of the mission. 70% of all open time will be scheduled at first, based on a preliminary (and conservative) estimate of the observatory's efficiency. A supplementary call for proposals for the remaining 30% of open time will be issued later. Subsequent AOs will be for periods of one year (TBC).

Policies concerning, e.g., duplication avoidance, proposal categories (GO, ToO) or target categories (stars, galaxies, AGNs etc.) are described in the AO-1 documentation and the XRPS Users' Manual.

[3] Observatory time is the allocated time for continuing calibration observations after the initial calibration and PV phase (see above).

5.3.1 XMM proposal preparation

In order to estimate the feasibility of an **XMM** observing proposal, users will need information from the following sources:

1. For all observations of targets with "simple" spectral characteristics, i.e., observations of point source targets with spectra that can be approximated by simple, single-component models to estimate the expected count rate for a given flux (as used for the production of the figures displaying the expected flux to count rate conversion factors above), the information contained in the instrument-specific chapters of this document should suffice.
2. For more complicated source geometries and/or spectra, modeling with SciSim or the use of PIMMS or *xspec* might be required.
3. To scale count rates from previous X-ray satellite missions to **XMM**, it is recommended to use PIMMS.
4. Target visibility can be assessed using the **XMM** Target Visibility Tool.
5. To check during which **XMM** orbits a certain position angle can be achieved in order to avoid nearby sources during RGS (or OM grism) observations, see § 4.4.

5.3.2 XMM proposal submission

XMM proposal submission is facilitated via the **XMM** Remote Proposal Submission software (XRPS). The required inputs into the XRPS forms are described in the XRPS Users' Manual.

Every XMM proposer must first register as an XRPS user.

5.3.2.1 XMM Remote Proposal Submission (XRPS)

XRPS is a software package interfacing with the **XMM** Archival Management Subsystem (AMS), the Proposal Handling Subsystem (PHS) and the archival data base, developed by Logica UK Limited. It is part of the **XMM** PHS and as such located under the PHS on the web server. Proposal submission is facilitated via a web interface.

5.3.2.2 How to fill out the RPS online forms

An XRPS Users' Manual is being developed to guide users through the online XRPS. It is highly recommended to **follow exactly the procedures outlined in the XRPS Users' Manual to ease the interaction with the software**. The XRPS Users' Manual will be available at the time of the XRPS release (§ 5.1).

5.4 Technical proposal optimisation

Upon successful receipt of a proposal by the SOC, the PI will receive an acknowledgement that it has been entered into the system. In the process of proposal preparation for OTAC review, potential conflicts will be identified. Then the proposal will undergo review by the OTAC. Parallel to OTAC review, proposals will be subjected to a technical review by SOC

personnel. Note that **it is the proposer's responsibility to ensure that the target coordinates (and, if necessary, the satellite position angle) are correct.** After OTAC acceptance, successful proposals will be technically optimised for implementation in the **XMM** observing program. Technical optimisation of proposals will be performed with the following suite of **XMM** Proposal Handling Subsystem (PHS) tools:

- EPIC

  1. EPIC expected X-ray count rate tool
     This tool calculates the expected X-ray counts for the specified target for each filter of each EPIC instrument.
  2. EPIC expected optical count rate tool
     This tool calculates the expected optical counts for each specified target for each filter of each EPIC instrument.
  3. EPIC telemetry bandwidth calculation tool
     This tool calculates the expected telemetry bandwidth for each EPIC exposure.
  4. EPIC signal to noise ratio tool
     This tool calculates the expected signal to noise ratio for each EPIC exposure.
  5. EPIC science parameter calculator tool
     This tool calculates for each EPIC exposure the:
     - expected pile-up
     - fraction of smeared photons
     - duty cycle
     - total number of counts
     - total area of the chosen field of view
     - counts per frame

- RGS

  1. RGS expected X-ray count rate tool
     This tool calculates the expected X-ray counts for the specified target for each RGS instrument.
  2. RGS expected optical count rate tool
     This tool calculates the expected optical counts for the specified target for each RGS instrument.
  3. RGS telemetry bandwidth calculation tool
     This tool calculates the expected telemetry bandwidth for each RGS exposure.
  4. RGS diagnostic downlink time estimation tool
     This tool calculates the downlink time associated with the diagnostic data when the RGS instrument is operating in spectroscopy mode.

- OM

1. OM image mode count rate estimation tool
   This tool calculates the counts expected in each imaging mode window of each OM exposure.
2. OM fast mode count rate estimation tool
   This tool calculates the counts expected in each fast mode window of each OM exposure.
3. OM fast mode time slice estimation tool
   This tool calculates the fast mode time slice duration, for each fast mode window, in units of the MIC frame time. GOs originally specify the time slice duration of each fast mode window in ms.
4. OM tracking frame time estimation tool
   This tool calculates the OM tracking frame time, for each exposure, in units of the DPU cycle. The exposure duration, originally specified by GOs in seconds, is then calculated as an integer multiple of this tracking frame time.
5. OM science windows tool
   This tool:
   - calculates the size of the window, in detector pixels, for each science window that is specified by the GO in arc-seconds. If the GO has specified a window in detector pixels then this value is output.
   - assigns a blue fast mode area (1 or 2) to each fast mode window.
   - calculates the number of memory windows required to enclose the specified science windows and their details (position and size).
6. OM telemetry bandwidth calculation tool
   This tool calculates whether the data generated during an exposure can be downlinked during the next exposure using the telemetry bandwidths available to the OM instrument. The tool also indicates the actual bandwidth which can be used and the time taken to downlink the data with this bandwidth.
7. OM bright object and guide star tool
   For each observation this tool will indicate:
   - whether the observation is possible with any filter (not just those specified by the GO).
   - for which filters there are potential bright sources in the field of view.
   - the position angle constraints, if any, which would ensure that these bright sources do not appear in the field of view.
   - the potential guide stars for the observation. The right ascension, declination and visible magnitude of up to 32 stars are generated.
8. OM science parameter calculator tool
   This tool calculates for each OM exposure the:
   - total count rate
   - source count rate
   - signal to noise ratio

- General

1. Assign telemetry look-up table tool
   This tool, using the telemetry bandwidths calculated for each instrument, identifies a telemetry allocation table for the observation.
2. View PHS tools information file
   This tool allows the Proposal Handler to view the information file.

For a more detailed, technical description of the tools listed above, we refer to the PHS Specific Software Requirement Document.

6 Analysing XMM data

This chapter currently contains placeholders for planned subjects only. It will be completed once the SAS software becomes available.

6.1 XMM analysis software – the Science Analysis Subsystem (SAS)

The Science Analysis Subsystem (SAS) will be the software package for the reduction of **XMM** data from all science instruments, EPIC MOS & pn, RGS and OM (§ 6.1.3) and the production of standard data products, such as images, spectra and lightcurves. This chapter provides a general description of the SAS in order to introduce users to it and some data reduction strategies. The SAS is a modular and open stand-alone software system tailored to the needs for **XMM** data analysis, to which programmers can add their own routines. The Pipeline Component of the Pipeline Processing Subsystem (PPS; § 6.1.2) will be an integral part of the SAS, which will be used by the Survey Science Centre (SSC; Appendix B) for standard processing of **XMM** data.

The scope of the SAS is to process all **XMM** science data. The first inflight data to test the SAS with will come from the calibration and PV observations.
In addition, the SOC will use the SAS for instrument calibration, i.e., the creation of updates to the existing calibration information (CCFs).

The SAS will be supported for computers running the Solaris 2.6 operating system. It is currently under development and not yet publicly available.
More technical information on the scope of the SAS and on the design and coding of tasks can be found in the SAS User Requirements Document and the SAS Software Specification Document.

More information will be added here when it becomes available.

6.1.1 Interactive XMM data analysis with the SAS

The SAS will operate from a GUI as well as from the command line. Interactive data analysis will normally be performed using the GUI, while the command line interface (CLI) is primarily intended for batch jobs.

The basic functionality groups for interactive analysis in the SAS are:

- Importing all science and non-science **XMM** data.
- Preparation of data (e.g., extraction of the most important housekeeping data, attitude-related event selection).
- Data calibration (e.g., conversion of the individual node energy-PHA relationship to a common [pulse-invariant] scale).
- Data processing (i.e., the creation of data products, such as images, spectra and timeseries) and data analysis (source detection; imaging, photometric, spectroscopic and timing analyses, etc.).
- Data display and output.

- Data quality checks.

Once the SAS is released, this chapter will describe basic interactive analysis techniques.

6.1.2 Pipeline processing of XMM data: the Pipeline Processing Subsystem (PPS)

One particular application for the use of batch jobs is the **XMM** Pipeline Processing Subsystem (PPS). The Pipeline Component (PC) of the PPS, i.e., the actual processing tasks (excluding additional software like, e.g., process control, pipeline management etc.) is entirely contained in the SAS. The pipeline will produce standard data products for all **XMM** science observations, which will enter the **XMM** data archive within 30 working days (but remain protected for the duration of the proprietary period, if any).

The PPS will create, among others, the following types of data products, which will be delivered to the **XMM** data archive:

- An observation summary,
- EPIC calibrated event lists,
- EPIC imaging, spectral, and timeseries data products,
- EPIC source list and image analysis products,
- EPIC timing analysis products,
- EPIC PPS summary products,
- RGS calibrated event list,
- RGS image and spectral products,
- RGS PPS summary products
- OM imaging, timeseries and source list products,
- OM PPS summary and miscellaneous (housekeeping and tracking history) products,
- catalogue and archive products (including the names of catalogues that are cross-correlated with EPIC source detection lists and the results of these cross-correlations)

A detailed description of the pipeline processing steps and the PPS data products, which are part of the delivery to observers, will be presented in the **XMM** Data Files Handbook (in preparation).

6.1.3 XMM Science data

XMM science data are contained in a set of files called Observation Data Files (ODFs). Each PI of an **XMM** observation receives, as soon as the observing data are pipeline-processed, the following data:

- The ODF of the observation,
- the appropriate CCF,
- all PPS data products produced for the observation, including
- calibrated event lists.

These data are delivered to the PI via CD-ROM.

6.1.4 What is an ODF?

An Observation Data File (ODF) is a set of files containing data from all **XMM** instruments obtained during a science observation, stripped of the telemetry headers and wrappers. ODFs are produced by the Observation Data Subsystem (ODS). The data are at that stage uncalibrated, in the format to be read into and processed by the SAS.

Similarly, Slew Data Files (SDFs) contain all data obtained during **XMM** slews, in the format to be read into and processed by the SAS.

ODFs/SDFs contain science files from each **XMM** instrument operating during the observation/slew, depending on the mode in which they are operated, and instrument housekeeping information. In addition, ODFs/SDFs also contain spacecraft files (e.g., an attitude history file, reconstructed orbit file etc.) and observation/slew summary files.

A complete description of the files contained in ODFs/SDFs will be presented in the **XMM** Data Files Handbook (in preparation).

6.2 XMM calibration data

XMM instrument calibration is performed as a mixture of so-called "forward" calibration (i.e., using simulations of the instruments to predict their response with SciSim) and the classical calibration using arrays, like e.g., flat fields, describing the measured instrument characteristics. The results of the calibration analyses by the SOC are contained in the calibration files delivered to the user in the Current Calibration Files (CCFs) that come with each science data delivery.

6.2.1 Current Calibration Files (CCFs)

XMM data calibration is based on the use of the "Current Calibration File" (CCF). A CCF is the collection of all calibration files for the calibration of data from all **XMM** science instruments that are valid at a particular time. Each calibration file, which is a constituent of a CCF, has an issue number and a start-of-validity date by which it can be identified uniquely. However, a CCF does not have a version number or validity date, because it is a mere collection of calibration files carrying individual identifiers that are valid at a given time. The most up-to-date version of a calibration file is always the one

with the highest issue number. Calibration files account for properties of either the **XMM** spacecraft, the X-ray telescopes or one or more of the payload instruments.

With each ODF, observers receive a corresponding CCF.

A detailed description of the CCF concept, including a list of the calibration files constituting a CCF, is currently in preparation as part of the **XMM** Data Files Handbook (in preparation).

7 XMM data archive

This chapter provides a general description of the access mechanisms to the **XMM** Data Archive, its contents and the proprietary data rights policies.

7.1 Contents of the XMM archive

The **XMM** data archive consists of two parts:

1. Raw data, as they come from the satellite, will be stored at the Mission Operations Centre (MOC) in Darmstadt. These data will not be accessible to the outside world.
2. ODFs/SDFs reside in the **XMM** Data Archive of the SOC. After pipeline processing, calibrated event lists and data products derived from the ODFs/SDFs enter the **XMM** Data Archive.

Among others, the science data archive, from which users can retrieve or request data, contains the following types of data:

- Observation and Slew Data Files (ODFs/SDFs; § 6.1.3),
- calibrated X-ray event lists and OM images (or OM event lists in case of fast mode observations),
- pipeline data products created from these (§ 6.1.2),
- CCFs (§ 6.2.1),
- a list of accepted proposals (including abstracts),
- the **XMM** catalogue,
- various others.

7.1.1 Pipeline data products contained in the XMM data archive

Besides the data types listed above, the **XMM** Data Archive contains the files created by the Pipeline Processing System (PPS) operated at the SSC (see Appendix B). As described in § 6, calibration of **XMM** science data is performed by applying the appropriate CCF. The PPS produces calibrated science data (e.g., X-ray event lists) and from these data products, such as, e.g., images, spectra, and time series (§ 6.1.2).

PPS data products are produced for every **XMM** observation and fed into the data archive. They form part of the standard delivery to PIs. After expiration of the proprietary period, if any, the pipeline data products will be retrievable from the archive.

A complete description of which kind of files/data the PPS produces will be provided in the **XMM** Data Files Handbook (in preparation).

The archival retrieval procedures are described in § 7.3 (below).

7.2 Proprietary rights

7.2.1 GO and GTO observations

XMM Guest Observer (GO) data will be protected for an initial period of one year after delivery to the GO. Precondition for the start of the proprietary period is the delivery not only of the data, but of all PPS data products, including in particular calibrated event lists.

Guaranteed Time Observers' (GTO) data are also protected for one year after delivery of the PPS products to the PI. For a list of GT targets, see below (Appendix D; Table 23).

The proprietary period of an observation can be extended, if the calibration provided by the SOC at the time of delivery should *a posteriori* turn out to be inaccurate so that reprocessing of the data is required.

7.2.2 Calibration and performance verification data

Data obtained during the Calibration (Cal) Program and the Performance Verification (PV) phase are public. Lists of the **XMM** calibration and PV targets are provided in Appendix D; Tabs. 21 and 22. These data will enter the **XMM** science data archive as soon as they have been pipeline-processed.

7.3 Access to the XMM data archive

Access to the **XMM** Data Archive is facilitated via the **XMM** Archive Management Subsystem (AMS). It can be accessed in different ways:

- Query via a web interface,
- request CD-ROM delivery of the entire data for a certain observation, including ODF, CCF, (calibrated) event lists etc. and the PPS data products,
- download constituents of the former, which have been flagged in the AMS as downloadable,
- obtain an updated CCF. (TBC)

Access is gained via the following mechanisms:

- Queries, e.g., of the proposal database (for example for accepted or executed observing programmes), are processed via the AMS web interface.
- PPS data products can be requested via the AMS interface. They will be staged in a public area, from where they can be downloaded.
- Requests for CD-ROM shipments are submitted via the AMS interface. Users requesting CD-ROMs must register first, if not yet registered as an **XMM** user from submitting an observing proposal.
- In case a complete, new CCF should be required, delivery is via a CD-ROM. However, those constituents of **XMM** CCFs which can be expected to change relatively frequently will be made available via ftp (requests being submitted through the AMS web interface). (TBC)

8 Documentation

We compile here links and references of additional sources of information on **XMM**.

1. Other online **XMM** SOC services

   - **XMM** Latest News
     `http://astro.estec.esa.nl/XMM/news/news_top.html`
   - The **XMM** Science Simulator (SciSim)
     `http://astro.estec.esa.nl/XMM/scisim/scisim.html`
   - **XMM** Target Visibility Tool
     `http://astro.estec.esa.nl/XMM/user/vis/vis_top.html`
   - **XMM** Proposal Handling Subsystem (PHS; in preparation)
     `http://www.xmmsoc.ops.esa.int`
   - **XMM** Remote Proposal Submission software (XRPS; in preparation)
     `http://www.xmmsoc.ops.esa.int`
   - **XMM** Archive Management Subsystem (AMS; in preparation)
     `http://www.xmmsoc.ops.esa.int`
   - "Building **XMM**" – an online picture gallery
     `http://astro.estec.esa.nl/XMM/user/build/buildxmm_top.html`
   - PIMMS (HEASARC)
     `http://heasarc.gsfc.nasa.gov/Tools/w3pimms.html`

2. Online **XMM** documents

   - Call for Proposals (AO-1)
     `http://astro.estec.esa.nl/XMM/news/AO/ao1_top.html`
   - XRPS Users' Manual (in preparation)
   - SAS User Requirements Document
     `ftp://astro.estec.esa.nl/pub/XMM/documents/XMM-PS-GM-12_i1.0.ps.gz`
   - SAS Software Specification Document
     `ftp://astro.estec.esa.nl/pub/XMM/documents/sas_ssd_issue2.0.ps.gz`
   - **XMM** Data Files Handbook (in preparation)
   - Constraints on the OM Window Configuration and Definition of the OM Default Configurations
     `ftp://astro.estec.esa.nl/pub/XMM/documents/xmm_ps_tn_026.ps.gz`

3. **XMM** documents that are available as paper copies only

   - **XMM** Science Management Plan ESA/SPC(88)20

Additional information on **XMM** can always be obtained from other locations under the SOC home page, at `http://astro.estec.esa.nl/XMM/`.

A XMM Science Simulator (SciSim)

SciSim is the tool developed by the SOC for modeling **XMM** observations. It can be downloaded by **XMM** users for modeling sources and observation scenarios that are not described in this document. SciSim (v. 2.0 and higher) is capable of creating output files in the Observation Data File (ODF) format. For the conversion of the (default) "temp..." output files (described in the following) to ODFs, SciSim contains so-called ODF converters (see the SciSim online help, under "Users Guide", "Detailed Users Guide", "ODF converters" for details). ODFs can, once it is developed, be analysed using the SAS software (§ 6.1), making a direct comparison between models and observations possible. Until the SAS becomes available, the SciSim tools listed in Appendix A.4 can be used to convert SciSim output to other formats.

In order to make this document self-contained, we include here a general description of SciSim. Note that this is meant to be only a short introduction. The following is not a complete description of SciSim. **For the most up-to-date information the SciSim online help should be consulted.**

A.1 SciSim – a brief general introduction

SciSim is a collection of programmes that can model **XMM** observations. Rays can be generated using a random generator and injected into the **XMM** telescope optics. Although all **XMM** instruments normally operate simultaneously, each can be excluded from SciSim model runs for the sole purpose of cutting back on processing time.

The individual SciSim components model one part of **XMM** each. Starting with the cosmic simulator (CSim), including the ray generator, which produces the input radiation (Appendix A.3.1), the propagation of the incoming radiation through the different parts of **XMM** is modeled, first through the mirrors (Appendix A.3.2) and then either directly onto the EPIC pn camera or onto the RGAs (Appendix A.3.4) and then on to either the EPIC MOS cameras (Appendix A.3.3) in the prime focus or the RFCs in the secondaries of two out of three **XMM** telescopes (Appendix A.3.4). Two examples of SciSim runs are presented in Appendix A.5.

SciSim has been programmed to resemble **XMM** as closely as possible. However, it is not a complete tool, because some quantities like, e.g., the relative alignment of the different science instruments with respect to each other is not yet known. Missing items are listed in Appendix A.6. Since SciSim produces output files in the ODF format and the SAS (which is the software package to process such ODFs) is still under development, the SciSim to SAS interface is not yet fully developed. During this time, the SciSim tools presented in Appendix A.4 can be used to convert SciSim output to formats that can be read by other software packages.

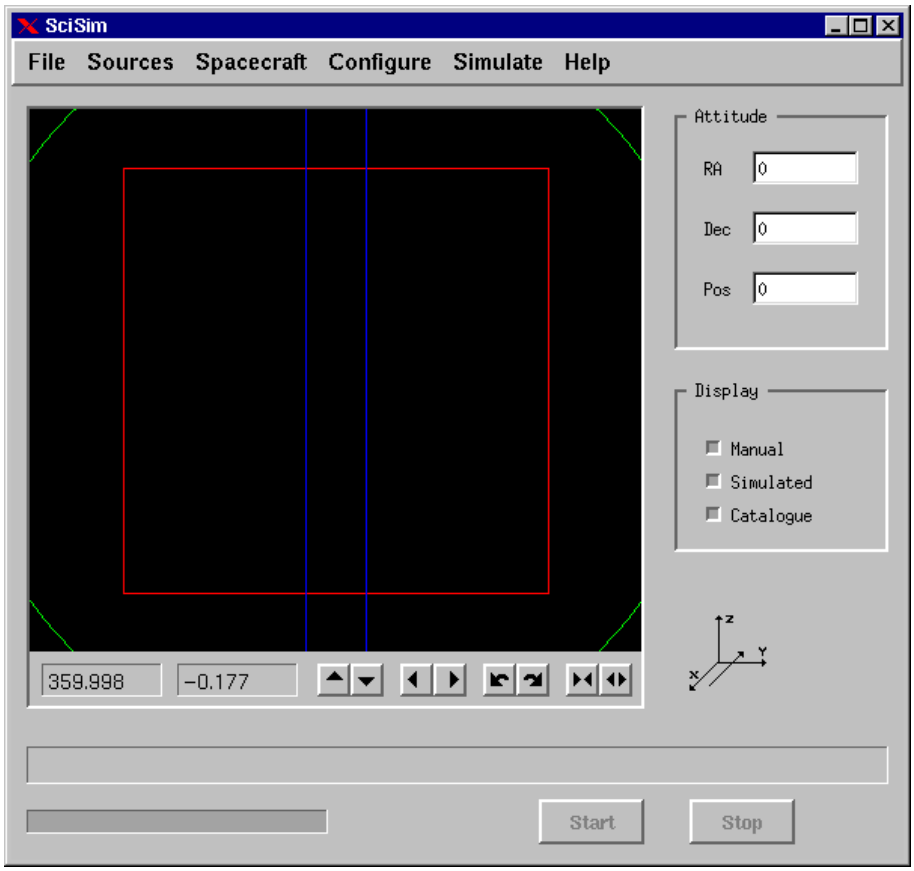

Figure 84: *The top-level GUI of the* **XMM** *Science Simulator (SciSim), presenting a field of view on the sky that will display any emitting sources that can be chosen from catalogues or defined by the user.*

A.2 SciSim Graphical User Interface

SciSim can be executed from both the command line and from a specially developed GUI. The top-level SciSim GUI is presented in Fig. 84. It offers several click-on buttons for choosing operations.

- "File"

  This offers various options to import or save source, configuration and default parameters.

- "Sources"

  Under this option the user manually edit model sources, simulate a random source distribution, import sources from catalogues and influence the properties of the modeled background.

- "Spacecraft"

Spacecraft effects will not need to be modeled by general **XMM** users. The options offered here are for instrument calibration purposes.

- "Configure"

  This spawns the instrument configuration GUI, which is used for configuring SciSim, see below.

- "Simulate"

  Start/stop a simulation.

- "Help"

  Information on the SciSim release version and the online help. Note that, in order to use the online help facility of SciSim, a viewer (Netscape or Internet Explorer) must be started on the same machine that runs SciSim.

A.2.1 SciSim configuration GUI

A particularly important GUI is the configuration GUI. This allows the user to choose which parts of **XMM** are to modeled, i.e., which sub-units of SciSim are to be executed. A screen capture of this GUI is provided in Fig. 85.

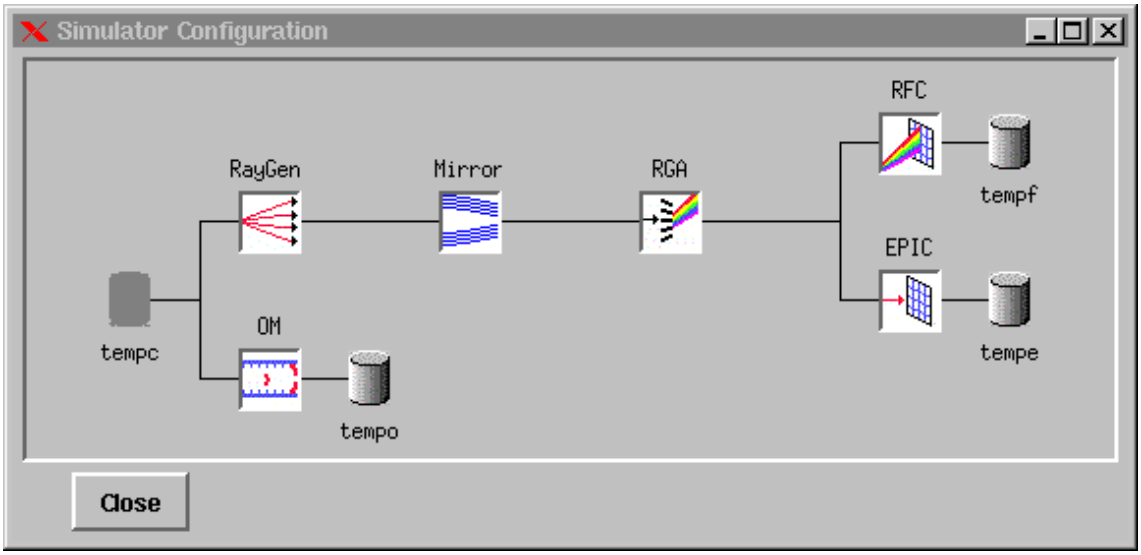

Figure 85: *The configuration GUI of SciSim, displaying which parts of* **XMM** *will be modeled. In the setup shown, all instruments will be modeled and the data will be stored in the files tempo (OM), tempe (EPIC) and tempf (RGS).*

Components of SciSim are switch on/off by clicking on an icon in the configuration GUI with the left mouse button. The name of the output data file for the chosen configuration will always be displayed.

By clicking on any of the icons in the configuration GUI with the right mouse button, a menu will pop up to configure that particular sub-unit of SciSim. These will be introduced briefly in the following.

A.3 SciSim components

SciSim consists of several parts, which simulate different entities. Each can be controlled via its own GUI. As an example, the GUI of the Ray Generator component of the Cosmic Simulator, CSim, is presented below.

The different simulators contained in SciSim are:

- CSim – Cosmic Simulator, including GSim – Ray Generator
- MSim – Mirror Simulator
- ESim – EPIC Simulator
- RSim – RGS Simulator

  RSim consists of the following subunits:

  - RGASim – Reflection Grating Array Simulator
  - RFCSim – RGS Focal Camera Simulator
- OSim – OM Simulator

A.3.1 CSim – The Cosmic Simulator

CSim is that part of SciSim creating a simulated piece of sky, with sources with user-specified properties. It includes a Ray Generator, called GSim. Csim can produce astronomical model data for subsequent processing by the other simulators within SciSim.

X-ray sources can be created interactively or by using source lists. The results from interactive sessions can be written into output files, which can later be reused as inputs to CSim.

The following source parameters can at present be defined in CSim:

- Spatial distribution
- Spectral distribution
- Optical Counterpart
- Field Coordinates

- Source Position Selection
- Source Database
- Artificial Stellar Distribution
- X-ray background
- Saving and loading the source list

All these parameters are described in more detail in the CSim online help.

A special part of CSim is the Ray Generator, GSim, which simulates the distribution of incoming photons from a given source (distribution). These rays are propagated later, by other parts of SciSim, through the telescope assemblies and into the detectors, thereby imaging the artificial view of the sky onto the detector plane.

A.3.1.1 The GSim GUI

The CSim GUI is displayed in Fig. 86. It allows users to specify the details of the simulation as listed above, by opening the different folders that are visible in the screen shot.

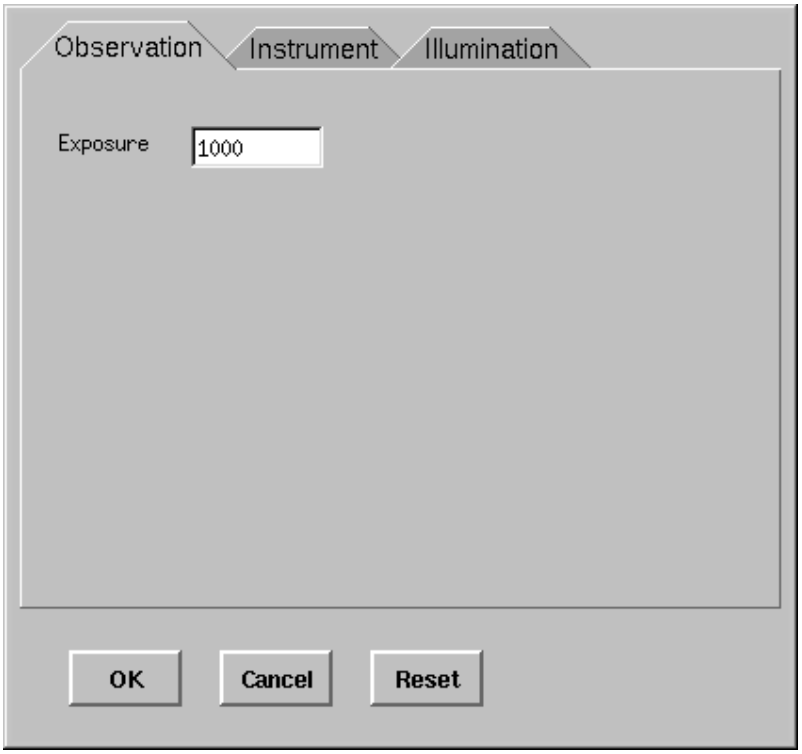

Figure 86: *The GUI of SciSim's Ray Generator.*

- Observation

  Here the integration time in seconds is entered.

- Instrument

  Here the user can enter the upper and lower boundary for the energy spectrum of the simulated radiation (these are not the energy thresholds for the bandpasses of the instruments!).

- Illumination

  This is the input field to vary the illumination over the FOV. These input parameters should not be changed for astronomical simulations.

The GUIs for the other components of SciSim are designed very similarly and therefore not shown here.

A.3.2 MSim – The Mirror Simulator

MSim simulates the X-ray response of **XMM**'s mirror modules. Therefore, it can also be called a "ray tracer". Not only the imaging characteristics of the mirrors, but also losses on the way from the entrance aperture to the detector surfaces are modeled.

Mirror models are approximated as closely as possible to measurements from the Panter facility, in which the hardware was tested. MSim is an important part of the **XMM** calibration activities, because it is the software module producing the empiric descriptions of such basic quantities as the mirror PSF and the effective area, A_e. These will be used for the highest accuracy instrument calibration instead of actual data arrays, because the multi-dimensional parameter space that would have to be represented by such calibration files is much too large for conventional calibration procedures. MSim, on the other hand, being a highly configurable software module, can take into account many free parameters.

The current version of MSim simulates the following features:

- Misalignment of all parts of the mirror module, including mirror shell tilt and decenter
- Misalignment of the entire module with respect to the satellite
- Photon and classical ray tracing
- Straylight rejection by the X-ray baffles
- Vignetting by the mirror entrance spider
- Figuring errors of the X-ray mirror shells
- Reflectivity and scattering by the mirror gold coating
- Vignetting by the exit magnetic deflector

A.3.3 ESim – The EPIC Simulator

ESim simulates the properties of both types of EPIC cameras, MOS and pn.

The two camera types are fundamentally different, the MOS chips, e.g., being front-illuminated, while the pn CCDs are back-illuminated. ESim models the interaction of X-ray photons with the CCDs and records the results in output files. These output files contain event lists, as they would also be obtained during real observations in orbit.

ESim, as the other instrument simulators, is capable of simulating all science data acquisition modes of the detectors. Other parts of ESim simulate event recognition patterns etc., including parts of the **XMM** onboard software.

ESim currently comprises routines to model the following features:

- Camera selection (MOS vs. pn)
- Exposure time
- Position of camera with respect to the mirrors
- Full image mode
- Window mode
- CCD selection
- Dead space in between CCDs
- Simple dead front and partially absorbing back layers (limiting the low energy X-ray detection efficiency)
- Photon shot noise at interaction within the CCD
- Si-K α fluorescence
- Diffusion/drift of generated electrons through various layers in a CCD
- Recombination losses
- Spreading of an event over several pixels
- Frame time analysis
- Grading (event recognition)
- Threshold selection
- Dark noise
- Electronic noise
- Background subtraction
- "Out of time" events received during CCD readout

A.3.4 RSim – The RGS Simulator

RSim consists of two major parts, RGASim and RFCSim. The former simulates the physical properties of the RGAs, the latter those of the RFCs.

RGASim represents the continuation of the ray tracing that is performed by MSim. Multiple reflections are allowed, so that every ray that enters RGASim either leaves the module or is absorbed. Those rays leaving the RGAs in the direction of the RFCs are picked up by RFCSim and projected on the 9 CCD surfaces.

The features currently contained in RGASim are:

- 3-D model of the grating array
- Grating positioning and alignment errors
- Exact geometry of the actual grating arrays
- Changing line density spacing of grooves as a function of the x coordinate
- Random errors in line density variation
- Grating efficiency model
- Multiple reflections in between grating plates
- A physical model for scattering by micro-roughness of the gratings
- Positioning of the whole RGA relative to other subsystems
- Gaps between the CCDs

Rays can be produced in individual spectral orders in order to speed up the calculations.

A.3.5 OSim – The OM Simulator

OSim is a partly independent simulator, because the OM has its own telescope. The commonality with the other subunits of SciSim is only in the relative alignment of the different telescopes with respect to each other on the spacecraft.

OSim contains the optical/UV ray tracer and it simulates the behaviour of the detector itself. The following features are currently supported:

- Imaging (coordinate transformation) by telescope
- Count rate calculation for each pixel

- Sky background
- Source spectra
- Gaussian PSF of optics
- Reflectivity of primary and secondary mirrors
- Reflectivity of selector (tertiary mirror)
- Transmission of various filters
- Magnification by magnifier
- Transmission of magnifier
- Transmission of detector window
- Photocathode quantum efficiency
- *FWHM* of detector
- Pixel sampling

Additional features are planned for the next release of OSim.

A.4 SciSim tools

Since the SAS is still under development, tools to perform a number of tasks are released together with SciSim:

- *reporter2fits*

  converts SciSim output into FITS format images

- *reporter2pha*

  converts SciSim output into PHA format (i.e., *xspec*-readable) spectra

- *image2sources*

  creates from an input image a decomposition into a list of sources that is then run through SciSim

- *cluster*

  interim routine to perform EPIC pn event reconstruction, which is not applied onboard.

A.5 Examples for the use of SciSim for proposal preparation

Here we present two examples of the use of SciSim in the preparation of an **XMM** observing proposal, one each for EPIC and RGS. Note that the SciSim online help also contains two tutorials for source simulations.

CAVEAT 1: When importing model spectra created in *xspec* into SciSim, these spectra **must** be created with an energy grid that is dense enough so as to be smaller than the energy resolution of the instruments (in particular RGS)! Otherwise, the input spectrum will already determine the "resolution" of the output "model". A 0.1 eV energy grid is sufficient to sample RGS spectra adequately. For EPIC simulations a spectral bin width of 10 eV should suffice. The energy grid should best be defined using the available response matrices. Alternatively, the grid can be defined in the *xspec* task *dummyrsp* as the increment parameter.

Until the **XMM** Data Archive will be populated with CCFs, preliminary response matrices can be retrieved from the XMM calibration area on the SOC web server.

A.5.1 Example for simulating EPIC observations

To produce the EPIC spectrum shown in Fig. 75 in § 3.7.1.2, a 6 keV Raymond-Smith thermal plasma model spectrum created with *xspec* was imported into SciSim. The energy resolution of the *xspec* input model was chosen to be 1 eV, i.e. higher than the energy resolution of EPIC. The adopted source flux is 10^{-12} erg s^{-1} cm^{-2} in the energy band from 0.5–4.5 keV. To import the spectrum from the SciSim GUI, users must choose option "Sources" in the top menu, then "new" in the source editor, then click on "Spectrum" and choose the option "*xspec*" from the menu. This will prompt the user for the input file name (FILENAME.DAT) from the current directory. The absorbing column density can also be provided in the source editor of SciSim (in units of 10^{24} atoms cm^{-2}; thus, no absorbing column density needs to be modeled in *xspec*.

Under the top-level GUI option "Configure", which spawns the configuration GUI, the "RayGen", "Mirror", "RGA" and "EPIC" modules are switched on by clicking on the icons with the left mouse button. Clicking on the RayGen icon with the right mouse button, the integration time was in the current example set to 30000 [s]. Clicking on the mirror module icon (with the right mouse button), one can choose between different mirror modules. The same procedure can be followed to choose a particular EPIC camera by clicking on the EPIC icon. For a "standard" model simulation neither any spacecraft effects nor other options regarding the mirrors and instruments need to be specified. Most of the options offered there are included for instrument calibration purposes. Spacecraft effects are included based on the current best guess of the expected pointing performance.

Once all inputs are specified, the simulation is started by clicking on the "start" button

at the bottom of the GUI (or "Simulate" "Start" in the top menu). While the simulation is running, a performance bar will inform the user of its progress.

Upon successful completion the results of the model run are contained in a file named, by default, "tempe" (the filename can be changed from the GUI), which is created in the current directory (i.e., the one from which SciSim has been started). To convert the data into a form readable by existing software, tools are provided (*reporter2pha* and *reporter2fits*) to produce a PHA format output spectrum. This spectrum can then be transfered into *xspec* for analysis or for display.

Extended sources can be modeled either by using an input image and using the tool *image2sources* described above or by using the top-level GUI menu option "Sources", choosing option "Edit" and then specifying in the folder "Shape" an ellipsoidal (either uniformly or non-uniformly emitting) shape (only options available), instead of the default ("point").

Note: Default configuration files, which have been derived from the best information available before the current release of SciSim, were used exclusively for the plots in this document. Users should be aware that a number of simple changes to the configuration files might be used either to aid some simple scenario modeling, or to investigate more practical problems of science analyses. The scope of data items that might be modifiable seems at first daunting, but we note a few here that are easily changed:

- The charge transfer efficiency (CTE) should be set to 1.0 if spatially variable spectra are to be analysed, as there is no representation yet of the SAS tools which correct for spatially varying gain. On the other hand, if the observer wants to investigate likely errors involved due to such CTE changes and the minor effect on the energy resolution the data values need not be modified
- The dead spaces between EPIC CCDs have been set to representative values in order to demonstrate the cosmetic effect on focal plane coverage. Users requiring to utilise 100% field coverage in order to estimate diffuse fluxes could run simulations with dead space modified to 0.0.
- The simulation assumes perfect set-up of offset tables within the camera, so that there is no gain and offset error predicted for optically bright targets. If users should wish to simulate the effect of a "thin" or "open" filter position with some light leakage loading, then this is best obtained by modifying the value of system noise. For example, based on the suggestions of maximum visible brightness usable per filter, one can estimate the additional light loading by the following method: For the thin filter, where $m_V = 17$ is a typical limiting magnitude (for 1 electron per pixel), the observation of an $m_V = 12$ target would produce a peak signal of about 100 electrons per pixel per full frame in MOS (16 in pn). Therefore, the additional shot noise is 10 (4) electrons rms. This should be added in quadrature to the existing noise and consequently the

noise field in the configuration file should be amended to 11 (6) electrons, and the resulting effect on resolution noted. Unfortunately, this does not correctly simulate the energy offset, nor the spatial variation of optical loading.

A.5.2 Example for an RGS simulation

As mentioned above, it is recommended to use the default RGS configuration in SciSim, which is FM2, until geometrical configuration files for other combinations have been added to SciSim.

To produce the RGS spectrum shown in Fig. 47 in § 3.4.2, a two-component Raymond-Smith thermal plasma model spectrum was created with *xspec* and imported into SciSim. The model consists of a 0.35 keV and a 2.0 keV component of equal flux. The adopted source intensity is 2.1×10^{-2} photons s^{-1} cm^{-2} in the RGS band (0.35–2.5 keV). The resolution of the *xspec*-created input model was chosen to be 0.1 eV, i.e., higher than the RGS's energy resolution. Importing the spectrum from the SciSim GUI works as described above in the example for an EPIC simulation.

Under the top-level GUI option "Configure", which spawns the configuration GUI, the "RayGen", "Mirror", "RGA" and "RFC" modules were switched on by clicking on the icons with the left mouse button. Clicking on the RayGen icon with the right mouse button, the integration time was set to 40000 [s]. Clicking on the mirror module icon (with the right mouse button), one can choose between different mirror modules. The same procedure can be followed to choose a particular RGA and RFC by clicking on the respective icon. Again, as for EPIC simulations, for a "standard" model simulation neither any spacecraft effects nor other options regarding the mirrors and instruments need to be specified. Most of the options offered there are included for instrument calibration purposes. Spacecraft effects are included based on the current best guess of the expected pointing performance.

Once all inputs are specified, the simulation is started by clicking on the "start" button at the bottom of the GUI (or "Simulate" "Start" in the top menu). While the simulation is running, a performance bar will inform the user of its progress.

Upon successful completion the results of the model run are contained in a file named "tempf", which is created on the current directory (i.e., the one from which SciSim has been started). To convert the data into a form readable by existing software, tools are provided (*reporter2pha* and *reporter2fits*) to produce a PHA format output spectrum. This spectrum can then be transfered into *xspec* for analysis or for display.

CAVEAT: When modeling RGS observations with SciSim, the default instrument configuration should be used, which is "FM2". FM2 (Flight Model 2) represents RGA-2, which is part of RGS-1. For this configuration the geometrical configuration is implemented correctly in SciSim. Using FM1 instead, users would need to obtain and manually insert the

geometrical configuration, because the geometrical alignment of both RGA-1 with respect to its mirror module and RFC-1 with respect to RGA-1 differs from those of FM2.

A.6 SciSim performance issues

Several features of **XMM** are currently not included in SciSim. The most important are:

1. General
   - CAVEAT: Only limited validation of SciSim was performed using ground calibration data!
   - SciSim run times for large numbers of rays or complicated input scenarios (as e.g., an input spectrum produced with *xspec*) can be very long (up to orders of hours).
   - SciSim contains no information on the (expected) relative instrument alignment. This leads to shortcomings in some simulations as, for example, seam losses in between EPIC and RGS CCDs of one detector which will in practice be covered by the other unit.
   - The CCD frame times for all instruments are not adjustable (from the GUI). They can only be influenced by choosing a certain instrument mode.
   - For those who are interested in calibration issues, it might be important to know that at present the instrument temperatures cannot be chosen.
   - Input of a sky image (emission distribution) is via a tool, which is at present still rudimentary and causes extremely long run times of the simulations.
   - The pointing direction of the model run is not propagated to the output ODF.
2. EPIC
   - SciSim does not account for pn columns that might be discarded because of the hit of a minimum ionising particle (MIP; i.e., a cosmic particle).
   - There is no SciSim routine to handle optical/UV loading of the EPIC cameras and, accordingly, also none to perform EPIC MOS offset calculation to correct for this effect.
   - There is no EPIC pn event reconstruction in SciSim, because this is an offline functionality performed by the SAS. Thus, the SciSim tool "cluster" should be used at interim (see § A.4).
3. RGS
   - The scattering model that is used has not yet been optimised for the high energy end of the bandpass, which causes an overestimation of the

amount of scattered light. The instrument's performance with respect to scattering wings at these energies is slightly better than predicted by SciSim.

- See above, regarding seam losses between CCDs. This is visible in Fig. 54.

4. OM

- OSim cannot simulate OM grism observations.
- OSim does not allow the modeling OM fast mode observations.
- There is no OM window selection option.
- OM detector distortion is not taken into account.
- OM detector response non-linearity is not included.

B XMM Survey Science Centre (SSC)

XMM Survey Scientist: Dr. M. G. Watson, Leicester University

The **XMM** Survey Science Centre (SSC) is an international collaboration involving a consortium of 8 institutions in the UK, France and Germany together with associate scientists in Spain, Italy, Belgium, Japan, USA and the UK. The major roles of the SSC in the **XMM** project are:

- The coordination of the XMM serendipitous survey via a ground-based follow-up/identification programme;
- the development, with the **XMM** SOC, of the **XMM** science analysis software (SAS);
- the routine pipeline processing of all **XMM** observations.

These activities are briefly summarised here with greater emphasis on the follow-up programme as this is not described elsewhere in any detail. The SSC follow-up programme will also be of interest as potential **XMM** observers are requested to consider agreeing to the serendipitous content of their **XMM** observations being used in the context of this programme.

Further information on the **XMM** SSC and its role in the project is available from the SSC web server at the URL `http://xmmssc-www.star.le.ac.uk/`.

B.1 SSC Follow-up Programme

Because of its large throughput and good angular resolution, pointed observations with the **XMM** EPIC X-ray cameras will reach very faint X-ray flux limits ($\approx$ a few $\times 10^{-15}$ erg cm^{-2} s^{-1}, 0.1–10 keV, in typical observations). At these fluxes, each **XMM** EPIC field at both high and low galactic latitudes will contain substantial numbers of "serendipitous" X-ray sources. Pointed **XMM** observations will thus provide a "serendipitous" X-ray survey (the "XMM Serendipitous Sky Survey", see Watson, 1998, Astr. Nach., 319, 117).

The role of the SSC in this area is to coordinate the follow-up of the serendipitous content of **XMM** observations in order to ensure that this valuable resource can be exploited effectively by the community. The key initial step will be the "identification" of the X-ray sources, i.e., classification into different object types. Literally identifying every **XMM** serendipitous source is not a realistic task, nor a sensible approach. Instead, the emphasis of the SSC programme will be on the characterisation of the **XMM** source population through the detailed follow-up of well-defined, small subsamples (as outlined below). The

SSC "follow-up" programme aims to bring together the **XMM** data themselves, existing catalogue and archival material and new ground-based observational data in an integrated fashion.

The overall programme strategy as currently conceived involves two main components:

The SSC "Core Programme" consisting of complete identifications of selected high galactic latitude X-ray samples based primarily on optical imaging and spectroscopy. The results from this programme will be used to "characterize" the content of the **XMM** serendipitous survey. The Core Programme will also include a parallel study for the low galactic latitude sky.

The SSC "Imaging Programme" which aims to obtain optical photometry and colours for a substantial fraction of all **XMM** fields. The rationale is based on the fact that a combination of X-ray flux and X-ray colours (from the **XMM** data) and optical magnitude and optical colours (e.g., from new ground-based observations) will provide the key parameters which make possible an accurate 'probabilistic' identification of the **XMM** sources. This will be possible using the results from the Core Programme which characterise the **XMM** source populations, thus providing the link, in a statistical sense, between the source identification and properties and these basic parameters.

Data from the **XMM** OM, depending on instrumental mode chosen by the observer, can also provide relatively deep optical and UV imaging over most of the EPIC field. The OM sensitivity will not, however, be sufficient to meet all of the Imaging Programme needs, in particular because of the lack of R & I band coverage. The OM UV data will however represent a unique resource.

The entire programme will be based on samples of serendipitous X-ray sources drawn from pointed **XMM** observations that are in the public domain, or are made available to the SSC by the observation PI. The programme is designed to support the community's access to, and exploitation of, the serendipitous data from **XMM**, and as such all the results will be made public through the **XMM** science archive.

B.2 Science analysis software development

In collaboration with the SOC, the SSC is making a major contribution to the development of the **XMM** Science Analysis Subsystem (SAS). The SAS provides **XMM**-specific software tools for all **XMM** science data. It allows the processing of the Observation Data Files (ODF s) sent to the observer through to high-level science products, but does not, in general, aim to provide the high-level analysis tools (e.g., spectral fitting) themselves.

B.3 Pipeline processing of XMM science data

The SSC is responsible for the task of processing all **XMM** observations to produce data products for all science instruments (e.g., source lists, images, spectral and time series data). These products, together with the ODF s, will be distributed by the SOC to observers, and after SOC validation, they will also be incorporated into the **XMM** data archive maintained by the SOC.

C XMM calibration and performance verification program

XMM will be observing a number of astronomical objects in the course of its calibration (Cal) and Performance Verification (PV) programmes.

C.1 XMM calibration program

We list the **XMM** calibration targets in Tab. 21. **XMM** calibration observations enter the public data archive as soon as they are processed and the calibration analysis is completed.

Table 21: **XMM** *calibration target list*

Target Name	$\alpha(2000)$	$\delta(2000)$	**Prime Instrument and Mode**	**Exp. time [ks] (total)**	**Purpose**
Abell 2690	00 00 21	-25 08 17	OM IMAGE	25.0	optical photometry
G158-100	00 33 54	-12 07 57	OM IMAGE	11.0	throughput (optical grism)
EG And	00 44 37	40 40 46	OM IMAGE	15.0	wavelength scale & grism PSF
EG And ^{off1}	00 44 40	40 42 40	OM IMAGE	10.0	wavelength scale
EG And ^{off2}	00 44 28	40 41 37	OM IMAGE	10.0	wavelength scale
EG And ^{off3}	00 44 23	40 46 13	OM IMAGE	10.0	wavelength scale
BPM16274	00 50 03	-52 08 40	OM IMG/FAST	22.0	UV photometry/PSF
BPM16274 ^{off1}	00 50 11	-52 04 50	OM IMG/FAST	8.0	UV photometry/PSF
BPM16274 ^{off2}	00 49 40	-52 07 02	OM IMG/FAST	8.0	UV photometry/PSF
BPM16274 ^{off3}	00 49 56	-52 12 30	OM IMG/FAST	8.0	UV photometry/PSF
BPM16274 ^{off4}	00 50 27	-52 10 17	OM IMG/FAST	8.0	UV photometry/PSF
1ES0102-72	01 04 02	-72 01 55	EPIC Pri Full	20.0	Gain/CTE
PG0136+251	01 38 53	25 23 20	EPIC Pri Full	25.0	Contamin reference
NGC 752	01 57 48	37 52 00	EPIC Pri Full	40.0	EPIC/OM alignment monitoring
3C58	02 05 38	64 49 26	EPIC Pri Full	50.0	Effective area
PKS0312-770	03 11 55	-76 51 51	EPIC Pri Full	20.0	MOS PSF and AXAF cross-check
PKS0312-770 ^{off1}	03 11 55	-76 51 51	EPIC Pri Full	15.0	MOS PSF $5' + X$
PKS0312-770 ^{off2}	03 11 55	-76 51 51	EPIC Pri Full	15.0	MOS PSF $5' - X$
PKS0312-770 ^{off3}	03 11 55	-76 51 51	EPIC Pri Full	15.0	MOS PSF $5' + Y$
PKS0312-770 ^{off4}	03 11 55	-76 51 51	EPIC Pri Full	15.0	MOS PSF $5' - Y$
PKS0312-770 ^{off5}	03 11 55	-76 51 51	EPIC Pri Full	15.0	MOS PSF $5'$ $Az = 45\,\mathrm{deg}$
PKS0312-770 ^{off6}	03 11 55	-76 51 51	EPIC Pri Full	30.0	MOS PSF $12' + X$
PKS0312-770 ^{off7}	03 11 55	-76 51 51	EPIC Pri Full	30.0	MOS PSF $12' - X$
PKS0312-770 ^{off8}	03 11 55	-76 51 51	EPIC Pri Full	30.0	MOS PSF $12' + Y$
PKS0312-770 ^{off9}	03 11 55	-76 51 51	EPIC Pri Full	30.0	MOS PSF $12' - Y$
PKS0312-770 ^{off10}	03 11 55	-76 51 51	EPIC Pri Full	30.0	MOS PSF $12'$ $Az = 45\,\mathrm{deg}$
MS0317.0+1834	03 19 52	18 45 35	EPIC Pri Full	70.0	Mirror Au edge and contam. monitor
ϵ Eri	03 32 59	-09 27 31	EPIC Transp	10.0	Stray light
HR1099	03 36 47	00 35 24	RGS, Spectr.	40.0	wavelength scale & bore-sight
HR1099 ^{off1}	03 36 47	00 35 24	RGS, Spectr.	40.0	bore-sight, off-axis dispers. $+3'$
HR1099 ^{off2}	03 36 47	00 35 24	RGS, Spectr.	40.0	bore-sight, off-axis dispers. $-3'$

HR1099 *off3*	03 36 47	00 35 24	RGS, Spectr.	40.0	bore-sight, off-axis dispers. $+7'$
HR1099 *off4*	03 36 47	00 35 24	RGS, Spectr.	40.0	bore-sight, off-axis dispers. $-7'$
HR1099 *off5*	03 36 47	00 35 24	RGS, Spectr.	40.0	bore-sight, off-axis X-dispers. $+1.5'$
HR1099 *off6*	03 36 47	00 35 24	RGS, Spectr.	40.0	bore-sight, off-axis X-dispers. $-1.5'$
SA95-42	03 53 43	-00 04 35	OM IMAGE	9.0	throughput (optical grism)
HZ 4	03 55 22	09 47 19	OM IMG/FAST	22.0	UV photometry/PSF
Abell 3195	03 59 11	-35 10 32	OM IMAGE	20.0	optical photometry
LB227	04 09 29	17 07 54	OM IMG/FAST	22.0	UV photometry/PSF
LB227 *off1*	04 09 23	17 04 04	OM IMG/FAST	8.0	UV photometry/PSF
LB227 *off2*	04 09 44	17 06 13	OM IMG/FAST	8.0	UV photometry/PSF
LB227 *off3*	04 09 36	17 11 43	OM IMG/FAST	8.0	UV photometry/PSF
LB227 *off4*	04 09 13	17 09 37	OM IMG/FAST	8.0	UV photometry/PSF
LB227 *off5*	04 09 08	17 05 44	OM IMG/FAST	8.0	UV photometry/PSF
MS 0419.3+1943	04 22 18	19 50 53	EPIC Pri Full	70.0	Mirror Au edge and contam. monitor
Hyades	04 32 00	18 10 00	EPIC Pri Full	60.0	Boresight & trend analysis
A496 *off1*	04 33 35	-13 14 46	EPIC Pri Full	30.0	Vignetting $5' + X$
A496 *off2*	04 33 35	-13 14 46	EPIC Pri Full	30.0	Vignetting $12' + X$
A496 *off3*	04 33 35	-13 14 46	EPIC Pri Full	30.0	Vignetting $5' - X$
A496 *off4*	04 33 35	-13 14 46	EPIC Pri Full	30.0	Vignetting $12' - X$
A496 *off5*	04 33 35	-13 14 46	EPIC Pri Full	30.0	Vignetting $5' + Y$
A496 *off6*	04 33 35	-13 14 46	EPIC Pri Full	30.0	Vignetting $12' + Y$
A496 *off7*	04 33 35	-13 14 46	EPIC Pri Full	30.0	Vignetting $5' - Y$
A496 *off8*	04 33 35	-13 14 46	EPIC Pri Full	30.0	Vignetting $12' - Y$
YY Men	04 58 18	-75 16 36	RGS, Spectr.	50.0	wavelength
Capella	05 16 41	46 00 14	RGS, Spectr.	100.0	wavelength
LMC X-2	05 20 29	-71 57 36	EPIC Pri Full	70.0	Straylight artefacts
N132D	05 25 00	-69 38 24	EPIC Pri Full	20.0	Gain and CTE monitoring
AB Dor	05 28 44	-65 27 02	RGS, Spectr.	50.0	wavelength scale
LMC X-3	05 38 56	-64 05 02	EPIC Small Win	30.0	PN PSF
LMC cal field	05 40 00	-69 30 00	EPIC Large WIn	50.0	EPIC PSF vs. field angle
PSR0540-69	05 40 11	-69 19 58	RGS, Spectr.	100.0	eff. area
PSR0540-69 *off1*	05 40 11	-69 19 58	RGS, Spectr.	50.0	eff. area, off-ax. dispers. $+7'$
PSR0540-69 *off2*	05 40 11	-69 19 58	RGS, Spectr.	50.0	eff. area, off-ax. dispers. $-7'$
PSR0540-69 *off3*	05 40 11	-69 19 58	RGS, Spectr.	50.0	eff. area, off-ax. dispers. $+14'$
PSR0540-69 *off4*	05 40 11	-69 19 58	RGS, Spectr.	50.0	eff. area, off-ax. dispers. $-14'$
PSR0540-69 *off5*	05 40 11	-69 19 58	RGS, Spectr.	50.0	eff. area, off-ax. X-dispers. $+1'$
PSR0540-69 *off6*	05 40 11	-69 19 58	RGS, Spectr.	50.0	eff. area, off-ax. X-dispers. $-1'$
PSR0540-69 *off7*	05 40 11	-69 19 58	RGS, Spectr.	50.0	eff. area, off-ax. X-dispers. $+2'$
PSR0540-69 *off8*	05 40 11	-69 19 58	RGS, Spectr.	50.0	eff. area, off-ax. X-dispers. $-2'$
PSR0540-69	05 40 11	-69 19 58	RGS, HTR EPIC Fast/Timing	20.0	timing
Cal 83	05 43 33	-68 22 23	EPIC Pri Full	80.0	Filter bandpass, contamination
Cal 87	05 46 45	-71 08 54	EPIC Pri Full	80.0	Filter bandpass, contamination
GD 71	05 52 28	15 53 16	OM IMG	14.0	throughput/PSF (UV grism)

GD 71 ^{off1}	05 52 25	15 51 22	OM IMG	14.0	throughput/PSF (UV grism)
GD 71 ^{off2}	05 52 35	15 52 25	OM IMG	14.0	throughput/PSF (UV grism)
GD 71 ^{off3}	05 52 30	15 55 12	OM IMG	14.0	throughput/PSF (UV grism)
GD 71 ^{off4}	05 52 20	15 54 09	OM IMG	10.0	throughput/PSF (UV grism)
GD 71 ^{off5}	05 52 07	15 51 08	OM IMG	10.0	throughput/PSF (UV grism)
PKS 0558-504	05 59 47	-50 26 51	EPIC Multi modes	80.0	Mode and Pile-up dependence
S5 0716+71	07 21 53	71 20 36	EPIC Pri Full	70.0	Mirror Au edge and contam. monitoring
MS 0737.9+7441	07 43 59	74 33 50	EPIC Pri Full	70.0	Mirror Au edge and contam. monitoring
EXO0748-67	07 48 25	-67 45 00	EPIC Pri Full	70.0	Stray light artefacts
NGC2516	07 58 20	-60 52 13	EPIC Pri Full	35.0	Primary Boresight
MS 0922.9+7459	09 28 06	74 46 34	EPIC Pri Full	70.0	Mirror Au edge and contam. monitoring
A1060	10 36 54	-27 30 59	EPIC Pri Full	30.0	Vignetting
A1060 ^{off1}	10 36 54	-27 30 59	EPIC Pri Full	30.0	Vignetting $5' + X$
A1060 ^{off2}	10 36 54	-27 30 59	EPIC Pri Full	30.0	Vignetting $12' + X$
A1060 ^{off3}	10 36 54	-27 30 59	EPIC Pri Full	30.0	Vignetting $5' - X$
A1060 ^{off4}	10 36 54	-27 30 59	EPIC Pri Full	30.0	Vignetting $12' - X$
A1060 ^{off5}	10 36 54	-27 30 59	EPIC Pri Full	30.0	Vignetting $5' + Y$
A1060 ^{off6}	10 36 54	-27 30 59	EPIC Pri Full	30.0	Vignetting $12' + Y$
A1060 ^{off7}	10 36 54	-27 30 59	EPIC Pri Full	30.0	Vignetting $5' - Y$
A1060 ^{off8}	10 36 54	-27 30 59	EPIC Pri Full	30.0	Vignetting $12' - Y$
Θ Car	10 42 57	-64 23 38	EPIC Pri Full	40.0	RGS/EPIC alignment monitor
Mkn 421	11 04 27	38 12 32	RGS, Spectr.	50.0	eff. area
Hz 21	12 13 56	32 56 31	OM IMG/FAST	22.0	UV photometry/PSF
Mkn 205	12 21 44	75 18 37	EPIC Multi modes	80.0	Mode and Pile-up dependence
3C273	12 29 07	02 03 09	RGS, Spectr.	100.0	eff. area
β Crucis	12 47 43	-59 41 19	EPIC Transp	15.0	Filter transm. & straylight
Coma	12 58 58	28 07 34	EPIC Pri Full	40.0	Flat field
Coma ^{offset1}	13 00 40	27 45 07	EPIC Pri Full	40.0	"
GD 153	12 57 02	22 01 56	OM IMAGE	18.0	throughput/PSF (UV grism)
GD 153 ^{off1}	12 57 05	22 03 54	OM IMAGE	13.0	throughput (UV grism)
GD 153 ^{off2}	12 56 54	22 02 51	OM IMAGE	13.0	throughput (UV grism)
GD 153 ^{off3}	12 57 00	22 00 05	OM IMAGE	13.0	throughput (UV grism)
GD 153 ^{off4}	12 57 10	22 01 09	OM IMAGE	13.0	throughput (UV grism)
GD 153 ^{off5}	12 57 24	22 04 05	OM IMAGE	13.0	throughput (UV grism)
HZ 43	13 16 22	29 06 00	EPIC Sm Win	50.0	PSF & filter transmission
β Cen	14 03 49	-60 22 22	EPIC Transp	15.0	Stray light
α Cen	14 39 37	-60 50 02	EPIC Transp	50.0	Stray light
Sco X-1	16 19 55	-15 38 24	RGS, Spectr. single CCD	20.0	CTE, geometry
G138-31	16 27 54	09 12 35	OM IMAGE	16.0	throughput/PSF (optical grism)
G138-31 ^{off1}	16 27 51	09 10 40	OM IMAGE	11.0	throughput (optical grism)
G138-31 ^{off2}	16 28 01	09 11 43	OM IMAGE	11.0	throughput (optical grism)
G138-31 ^{off3}	16 27 56	09 14 30	OM IMAGE	11.0	throughput (optical grism)
G138-31 ^{off4}	16 27 46	09 13 26	OM IMAGE	11.0	throughput (optical grism)
G138-31 ^{off5}	16 27 36	09 10 20	OM IMAGE	11.0	throughput (optical grism)

PG 1634+706	16 34 29	70 31 40	EPIC Multi-modes	100.0	Mode and Pile-up dependence
PG1658+441	16 59 49	44 01 05	EPIC Pri Full	25.0	Contamin. reference
Her1720+50	17 20 57	49 48 07	OM IMAGE	20.0	optical photometry
Her1720+50 ^{off1}	17 20 54	49 46 12	OM IMAGE	15.0	optical photometry
Her1720+50 ^{off2}	17 21 09	49 47 16	OM IMAGE	15.0	optical photometry
Her1720+50 ^{off3}	17 21 01	49 50 02	OM IMAGE	15.0	optical photometry
Her1720+50 ^{off4}	17 20 46	49 48 59	OM IMAGE	15.0	optical photometry
Terzan 2	17 27 33	-30 48 08	EPIC Pri Full	30.0	High energy effective area
RT SER	17 39 52	-11 56 40	OM IMAGE	12.0	wavelength scale/PSF
RT SER ^{off1}	17 39 49	-11 58 35	OM IMAGE	9.0	wavelength scale
RT SER ^{off2}	17 39 59	-11 57 32	OM IMAGE	9.0	wavelength scale
RT SER ^{off3}	17 39 54	-11 54 44	OM IMAGE	9.0	wavelength scale
RT SER ^{off4}	17 39 44	-11 55 48	OM IMAGE	9.0	wavelength scale
RT SER ^{off5}	17 39 31	-11 58 53	OM IMAGE	9.0	wavelength scale
NGC 6475	17 53 54	-34 49 00	EPIC Pri Full	40.0	OM/EPIC alignment monitoring
V2416 SGR	17 57 16	-21 41 29	OM IMAGE	9.0	wavelength scale
GX 13+1	18 14 31	-17 09 26	RGS, Spectr.	40.0	eff. area
G 21.5 - 09	18 33 33	-10 34 07	EPIC Pri Full	50.0	RGS (Spectr.): eff. area
NGC 6712	18 53 04	-08 42 21	OM IMAGE	20.0	optical photometry
RXJ1856-3754	18 56 35	-37 54 40	EPIC Pri Full	50.0	Contamin. reference
LDS 749B	21 32 16	00 15 14	OM IMG/FST	22.0	UV photometry/PSF
Ar Lac	22 08 41	45 44 28	EPIC Lg Window	50.0	Back-up PSF
LTT 9491	23 19 34	-17 05 28	OM IMAGE	14.0	throughput/PSF (optical grism)
LTT 9491 ^{off1}	23 19 37	-17 03 35	OM IMAGE	9.0	throughput (optical grism)
LTT 9491 ^{off2}	23 19 27	-17 04 37	OM IMAGE	9.0	throughput (optical grism)
LTT 9491 ^{off3}	23 19 32	-17 07 23	OM IMAGE	9.0	throughput (optical grism)
LTT 9491 ^{off4}	23 19 41	-17 06 19	OM IMAGE	9.0	throughput (optical grism)
LTT 9491 ^{off5}	23 19 55	-17 03 26	OM IMAGE	9.0	throughput (optical grism)
λ And	23 37 33	46 27 51	RGS, Spectr.	50.0	wavelength

C.2 List of XMM PV targets

To demonstrate the observing potential of **XMM**, a performance verification (PV) programme is executed in an early stage of the mission. Tab. 22 contains the list of **XMM** PV targets. Depending on the launch date of the satellite, individual targets from this list may or may not actually be observed. This will be decided at a later stage. The current list only gives an overview of which objects are likely to be observed in the course of the PV phase. Proposers intending to observe an **XMM** PV target will have to await the execution of the PV programme first to see if the PV data satisfy the science requirements of the intended observations.

Table 22: **XMM** *performance verification target list*

Target Name	α(2000)	δ(2000)	**Prime Instrument and Mode**	**Exposure time [ks]**	**Goal**
Tycho	00 25 22	64 08 24	EPIC	40.0	Imaging of an Extended Source
Tycho offset1	00 25 22	65 18 24	EPIC	30.0	X-ray Baffle Leak
Tycho offset2	00 25 22	62 58 24	EPIC	30.0	X-ray Baffle Leak
Tycho offset3	00 35 30	64 08 24	EPIC	30.0	X-ray Baffle Leak
Tycho offset4	00 15 10	64 08 24	EPIC	30.0	X-ray Baffle Leak
M31	00 42 43	41 16 12	EPIC	50.0	Sources in diffuse emission.
NGC 253	00 47 34	-25 17 24	EPIC	60.0	Sources in diffuse emission
WW Hor	02 36 12	-52 19 12	OM	20.0	Optical timing
UZ For	03 35 29	-25 44 23	OM	20.0	Optical Timing
Capella	05 16 41	46 00 14	RGS	20.0	RGS Spectral capability
N132D	05 25 00	-69 38 24	RGS	40.0	RGS capability extended source
AB Dor	05 28 45	-65 27 02	RGS	100.0	Phase resolved spectroscopy
IC 443 #1	06 17 45	22 45 00	EPIC	30.0	Image irregular morphology
IC 443 #2	06 16 15	22 42 00	EPIC	30.0	”
IC 443 #3	06 17 35	22 20 00	EPIC	30.0	”
IC 443 #4	06 16 00	22 20 00	EPIC	30.0	”
RXJ 0720.4-3125	07 20 24	-31 25 12	RGS	50.0	Phase resolved spectroscopy
YY Gem	07 34 38	31 52 15	RGS	100.0	Phase resolved spectroscopy
Procyon	07 39 20	05 14 21	RGS	100.0	RGS Spectral capability
Zeta Pup	08 03 35	-40 00 12	RGS	50.0	Velocity/bulk motion diagnosis
OY Car	10 06 23	-70 14 06	OM	50.0	Optical grism & timing
Lockman Hole	10 52 43	57 28 48	EPIC	150.0	Sensitivity and confusion limits
DP Leo	11 17 16	17 57 37	OM	20.0	Optical timing
Mkn 766	12 18 26	29 48 46	RGS	30.0	Complex spectra
Virgo M87	12 30 50	12 23 24	EPIC	50.0	Spatially resolved spectroscopy
Coma Cluster #1	13 02 22	28 30 00	EPIC	40.0	Mosaicing fields
Coma Cluster #2	13 01 31	28 18 47	EPIC	40.0	”
Coma Cluster #3	13 00 40	28 07 34	EPIC	40.0	”
Coma Cluster #4	12 59 49	27 56 29	EPIC	40.0	”
Coma Cluster #5	12 58 58	27 45 07	EPIC	40.0	”
Coma Cluster #6	12 58 07	27 33 54	EPIC	40.0	”
Coma Cluster #7	12 57 16	27 23 41	EPIC	40.0	”

Coma Cluster #8	12 56 25	27 11 28	EPIC	40.0	”
IRAS13349+2438	13 37 19	24 23 03	RGS	80.0	Complex spectra
A1795	13 48 53	26 35 32	RGS	70.0	Spatially resolved spectra
A1835	14 01 02	02 52 41	RGS	50.0	Extended source RGS spectra
4U1624-49	16 28 04	-49 12 03	RGS	80.0	Absorption spectra
HER X-1	16 57 50	35 20 33	EPIC	10.0	Phase resolved spectroscopy
PSR 1821-24	18 24 32	-24 52 11	EPIC	50.0	Fast timing
SS 433	19 11 49	04 58 58	RGS	20.0	Bulk motions
MRK 509	20 44 10	-10 43 24	EPIC	70.0	Spectroscopy of Fe-K complex
CAS A	23 23 12	58 48 36	RGS	40.0	Spatially resolved spectra

D XMM Guaranteed Time Program

XMM will be observing a number of astronomical objects in the course of its Guaranteed Time Observation (GTO) program. Because GTO targets are protected by proprietary data rights, these sources are not allowed as GO targets in response to the AO-1 (with the possible exceptions listed in the AO-1 documentation).

D.1 List of XMM GTO targets

This table has been endorsed by the **XMM** OTAC.

Table 23: **XMM** *Guaranteed Time targets*

Version 1.1
NOTE: Final version as of 1-Feb-1999

Target Name	α(2000)	δ(2000)	**Prime Instrument**	**PI**	**Exposure Time [ks]**
Q0000-263	00 03 23	-26 03 17	EPI	B. Aschenbach	50.0
HD 108	00 06 03	63 40 48	EPI	K. Mason	30.0
Mrk 335	00 06 19	20 12 11	RGS	F. Jansen	33.0
III ZW 2	00 10 34	10 58 41	EPI	K. Mason	10.0
WW Cet	00 11 25	-11 28 43	EPI	K. Mason	10.0
S5 0014+813	00 17 08	81 35 08	EPI	M. Turner	40.0
CL 0016+16	00 18 33	16 26 18	EPI	M. Watson	40.0
PSR J0030+0453	00 30 30	04 53 17	EPI	B. Aschenbach	20.0
M31 South 2	00 40 06	40 35 24	EPI	M. Watson	60.0
M31 South 1	00 41 25	40 55 35	EPI	M. Watson	64.0
M31 Core	00 42 43	41 15 46	EPI	K. Mason	50.0
M31 Core	00 42 43	41 15 46	EPI	M. Watson	64.0
HR 188	00 43 35	-17 59 14	EPI	B. Aschenbach	10.0
M31 north1	00 44 01	41 35 57	EPI	K. Mason	63.0
I-1(NGC188)	00 44 22	85 20 25	RGS	F. Jansen	70.0
M31 north2	00 45 20	41 56 09	EPI	K. Mason	63.0
M31 north3	00 46 38	42 16 20	EPI	K. Mason	63.0
NGC247/PHL6625	00 46 52	-20 43 29	EPI	M. Watson	10.0
NGC 253 NW	00 47 23	-25 15 14	EPI	M. Watson	30.0
IKT 5	00 49 07	-73 14 06	EPI	J. Bleeker	25.0
CF Tuc	00 53 05	-74 39 07	EPI	B. Aschenbach	35.0
I Zwicky 1	00 53 35	12 41 36	EPI	M. Watson	20.0
NGC 300	00 54 55	-37 40 60	EPI	M. Turner	45.0
NGC 300	00 54 55	-37 40 60	EPI	M. Turner	27.5
SGP-1	00 55 19	-27 36 00	EPI	M. Watson	5.0
SGP-4	00 55 19	-28 00 00	EPI	M. Watson	5.0
SGP-7	00 55 19	-28 23 60	EPI	M. Watson	5.0
SGP-2	00 57 00	-27 36 00	EPI	M. Watson	5.0

SGP-5	00 57 00	-28 00 00	EPI	M. Watson	5.0
SGP-8	00 57 00	-28 23 60	EPI	M. Watson	5.0
Ton S 180	00 57 20	-22 22 59	EPI	M. Watson	30.0
Q 0056-363	00 58 37	-36 06 05	RGS	F. Jansen	11.0
SGP-3	00 58 51	-27 36 00	EPI	M. Watson	5.0
SGP-6	00 58 51	-28 00 00	EPI	M. Watson	5.0
SGP-9	00 58 51	-28 23 60	EPI	M. Watson	5.0
RX J0059.2-7	00 59 13	-71 38 50	EPI	M. Turner	5.0
IKT 18	00 59 26	-72 10 11	EPI	J. Bleeker	15.0
G133-6 29	01 03 60	-06 42 00	EPI	B. Aschenbach	20.0
0102-72.3	01 04 02	-72 01 56	RGS	B. Brinkman	20.0
G133-69 1	01 04 24	-06 24 00	EPI	B. Aschenbach	20.0
IKT 23	01 04 52	-72 23 10	RGS	J. Bleeker	25.0
ESO 113- G 010	01 05 17	-58 26 13	EPI	B. Aschenbach	5.0
HT Cas	01 10 13	60 04 35	EPI	M. Watson	45.0
PSR J0117+5914	01 17 39	59 14 38	EPI	K. Mason	5.0
4U 0115+63	01 18 32	63 44 24	EPI	M. Turner	5.0
ESO 244- 17	01 20 19	-44 07 48	EPI	B. Aschenbach	15.0
ESO 244- G 017	01 20 20	-44 07 43	EPI	B. Aschenbach	5.0
TON S210	01 21 51	-28 20 57	EPI	M. Watson	6.0
Fairall 9	01 23 46	-58 48 21	RGS	F. Jansen	25.0
NGC 526A	01 23 54	-35 03 56	EPI	K. Mason	10.0
A 189	01 25 32	01 45 30	RGS	B. Brinkman	40.0
Mrk 359	01 27 32	19 10 39	EPI	M. Turner	8.0
RX J0132-65	01 32 42	-65 54 32	EPI	K. Mason	5.0
M33_#11	01 32 46	30 28 19	EPI	B. Aschenbach	10.0
M33_#4	01 32 51	30 36 49	EPI	B. Aschenbach	10.0
QSO 0130-403	01 33 02	-40 06 31	EPI	M. Turner	35.0
M33_#5	01 33 02	30 21 24	EPI	B. Aschenbach	10.0
M33_#10	01 33 07	30 45 02	EPI	B. Aschenbach	10.0
M33_#3	01 33 32	30 52 13	EPI	B. Aschenbach	10.0
M33_#15	01 33 33	30 33 07	EPI	B. Aschenbach	10.0
M33_#12	01 33 38	30 21 49	EPI	B. Aschenbach	10.0
M33_#1	01 33 51	30 39 37	EPI	B. Aschenbach	10.0
M33_#9	01 34 04	30 57 25	EPI	B. Aschenbach	10.0
M33_#6	01 34 08	30 46 06	EPI	B. Aschenbach	10.0
M33_#7	01 34 10	30 26 60	EPI	B. Aschenbach	10.0
M33_#13	01 34 34	30 34 11	EPI	B. Aschenbach	10.0
M33_#2	01 34 40	30 57 48	EPI	B. Aschenbach	10.0
M33_#8	01 34 51	30 42 22	EPI	B. Aschenbach	10.0
M33_#14	01 34 56	30 50 52	EPI	B. Aschenbach	10.0
UV Cet	01 39 01	-17 57 02	RGS	B. Brinkman	30.0
PSR B0136+57	01 39 20	58 14 31	EPI	F. Jansen	5.0
PHL 1092	01 39 56	06 19 21	EPI	M. Watson	24.0

Deep Field 0145-04	01 45 27	-04 34 42	EPI	K. Mason	200.0
4U 0142+61	01 46 22	61 45 12	EPI	M. Turner	5.0
NGC 676	01 48 57	05 54 26	EPI	M. Turner	15.0
A 262	01 52 46	36 09 07	EPI	J. Bleeker	25.0
WARPJ0152.7-1357	01 52 42	-13 57 55	EPI	K. Mason	55.0
NGC 720	01 53 01	-13 44 14	EPI	M. Turner	45.0
RX J0153-59	01 54 01	-59 47 36	EPI	K. Mason	5.0
Mrk 1014	01 59 50	00 23 41	EPI	B. Aschenbach	10.0
47 Cas	02 05 07	77 16 53	RGS	B. Brinkman	40.0
WX Hyi	02 09 51	-63 18 41	EPI	K. Mason	10.0
Mrk 590	02 14 34	-00 46 00	EPI	K. Mason	10.0
LMC	02 15 00	-73 58 00	EPI	R. Mushotzky	10.0
SDS-5	02 16 24	-05 00 00	EPI	M. Watson	50.0
SDS-4	02 17 12	-04 39 13	EPI	M. Watson	50.0
SDS-6	02 17 12	-05 20 47	EPI	M. Watson	50.0
SDS-1	02 17 60	-05 00 00	EPI	M. Watson	100.0
PSR J0218+42	02 18 06	42 32 17	EPI	M. Watson	35.0
SDS-3	02 18 48	-04 39 13	EPI	M. Watson	50.0
SDS-7	02 18 48	-05 20 47	EPI	M. Watson	50.0
SDS-2	02 19 36	-05 00 00	EPI	M. Watson	50.0
XMDS OM_6	02 21 00	-04 52 30	EPI	K. Mason	20.0
XMDS OM_1	02 21 50	-04 30 00	EPI	K. Mason	20.0
XMDS SSC_5	02 21 50	-05 15 00	EPI	M. Watson	20.0
NGC 891	02 22 31	42 20 15	EPI	M. Turner	15.0
MLS4	02 22 40	-04 07 30	EPI	M. Turner	8.0
XMDS OM_5	02 22 40	-04 52 30	EPI	K. Mason	20.0
MLS8	02 23 30	-04 30 00	EPI	M. Turner	20.0
XMDS SSC_4	02 23 30	-05 15 00	EPI	M. Watson	20.0
MLS3	02 24 20	-04 07 30	EPI	M. Turner	20.0
XMDS OM_4	02 24 20	-04 52 30	EPI	K. Mason	20.0
MLS7	02 25 10	-04 30 00	EPI	M. Turner	40.0
XMDS SSC_3	02 25 10	-05 15 00	EPI	M. Watson	20.0
MLS2	02 25 60	-04 07 30	EPI	M. Turner	20.0
XMDS OM_3	02 25 60	-04 52 30	EPI	K. Mason	20.0
MLS6	02 26 50	-04 30 00	EPI	M. Turner	40.0
XMDS SSC_2	02 26 50	-05 15 00	EPI	M. Watson	20.0
MLS1	02 27 40	-04 07 30	EPI	M. Turner	20.0
XMDS OM_2	02 27 40	-04 52 30	EPI	K. Mason	20.0
MLS5	02 28 30	-04 30 00	EPI	M. Turner	20.0
XMDS SSC_1	02 28 30	-05 15 00	EPI	M. Watson	20.0
Q0226-1024	02 28 56	-10 10 39	EPI	R. Griffiths	5.0
MRK 1044	02 30 05	-08 59 53	EPI	M. Turner	8.0
ESO 416- G002	02 35 13	-29 36 18	EPI	B. Aschenbach	5.0
WW Hor	02 36 12	-52 19 14	EPI	K. Mason	5.0

ESO 198-G24	02 38 11	-52 10 40	EPI	M. Turner	8.0
AO0235+164	02 38 38	16 37 00	EPI	M. Watson	10.0
GT 0236+610	02 40 32	61 13 47	EPI	M. Turner	5.0
GT 0236+610	02 40 32	61 13 47	EPI	M. Turner	5.0
GT 0236+610	02 40 32	61 13 47	EPI	M. Turner	5.0
GT 0236+610	02 40 32	61 13 47	EPI	M. Turner	5.0
NGC 1068	02 42 41	-00 00 48	RGS	B. Brinkman	90.0
NGC 1058	02 43 29	37 20 27	EPI	M. Turner	10.0
VY Ari	02 48 44	31 06 55	RGS	B. Brinkman	40.0
MBM 12 Pos.2	02 54 30	19 48 18	EPI	B. Aschenbach	20.0
MBM 12 Pos.1	02 56 50	19 32 03	EPI	B. Aschenbach	20.0
A399/401	02 57 53	13 01 60	EPI	M. Turner	9.0
A399/401	02 58 25	13 18 00	EPI	M. Turner	9.0
A399/401	02 58 58	13 34 00	EPI	M. Turner	9.0
A399/401	02 59 51	13 46 60	EPI	M. Turner	8.0
MS0302.5+1717	03 05 19	17 28 38	EPI	K. Mason	10.0
Algol	03 08 10	40 57 20	EPI	B. Aschenbach	50.0
EF Eri	03 14 13	-22 35 42	EPI	M. Watson	18.0
Marano04	03 14 30	-55 04 16	EPI	M. Watson	5.5
Marano03	03 14 30	-55 09 25	EPI	M. Watson	5.5
Marano02	03 14 30	-55 14 35	EPI	M. Watson	5.5
Marano01	03 14 30	-55 19 44	EPI	M. Watson	5.5
Marano08	03 15 06	-55 04 16	EPI	M. Watson	5.5
Marano07	03 15 06	-55 09 25	EPI	M. Watson	5.5
Marano06	03 15 06	-55 14 35	EPI	M. Watson	5.5
Marano05	03 15 06	-55 19 44	EPI	M. Watson	5.5
Marano pointing #12	03 15 42	-55 04 16	EPI	M. Turner	6.2
Marano pointing #11	03 15 42	-55 09 25	EPI	M. Turner	6.2
Marano pointing #10	03 15 42	-55 14 39	EPI	M. Turner	6.2
Marano pointing #9	03 15 42	-55 19 44	EPI	M. Turner	6.2
Marano pointing #16	03 16 18	-55 04 16	EPI	M. Turner	6.2
Marano pointing #15	03 16 18	-55 09 25	EPI	M. Turner	6.2
Marano pointing #14	03 16 18	-55 14 35	EPI	M. Turner	6.2
Marano pointing #13	03 16 18	-55 19 44	EPI	M. Turner	6.2
A3112	03 17 56	-44 14 06	EPI	F. Jansen	20.0
NGC 1313	03 18 14	-66 30 00	EPI	B. Aschenbach	40.0
kap Cet	03 19 22	03 22 13	RGS	B. Brinkman	35.0
MBM 16	03 20 00	11 13 60	EPI	F. Jansen	10.0
Mrk 609	03 25 25	-06 08 30	EPI	B. Aschenbach	5.0
alpha Persei 1	03 26 16	48 50 29	EPI	R. Pallavicini	50.0
UX Ari	03 26 35	28 42 54	RGS	B. Brinkman	40.0
EX0 032957-2606.9	03 32 05	-25 56 57	EPI	K. Mason	5.0
AXAF Ultra Deep Fiel	03 32 22	-27 48 30	EPI	J. Bergeron	55.0
AXAF Ultra Deep Fiel	03 32 22	-27 48 30	EPI	J. Bergeron	55.0

AXAF Ultra Deep Fiel	03 32 22	-27 48 30	EPI	J. Bergeron	55.0
AXAF Ultra Deep Fiel	03 32 22	-27 48 30	EPI	J. Bergeron	54.0
AXAF Ultra Deep Fiel	03 32 22	-27 48 30	EPI	J. Bergeron	55.0
AXAF Ultra Deep Fiel	03 32 22	-27 48 30	EPI	J. Bergeron	55.0
AXAF Ultra Deep Fiel	03 32 22	-27 48 30	EPI	J. Bergeron	55.0
HR 1084	03 32 59	-09 27 31	EPI	B. Aschenbach	10.0
UZ For	03 35 29	-25 44 23	EPI	M. Watson	12.0
UZ For	03 35 29	-25 44 23	EPI	M. Watson	12.0
HR 1099	03 36 47	00 35 16	RGS	B. Brinkman	30.0
SHARC-4	03 37 45	-25 22 26	EPI	M. Turner	15.0
SHARC-4 (linked with	03 37 45	-25 22 26	EPI	F. Jansen	50.0
2A 0335+096	03 38 35	09 57 54	RGS	B. Brinkman	30.0
Pleiades 1	03 43 44	24 43 17	EPI	M. Turner	60.0
IC348	03 45 00	32 07 60	EPI	M. Watson	40.0
Pleiades-1	03 47 18	24 22 31	EPI	M. Watson	50.0
MBM 12	03 57 00	19 53 60	EPI	F. Jansen	10.0
Hawaii 167	03 57 22	01 10 56	EPI	M. Watson	20.0
PSR J0358+5413	03 58 54	54 13 14	EPI	K. Mason	30.0
NGC 1511	03 59 36	-67 38 07	EPI	F. Jansen	40.0
VW Hyi	04 09 12	-71 17 46	EPI	K. Mason	20.0
A478 offset-1	04 12 35	10 15 45	EPI	M. Turner	19.0
A478 offset-2	04 12 35	10 15 45	EPI	M. Turner	21.0
A 478	04 13 25	10 27 54	RGS	B. Brinkman	110.0
Taurus HD283572	04 21 59	28 18 08	RGS	R. Pallavicini	42.0
[HB89]0420-388	04 22 15	-38 44 53	EPI	K. Mason	20.0
Hyades VB50	04 24 13	14 45 30	RGS	R. Pallavicini	50.0
1H0419-577	04 25 44	-57 13 35	EPI	M. Turner	8.0
Hyades VB71	04 28 35	15 57 45	RGS	R. Pallavicini	50.0
A3266_field4	04 29 50	-61 14 40	EPI	B. Aschenbach	15.0
A3266_field6	04 29 50	-61 36 50	EPI	B. Aschenbach	15.0
A3266_field2	04 30 35	-61 30 10	EPI	B. Aschenbach	15.0
NGC 1569	04 30 46	64 50 53	EPI	M. Turner	15.0
L1551 field 1	04 31 39	18 10 00	EPI	F. Jansen	50.0
A3266_field1	04 31 60	-61 20 10	EPI	B. Aschenbach	15.0
A3266_field3	04 32 40	-61 14 40	EPI	B. Aschenbach	15.0
A3266_field5	04 32 40	-61 36 50	EPI	B. Aschenbach	15.0
3C 120	04 33 11	05 21 16	EPI	K. Mason	10.0
A 496	04 33 38	-13 15 43	EPI	J. Bleeker	30.0
ESO 15- IG 011	04 35 16	-78 01 57	EPI	B. Aschenbach	5.0
J0437-4715	04 37 16	-47 15 08	EPI	B. Aschenbach	70.0
[HB89]0438-436	04 40 17	-43 33 09	EPI	K. Mason	10.0
MCG -01-13-025	04 51 41	-03 48 34	EPI	B. Aschenbach	5.0
RE J0453-42	04 53 25	-42 13 41	EPI	K. Mason	5.0
Taurus SU Aur	04 55 59	30 34 02	RGS	R. Pallavicini	52.0

LH 9 - LH 10	04 57 00	-66 25 60	EPI	K. Mason	30.0
Gl 182	04 59 35	01 47 09	EPI	B. Aschenbach	17.0
CL0500-24	05 01 06	-24 25 03	EPI	M. Watson	25.0
RE J0501-03	05 01 46	-03 59 27	EPI	K. Mason	5.0
SHARC-2	05 05 20	-28 49 05	EPI	M. Watson	44.5
DEM L71	05 05 43	-67 52 36	RGS	J. Bleeker	40.0
2E 0506.0-6805	05 05 55	-68 01 57	EPI	M. Watson	20.0
NGC 1808	05 07 42	-37 30 46	EPI	F. Jansen	40.0
N103B	05 08 59	-68 43 34	RGS	B. Brinkman	25.0
2E 0509.5-6734	05 09 32	-67 31 17	EPI	M. Watson	39.0
HD33798	05 15 15	47 10 19	RGS	F. Jansen	24.0
HD33798	05 15 15	47 10 19	RGS	F. Jansen	24.0
MCG -02-14-009	05 16 21	-10 33 40	EPI	B. Aschenbach	5.0
0519-69.0	05 19 34	-69 02 10	RGS	B. Brinkman	40.0
2E 0525.3-6601	05 25 29	-65 59 15	EPI	M. Watson	18.0
N49	05 26 02	-66 05 04	RGS	B. Brinkman	25.0
LMC deep field	05 31 20	-65 57 38	EPI	B. Aschenbach	60.0
RE J0531-46	05 31 35	-46 24 08	EPI	K. Mason	5.0
thet Ori	05 35 15	-05 23 29	RGS	B. Brinkman	20.0
iota Ori "field"	05 35 26	-05 54 36	RGS	B. Brinkman	20.0
SN 1987A (1)	05 35 28	-69 16 11	EPI	M. Watson	24.0
LHA 120-N 63A	05 35 43	-66 01 58	RGS	J. Bleeker	10.0
EPSILON ORI	05 36 12	-01 12 07	EPI	M. Turner	10.0
N157B	05 37 53	-69 10 12	EPI	B. Aschenbach	40.0
NGC 2024	05 38 18	-02 36 00	EPI	R. Pallavicini	45.0
PSR J0538+2817	05 38 25	28 17 11	EPI	K. Mason	20.0
LMC X-3	05 38 56	-64 05 01	RGS	K. Mason	15.0
LMC X-1	05 39 39	-69 44 36	EPI	M. Turner	5.0
0540-69.3	05 40 11	-69 19 58	RGS	B. Brinkman	35.0
zeta Ori	05 40 45	-01 56 30	RGS	B. Brinkman	30.0
NGC 2024	05 41 43	-01 54 35	EPI	B. Aschenbach	25.0
NGC 2023	05 41 47	-02 16 37	EPI	B. Aschenbach	25.0
BY Cam	05 42 49	60 51 31	EPI	K. Mason	5.0
PSR B0540+23	05 43 10	23 29 06	EPI	F. Jansen	5.0
PKS0548-32	05 50 41	-32 16 18	RGS	B. Brinkman	20.0
chi1 Ori	05 54 23	20 16 34	RGS	B. Brinkman	35.0
RX J0558.0+5353	05 58 00	53 53 59	EPI	M. Watson	13.0
H0557-385	05 58 02	-38 20 05	EPI	K. Mason	10.0
21P/Giacobini-Zinner	06 04 42	-03 50 04	EPI	F. Jansen	22.0
PSR B0611+22	06 14 17	22 29 56	EPI	F. Jansen	5.0
MRK 3	06 15 35	71 02 04	EPI	M. Turner	40.0
Mkn 3	06 15 36	71 02 05	RGS	B. Brinkman	60.0
X0614+091	06 17 07	09 08 13	RGS	B. Brinkman	20.0
NGC2146	06 18 40	78 21 23	EPI	M. Watson	23.0

A 0620-00	06 22 44	-00 20 45	EPI	M. Watson	40.0
PMN J0623-6436	06 23 08	-64 36 21	EPI	B. Aschenbach	5.0
PSR J0631+1036	06 31 28	10 36 58	EPI	F. Jansen	5.0
Geminga	06 33 54	17 46 13	EPI	M. Turner	40.0
1E 0630+178	06 33 55	17 46 12	RGS	B. Brinkman	40.0
HD49798	06 48 05	-44 18 54	EPI	M. Turner	15.0
RXJ0658-5557	06 58 17	-55 57 36	EPI	M. Turner	40.0
PSR 0656+14	06 59 48	14 14 21	RGS	B. Brinkman	10.0
PSR 0656+14	06 59 48	14 14 21	EPI	M. Turner	15.0
PSR 0656+14	06 59 48	14 14 22	EPI	K. Mason	15.0
1H 0707-495	07 08 41	-49 33 06	EPI	M. Watson	43.0
RXJ 0720-3125	07 20 25	-31 25 52	RGS	M. Watson	49.0
YY Gem	07 34 38	31 52 15	EPI	B. Aschenbach	50.0
0738+313	07 41 11	31 12 00	EPI	R. Griffiths	28.0
UGC 3973	07 42 33	49 48 30	EPI	B. Aschenbach	5.0
PSR B0740-28	07 42 49	-28 22 44	EPI	F. Jansen	5.0
sig Gem	07 43 19	28 52 60	RGS	B. Brinkman	40.0
YZ CMi	07 44 42	03 33 20	RGS	B. Brinkman	20.0
PKS 0754	07 47 31	-19 17 40	EPI	B. Aschenbach	20.0
PKS 0754 offset	07 48 25	-19 06 00	EPI	B. Aschenbach	30.0
PSR J0751+18	07 51 09	18 07 39	EPI	M. Watson	35.0
PQ GEM	07 51 17	14 44 23	EPI	K. Mason	40.0
U Gem	07 55 05	22 00 05	EPI	K. Mason	20.0
fragment E	07 59 36	-44 22 33	EPI	B. Aschenbach	40.0
RXJ0806.4-4123	08 06 23	-41 22 33	EPI	B. Aschenbach	20.0
gam Vel (phase 1)	08 09 32	-47 20 12	RGS	B. Brinkman	95.0
PG 0804+761	08 10 59	76 02 43	RGS	F. Jansen	7.0
SU UMa	08 12 28	62 36 22	EPI	K. Mason	15.0
IX Vel	08 15 19	-49 13 21	EPI	K. Mason	20.0
Holmberg II	08 19 29	70 42 23	EPI	M. Watson	20.0
NGC 2563	08 20 36	21 04 08	EPI	R. Mushotzky	20.0
Puppis-A NS	08 22 06	-43 02 60	EPI	B. Aschenbach	50.0
PSR B0823+26	08 26 51	26 37 26	EPI	F. Jansen	50.0
A665	08 30 45	65 52 55	EPI	M. Turner	45.0
A 665	08 30 58	65 50 20	RGS	B. Brinkman	65.0
HVC Complex A	08 35 00	34 32 60	EPI	F. Jansen	10.0
PSR B0833-45	08 35 22	-45 10 48	RGS	B. Brinkman	90.0
VELA REG D	08 35 43	-42 35 37	EPI	M. Turner	30.0
EI UMa	08 38 22	48 38 01	EPI	K. Mason	10.0
pi1 UMa	08 39 12	65 01 15	RGS	B. Brinkman	40.0
Praesepe	08 39 58	19 32 29	EPI	R. Pallavicini	50.0
S5 0836+71	08 41 24	70 53 41	EPI	M. Turner	30.0
IC 2391	08 41 59	-53 00 35	EPI	M. Turner	45.0
Vik 59	08 47 11	34 49 16	EPI	F. Jansen	40.0

PG 0844 + 349	08 47 42	34 45 05	EPI	B. Aschenbach	20.0
fragment GW	08 47 45	-46 28 51	EPI	B. Aschenbach	33.0
fragment GN	08 48 58	-45 39 03	EPI	B. Aschenbach	23.0
EU Cnc	08 51 27	11 46 58	EPI	K. Mason	5.0
fragment GC	08 51 50	-46 18 45	EPI	B. Aschenbach	20.0
fragment GS	08 53 14	-47 13 53	EPI	B. Aschenbach	45.0
fragment A	08 57 40	-41 51 07	EPI	B. Aschenbach	50.0
Vela X-1	09 02 07	-40 33 17	RGS	B. Brinkman	50.0
G272.2-3.2	09 06 46	-52 07 12	EPI	B. Aschenbach	30.0
A754_field2	09 08 14	-09 36 23	EPI	M. Turner	12.5
PSR B0906-49	09 08 36	-49 13 05	EPI	F. Jansen	5.0
A754_field4	09 08 50	-09 45 53	EPI	M. Turner	12.5
A754_field3	09 09 00	-09 31 53	EPI	M. Turner	10.0
A754_field1	09 09 27	-09 40 09	EPI	M. Turner	12.5
Hydra A	09 18 06	-12 05 44	EPI	J. Bleeker	30.0
RX J0925.7-4758	09 25 46	-47 58 17	RGS	M. Watson	50.0
MN Hya	09 29 07	-24 05 05	EPI	K. Mason	5.0
IZw18	09 34 02	55 14 20	EPI	M. Watson	25.0
I Zw 18	09 34 02	55 14 25	EPI	M. Watson	30.0
HD82210	09 34 29	69 49 45	RGS	F. Jansen	8.0
Q0932+5006	09 35 53	49 53 13	EPI	R. Griffiths	5.0
Cl0939+472	09 43 00	46 59 30	EPI	B. Aschenbach	50.0
MCG -5-23-16	09 47 40	-30 56 54	EPI	R. Griffiths	40.0
PG0947+396	09 50 48	39 26 51	EPI	M. Watson	17.0
PSR B0950+08	09 53 10	07 55 48	EPI	F. Jansen	100.0
0952+179	09 54 57	17 43 31	EPI	R. Griffiths	30.0
M81	09 55 33	69 03 55	RGS	B. Brinkman	100.0
M82	09 55 50	69 40 45	EPI	M. Turner	30.0
PG0953+414	09 56 52	41 15 22	EPI	M. Watson	10.0
Holmberg IX	09 57 53	69 03 40	EPI	M. Watson	15.0
NGC3079	10 01 58	55 40 47	EPI	M. Watson	20.0
RX J1002-19	10 02 11	-19 25 34	EPI	K. Mason	5.0
RX J1007-20	10 07 34	-20 17 31	EPI	K. Mason	5.0
PSR J1012+53	10 12 33	53 07 03	EPI	M. Watson	20.0
RX J1015+09	10 15 35	09 04 42	EPI	K. Mason	5.0
NGC 3185	10 17 38	21 41 17	EPI	M. Turner	10.0
AD Leo	10 19 36	19 52 12	RGS	B. Brinkman	25.0
NGC 3227	10 23 31	19 51 55	RGS	F. Jansen	33.0
ZW3146	10 23 41	04 11 24	RGS	R. Mushotzky	50.0
PSR J1024-0719	10 24 39	-07 19 19	EPI	B. Aschenbach	80.0
NGC 3256	10 27 50	-43 54 14	EPI	M. Turner	15.0
B2 1028+31	10 30 59	31 02 56	RGS	F. Jansen	20.0
HE 1029-1401	10 31 54	-14 16 51	EPI	M. Watson	6.0
REJ1034+396	10 34 39	39 38 29	EPI	K. Mason	10.0

NGC 3310	10 38 45	53 30 11	EPI	M. Turner	15.0
WR 22	10 41 18	-59 40 37	EPI	K. Mason	10.0
WR 22	10 41 18	-59 40 37	EPI	K. Mason	10.0
WR 22	10 41 18	-59 40 37	EPI	K. Mason	10.0
WR 22	10 41 18	-59 40 37	EPI	K. Mason	10.0
WR 22	10 41 18	-59 40 37	EPI	K. Mason	10.0
WR 22	10 41 18	-59 40 37	EPI	K. Mason	10.0
WR 22	10 41 18	-59 40 37	EPI	K. Mason	10.0
IC 2602	10 42 41	-64 21 01	EPI	R. Pallavicini	45.0
WR 25	10 44 11	-59 43 11	RGS	B. Brinkman	50.0
WR 25	10 44 11	-59 43 11	RGS	K. Mason	20.0
WR 25	10 44 11	-59 43 11	RGS	K. Mason	20.0
Eta Carinae	10 45 02	-59 40 48	RGS	B. Brinkman	50.0
HD 93403	10 45 44	-59 24 28	EPI	K. Mason	5.0
HD 93403	10 45 44	-59 24 28	EPI	K. Mason	5.0
HD 93403	10 45 44	-59 24 28	EPI	K. Mason	5.0
HD 93403	10 45 44	-59 24 28	EPI	K. Mason	5.0
FH UMa	10 47 10	63 35 13	EPI	K. Mason	5.0
1E 1048.1-5937	10 50 09	-59 53 19	EPI	M. Turner	5.0
EK UMa	10 51 35	54 04 36	EPI	K. Mason	5.0
PG1048+342	10 51 43	33 59 27	EPI	K. Mason	30.0
MS1054.4-0321	10 56 60	-03 37 27	EPI	M. Watson	40.0
PSR 1055-52	10 57 59	-52 26 56	EPI	M. Turner	80.0
NGC 3486	11 00 23	28 58 29	EPI	M. Turner	10.0
Polaris flare	11 01 00	86 10 00	EPI	F. Jansen	10.0
MK 728	11 01 01	11 02 46	EPI	B. Aschenbach	5.0
TW Hya	11 01 58	-34 42 12	EPI	B. Aschenbach	21.0
G290.1-0.8	11 03 00	-60 53 60	EPI	M. Watson	9.0
AN UMa	11 04 26	45 03 14	EPI	K. Mason	5.0
ST LMi	11 05 40	25 06 28	EPI	K. Mason	5.0
WR 40	11 06 17	-65 30 35	EPI	K. Mason	15.0
HE 1104-1805	11 06 33	-18 21 24	EPI	M. Turner	35.0
NGC 3516	11 06 42	72 33 26	EPI	M. Turner	5.0
NGC 3516	11 06 47	72 34 08	RGS	R. Mushotzky	140.0
[SP89]1107+487	11 10 38	48 31 16	EPI	K. Mason	80.0
AR UMa	11 15 45	42 58 23	EPI	K. Mason	5.0
PG1114+445	11 17 06	44 13 33	EPI	K. Mason	45.0
DP Leo	11 17 16	17 57 41	EPI	K. Mason	5.0
PG1115+407	11 18 30	40 25 54	EPI	M. Watson	18.0
PG1116+215	11 19 09	21 19 18	EPI	M. Watson	7.0
RXJ 1120.1	11 20 07	43 18 05	EPI	F. Jansen	20.0
NGC 3628	11 20 17	13 35 20	EPI	F. Jansen	60.0
Cen X-3	11 21 15	-60 37 24	RGS	B. Brinkman	50.0
HCG51	11 22 21	24 17 35	EPI	M. Turner	10.0

Z 1121.5+0630	11 24 08	06 12 56	EPI	B. Aschenbach	5.0
MSH 11-54	11 24 36	-59 16 00	RGS	J. Bleeker	24.0
HVC Complex M	11 26 00	42 52 60	EPI	F. Jansen	10.0
NGC 3690	11 28 30	58 33 43	EPI	M. Turner	20.0
1127-145	11 30 07	-14 49 27	EPI	R. Griffiths	30.0
B2 1128+31	11 31 09	31 14 07	RGS	F. Jansen	18.0
CoD-33_7795	11 31 55	-34 36 25	EPI	B. Aschenbach	29.0
T Leo	11 38 27	03 22 07	EPI	K. Mason	10.0
NGC 3783	11 39 02	-37 44 19	RGS	B. Brinkman	30.0
MS1137.5+6625	11 40 23	66 08 41	EPI	M. Watson	40.0
RX J1141-6410	11 41 23	-64 10 15	EPI	K. Mason	5.0
RE J1149+28	11 49 56	28 45 08	EPI	K. Mason	5.0
NGC 3941	11 52 55	36 59 10	EPI	M. Turner	10.0
A1413	11 55 19	23 24 36	EPI	M. Turner	24.0
NGC 4051	12 03 10	44 31 53	EPI	K. Mason	150.0
N79-299A	12 04 10	20 13 18	EPI	M. Turner	10.0
PG1202+281	12 04 42	27 54 11	EPI	K. Mason	17.0
WR 46	12 05 19	-62 03 08	EPI	K. Mason	80.0
NGC 4138	12 09 30	43 41 04	EPI	M. Turner	10.0
1E 1207-5209 / PKS 1	12 10 01	-52 26 20	EPI	M. Turner	30.0
NGC 4151	12 10 25	39 23 43	EPI	M. Turner	10.0
NGC 4151	12 10 32	39 24 20	EPI	M. Turner	20.0
NGC 4151	12 10 33	39 24 21	EPI	R. Griffiths	72.0
MS1208.7+3928	12 11 16	39 12 06	EPI	K. Mason	10.0
NGC 4168	12 12 16	13 12 23	EPI	M. Turner	20.0
PG 1211+143	12 14 17	14 03 12	EPI	M. Turner	50.0
G299.2-2.9	12 15 12	-65 30 00	EPI	B. Aschenbach	10.0
Mkn 766	12 18 26	29 48 46	EPI	K. Mason	150.0
NGC 4258	12 18 58	47 18 14	EPI	M. Watson	20.0
PG1216+069	12 19 21	06 38 38	EPI	M. Watson	17.0
1H1219+301	12 21 22	30 10 37	RGS	B. Brinkman	20.0
RXJ122135.6+280613	12 21 36	28 06 14	EPI	K. Mason	40.0
NGC 4321	12 22 55	15 49 12	EPI	B. Aschenbach	30.0
NGC 4325	12 23 07	10 37 16	EPI	R. Mushotzky	20.0
PSR B1221-63	12 24 22	-64 07 55	EPI	F. Jansen	5.0
NGC 4388	12 25 46	12 39 40	EPI	M. Turner	5.0
NGC 4388	12 25 47	12 39 41	EPI	M. Watson	10.0
NGC 4395	12 25 48	33 32 50	EPI	M. Turner	10.0
NGC 4395	12 26 01	33 31 23	EPI	M. Watson	15.0
NGC 4406 (M86)	12 26 12	12 56 48	EPI	B. Aschenbach	84.0
HI1225+01	12 27 19	01 29 24	EPI	M. Watson	20.0
NGC 4449	12 28 09	44 05 10	EPI	M. Watson	25.0
3C 273	12 29 06	02 03 07	EPI	M. Turner	40.0
NGC 4472	12 29 46	07 59 47	EPI	M. Turner	20.0

NGC 4477	12 30 02	13 38 10	EPI	M. Turner	10.0
NGC 4490	12 30 36	41 38 41	EPI	M. Turner	15.0
Virgo 1	12 30 50	12 43 30	EPI	B. Aschenbach	5.0
Virgo 2	12 30 50	13 03 30	EPI	B. Aschenbach	5.0
Virgo 3	12 30 50	13 23 30	EPI	B. Aschenbach	6.0
Virgo 4	12 30 50	13 43 30	EPI	B. Aschenbach	7.5
Virgo 5	12 30 50	14 03 30	EPI	B. Aschenbach	10.0
Virgo 6	12 30 50	14 23 30	EPI	B. Aschenbach	11.0
Virgo 7	12 30 50	14 43 30	EPI	B. Aschenbach	7.5
Virgo 8	12 30 50	15 03 30	EPI	B. Aschenbach	9.0
Virgo 9	12 30 50	15 23 30	EPI	B. Aschenbach	11.0
Virgo 10	12 30 50	15 43 30	EPI	B. Aschenbach	12.0
Virgo 11	12 30 50	16 03 30	EPI	B. Aschenbach	12.0
Virgo 12	12 30 50	16 23 30	EPI	B. Aschenbach	12.0
Virgo 13	12 30 50	17 53 30	EPI	B. Aschenbach	12.0
NGP Rift 1	12 31 12	20 48 00	EPI	B. Aschenbach	20.0
NGP Rift 2	12 31 12	21 18 00	EPI	B. Aschenbach	20.0
NGP Rift 3	12 31 12	21 48 00	EPI	B. Aschenbach	20.0
NGC 4501	12 31 58	14 25 09	EPI	M. Turner	10.0
NGC 4565	12 36 20	25 59 16	EPI	M. Turner	10.0
HDF	12 36 48	62 13 12	EPI	R. Griffiths	90.0
Hubble Deep Field	12 36 50	62 12 58	EPI	F. Jansen	135.0
NGC 4579	12 37 43	11 49 04	EPI	M. Turner	10.0
NGC 4579	12 37 44	11 49 05	EPI	R. Griffiths	10.0
NGC 4593	12 39 39	-05 20 39	RGS	B. Brinkman	20.0
NGC 4631	12 42 06	32 32 21	EPI	M. Watson	50.0
NGC4636	12 42 48	02 41 18	RGS	B. Brinkman	100.0
NGC 4639	12 42 52	13 15 26	EPI	M. Turner	10.0
WR 47	12 44 25	-63 05 16	EPI	K. Mason	50.0
WR 47	12 44 25	-63 05 16	EPI	K. Mason	50.0
WR 47	12 44 25	-63 05 16	EPI	K. Mason	50.0
NGC 4666	12 45 09	-00 27 38	EPI	F. Jansen	60.0
NGC 4698	12 48 22	08 29 14	EPI	M. Turner	10.0
NGC 4725	12 50 26	25 30 05	EPI	M. Turner	15.0
EX Hya	12 52 25	-29 14 57	RGS	B. Brinkman	100.0
HCG62	12 53 06	-09 11 60	EPI	M. Turner	10.0
HD113226	13 02 11	10 57 32	RGS	F. Jansen	24.0
NGC 4945	13 05 26	-49 28 14	EPI	M. Turner	20.0
EV UMa	13 07 54	53 51 30	EPI	K. Mason	5.0
PG 1307+085	13 09 47	08 19 49	EPI	M. Watson	12.0
NGC5005	13 10 56	37 03 33	EPI	M. Watson	10.0
PG1309+355	13 12 18	35 15 21	EPI	K. Mason	25.0
RE J1313-32	13 13 17	-32 59 09	EPI	K. Mason	5.0
NGC 5033	13 13 27	36 35 39	EPI	M. Turner	5.0

RGH80	13 20 13	33 07 54	EPI	B. Aschenbach	30.0
H1320+551	13 22 49	54 55 29	EPI	M. Watson	20.0
PG1322+659	13 23 49	65 41 48	EPI	K. Mason	13.0
NGC 5129	13 24 10	13 58 34	EPI	R. Mushotzky	25.0
IRAS 13224-3809	13 25 20	-38 24 55	EPI	M. Watson	70.0
Omega Cen (NGC 5139)	13 26 47	-47 28 35	EPI	M. Turner	40.0
LSS 3074	13 26 59	-62 02 16	EPI	K. Mason	20.0
A3558	13 27 55	-31 29 24	EPI	B. Aschenbach	50.0
A 3558	13 27 57	-31 30 24	EPI	J. Bleeker	25.0
NGC 5194	13 29 52	47 11 53	EPI	M. Turner	10.0
M51	13 29 52	47 11 54	EPI	R. Griffiths	10.0
HD117555	13 30 47	24 13 59	RGS	F. Jansen	24.0
HD117555	13 30 47	24 13 59	RGS	F. Jansen	24.0
A 1750	13 30 54	-01 49 60	EPI	M. Turner	30.0
A3562_field2	13 31 51	-31 48 00	EPI	B. Aschenbach	15.0
A3562_field4	13 31 60	-31 39 40	EPI	B. Aschenbach	15.0
A3562_field5	13 32 25	-31 53 40	EPI	B. Aschenbach	15.0
A3562_field1	13 33 11	-31 41 60	EPI	B. Aschenbach	15.0
A3562_field3	13 33 60	-31 30 25	EPI	B. Aschenbach	15.0
RXJ 1334.3	13 34 20	50 30 54	EPI	M. Watson	40.0
A3562_field6	13 34 20	-31 44 25	EPI	B. Aschenbach	15.0
Deep Field 1334+37	13 34 37	37 54 44	EPI	K. Mason	200.0
MS1333.3+1725	13 35 49	17 09 53	EPI	K. Mason	10.0
MCG-6-30-15	13 35 54	-34 17 45	RGS	B. Brinkman	50.0
MCG-6-30-15	13 35 54	-34 17 42	EPI	M. Turner	25.0
MCG-6-30-15	13 35 54	-34 17 42	EPI	M. Turner	25.0
M 83	13 37 00	-29 51 51	EPI	M. Watson	30.0
QSO Concentration N	13 38 31	28 05 47	EPI	M. Watson	25.0
1WGA 1339.2+2717	13 39 14	27 17 25	EPI	K. Mason	10.0
F864-4	13 41 24	00 00 00	EPI	M. Watson	5.0
F864-1	13 41 24	00 24 00	EPI	M. Watson	5.0
F864-7	13 41 24	-00 24 00	EPI	M. Watson	5.0
Abell 1775	13 41 50	26 21 00	EPI	R. Mushotzky	32.0
NGC 5273	13 42 08	35 39 14	EPI	M. Turner	10.0
F864-5	13 43 00	00 00 00	EPI	M. Watson	5.0
F864-2	13 43 00	00 24 00	EPI	M. Watson	5.0
F864-8	13 43 00	-00 24 00	EPI	M. Watson	5.0
F864-6	13 44 36	00 00 00	EPI	M. Watson	5.0
F864-3	13 44 36	00 24 00	EPI	M. Watson	5.0
F864-9	13 44 36	-00 24 00	EPI	M. Watson	5.0
Mrk 273	13 44 42	55 53 13	EPI	B. Aschenbach	20.0
RXJ1347-1145	13 47 31	-11 45 09	EPI	M. Turner	40.0
QSO 1345+584	13 47 41	58 12 42	EPI	M. Turner	50.0
E1346+266	13 48 35	26 22 07	EPI	K. Mason	80.0

IC 4329a	13 49 19	-30 18 34	RGS	F. Jansen	11.0
SHARC-1	13 54 17	-02 21 46	EPI	M. Turner	30.0
PG1352+183	13 54 36	18 05 18	EPI	K. Mason	15.0
A 1837	14 01 36	-11 07 44	RGS	B. Brinkman	50.0
M101	14 03 10	54 20 24	EPI	M. Watson	45.0
NGC 5408	14 03 17	-41 22 48	EPI	M. Turner	10.0
NGC 5408	14 03 19	-41 23 05	EPI	M. Watson	10.0
PG1402+261	14 05 16	25 55 34	EPI	K. Mason	9.0
V834 Cen	14 09 08	-45 17 18	EPI	K. Mason	5.0
Circinus Galaxy	14 13 09	-65 20 20	RGS	B. Brinkman	91.0
PG 1411+442	14 13 48	44 00 14	EPI	B. Aschenbach	40.0
H1413+117	14 15 46	11 29 44	EPI	M. Turner	50.0
PG1415+451	14 17 01	44 56 06	EPI	K. Mason	20.0
Groth-Westphal HST s	14 17 12	52 23 60	EPI	R. Griffiths	70.0
NGC 5548	14 17 59	25 08 12	RGS	B. Brinkman	20.0
H1419+480	14 21 30	47 47 27	EPI	M. Watson	20.0
A1914	14 26 02	37 49 48	EPI	M. Turner	24.0
PG1425+267	14 27 35	26 32 14	EPI	M. Watson	60.0
H1426+42	14 28 33	42 40 21	RGS	B. Brinkman	50.0
MARK 1383	14 29 06	01 17 06	RGS	F. Jansen	8.0
V895 Cen	14 29 27	-38 04 10	EPI	K. Mason	5.0
PG1427+480	14 29 43	47 47 27	EPI	K. Mason	40.0
GB1428+4217	14 30 24	42 04 36	EPI	M. Watson	20.0
NGC5689	14 35 30	48 44 30	EPI	M. Watson	10.0
EK Dra	14 39 00	64 17 32	RGS	B. Brinkman	40.0
RCW 86 (SW-N)	14 40 33	-62 36 04	EPI	J. Bleeker	8.0
RCW 86 (SW-S)	14 40 57	-62 43 07	EPI	J. Bleeker	7.0
RCW 86 (NW)	14 42 02	-62 12 57	EPI	J. Bleeker	15.0
PG1440+356	14 42 07	35 26 23	EPI	M. Watson	6.0
Mkn478	14 42 07	35 26 24	RGS	R. Mushotzky	20.0
RCW 86 (SE)	14 42 55	-62 37 38	EPI	J. Bleeker	15.0
Q1442+2931	14 44 54	29 19 05	EPI	B. Aschenbach	40.0
RCW 86 (NE)	14 45 15	-62 22 26	EPI	J. Bleeker	15.0
PG1444+407	14 46 46	40 35 06	EPI	K. Mason	20.0
PSR B1449-64	14 53 33	-64 13 16	EPI	F. Jansen	5.0
E1455+2232	14 57 14	22 20 24	RGS	R. Mushotzky	50.0
1WGA 1501.9+4009	15 01 58	40 09 38	EPI	K. Mason	10.0
SN 1006 SW	15 01 60	-42 07 00	EPI	M. Watson	5.0
SN 1006 NW	15 02 50	-41 46 60	EPI	M. Watson	5.0
44 BOO	15 03 49	47 39 14	RGS	F. Jansen	25.0
SN 1006 NE	15 03 50	-41 46 60	EPI	M. Watson	5.0
SN 1006 SE	15 03 50	-42 07 00	EPI	M. Watson	5.0
MKN 841	15 03 53	10 25 52	EPI	M. Turner	7.0
GB1508+5714	15 10 03	57 02 44	EPI	M. Watson	20.0

A2029	15 10 56	05 44 42	EPI	M. Watson	20.0
PG1512+370	15 14 43	36 50 50	EPI	M. Watson	20.0
CGCG 21-63	15 16 40	00 14 54	EPI	B. Aschenbach	10.0
A 2052	15 16 44	07 01 18	RGS	B. Brinkman	40.0
MKW 3s	15 21 50	07 41 27	RGS	B. Brinkman	50.0
A 2065	15 22 42	27 43 00	EPI	M. Turner	20.0
Q1524+5147	15 25 54	51 36 50	EPI	R. Griffiths	5.0
UZ LIB	15 32 23	-08 32 05	RGS	F. Jansen	24.0
UZ LIB	15 32 23	-08 32 05	RGS	F. Jansen	24.0
alph CrB	15 34 41	26 42 53	RGS	B. Brinkman	40.0
Arp 220	15 34 57	23 30 16	EPI	B. Aschenbach	25.0
MS1532.5+0130	15 35 03	01 20 58	EPI	K. Mason	10.0
RXJ1548.2-4528	15 48 14	-45 28 45	EPI	B. Aschenbach	20.0
HD141714	15 49 36	26 04 09	RGS	F. Jansen	11.0
MR Ser	15 52 47	18 56 27	EPI	K. Mason	5.0
SCO-CEN PT1	15 56 25	-23 37 47	EPI	M. Turner	45.0
1556+3517	15 56 34	35 17 57	EPI	M. Watson	6.0
IRAS 16007+8137	15 56 51	81 28 56	EPI	K. Mason	10.0
Abell 2142	15 58 20	27 13 48	EPI	F. Jansen	70.0
Mrk 493	15 59 10	35 01 45	EPI	M. Turner	8.0
A 2142 PTG2	15 59 16	27 28 08	EPI	M. Turner	10.0
MARK 876	16 13 57	65 43 09	RGS	F. Jansen	10.0
Sco Cen field 1	16 14 00	-23 00 00	EPI	F. Jansen	50.0
A2163 offset-3	16 14 34	-06 09 00	EPI	M. Turner	25.0
sig CrB	16 14 41	33 51 30	RGS	B. Brinkman	40.0
A2163 offset-2	16 15 46	-05 50 60	EPI	M. Turner	25.0
A2163	16 15 46	-06 09 00	EPI	M. Turner	20.0
A2163 offset-4	16 15 46	-06 27 00	EPI	M. Turner	25.0
A2163 offset-1	16 16 48	-06 09 00	EPI	M. Turner	25.0
1E 1613-5055 / RCW 1	16 17 35	-51 02 25	EPI	M. Turner	50.0
HVCs/Draco #1	16 18 60	60 00 00	EPI	F. Jansen	10.0
MS1621.5+2640	16 23 36	26 33 50	EPI	K. Mason	10.0
Rho Oph field 1	16 25 17	-24 16 48	EPI	F. Jansen	50.0
RHO OPH CORE	16 27 26	-24 40 48	EPI	M. Watson	25.0
PG1626+554	16 27 56	55 22 31	EPI	K. Mason	9.0
4U 1627-67	16 32 17	-67 27 42	RGS	B. Brinkman	20.0
A2204	16 32 46	05 34 48	EPI	M. Turner	20.0
HVCs/Draco #2	16 34 60	63 52 60	EPI	F. Jansen	10.0
A2218	16 35 48	66 12 36	EPI	M. Turner	40.0
tau Sco	16 35 53	-28 12 58	RGS	B. Brinkman	20.0
PSR B1634-45	16 37 59	-45 53 28	EPI	F. Jansen	5.0
A2219	16 40 24	46 42 36	EPI	M. Turner	30.0
Ophiuchus cloud	16 40 48	-24 06 00	EPI	B. Aschenbach	15.0
Ophiuchus cloud 2	16 40 48	-24 23 60	EPI	B. Aschenbach	15.0

Ophiuchus cloud 3	16 40 48	-24 41 60	EPI	B. Aschenbach	15.0
X1636-536	16 40 55	-53 45 05	EPI	B. Aschenbach	20.0
Draco cloud #1	16 51 00	60 58 00	EPI	F. Jansen	10.0
NGC 6240	16 52 59	02 24 04	EPI	B. Aschenbach	20.0
Mkn 501	16 53 52	39 45 37	RGS	B. Brinkman	20.0
North Polar Spur	16 53 60	14 18 00	EPI	B. Aschenbach	20.0
North Polar Spur 2	16 53 60	14 54 00	EPI	B. Aschenbach	20.0
North Polar Spur 3	16 53 60	15 30 00	EPI	B. Aschenbach	20.0
GRO J1655-40	16 54 00	-39 50 45	EPI	M. Watson	17.0
GRO J1655-40	16 54 00	-39 50 45	EPI	M. Watson	35.0
GRO J1655-40	16 54 00	-39 50 45	EPI	M. Turner	20.0
HD 152248	16 54 10	-41 49 30	EPI	K. Mason	30.0
HD 152248	16 54 10	-41 49 30	EPI	K. Mason	30.0
HD 152248	16 54 10	-41 49 30	EPI	K. Mason	30.0
HD 152248	16 54 10	-41 49 30	EPI	K. Mason	30.0
HD 152248	16 54 10	-41 49 30	EPI	K. Mason	30.0
HD 152248	16 54 10	-41 49 30	EPI	K. Mason	30.0
Her X-1	16 57 50	35 20 33	RGS	B. Brinkman	100.0
Draco cloud #2	16 57 60	61 32 60	EPI	F. Jansen	10.0
A2256_field2	16 59 22	78 38 56	EPI	M. Turner	10.0
A2256_field4	16 59 46	78 58 28	EPI	M. Turner	10.0
A2256_field6	16 59 59	78 19 13	EPI	M. Turner	10.0
Finger/Draco #1	17 00 00	59 40 00	EPI	F. Jansen	10.0
RXJ 1701.3	17 01 23	64 14 08	EPI	F. Jansen	20.0
GX 339-4	17 02 46	-48 47 37	EPI	B. Aschenbach	9.0
GX 339-4	17 02 49	-48 47 22	EPI	M. Turner	5.0
IRAS17020+4544	17 03 30	45 40 44	EPI	M. Turner	10.0
Abell 2256	17 03 36	78 43 00	EPI	F. Jansen	50.0
G344.7-0.1	17 03 60	-41 42 30	EPI	M. Watson	9.0
PSR J1705-1906	17 05 36	-19 06 38	EPI	K. Mason	5.0
Finger/Draco #2	17 07 00	59 00 00	EPI	F. Jansen	10.0
A2256_field5	17 07 43	78 19 41	EPI	M. Turner	10.0
A2256_field3	17 07 52	78 57 41	EPI	M. Turner	10.0
A2256_field1	17 07 55	78 37 56	EPI	M. Turner	10.0
X1705-440	17 08 55	-44 06 02	EPI	B. Aschenbach	10.0
PSR J1709-4428	17 09 42	-44 28 57	EPI	K. Mason	90.0
RXJ1712.6-2414	17 12 36	-24 14 41	EPI	B. Aschenbach	20.0
A2255	17 12 45	64 04 00	EPI	M. Turner	20.0
GRS 1716-249	17 19 37	-25 01 03	EPI	M. Turner	10.0
PSR B1719-37	17 22 59	-37 12 04	EPI	F. Jansen	5.0
B2 1721+34	17 23 21	34 17 59	RGS	F. Jansen	9.0
46P/Wirtanen	17 29 56	-22 51 18	EPI	F. Jansen	22.0
PSR J1730-3350	17 30 33	-33 50 43	EPI	K. Mason	5.0
GC9	17 43 27	-29 47 34	EPI	M. Turner	15.0

1E1740.7-2942	17 44 03	-29 43 25	EPI	M. Turner	10.0
GC8	17 44 04	-29 34 25	EPI	M. Turner	20.0
GRO J1744-28	17 44 34	-28 45 22	EPI	M. Turner	5.0
GC7	17 44 44	-29 20 23	EPI	M. Turner	20.0
Sgr A*	17 45 40	-29 00 28	EPI	B. Aschenbach	50.0
GC6	17 45 40	-29 00 23	EPI	M. Turner	25.0
PSR B1742-30	17 45 56	-30 40 23	EPI	F. Jansen	5.0
GC10	17 46 08	-29 23 04	EPI	M. Turner	15.0
GC4	17 46 10	-28 38 37	EPI	M. Turner	20.0
GC5	17 46 26	-28 51 06	EPI	M. Turner	20.0
GC3	17 47 10	-28 28 03	EPI	M. Turner	20.0
GC2	17 47 21	-28 09 02	EPI	M. Turner	15.0
GC1	17 48 44	-28 05 06	EPI	M. Turner	15.0
PSR J1757-2421	17 57 41	-24 21 57	EPI	K. Mason	5.0
HD163993	17 57 46	29 14 53	RGS	F. Jansen	12.0
NGC 6552	18 00 07	66 36 54	EPI	M. Turner	10.0
V2301 Oph	18 00 36	08 10 12	EPI	K. Mason	5.0
PSR B1757-244	18 01 00	-24 51 29	EPI	F. Jansen	5.0
GRS 1758-258	18 01 13	-25 44 29	EPI	M. Turner	10.0
RE J1802+18	18 02 07	18 04 43	EPI	K. Mason	5.0
Comet 10P / Tempel 2	18 11 24	-28 54 17	EPI	B. Aschenbach	40.0
PSR 1811-19	18 11 33	-19 25 60	EPI	M. Turner	30.0
AM Her	18 16 13	49 52 03	RGS	B. Brinkman	86.0
Comet 10P / Tempel 2	18 16 22	-29 17 40	EPI	B. Aschenbach	30.0
Comet 10P / Tempel 2	18 21 29	-29 39 31	EPI	B. Aschenbach	30.0
KUV 18217+61419	18 21 57	64 20 36	EPI	M. Watson	6.0
P/Shoemaker	18 24 34	-41 47 57	EPI	F. Jansen	22.0
PSR J1825-0935	18 25 31	-09 35 23	EPI	K. Mason	5.0
X1822-371	18 25 47	-37 06 18	OM	M. Watson	50.0
Ridge_1	18 25 56	-12 13 33	EPI	M. Watson	9.0
Ridge_2	18 26 44	-11 51 26	EPI	M. Watson	9.0
Ridge_3	18 27 32	-11 29 19	EPI	M. Watson	9.0
Aquila Rift	18 27 60	-03 30 00	EPI	B. Aschenbach	20.0
Ridge_4	18 28 19	-11 07 11	EPI	M. Watson	9.0
Ridge_5	18 29 06	-10 45 03	EPI	M. Watson	9.0
Aquila Rift 2	18 29 36	-03 30 00	EPI	B. Aschenbach	20.0
Aquila Rift 3	18 31 12	-03 30 00	EPI	B. Aschenbach	20.0
NGC 6656 (M22)	18 36 24	-23 54 07	EPI	M. Turner	40.0
ESO 103-G35	18 38 20	-65 25 42	EPI	K. Mason	10.0
V347 Pav	18 44 48	-74 18 33	EPI	K. Mason	5.0
RX J1846.9+5538	18 46 59	55 38 34	EPI	K. Mason	5.0
PSR J1856+0113	18 56 11	01 13 21	EPI	K. Mason	5.0
RXJ1856.6-3754	18 56 35	-37 54 34	EPI	B. Aschenbach	50.0
R CR A	19 01 54	-36 57 04	EPI	M. Watson	20.0

EP Dra	19 07 06	69 08 42	EPI	K. Mason	5.0
Aql X-1	19 11 16	00 35 06	EPI	M. Turner	13.0
SS 433	19 11 50	04 58 58	RGS	B. Brinkman	150.0
SS433	19 11 50	04 58 58	EPI	B. Aschenbach	40.0
SS433 / 2	19 11 50	04 58 58	EPI	B. Aschenbach	40.0
RX J1914.4+2456	19 14 26	24 56 40	EPI	K. Mason	20.0
RXJ1914.4+2456	19 14 26	24 56 45	EPI	B. Aschenbach	20.0
GRS 1915+105	19 15 11	10 56 44	EPI	M. Turner	10.0
GRS 1915+105	19 15 11	10 56 44	EPI	M. Turner	10.0
GRS 1915+105	19 15 11	10 56 44	EPI	M. Watson	23.0
ESO 141-G55	19 21 14	-58 40 12	RGS	F. Jansen	33.0
PSR 1929+10	19 32 13	10 59 31	EPI	M. Turner	35.0
M55	19 39 59	-30 57 44	EPI	M. Watson	25.0
RX J1940.1-1025	19 40 12	-10 25 26	EPI	M. Turner	25.0
AB Dra	19 49 07	77 44 23	EPI	K. Mason	10.0
4P/Faye	19 57 05	-10 28 40	EPI	F. Jansen	22.0
RE J1957-57	19 57 11	-57 38 22	EPI	K. Mason	5.0
[HB89]2000-330	20 03 24	-32 51 45	EPI	K. Mason	30.0
V2009-65	20 08 56	-65 27 22	EPI	K. Mason	5.0
A3667_field5	20 10 26	-56 43 60	EPI	B. Aschenbach	15.0
A3667_field2	20 10 51	-56 39 10	EPI	B. Aschenbach	15.0
A3667_field4	20 11 25	-56 33 30	EPI	B. Aschenbach	15.0
A3667_field6	20 12 44	-57 01 15	EPI	B. Aschenbach	15.0
A3667_field1	20 13 15	-56 55 30	EPI	B. Aschenbach	15.0
A3667_field3	20 13 48	-56 49 30	EPI	B. Aschenbach	15.0
AXJ2019+112	20 19 18	11 27 15	EPI	M. Turner	40.0
55P/Tempel-Tuttle	20 22 14	-34 29 30	EPI	F. Jansen	22.0
RX J2022-39	20 22 37	-39 54 13	EPI	K. Mason	5.0
Cygnus X-3 (4U1822-3	20 32 26	40 57 28	EPI	M. Turner	20.0
VW CEP	20 37 17	75 35 35	RGS	F. Jansen	25.0
AE Aqr	20 40 10	-00 52 16	EPI	M. Watson	7.0
AT Mic	20 41 51	-32 26 07	RGS	B. Brinkman	20.0
AU Mic	20 45 09	-31 20 26	RGS	B. Brinkman	40.0
MRK 896	20 46 20	-02 48 46	EPI	M. Turner	8.0
HD199178	20 53 53	44 23 11	RGS	F. Jansen	6.0
HD199178	20 53 53	44 23 11	RGS	F. Jansen	6.0
MS2053.7-0449	20 56 22	-04 37 43	EPI	K. Mason	10.0
HU Aqr	21 07 58	-05 17 42	EPI	M. Watson	26.0
V1500 Cyg	21 11 37	48 09 02	EPI	K. Mason	5.0
EUVE J2115.7-5840	21 15 41	-58 40 52	EPI	M. Watson	100.0
PSR J2124-3358	21 24 44	-33 58 44	EPI	B. Aschenbach	70.0
PKS2126-158	21 29 12	-15 38 42	EPI	M. Watson	10.0
PKS 2126-158	21 29 12	-15 38 41	EPI	B. Aschenbach	20.0
CE Gru	21 37 56	-43 42 14	EPI	K. Mason	5.0

SS Cyg	21 42 43	43 35 09	EPI	M. Watson	7.0
Cyg X-2	21 44 40	38 19 14	EPI	B. Aschenbach	21.0
PKS 2149-306	21 51 56	-30 27 54	EPI	B. Aschenbach	20.0
A2390	21 53 37	17 41 45	EPI	M. Watson	20.0
NGC 7158	21 56 56	-11 39 32	EPI	B. Aschenbach	5.0
PKS 2155-304	21 58 51	-30 13 29	EPI	M. Turner	30.0
PKS 2155-304	21 58 53	-30 13 12	RGS	B. Brinkman	30.0
AR Lac	22 08 41	45 44 31	RGS	B. Brinkman	20.0
NGC 7213	22 09 16	-47 10 00	RGS	B. Brinkman	40.0
LBQS 2212-1759	22 15 32	-17 44 06	RGS	F. Jansen	75.0
Mark 304	22 17 12	14 14 21	EPI	B. Aschenbach	40.0
IIZw 177	22 19 19	12 07 57	EPI	B. Aschenbach	5.0
PHL 5200	22 28 30	-05 18 55	EPI	B. Aschenbach	50.0
NGC 7314	22 35 46	-26 03 02	RGS	B. Brinkman	40.0
ESO 602- G 031	22 36 56	-22 13 12	EPI	B. Aschenbach	5.0
NGC 7331	22 37 06	34 25 19	EPI	B. Aschenbach	10.0
UGC 12138	22 40 18	08 03 16	EPI	B. Aschenbach	5.0
Q2237+0305	22 40 30	03 21 30	EPI	M. Watson	40.0
EV Lac	22 46 49	44 20 49	RGS	B. Brinkman	20.0
REJ2248-511	22 48 41	-51 09 54	EPI	K. Mason	10.0
REJ2248-511(2)	22 48 41	-51 09 54	EPI	K. Mason	10.0
REJ2248-511(3)	22 48 41	-51 09 54	EPI	K. Mason	10.0
TY PsA	22 49 40	-27 06 55	EPI	K. Mason	10.0
A 3921	22 49 48	-64 22 60	EPI	M. Turner	30.0
2P/Encke	22 49 52	-02 22 53	EPI	F. Jansen	22.0
MR 2251-178	22 53 59	-17 33 50	EPI	M. Turner	5.0
NGC 7469	23 03 16	08 52 26	RGS	B. Brinkman	30.0
MCG -2-58-22	23 04 43	-08 41 08	EPI	K. Mason	10.0
SC2311-43	23 13 59	-42 43 36	RGS	B. Brinkman	30.0
CP Tuc	23 15 19	-59 10 28	EPI	K. Mason	5.0
NGC 7582	23 18 23	-42 22 11	EPI	M. Turner	20.0
Cas A (N)	23 23 21	58 49 06	RGS	J. Bleeker	25.0
Cas A (W)	23 23 21	58 49 06	RGS	J. Bleeker	25.0
Cas A (SE)	23 23 26	58 48 28	RGS	J. Bleeker	25.0
Abell 2597	23 25 18	-12 06 30	EPI	R. Mushotzky	20.0
EQ Peg	23 31 50	19 56 17	EPI	B. Aschenbach	15.0
NGC 7714	23 36 15	02 09 18	EPI	M. Watson	30.0
lamb And	23 37 34	46 27 30	RGS	B. Brinkman	25.0
HD223460	23 49 41	36 25 33	RGS	F. Jansen	6.0
HD223460	23 49 41	36 25 33	RGS	F. Jansen	6.0
Abell 2670	23 54 10	-10 24 18	EPI	R. Mushotzky	32.0
A 4059	23 57 01	-34 45 47	RGS	B. Brinkman	40.0
AM2354-304S	23 57 28	-30 27 39	EPI	B. Aschenbach	10.0